THE SETTLING BEHAVIOR OF RIGID SPHERES IN VISCOELASTIC NON-NEWTONIAN FLUIDS

By

Temitope Oluwaseun Okesanya

A thesis submitted in partial fulfillment of the requirements for the degree of

Master of Science

In

Petroleum Engineering

Department of Civil and Environmental Engineering

University of Alberta

ABSTRACT

Fluid-particle transport systems are ubiquitous in various industries. In the petroleum industry they are encountered in hydraulic fracturing where solid proppants are transported through fracturing fluids to induced fractures and in drilling operations where solid cuttings are circulated back to the surface. In the chemical industry, majority of the processes that deal with slurries and particle transport likewise involve fluid-particle transport systems. It is desirable that transported solids are suspended and reach their destination before settling in order to improve operational efficiency. However, in order to ensure particle suspension and cognize what conditions necessitate or hinder settling; the settling behavior of particles in these complex non-Newtonian fluids must be fully demystified. The accurate prediction and description of particle settling behavior in these non-Newtonian fluids is paramount for the design, analysis, and optimization of a wide spectrum of these fluid-particle industrial processes. It is therefore imperative to study and elucidate the settling behavior of particles in these types of fluids.

Hence, an experimental study was conducted to explicate and describe the settling behavior of spheres in non-Newtonian fluids by developing accurate predictive models of particle settling behavior in non-Newtonian fluids. Using a semi-mechanistic model based on the balance of the forces acting on the settling particle and detailed statistical analyses of the settling test measurement results, mathematical generalized models were developed for predicting settling velocity of spherical particles in viscoelastic and viscoinelastic power-law and viscoplastic fluids.

For the viscoelastic power-law fluids, comparative analysis showed that an increase in the fluid elasticity gave a corresponding decrease in the particle Reynolds number and dampened the particle settling velocity. This dampening effect can be attributed to the unique ability of elastic fluids to partially or fully regain their original structure after deformation. Statistical analyses

showed that the presented new models predict settling velocity accurately with a very low Percentage Mean Absolute Error (PMAE) of 7.5 % and 11% for viscoinelastic and viscoelastic power-law fluids respectively. The proposed models also exhibited very low Root Mean Square Error (RMSE) values of 0.04m/s and 0.03m/s for viscoinelastic and viscoelastic fluids respectively.

For the viscoplastic fluids, statistical and investigative analyses showed that presented new model predicts settling velocity better than existing models with the lowest approximate Percentage Mean Absolute Error (PMAE) of 24.5 % for all data points. In addition to enhanced prediction accuracy, this new model occludes application constraints and offers prediction versatility that is lacking in current existing models by being valid for diverse rheological models of non-Newtonian viscoplastic fluids. The proposed generalized model was further evaluated with viscoelastic yield stress fluids in order to investigate the effects of elasticity on the settling behavior and to assess its prediction performance. Experimental results showed that generalized model was able to provide settling velocity prediction for the elastic yield stress fluids with reasonable accuracy achieving a low Percentage Mean Absolute Error of 30.15 % and Root Mean Square Error (RMSE) of 0.02 m/s. While elasticity reduces the settling velocity in certain non-Newtonian fluids; however, in viscoplastic fluids the presence of a yield stress may eclipse the elastic property of the fluid leading to uniformity in settling behavior, which can be predicted with the generalized model.

Furthermore, in order to obtain a profound understanding of the individual effects of elasticity and viscous yield stress on the settling behavior of spherical particles and shape of induced yielded regions (which illustrates the influence of fluid properties on particle settling behavior) in these viscoplastic non-Newtonian fluids; an experimental study was conducted to

visualize and evaluate the flow field surrounding the spherical particles settling in viscoplastic fluids exhibiting elastic and inelastic behavior. Experimental results showed that for the same shear viscosity, increasing elasticity can dampen the particle settling velocity and fluid velocity profile significantly, which is beneficial for particle suspension during fluid transport. This inhibiting effect can also be achieved with greater potency by increasing the yield stress as well. Experimental images also showed that the shape of sheared region depends on the mean surficial stress exerted on the fluid by the settling particle and the physical property of the fluid. The set of fluids with different elastic property (but identical viscous property) gave similar shapes of yielded region when sheared by the same particle, however, increasing the viscous yield stress reduces the shape of the yielded region and changes the shape of the yielded region. This indicates the prominence of viscous yield stress as a major deciding factor in determining the shape of the yielded region. Finally, the existence of theoretical unyielded regions adjacent to the settling particle were observed experimentally for the first time in this study.

PREFACE

The research work done in this experimental study are presented in Chapter 4, Chapter 5 and Chapter 6 of this thesis. These three chapters are completely based on four distinct papers. I carried out all the experimental work in Chapter 5 and Chapter 6 by myself. Aibek Abdukarimov and I conducted all the experiments in Chapter 4. While I conducted the data analysis and authored the manuscripts for four papers related to these chapters, Dr. Ergun Kuru was the supervisory author and responsible for the manuscript revisions of all the four papers.

Chapter 5 of this thesis is partially based on two papers. The major sections of the chapter has been submitted and accepted as Temitope Okesanya and Ergun Kuru, "A New Generalized Model for Predicting Particle Settling Velocity in Viscoplastic Fluids." with paper number SPE-196104-MS for presentation at the 2019 SPE Annual Technical Conference and Exhibition to be held 30 September – 2 October 2019 in Calgary, Canada. The extended version of the chapter will also be submitted to the SPE (Society of Petroleum Engineers) Journal for review and possible publication.

The other remaining papers (Chapter 4 and 6) will be submitted to relevant journals for publication. Chapter 4 is titled "Generalized Models for Predicting the Drag Coefficient and Settling Velocity of Rigid Spheres in Viscoelastic and Viscoinelastic Power- Law Fluids" while Chapter 6 is titled "Experimental Visualization and Analysis of Elastic and Viscous Effects on the Flow Field Surrounding a Settling Particle in Viscoplastic Fluids using Particle Image Velocimetry (PIV)".

DEDICATION

This project is dedicated to the Almighty God (Ọlọrun) for His faithfulness, provision, direction and protection over me throughout my stay in the University of Alberta; and also to my amazing family for all their love, support and prayers.

ACKNOWLEDGEMENTS

First of all, I am immensely grateful to my supervisor, Dr. Ergun Kuru for his invaluable guidance and constant support throughout the authorship of this project. His commitment towards research and his students are exceptional and highly appreciated. He took so much interest in ensuring that I gave my all towards the success of this project. Without him, I never would have completed this thesis.

I would also like to express my sincere appreciation to Mr. Todd Kinnee, and Mr. John Czuroski for their technical advice and assistance in procuring essential materials needed for this study. Special thanks to Majid Bizhani, Sumanth Arnipally, Xinxiang Yang, Mehmet Hirpa and Aibek Abdukarimov for assisting me in the experimental setup and also for their expert technical advice whenever I faced difficulties.

I am indeed grateful to God for his mercies thus far. My profound gratitude goes to my parents Engr. and Mrs. Okesanya for their encouragement and support throughout my stay in the University. I also owe a huge thank you to my wonderful sisters, Dr. Jola Adeaga and Engr. Tolu Kotti for their outstanding support during the entirety of my program. The success of this project is predominantly due to the encouragement and support I had from my family members and friends.

I also appreciate all professors in the department Petroleum Engineering who directly or indirectly have deposited knowledge and virtues in me, which helped in the overall success of this project. I would like to acknowledge Professor Dr. David S. Nobes. He was vastly instrumental in

ameliorating my MATLAB programming skills and in my overall practical development as an engineer.

This research is financially supported through the funds available from Natural Sciences and Engineering Research Council of Canada (NSERC RGPIN-2016-04647 KURU and NSERC RGPIN 238623 KURU).

TABLE OF CONTENTS

ABSTRACT ii

PREFACE v

DEDICATION vi

ACKNOWLEDGEMENTS vii

TABLE OF CONTENTS ix

TABLE OF FIGURES xxii

LIST OF TABLES xxx

NOMENCLATURE AND ABREVIATIONS xxxii

CHAPTER 1 : INTRODUCTION 1

1.1 Overview 2

1.2 Problem Statement 3

1.3 Objectives and Scope of Study 6

1.3.1 The Objectives of "Generalized Models for Predicting the Drag Coefficient and Settling Velocity of Rigid Spheres in Viscoelastic and Viscoinelastic Power-Law Fluids" 6

1.3.2 The Objectives of "A New Generalized Model for Predicting the Drag Coefficient and Settling Velocity of Rigid Spheres in Viscoplastic Fluids" 7

1.3.3 The Objectives of "Experimental Visualization and Analysis of Elastic and Viscous Effects on the Flow Field Surrounding a Settling Particle in Viscoplastic Fluids using Particle Image Velocimetry (PIV)". 8

1.4 Contributions of the Current Study 9

1.4.1 The Contributions of "Generalized Models for Predicting the Drag Coefficient and Settling Velocity of Rigid Spheres in Viscoelastic and Viscoinelastic Power- Law Fluids" 9

1.4.2 The Contributions of "A New Generalized Model for Predicting Particle Settling Velocity in Viscoplastic Fluids"..... 10

1.4.3 The Contributions of "Experimental Visualization and Analysis of Elastic and Viscous Effects on the Flow Field Surrounding a Settling Particle in Viscoplastic Fluids using Particle Image Velocimetry (PIV)". 11

1.5 Structure of Thesis 12

1.6 References 15

CHAPTER 2 : LITERATURE REVIEW 18

2.1 Background 19

2.2 Fluid Rheology 19

2.2.1 Shear Stress 20

2.2.2 Shear Rate 21

2.2.3 Viscosity 21

2.2.4 Newtonian Fluids 22

2.2.5 Non-Newtonian Fluids 23

2.2.6 Time Independent non-Newtonian Fluids 23

2.2.6.1 Pseudoplastic (Shear-Thinning) Fluids 24

2.2.6.2 Viscoplastic Fluids 26

2.2.6.3 Dilatant (Shear Thickening) Fluids 27

2.2.7 Time Dependent Fluids 27

2.2.7.1 Measurements of the Thixotropy 28

2.2.8 Viscoelastic Fluids 29

2.2.8.1 The Longest Relaxation Time 31

2.3 Yield Stress Phenomena 33

2.3.1 Complexities of the Yield Stress 34

2.3.2 Relationship between Yield Stress and Thixotropy 37

2.3.3 Measurements of the Yield Stress 38

2.4 The Settling Behavior of Particles 40

2.4.1 Terminal Settling Velocity and Drag Force 40

2.4.2 Settling Behavior of Particles in Newtonian Fluids 43

2.4.3 Prediction of Settling Velocity in Newtonian Fluids..... 45

2.4.4 Settling Behavior of Particles in non-Newtonian Viscoplastic Fluids 48

2.4.5 Prediction of Settling Velocity in non-Newtonian Viscoplastic Fluids 50

2.4.6 Influence of Elasticity on Particle Settling Behavior in non-Newtonian Viscoelastic Fluids 54

2.4.7 Effect of Elasticity and Viscosity on the Flow field and Shape of Yielded Regions surrounding a Settling Particle in a non-Newtonian Viscoplastic Fluid. 55

2.5 Particle Image Shadowgraphy (Literature Review) 59

2.5.1 Techniques used for measuring Terminal Settling Velocity in Literature. 59

2.5.2 Particle Image Shadowgraphy: History and Underlying Physics..... 61

2.5.3 Other Applications of Particle Image Shadowgraphy 63

2.5.4 Advantages of Image Shadowgraphy Over Other Measurement Techniques.. 64

2.6 References 66

CHAPTER 3 : EXPERIMENTAL PROGRAM 75

3.1 Experimental Materials 76

3.1.1 Glass Spheres 76

3.1.2 Fluid Column 78

3.1.3 Calibration Target 79

3.1.4 Polymers 79

3.1.4.1 Carbopol® (ETD 2020 and 940) 79

3.1.4.2 Hydrolyzed Polyacrylamide (HPAM) 80

3.1.4.3 Tylose® (Carboxymethyl Cellulose) 82

3.2 Polymer Preparation 83

3.2.1 Preparation Procedure for Carbopol 83

3.2.2 Preparation Procedure for Tylose and Hydrolyzed Polyacrylamide (HPAM) . 86

3.3 Rheological and Physical Characterization of Test Fluids 86

3.3.1 Measurement of Fluid Density 86

3.3.2 Rheological Measurements 87

3.3.2.1 Fann Viscometer (Model 35A) 87

3.3.2.2 Bohlin Rheometer 90

3.4 Rheological Measurements 91

3.4.1 Shear Viscometry Tests 91

3.4.2 Oscillation Frequency Sweep Test 92

3.5 Particle Image Shadowgraphy 94

3.5.1 The Mechanism and Technique of Particle Image Shadowgraphy 94

3.5.2 The Experimental Setup and Equipment of the Particle Image Shadowgraphy Experiment 95

3.5.2.1 Image Acquisition Device - The LaVision Imager Intense CCD Camera 97

3.5.2.2 Camera Lens – 12x Navitar Lens 98

3.5.2.3 Light source - A Double Pulse Solo III Laser 98

3.5.2.4 Diffuser – A LaVision High Efficiency Circular Diffuser Pair 99

3.5.2.5 Data Acquisition (DAQ) Software – Davis 8.3 software 101

3.5.3 Camera Position 102

3.5.4 Determination of Maximum Working Distance for Camera 103

3.5.5 Particle Image Shadowgraphy System Calibration 104

3.5.6 Experimental Procedure to Measure Particle Settling Velocity 106

3.5.7 Verification of Particle Image Shadowgraphy Measurements. 110

3.6 Particle Image Velocimetry (PIV)..... 112

3.6.1 The Mechanism and Technique of Particle Image Velocimetry (PIV) 112

3.6.2 The Experimental Setup and Equipment of the Particle Image Velocimetry Experiment 113

3.6.3 The Experimental Procedure to Determine Fluid Flow Field Using PIV 115

3.7 Sources of Errors and Mitigating Precautions to Prevent Them. 117

3.7.1 Error Sources in Experimental Fluid Preparation and Rheological Measurements 117

3.7.2 Error Sources in PIS and PIV Experimental Setup and Procedure 118

3.8 Safety Practices during Experiment 119

3.9 References 121

CHAPTER 4 : GENERALIZED MODELS FOR PREDICTING THE DRAG COEFFICIENT AND SETTLING VELOCITY OF RIGID SPHERES IN VISCOELASTIC AND VISCOINELASTIC POWER-LAW FLUIDS 124

4.1 Abstract 125

4.2 Introduction 127

4.3 Experimental Materials and Methodology 131

4.3.1 Test Materials. 131

4.3.2 Experimental Fluids 132

4.3.3 Rheological Measurements and Characterizations. 133

4.3.4 Experimental Setup 134

4.3.5 Verification of Particle Image Shadowgraphy Measurements. 136

4.3.6 Experimental Procedure. 137

4.4 Analysis and Discussion 139

4.4.1 Fluid Properties 139

4.4.2 Quantifying non-Newtonian Power-law Viscosity 141

4.4.3 Developing the Predictive Model for Viscoinelastic Power-law Fluids 142

4.4.4 Prediction of Particle Settling Velocity in Viscoinelastic Fluids 145

4.4.5 Statistical Evaluation of the Accuracy of the Model Developed for Prediction of the Settling Velocity in Viscoinelastic Power-law Fluids 145

4.4.6 Developing the Predictive Model for Viscoelastic Power-law Fluids 147

4.4.7 Statistical Evaluation of the Accuracy of the Model Developed for Prediction of the Settling Velocity in Viscoelastic Power-law Fluids 151

4.5 Conclusions 153

4.6 Acknowledgment 154

4.7 Nomenclature 155

Appendix A – Experimental Results 156

Appendix B – Settling Velocity Calculation Procedure and Example 161

References 164

CHAPTER 5 : A NEW GENERALIZED MODEL FOR PREDICTING THE DRAG COEFFICIENT AND SETTLING VELOCITY OF RIGID SPHERES IN VISCOPLASTIC FLUIDS 169

5.1 Abstract 170

5.2 Introduction 173

5.3 Experimental Materials and Methodology 180

5.3.1 Experimental Setup 180

5.3.2 Verification of Particle Image Shadowgraphy Measurements. 182

5.3.3 Test Materials. 183

5.3.4 Rheological Measurements and Characterizations. 185

5.3.5 Experimental Procedure. 187

5.4 Analysis and Discussion 189

5.4.1 Fluid Properties 189

5.4.2 Drag Curve for Viscoplastic Fluids. 193

5.4.3 Developing the Generalized Model. 197

5.4.3.1 Developing the Vt/V* vs $\boldsymbol{ReT}*$ Plot. 197

5.4.3.2 Direct Method to Predict Velocity 201

5.4.3 Statistical Evaluation. 204

5.4.4 The Settling Behavior of Spheres in Elastic Yield Stress Fluids. 207

5.4.4.1 Assessing the Generalized Drag Curve's Performance on Elastic Yield-Stress Fluids 208

5.4.4.2 Assessing the Generalized Vt/V* vs $\boldsymbol{ReT}*$ Curve's Performance on Elastic Yield-Stress Fluids 209

5.5 Conclusions 211

5.6 Acknowledgment 212

5.7 Nomenclature 213

Appendix A – Experimental Results 214

Appendix B – Settling Velocity Calculation Procedure and Example 220

Example Calculation of Particle Settling Velocity in Bingham Plastic Type Fluid (Comparison versus the measured data using present study experimental set-up) 222

Data 222

Appendix C – MATLAB Codes for Correlation Development 224

References 226

CHAPTER 6 : EXPERIMENTAL VISUALIZATION AND ANALYSIS OF ELASTIC AND VISCOUS EFFECTS ON THE FLOW FIELD SURROUNDING A SETTLING PARTICLE IN VISCOPLASTIC FLUIDS USING PARTICLE IMAGE VELOCIMETRY (PIV). 233

6.1 Abstract 234

6.2 Introduction 236

6.3 Experimental Materials and Methodology 241

6.3.1 Experimental Materials 241

6.3.2 Experimental Fluids and Preparation Procedure 241

6.3.3 Rheological Measurements and Characterizations. 243

6.3.4 Experimental Setup 243

6.3.5 Experimental Procedure 246

6.4 Results and Discussions 248

6.4.1 Test Fluid Properties 248

6.4.2 Velocity Field in a Sample Newtonian Fluid (Water). 252

6.4.3 Velocity Fields in the Carbopol Solutions 253

6.4.3.1 Effect of Fluid Elasticity on the Velocity Field around the Settling Particle 253

6.4.3.2 Effect of Fluid Shear Viscosity and the Yield Stress on the Velocity Field around the Settling Particle 257

6.4.4 Shape of Sheared Region 262

6.4.4.1 Shape of Sheared Regions Induced by a 2mm Spherical Particle Settling in Fluid A 262

6.4.4.2 Shape of Sheared Regions Induced by 2mm & 3mm Spherical Particles Settling in Fluid B 263

6.4.4.3 Shape of Sheared Regions Induced by 2mm Settling in Fluid C 266

6.5 Conclusions 267

6.6 Nomenclature 269

References 270

CHAPTER 7 : CONCLUSIONS AND RECOMMENDATIONS. 276

7.1 Major Summary and Conclusions of the Entire Study..... 277

7.2 Conclusions from “Generalized Models for Predicting the Drag Coefficient and Settling Velocity of Rigid Spheres in Viscoelastic and Viscoinelastic Power-Law Fluids” .. 282

7.3 Conclusions from “A New Generalized Model for Predicting the Drag Coefficient and Settling Velocity of Rigid Spheres in Viscoplastic Fluids.” 283

7.4 Conclusions from “Experimental Visualization and Analysis of Elastic and Viscous Effects on the Flow Field Surrounding a Settling Particle in Viscoplastic Fluids using Particle Image Velocimetry (PIV)”. 285

7.5 Recommendations for future study. 286

REFERENCES 288

TABLE OF FIGURES

Figure 2.1: Schematic Representation of Shear Flow (Barnes, 2000) 20

Figure 2.2: Shear Stress/Rate Relationships of various fluids 22

Figure 2.3: Region of constant viscosity observed in Polymeric solutions (Chhabra, 2006) 24

Figure 2.4: Results from a Thixotropic Loop Test (Kealy, 2007) 28

Figure 2.5: Mechanical Models Depicting Linear Elastic and Viscous Responses (Barnes, 2000) 31

Figure 2.6: Sample Oscillation Test Result 32

Figure 2.7: Different Definitions of the Yield Stress (Møller, Mewis and Bonn, 2006) 35

Figure 2.8: Tangent Method for Determining Yield Stress (Mezger, 2006). 39

Figure 2.9: amplitude Test Result showing the Yield Point (τy) and Flow Point (τf) 40

Figure 2.10: Schematic description of terminal velocity. 41

Figure 2.11: A graphical description of terminal velocity. 43

Figure 2.12: Universal Newtonian Drag Curve (Clift, Grace and Weber, 1978) 45

Figure 2.13: Standard Curve for a Sphere falling in a Newtonian Fluid (Wilson *et al.*, 2003; Shokrollahzadeh, 2015) 47

Figure 2.14 : Postulated shapes of the sheared envelope surrouding a sphere in creeping motion in Viscoplastic (Chhabra, 2006)..... 57

Figure 2.15: Schematic of the operating principle of image shadowgraphy 62

Figure 3.1: Fluid Column..... 78

Figure 3.2: Calibration sheet used to calibrate the camera 79

Figure 3.3: Molecular Chain Structure of Polyacrylic Acid (Wikipedia, 2019)..... 80

Figure 3.4: The Molecular Chain Structure of HPAM and PAM (Sorbie, 1992)..... 81

Figure 3.5: Molecular Structure of Carboxymethyl (Wikipedia, 2019). 82

Figure 3.6: Overhead Mixer for Preparing Polymer Sample..... 83

Figure 3.7: pH Benchtop Meter from Fisherbrand™ 84

Figure 3.8: Magnetic Stirrer for Preparing Smaller Samples of Polymers..... 85

Figure 3.9: ExplorerPro Weighing Balance..... 87

Figure 3.10: Fann Viscometer..... 88

Figure 3.11: Fann Viscometer Model 35A Schematic..... 89

Figure 3.12: Bohlin Rheometer..... 90

Figure 3.13: Shear Stress Vs Shear Rate 91

Figure 3.14: Shear Viscosity Vs Shear Rate 91

Figure 3.15: Sample Oscillation Test Result 93

Figure 3.16: Experimental Setup of Particle Image Shadowgraphy 95

Figure 3.17: The LaVision Imager Intense CCD Camera 97

Figure 3.18: 12x Navitar Lens 98

Figure 3.19: Double Pulse Solo III Laser from New Wave Research 99

Figure 3.20: The Action of a Diffuser. 100

Figure 3.21: Diffuser 100

Figure 3.22: High Efficiency Diffuser 100

Figure 3.23: Schematic of the Software algorithm to determine terminal velocity 101

Figure 3.24: Correct position and working distance 104

Figure 3.25: Wrong position and working distance. 104

Figure 3.26: Calibration Target 105

Figure 3.27: The process of System Calibration in Davis 8.3 software (Arnipally, 2017) 106

Figure 3.28: Experimental Image of Settling Particle Captured in the DaVis 8.3 Software 109

Figure 3.29: Davis 8.3 Processed Output Image after Particle Sizing Function (Shahi, 2014) .. 110

Figure 3.30: C_D vs Re_p Plot for the Verification of the PIS Measurements 111

Figure 3.31: A Schematic of the PIV Processing Algorithm 113

Figure 3.32: PIV Experimental Setup 114

Figure 4.1: Particle Image Shadowgraphy (PIS) Experimental Setup Used in the Current Study 134

Figure 4.2: Schematic of the Davis 8.3 software algorithm to determine terminal settling velocity (Okesanya and Kuru, 2019) 136

Figure 4.3: C_D vs Re_p Plot for the Verification of the PIS Measurements 137

Figure 4.4: Calibration Sheet 138

Figure 4.5: Shear Stress Vs Shear Rate plots for Tylose (0.24 wt. %) and HPAM (0.075 wt. %) 139

Figure 4.6: Viscosity Vs Shear Rate plots for Tylose (0.24 wt. %) and HPAM (0.075 wt. %) . 139

Figure 4.7: Oscillation Test Result for Tylose (0.24 wt.%) 140

Figure 4.8: Oscillation Test Result for HPAM (0.075 wt. %) 140

Figure 4.9: Re_p vs $CD.Rep$ Plot of Viscoinelastic Power-law Type fluids 144

Figure 4.10: Re_p vs $CD.Rep$ Plot of Viscoinelastic Power-law Type fluids 144

Figure 4.11: A plot of Predicted Settling Velocity vs. Measured Settling Velocity for the Viscoinelastic Power-law Type Fluids 147

Figure 4.12: $CD.Rep$vs Re_p Plot Based on the Available Data for Particle Settling Velocity in Viscoelastic and Viscoinelastic Power-law Type Fluids 148

Figure 4.13: Re_p vs $CD.Rep$ Plot based on the Available Data for Particle Settling Velocity in Viscoelastic Power-law Type Fluids 150

Figure 4.14: A plot of Predicted Settling Velocity vs. Measured Settling Velocity for Viscoelastic Fluids..... 152

Figure 5.1 Particle Image Shadowgraphy (PIS) Experimental Setup Used in the Current Study 180

Figure 5.2: Schematic of the Davis 8.3 software algorithm to determine terminal settling velocity 182

Figure 5.3: C_D vs Re_p Plot for the Verification of the PIS Measurements 183

Figure 5.4: Shear stress vs shear rate diagram of a selected Carbopol solution. 187

Figure 5.5: Calibration sheet used to calibrate the camera 188

Figure 5.6: Shear Stress Vs Shear Rate plots for Carbopol ETD 2020 (0.04 wt. %) and Carbopol 940 (0.06 wt. %)..... 190

Figure 5.7: Viscosity Vs Shear Rate plots for Carbopol ETD 2020 (0.04 wt. %) and Carbopol 940 (0.06 wt. %)..... 190

Figure 5.8: Oscillation Test Result for Carbopol ETD 2020 (0.04 wt. %) 192

Figure 5.9: Oscillation Test Result for Carbopol 940 (0.06 wt. %) 192

Figure 5.10: Plot of drag coefficient (C_D) vs particle Reynolds number (Re_p) with the Turton-Levenspiel Curve 194

Figure 5.11: Plot of drag coefficient (C_D) vs particle Reynolds number (Re_p) with the Present's Study Proposed Correlation Curve 195

Figure 5.12: V_t/V^* vs Re_T^* 200

Figure 5.13: V_t/V^* vs Re_T^* with entire data base. 201

Figure 5.14: Schematic Description of Shape Factor, ... 202

Figure 5.15: V_t/V^* vs Re_T^* for particle settling in Laminar flow regime. 207

Figure 5.16: Proposed Drag Curve Including Settling Velocity Data in Elastic Yield Stress Fluids. 208

Figure 5.17: V_t/V^* vs ReT $*$ curve Including Settling Velocity Data in Elastic Yield Stress Fluids. 210

Figure 6.1: Postulated shapes of the sheared envelope surrouding a sphere in creeping motion in Viscoplastic (Chhabra, 2006) 238

Figure 6.2: PIV Experimental Setup 244

Figure 6.3: A Schematic of the PIV Processing Algorithm 245

Figure 6.4: Processed PIV Image 246

Figure 6.5: Calibration Sheet 247

Figure 6.6: Flow Curves for Test Fluids 248

Figure 6.7: Shear Viscosity vs. Shear Rate Profiles of Test Fluids 248

Figure 6.8: Oscillation Frequency Sweep Test Result for Fluid A 250

Figure 6.9: Oscillation Frequency Sweep Test Result for Fluid B 250

Figure 6.10: Oscillation Frequency Sweep Test Result for Fluid C 251

Figure 6.11: Velocity Field induced by 2mm Sphere in Water. 252

Figure 6.12: Velocity field induced by 2mm sphere in Fluid A 253

Figure 6.14: Velocity field induced by 2mm sphere in Fluid C 254

Figure 6.14: Vector Velocity Profile along the Centerline of the Sphere 256

Figure 6.16: Velocity Field Induced by 2mm Sphere in Fluid B 258

Figure 6.16: Velocity field Induced by 3mm Sphere in Fluid B 259

Figure 6.17: Vector Velocity Profile along the Centerline of the Sphere for 2.00mm in Fluid A and Fluid B 261

Figure 6.19: Shape of Sheared Regions Induced by a 2mm Spherical Particle Settling in Fluid A (Black represents the unyielded zone and the colored region represents the yielded zones. The blended raw image is attached to the right) 262

Figure 6.20: Innermost Yielded Region obtained in this current study. 263

Figure 6.21: Shape of Yielded Region from Holenberg *et al.*, 2012 263

Figure 6.21: Shape of Sheared Regions Induced by a 2mm sphere Settling in Fluid B (The raw blended image is shown at the right) 264

Figure 6.22: Shape of Sheared Regions Induced by a 3mm sphere Settling in Fluid B (The raw blended image is shown at the right) 264

Figure 6.23: Shape of Sheared Regions Induced by a 3mm sphere Settling in Fluid B (The raw blended image is shown at the right) 267

LIST OF TABLES

Table 3.1: Physical Properties of the Spherical Particles 77

Table 3.2: HPAM Grades and Molecular weights..... 81

Table 3.3: Verification of PIS Measurements based on Measured Diameters 112

Table 4.1: Physical Properties of Spherical Particles 131

Table 5.1: Physical Properties of Spherical Particles 184

Table 5.2: Mathematical Equations for some popular viscoplastic models..... 186

Table 5.3: Fluid Rheological Properties Measured by the Fann Viscometer 191

Table 5.4: C_D Vs Re_p Statistical Evaluation Results for Proposed Correlation..... 196

5.5: R^2 Model Comparison 205

5.6: RMSE Model Comparison..... 205

5.7: PMAE Model Comparison 206

5.8: Newtonian Statistical Results 206

Table 6.1: Fluid Property measured by the Fann Viscometer 249

Table 6.2: Power Law Parameters of fluids..... 250

Table 6.3: Measured Particle Settling Velocity in Fluid A and Fluid C..... 257

Table 6.4: Measured Particle Settling Velocity in Fluid A and Fluid B..... 260

NOMENCLATURE AND ABREVIATIONS

Symbol	Description
Re*	Shear Reynolds number
Re_T^*	Present study's modified shear Reynolds number
Re_G^*	Rushd et al. modified shear Reynolds number
Re_p	Particle Reynolds number
V_t	Terminal settling velocity
$V*$	Particle shear velocity
V_{tm}	Measured settling velocity
V_{tp}	Predicted terminal settling velocity
α	Rheogram shape factor
$\dot{\gamma}$ or γ	Shear rate
C_{DP}	Predicted drag coefficient
C_{Dm}	Measured drag coefficient
μ	Viscosity

μ_B	Bingham plastic viscosity
μ_c	Casson plastic viscosity
ξ	Relative shear stress
ρ_s	Particle (sphere) density
ρ_f	Fluid density
τ or τ_y	Shear stress
C_D	Drag coefficient
V_t	Terminal settling velocity
V_{tm}	Measured settling velocity
V_{tp}	Predicted terminal settling velocity
α	Fluid Calibration Constant
Ƙ	Elasticity Factor
$\dot{\gamma}$ or γ	Shear rate
μ	Viscosity
R	Coefficient of Determination

Re_p	Reynolds Particle Number
d	Particle Diameter
ρ_s	Particle (sphere) density
ρ_f	Fluid density
τ	Shear Stress
$\bar{\tau}$	Mean Surficial Stress
k	Power-law consistency index
n	Power-law flow behavior index
g	Acceleration due to gravity
λ	Longest Relaxation Time
$\bar{\tau}$	Mean surficial stress on a falling sphere
τ_B	Bingham yield stress
τ_{HB}	Herschel-Bulkley yield stress
τ_c	Casson yield stress
k	Herschel-Bulkley consistency index

n	Herschel-Bulkley flow behaviour index
g	Acceleration due to gravity
CCD	Couple Charged Device
PIS	Particle Image Shadowgraphy
Ns	Nanoseconds
PPE	Personal Protective Equipment
SOP	Standard Operating Procedure
Nd:YAG	Neodymium-Doped Yttrium Aluminium Garnet
LED	Light-Emitting Diode
C_D	Drag Coefficient
g	Acceleration due to gravity
ρ_s	Density of solid
ρ_f	Density of fluid
D_p	Diameter of particle
Re_p	Reynolds number

V_s	Settling Velocity
μ_f	Viscosity of fluid
A	Area
t	Time
Δt	Time between frames
(X,Y)	Position of particles in Cartesian coordinates.

CHAPTER 1 : INTRODUCTION

1.1 Overview

Fluid-particle transport systems are ubiquitous in various industries. In the petroleum industry they are encountered in hydraulic fracturing where solid proppants are transported through fracturing fluids to induced fractures and in drilling operations where solid cuttings are circulated back to the surface (Kelessidis and Mpandelis, 2004; Agwu *et al.*, 2018). In the chemical industry, majority of the processes that deal with slurries and particle transport likewise involve fluid-particle transport systems. It is desirable that transported solid are suspended and reach their destination before settling in order to improve operational efficiency. However, in order to ensure particle suspension and cognize what conditions necessitate or hinder settling; the settling behavior of particles in these complex non-Newtonian fluids must be fully demystified. These complex fluids are termed non-Newtonian because of their eccentric property and lack of a constant viscosity in contrast to Newtonian fluids. Non-Newtonian fluids may possess an apparent yield stress (viscoplastic) or not (pseudoplastic).

Despite the fact that particle settling behavior in Newtonian fluids has been fully elucidated by several authors (Clift, Grace and Weber, 1978; Turton and Levenspiel, 1986; Chhabra, 2006; Shah, El-Fadili and Chhabra, 2007); however settling behavior in non-Newtonian has not been fully demystified (Dolejš, Doleček and Šiška, 1998; Shah, El-Fadili and Chhabra, 2007; Terfous, Hazzab and Ghenaim, 2013; Shahi and Kuru, 2015; Arnipally and Kuru, 2018). These non-Newtonian fluids are of prime importance because most of the complex fluids described in the processes above are shear thinning non-Newtonian fluids. As a result of this wide range of application, accurate knowledge and understanding of solid-liquid interaction and the settling

behavior of spheres in the non-Newtonian fluids are needed to model and optimize these industrial processes.

The major parameters needed to optimize these processes are the terminal (or settling) velocity of the particle and the drag coefficient both of which are interwoven and describe the rate of sedimentation of solid particles in liquids. The Terminal Settling velocity (V_t) is defined as the constant and unimpeded free falling velocity attained by a particle settling in a fluid when all the forces acting on the particle are balanced (i.e. under equilibrium). The settling velocity is termed hindered settling if the falling particle is impeded by other particles or a neighboring wall (McCabe and Harriot, 1987; Rushd *et al.*, 2018), which is common in industrial processes. Conversely, the hindered settling velocity is reportedly related to free terminal particle settling velocity (Kelessidis and Mpandelis, 2004; Rushd *et al.*, 2018); hence ensuing the priority for the estimation of free particle settling velocity. The settling velocity and drag coefficient is acknowledged to be affected by the particle and the fluid properties (Arnipally & Kuru, 2017; McCabe & Harriot, 1987).

1.2 Problem Statement

Due to complexities in particle properties and disparities in fluid properties, developing analytical solutions to describe the settling behavior of spheres in these fluids are problematic hence empirical correlations and experimental methods are utilized (Arnipally & Kuru, 2017; Kesely & Matoušek, 2016; Machač et al., 1995). This has resulted in a lot of research efforts put into accurately developing empirical correlations over a wide range of conditions to describe and model the settling behavior of spheres in non-Newtonian fluids. Describing settling behavior primarily entails the determination of the terminal settling velocity and drag coefficient; which is

the fundamental hydrodynamic characteristic of the particle motion falling through a fluid (Machač *et al.*, 1995).

The drag coefficient (C_D) defined as the ratio of the viscous drag force to the kinetic energy acting on the particle (Rushd *et al.*, 2018). It expressed mathematically as:

$$C_D = \frac{4(\rho_s - \rho_f)dg}{3V_t^2\rho_f} \tag{1.1}$$

Where d is diameter of the particle, ρ_f is the fluid density, ρ_s is the solid particle density and g is acceleration due to gravity. As earlier stated, due to the difficulty in developing analytical solutions, empirical correlations and experimental methods are employed in the determination of C_D. The solution method involves the development of a drag coefficient and particle Reynolds number correlation. The particle Reynolds number, Re_p which is another significant hydrodynamic dimensionless number that describes the ratio is kinetic forces to viscous forces experienced by the settling particle. It is expressed mathematically as;

$$Re_p = \frac{\rho_f V_t d}{\mu} \tag{2.2}$$

Where μ is Newtonian viscosity of the fluid medium. If the drag coefficient can be accurately determined with the aid of C_D-Re_p correlation, predicting the settling velocity can be achieved iteratively. In order to simplify the task for Viscoplastic non-Newtonian fluids, considerable amount of research efforts have been undertaken resulting in several numerical solutions as well as empirical correlations for predicting settling behavior in non-Newtonian fluids

each with their associated limitations that will be highlighted in subsequent chapters. In fact, there is currently no explicit direct method of prediction that is applicable to various models of viscoplastic fluids (Herschel Bulkley, Bingham Plastic, Casson Models etc). Consequently, there is still a need for a universal predictive model for all that offers versatility in application by occluding the practical constraints in current existing models and yields relatively more accurate results in inelastic viscoplastic fluids.

Furthermore, it is also possible for non-Newtonian fluids to exhibit elastic properties (Viscoelastic fluids). While several studies have demonstrated the influence of elasticity on a particle's settling behavior (Acharya, 1986; van den Brule and Gheissary, 1993; Malhotra and Sharma, 2012; Fraggedakis, Dimakopoulos and Tsamopoulos, 2016; Arnipally and Kuru, 2018; Arnipally, Bizhani and Kuru, 2019); However, current conventional approaches to estimate settling velocity and drag coefficient often occlude the effect of elasticity on particle settling which can lead to erroneous estimation. A study conducted by Arnipally and Kuru (2018) showed that settling velocity could be overestimated by up to 50 times if the effect of elasticity is not considered. Such large margin of error is unacceptable for most models where the particle settling velocity is required as an input for optimization and design calculations. Even still, elasticity effect is sometimes not considered in some drilling and fracturing operations which can affect operational efficiency (Bui et al., 2012; Arnipally and Kuru, 2018). It is therefore imperative to devise a means to mathematically and accurately account for elasticity in particle settling in viscoelastic fluids.

In addition to all these, another conundrum arises in the bid to determine what conditions necessitate or hinder settling. The isolated effect of elasticity and viscosity in inhibiting settling of suspended particles is still a widely discussed and debated topic (Arnipally and Kuru, 2018). It is

vital to ascertain which of these intrinsic factors can inhibit particle settling to facilitate better and more efficient design of engineering transport fluids for a variety of conditions as well as the optimization of a wide spectrum of industrial processes.

In order to optimize these fluid-transport processes, it is therefore imperative to develop models that accurately describe the settling behavior of particles in various types of non-Newtonian fluids. In cases where elasticity effects are expected, it is also essential to include and account for the drag effect caused by elasticity in these cases. Even after modelling particle settling behavior, it is also essential to determine what optimum fluid conditions hinder settling so as to design better transport fluids. To the best of my knowledge, there is no current study that has carried out any of these in Literature. Therefore, an experimental study was carried out to tackle each of the problems listed above and provide lasting engineering solutions.

1.3 Objectives and Scope of Study

The main aims and objectives of this essential experimental study are divided into three sections based on the individual papers that this thesis is comprised of:

1.3.1 The Objectives of "Generalized Models for Predicting the Drag Coefficient and Settling Velocity of Rigid Spheres in Viscoelastic and Viscoinelastic Power-Law Fluids"

- To measure the terminal settling velocity of particles in various viscoelastic fluids for augmenting the present corpus of experimental data in literature.
- To develop a new drag coefficient and particle Reynolds number correlation that is applicable to both viscoelastic and viscoinelastic Power law fluids

- To present a general explicit approach for predicting settling velocities of particles in viscoelastic and viscoinelastic power-law type fluids.

The following tasks were carried out in order to achieve the aims and objectives listed above:

- Elastic (Hydrolyzed Polyacrylamide) and Inelastic polymers (Tylose) were prepared.
- The investigative results were joined with various data published in the literature to create an extensive database and widen scope for empirical analysis.
- A new drag coefficient and Reynold number correlation for viscoelastic and viscoinelastic power law fluids was developed based on mechanistic analysis with elasticity being accounted for by the longest relaxation time
- The newly developed correlation and an advanced statistical modelling program (OriginPro 9.0) were used to mathematically create an explicit model that can be used for predicting particle settling velocity in viscoelastic and viscoinelastic fluids.

1.3.2 The Objectives of "A New Generalized Model for Predicting the Drag Coefficient and Settling Velocity of Rigid Spheres in Viscoplastic Fluids"

- To measure the terminal settling velocity of particles in various viscoplastic fluids intending to expand the present database of experimental data
- To develop a new Drag coefficient-particle Reynolds number (C_D-Re_p) correlation that is applicable to both Newtonian and non-Newtonian viscoplastic fluids

- To present a general non-iterative approach for predicting settling velocities of particles in Newtonian and non-Newtonian viscoplastic fluids irrespective of their rheological models (Casson Model, Herschel Bulkley Model, and Bingham Model etc.).

The following tasks were carried out in order to achieve the aims and objectives listed above:

- Inelastic and elastic viscoplastic polymers (Carbopol ETD 2020 and Carbopol 940) were prepared.
- The settling velocity of different spherical particles in these polymer solutions were measured using Particle Image Shadowgraphy (PIS) to get a database of settling test results.
- The experimental results were combined with experimental data published in the literature to broaden the range and applicability of empirical analysis.
- Advanced statistical analysis programs (OriginPro 9.0 and MATLAB r2018b) were utilized together with extensive experimental data to develop a new C_D-Re_p correlation.
- The newly developed C_D-Re_p correlation was used to develop a generalized model that can be used for predicting particle settling velocity in viscoplastic fluids.

1.3.3 The Objectives of "Experimental Visualization and Analysis of Elastic and Viscous Effects on the Flow Field Surrounding a Settling Particle in Viscoplastic Fluids using Particle Image Velocimetry (PIV)".

- To depict and visualize the intrinsic flow field surrounding a settling particle in such fluids using Particle Image Velocimetry (PIV),
- To investigate the isolated effects of viscous yield stress and elasticity on the fluid velocity profile and flow field surrounding the settling particle,

- And to corroborate valid postulates about the negative wake phenomena and the shape of the yielded region surrounding a settling particle using visual experimental evidence.

The following tasks were carried out in order to achieve the aims and objectives listed above.

- Two sets of fluids were prepared from two distinct Carbopol polymers (ETD 2020 and 940). First set of fluids exhibited similar shear viscosity and yield stress but differed in elastic properties while the second set of fluids had almost identical elasticity but disparate shear viscosity and yield stress.
- The settling velocities of the spherical particles (Specific gravity ranging from 2.5 – 3.9; Diameters: ranging from 2.00mm - 3.00 mm) in the various Carbopol solutions were measured using Particle Image Shadowgraphy (PIS).
- The fluid flow field and sheared region surrounding the settling particle was determined using the advanced Particle Image Velocimetry (PIV) technique.

It is important to note that this study has a streamline focus on non-Newtonian fluids only. The fifth and sixth papers are solely focused on elastic and inelastic viscoplastic fluids (presence of apparent yield stress). The fourth chapter is focused on elastic and inelastic power law type non-Newtonian fluids

1.4 Contributions of the Current Study

There were key contributions of this study to the general body of literature knowledge. Each coming from the individual papers that make up this study;

1.4.1 The Contributions of "Generalized Models for Predicting the Drag Coefficient and Settling Velocity of Rigid Spheres in Viscoelastic and Viscoinelastic Power- Law Fluids"

- A novel approach was presented in this study that can be used for estimating drag coefficient of settling particles in viscoelastic and viscoinelastic fluids.
- An explicit mathematical model was also presented to estimate settling velocity of spherical particles in viscoelastic and viscoinelastic fluids.
- This essential study supplements and provides vital particle settling velocity data that can be used for modeling relevant transport processes that involve elastic fluids.
- The experimental data obtained from this experimental study can also provide the basis for the optimized design of engineering transport viscoelastic fluids for a variety of conditions.

1.4.2 The Contributions of "A New Generalized Model for Predicting Particle Settling Velocity in Viscoplastic Fluids"

- The knowledge of particle settling velocity in viscoplastic fluids is indispensable for the design, analysis, and optimization of a wide spectrum of industrial processes such as cuttings transport in oil and gas well drilling and proppant transport in hydraulic fracturing operations.

- By augmenting the current corpus of experimental data; we have provided much-needed particle settling velocity database that can be used for modeling of relevant transport processes (i.e. cuttings and/or proppants transport).

- Finally, by combining a mechanistic model describing the forces acting on the settling particles with the newly developed C_D-Re_p correlation, we have presented a new generalized predictive model for particle settling velocity in elastic and inelastic

viscoplastic fluids that can be used for the optimization of particle transport in oil and gas well drilling and hydraulic fracturing operations.

1.4.3 The Contributions of "Experimental Visualization and Analysis of Elastic and Viscous Effects on the Flow Field Surrounding a Settling Particle in Viscoplastic Fluids using Particle Image Velocimetry (PIV)".

- The technical knowledge of particle settling in Non-Newtonian fluids is applicable to many operations ranging from hole cleaning in oil and gas drilling operations to slurry transport in mining engineering. By visualizing and investigating the individual effects of yield and elasticity we were able to show how these two rheological properties influence particle settling and its surrounding flow field.

- This study was able to corroborate the dampening effect of elasticity by providing authentic visual data that can provide the experimental basis for the optimized design of engineering transport fluids for a variety of conditions.

- The study provided experimental basis supporting the primacy of yield stress over elasticity when the two forces are simultaneously present in a fluid.

- Furthermore, for the first time in literature, the existence of theoretical unyielded regions adjacent to the settling particle were observed experimentally.

1.5 Structure of Thesis

The presented work is the entirety of an experimental study of settling behavior in non-Newtonian fluids.

- **Chapter 1: Introduction**
  - This chapter serves to give a general background and overview of the experimental study carried out in this thesis. It gives an adept summary of the key research problems, the aims and objectives of the study with the steps followed to tackle these problems. It is concluded by giving the advantageous contributions of this study as well as the structure.

- **Chapter 2: Literature Review**
  - The main aim of this chapter is to review previous literature to aid the understanding of technical aspects of the experiment study and introduce basic scientific principles relevant to the settling behavior of particles in fluids. Necessary scientific concepts were elucidated including the Yield Stress Phenomena.

- **Chapter 3: Experimental Program**
  - The main aim of this chapter is to give a general overview of the experimental setup and equipment used in this research study. Details on the experimental materials were also presented and how to obtain them. The detailed experimental procedure was also

presented. The main reason of this chapter is to provide an outline for new researchers to follow if they want to repeat this experimental procedure and obtain similar results.

- **Chapter 4: Generalized Models for Predicting the Drag Coefficient and Settling Velocity of Rigid Spheres in Viscoelastic and Viscoinelastic Power- Law Fluids**
  - The entirety of the first paper is presented in this chapter. The scientific approach followed to develop the model is explained in details and the settling velocity results of various particles in viscoelastic and viscoinelastic power-law type fluids are shown. The statistical analysis of the model are shown to authenticate the accuracy of the model. The chapter is concluded by presenting a practical example to calculate the terminal velocity of a spherical particle in a viscoelastic and viscoinelastic power-law type fluid using the model.

- **Chapter 5: A New Generalized Model for Predicting the Drag Coefficient and Settling Velocity of Rigid Spheres in Viscoplastic Fluids.**
  - The entirety of the second set of papers and the main results of the experimental study are presented in this chapter. The scientific approach followed to develop the model is explained in details and the settling velocity results of various particles in viscoplastic fluids using Particle Image Shadowgraphy (PIS) are shown. The statistical analysis of the model are shown to authenticate the accuracy of the model.

- **Chapter 6: Experimental Visualization and Analysis of Elastic and Viscous Effects on the Flow Field Surrounding a Settling Particle in Viscoplastic Fluids using Particle Image Velocimetry (PIV).**
  - The entirety of the third paper is presented in this chapter. The experimental results and images from the PIV tests are provided in this chapter. Relevant scientific discussions and conclusions were shown as well.

- **Chapter 7: Conclusions and Recommendations.**
  - The chapter provides a comprehensive summary of the entire study. It also provides future recommendations for subsequent and future experimental study. Thereby providing a direction for enthusiastic researchers

1.6 References

Acharya, A. (Ruma) (1986) 'Particle Transport in Viscous and Viscoelastic Fracturing Fluids.pdf', *SPE Production Engineering*, 34(March), pp. 104–110. doi: 10.2118/13179-PA.

Agwu, O. E. *et al.* (2018) 'Settling velocity of drill cuttings in drilling fluids: A review of experimental, numerical simulations and artificial intelligence studies', *Powder Technology*. Elsevier B.V., 339, pp. 728–746. doi: 10.1016/j.powtec.2018.08.064.

Arnipally, S. K., Bizhani, M., & Kuru, E. (2018). Experimental Investigation Of Flow Field Past A Spherical Particle Settling In Viscoelastic Fluids Using Particle Image Velocimetry. In ASME 2018 37th International Conference on Ocean, Offshore and Arctic Engineering (OMAE 2018) (pp. 1–10).

Arnipally, S. K., & Kuru, E. (2017). Settling Velocity of Particles in Viscoelastic Fluids: A Comparison of the Shear Viscosity vs Elasticity Effect. In SPE Annual Technical Conference and Exhibition held in San Antonio, Texas, 9-11 October 2017.Barnes, H. A. (2000) *A handbook of elementary rheology*, *Science*. doi: 10.1126/science.1201543.

Van den Brule, B. H. A. A. and Gheissary, G. (1993) 'Effects of fluid elasticity on the static and dynamic settling of a spherical particle', *Journal of Non-Newtonian Fluid Mechanics*, 49(1), pp. 123–132. doi: 10.1016/0377-0257(93)85026-7.

Chhabra, R. (2006) *Bubbles, Drops, and Particles in Non-Newtonian Fluids, Second Edition*. doi: 10.1201/9781420015386.

Chhabra, R. P. (1983) 'Some remarks on "Drag coefficients of a slowly moving sphere in

Non-Newtonian fluids"', *Journal of Non-Newtonian Fluid Mechanics*, 13(2), pp. 225–227. doi: 10.1016/0377-0257(83)80018-4.

Clift, R., Grace, J.R. and Weber, M.E. (1978) Bubbles, Drops and Particles. Academic Press, New York.

Dolejš, V., Doleček, P. and Šiška, B. (1998) 'Drag and fall velocity of a spherical particle in generalized newtonian and viscoplastic fluids', *Chemical Engineering and Processing: Process Intensification*, 37(2), pp. 189–195. doi: 10.1016/S0255-2701(97)00054-8.

Fraggedakis, D., Dimakopoulos, Y. and Tsamopoulos, J. (2016) 'Yielding the yield-stress analysis: A study focused on the effects of elasticity on the settling of a single spherical particle in simple yield-stress fluids', *Soft Matter*. Royal Society of Chemistry, 12(24), pp. 5378–5401. doi: 10.1039/c6sm00480f.

Kelessidis, V. C. and Mpandelis, G. (2004) 'Measurements and prediction of terminal velocity of solid spheres falling through stagnant pseudoplastic liquids', *Powder Technology*, 147(1–3), pp. 117–125. doi: 10.1016/j.powtec.2004.09.034.

Machač, I. *et al.* (1995) 'Fall of spherical particles through non-Newtonian suspensions', *Chemical Engineering Science*, 50(20), pp. 3323–3327. doi: 10.1016/0009-2509(95)00168-5.

Malhotra, S. and Sharma, M. M. (2012) 'Settling of spherical particles in unbounded and confined surfactant-based shear thinning viscoelastic fluids: An experimental study', *Chemical Engineering Science*, 84(January), pp. 646–655. doi: 10.1016/j.ces.2012.09.010.

McCabe, W. and Harriot, P. (1987) 'Unit Operations Of Chemical Engineering, 5th Ed,

McCabe And .pdf', pp. 500–528. doi: 10.1016/j.eplepsyres.2011.07.014.

Mezger, T. G. (2006) "*The Rheology Handbook"* 2nd Revised Edition. Hannover: Vincentz Network, 2006

Rushd, S. *et al.* (2018) 'Terminal settling velocity of a single sphere in drilling fluid', *Particulate Science and Technology*. Taylor & Francis, 0(0), pp. 1–10. doi: 10.1080/02726351.2018.1472162.

Shah, S. N., El-Fadili, Y. E. and Chhabra, R. P. (2007) 'New model for single spherical particle settling velocity in power law (viscoinelastic) fluids', 33, pp. 51–66. doi: 10.1016/j.ijmultiphaseflow.2006.06.006.

Shahi, S. and Kuru, E. (2015) 'An experimental investigation of settling velocity of natural sands in water using Particle Image Shadowgraph', *Powder Technology*. Elsevier B.V., 281, pp. 184–192. doi: 10.1016/j.powtec.2015.04.065.

Terfous, A., Hazzab, A. and Ghenaim, A. (2013) 'Predicting the drag coefficient and settling velocity of spherical particles', *Powder Technology*. Elsevier B.V., 239, pp. 12–20. doi: 10.1016/j.powtec.2013.01.052.

Turton, R. and Levenspiel, O. (1986) 'A short note on the drag correlation for spheres', *Powder Technology*, 47(1), pp. 83–86. doi: 10.1016/0032-5910(86)80012-2.

CHAPTER 2 : LITERATURE REVIEW

The main aim of this chapter is to review previous literature to aid the understanding of technical concepts of this experimental study and introduce basic scientific principles relevant to the settling behavior of particles in fluids. Necessary scientific concepts were elucidated including the Yield Stress Phenomena and Thixotropy as well as the available techniques and methods for measuring them. The chapter is completed by carrying a detailed review of the experimental method utilized in the study.

2.1 Background

When particles are transported by fluids, it is desirable to know what conditions induce suspension and what conditions prompt sedimentation. Even if sedimentation occurs, it is also desirable to know the rate the particles are settling in order to improve operational efficiency. The accurate estimation of particle settling velocity in fluids is imperative for the design and optimization of fluid-particle transport systems. These systems are encountered in various processes including drill cuttings transport in oil and gas well drilling operations and proppant transport in hydraulic fracturing operations. The knowledge of particle settling behavior in fracturing fluid is vital in estimating fracture closure and fracture conductivity which are used in ameliorating well productivity (Shah, El-Fadili and Chhabra, 2007). Relevant work has been done on this topic in anteceding decades. This chapter reviews previous literature and concepts relevant to this research.

2.2 Fluid Rheology

Different fluids exhibit different properties especially when acted on by a shearing force. A summary of various fluid types and rheology is presented below. However discussing the types of fluids, it is necessary to explain some key concepts including the yield stress phenomena.

2.2.1 Shear Stress

This is defined as the tangential stress acting on a fluid causing fluid layers to slide over each other. It is mathematically denoted as the ratio of shear force to the unit area it is acting on and it is denoted by τ. The shear force (F) always act parallel to the fluid layers and surface plane as shown in the figure below.

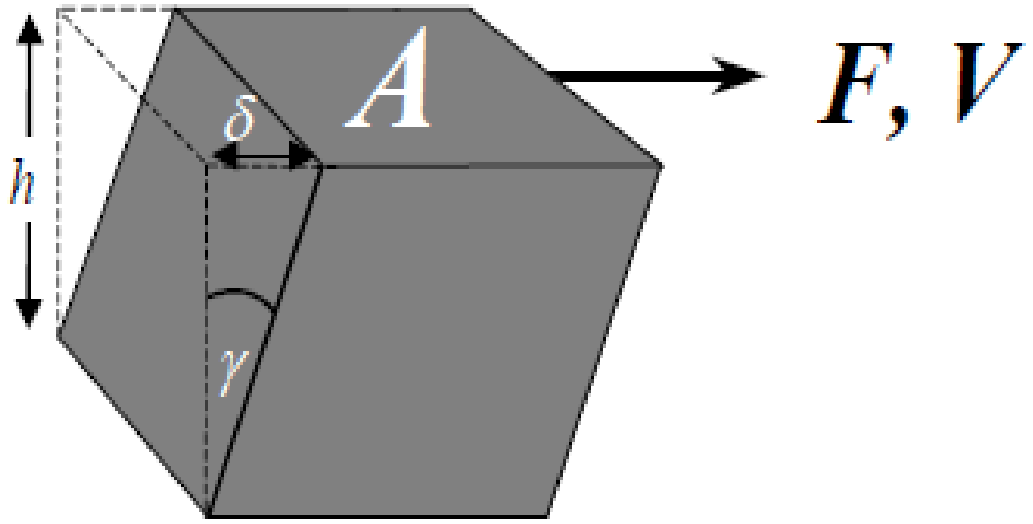

Figure 2.1: Schematic Representation of Shear Flow (Barnes, 2000)

If F is the shearing force acting on the unit of fluid and A is the area it is acting upon. Therefore, the shear stress is given by,

$$\tau = \frac{F}{A} \tag{2.1}$$

The S.I unit of shear stress is Pascal. In the Petroleum industry lb/100ft^2 is used.

2.2.2 Shear Rate

This is defined as the rate of deformation of a fluid. When a shear force acts upon a fluid, it deforms the fluid causing it to slide (or flow). The rate at which it flows is known as the shear rate. The layers will be sliding at different speeds over themselves and the speed increases towards the shearing force. The shear rate is defined as the velocity gradient between the fluid layers in the flow's perpendicular direction (Barnes, 2000; Mezger, 2006). It is denoted by $\dot{\gamma}$. If V is the velocity at the top layer induced by shear force and h is the distance between the layers, then the shear rate is given by the equation below.

$$\dot{\gamma} = \frac{V}{\mathrm{h}} \tag{2.2}$$

The S.I unit of shear rate is s^{-1}.

2.2.3 Viscosity

Viscosity is defined as the resistance of flow. It occurs as a result of the internal friction between layers of the fluid. If the internal friction is high, there will be a greater difficulty in layers sliding over themselves. It is denoted by μ. Mathematically, it is defined as the ratio of shear stress to shear rate.

$$\mu = \frac{\tau}{\dot{\gamma}} \tag{2.2}$$

It has an S.I unit of Pa.s. Viscosity is a function of pressure and temperature.

2.2.4 Newtonian Fluids

A Newtonian fluid is a fluid whose viscosity is independent on the shearing rate acting on it. In order words, a graphical plot of the shear stress vs shear rate also known as the flow curve or rheogram will give a straight line that passes through the origin with the slope equal to the viscosity of the fluid (Figure 2.2). This single constant viscosity characterizes a Newtonian fluid at a fixed temperature and pressure. Examples include water, glycerin, all gases, low molecular weight liquids and their solutions, molten salts, and liquid metals (Chhabra, 2006).

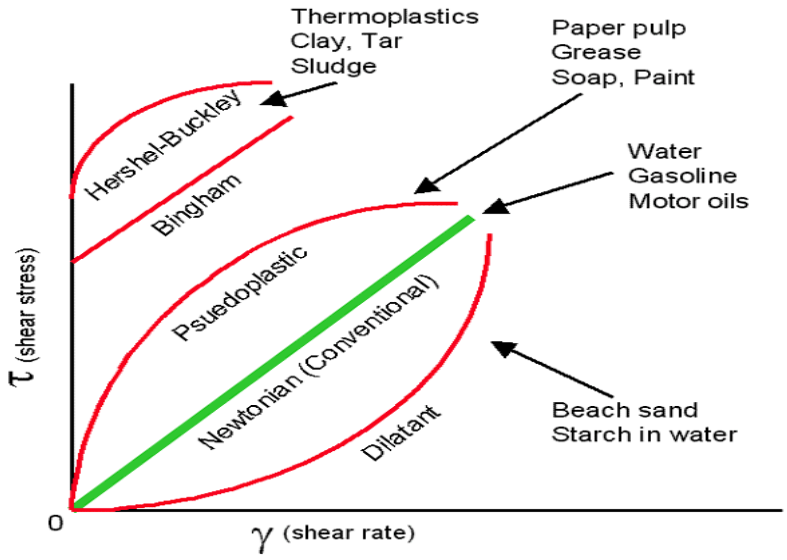

Figure 2.2: Shear Stress/Rate Relationships of various fluids

The Newtonian flow curve is modelled by the equation show. It is the basic version of the shear stress/rate relaionship

$$\tau = \mu\dot{\gamma} \tag{2.3}$$

2.2.5 Non-Newtonian Fluids

In contrast to Newtonian fluids, non-Newtonian fluids do not possess a single constant viscosity. Its flow curve is non-linear or if linear it doesn't pass through the origin. Their viscosity is dependent on the a variety of factors including shear rate, shear stress, flow conditions, kinematic history of the fluid etc. (Chhabra, 1983; Barnes, 2000). There are various types of non-Newtonian fluids depending on their flow properties. Chhabra (2006) classified non-Newtonian fluids into three major categories. While this may serve as a general guideline however this categorization should not be taken arbitrarily because in reality fluids may exhibit a combination of two or more properties of these categories. The categories include;

- Time Independent non-Newtonian Fluid
- Time Dependent non-Newtonian Fluid
- Viscoelastic non-Newtonian Fluid.

2.2.6 Time Independent non-Newtonian Fluids

These are fluids whose flow properties are independent on their shear history. In other words, their rate of shear is solely determined by the current value of shear stress or vice versa (Chhabra, 2006). These type of fluid fluids may be further subdivided into three different types of non-Newtonian fluids;

- Pseudoplastic (Shear Thinning) Fluids.
- Viscoplastic Fluids.
- Dilatant (Shear Thickening) Fluids.

2.2.6.1 Pseudoplastic (Shear-Thinning) Fluids

These are fluids whose apparent viscosity decreases with increasing shear rate (Figure 2.2). In order words, it thins out due to shear hence the name shear thinning. It is the most commonly encountered type of fluid behavior. Another major characteristic of the Pseudoplastic is the lack of an apparent yield stress, hence its non-Linear flow curve starts from origin as shown in Figure 2.1. The rate of decrease is characteristic to each fluid and differs from that of other fluids. For most polymers that are sheared over an extremely wide range of shear rates, regions of constant viscosity at very high and low shear rates are observed as shown in figure below.

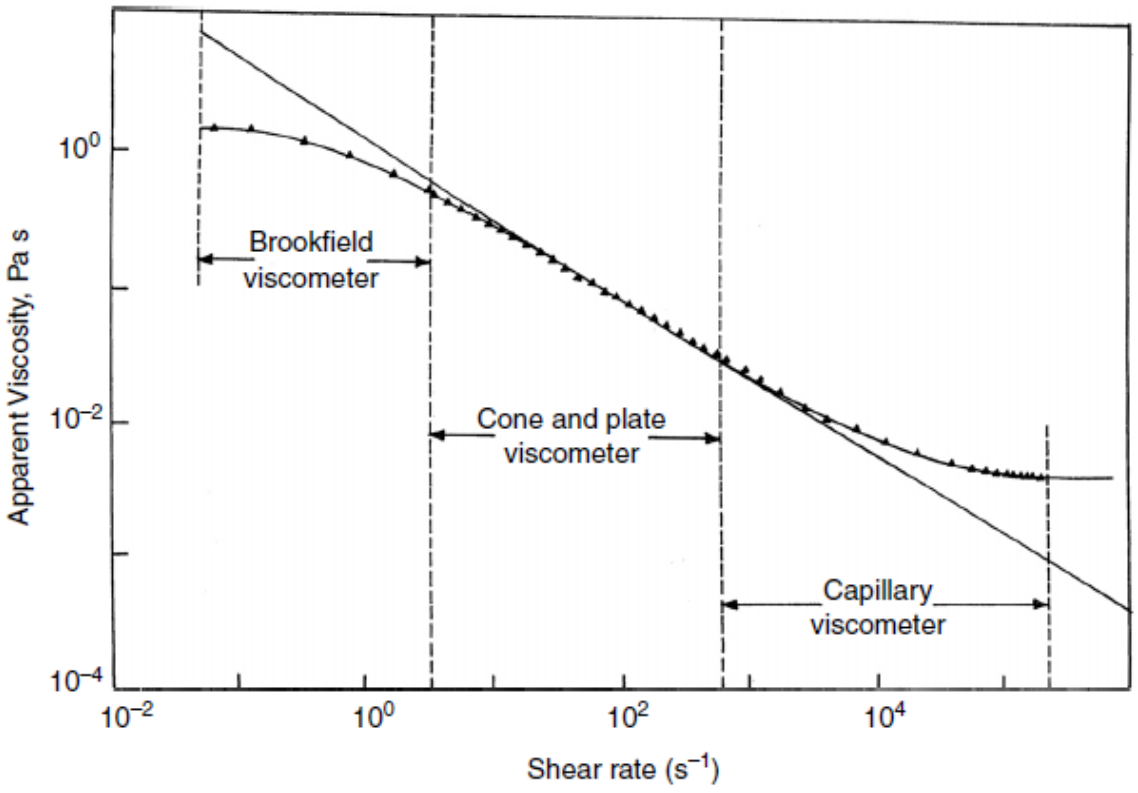

Figure 2.3: Region of constant viscosity observed in Polymeric solutions (Chhabra, 2006)

The flow behavior of pseudoplastic fluids can be mathematical modelled in various ways.

Below is a table showing various models;

Model	Equation
The Power-Law or Ostwald-De Waele Model	$\tau = k\dot{\gamma}^n$
The Cross Model	$\frac{\mu - \mu_\infty}{\mu_0 - \mu_\infty} = \frac{1}{1 + (\lambda\dot{\gamma}_{yx})^{2/3}}$
The Carreau Model	$\frac{\mu - \mu_\infty}{\mu_0 - \mu_\infty} = [1 + (\lambda\dot{\gamma}_{yx})^2]^{(n-1)/2}$
The Ellis Fluid Model	$\mu = \frac{\mu_0}{1 + (\tau_{yx}/\tau_{1/2})^{\alpha-1}}$

Where;

τ_{yx} *or* $\tau = Shear\ Stress$

$\tau_{1/2} = Model\ parameter\ Shear\ Stress$

$\dot{\gamma}_{yx}$ *or* $\dot{\gamma} = Shear\ Rate$

μ_0 *and* $\mu_\infty = Zero\ and\ Infinite\ Shear\ Viscosities\ (Figure\ 2.3)$

$\alpha = Characteristic\ Shear\ thinning\ Behavior$

$k = Power\ Law\ Consistency\ Index$

$n = Power\ Law\ flow\ behavior\ index$

2.2.6.2 Viscoplastic Fluids

Viscoplastic fluids are non-Newtonian fluids that undergo no permanent deformation unless the applied shear stress exceeds the minimum yield stress of the fluid. In other words, a viscoplastic fluid is a type of non-Newtonian fluid that possesses a threshold stress which must be exceeded before the fluid can flow or deform (Chhabra, 2006). Examples include drilling fluids, butter, jam, margarine etc. Once the yield stress is exceeded the flow curve becomes linear or non-linear. This substance exhibit both solid and liquid properties depending on the magnitude of the applied stress. For stress levels lower than the yield stress, the substance behave like a solid and if the applied stress is greater than the yield stress it behaves like a liquid. The yield stress can be seen as a measure of strength of the internal structure which resists deformation until the stress applied disintegrate the internal structure.

There are several mathematical models that describe the flow behavior of a viscoplastic fluid depending on how the fluid behaves after deformation (Figure 2.2). A list of viscoplastic mathematical models are shown below

Rheological Model	**Equations**
Bingham Plastic Model	$\tau = \tau_B + \mu_B \dot{\gamma}$
Casson Model	$\tau^{0.5} = {\tau_c}^{0.5} + (\mu_c \dot{\gamma})^{0.5}$
Herschel Bulkley	$\tau = \tau_{HB} + k\dot{\gamma}^n$

Where

$\tau = Shear\ Stress$

$\tau_{HB}\ or\ \tau_B\ or\ \tau_c = Yield\ Stress\ of\ respective\ models$

$\dot{\gamma} = Shear\ Rate$

$\mu_C = Casson\ Viscosity$

The Herschel Bulkley model has been reported by multiple authors to be the relatively accurate description of the drilling fluid rheology (Hemphill, Campos and Pilehvari, 1993; Rushd *et al.*, 2018).

2.2.6.3 Dilatant (Shear Thickening) Fluids

These are fluids whose apparent viscosity increases with increasing shear rate. They behave in direct contrast to Pseudoplastic fluids as shown in Figure 2.2. They are observed in corn starch. Qualitatively speaking, the increase in viscosity is believed to be caused by increased internal stability as a result of increased shear rate due to forces of attraction between molecules that make up of the polymer.

2.2.7 Time Dependent Fluids

These are fluids whose flow properties are dependent on their shear history or duration of shearing. In other words, their rate of shear is not solely determined by the current value of shear stress. For example if a particular fluid is sheared at a constant shear rate, after a while if the apparent viscosity increases or decreases then the fluid is said to be Time dependent. Examples include drilling fluids, crude oils etc. This behavior is due to continuous disintegration or integration of internal structures due to continuous shearing. In other words, a single value of shear rate can have multiple corresponding values of viscosity depending on the shearing history and duration of shear. This type of fluids can be subdivided into two other groups – Thixotropy or Rheopexy.

Thixotropic fluids are fluids whose apparent viscosity decreases with time at a constant shearing rate. In contrast to Rheopectic fluids whose apparent viscosity increases with time at a constant shear rate. They are both similar to shear thinning and shear thickening fluids just that their own apparent viscosity changes with respect to time at a constant value of shear while the later change apparent viscosity due changes in shear rate/stress.

2.2.7.1 Measurements of the Thixotropy

Thixotropy is a complicated property to measure due to the fact it is partially dependent on time. Kealy (2007) made a comprehensive review of the various methods of measuring Thixotropy. He identified three main methods that will be highlighted in this section.

The first method is known as the thixotropic loop test. It involves an upward Controlled Shear Stress (CSS) or Rate (CSR) ramp test followed by a downward ramp test.

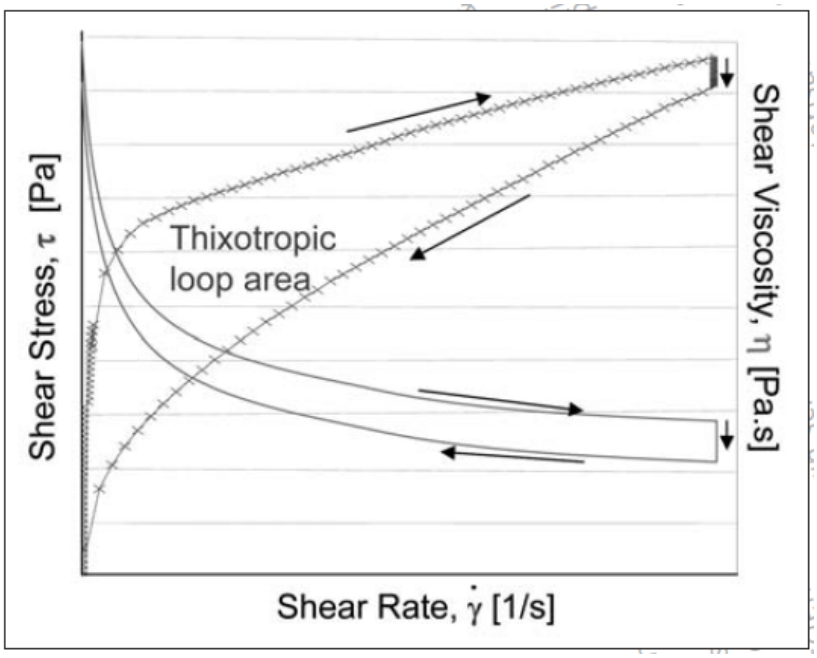

Figure 2.4: Results from a Thixotropic Loop Test (Kealy, 2007)

In order words, it involves a flow curve ramp test from zero shear rate to a maximum defined shear rate and a reversal ramp decrease from the maximum shear rate to the zero shear rate.The area within the curve gives a measure of thixotropy. If the fluid's microstructure wasn't affected by shear then it will give a similar curve both upwards and downwards but this isn't always the case due to thixotropy. So the greater the area under curve, the more thixotropic the fluid is.

The second method is known as the constant Shear test. As the name implies, it involves imposing a constant shear to a fluid and monitoring the response. The rate of degradation of viscous property or the time taken to reach an equilibrium value can be seen as a measure of thixotropy. It can be used as a yard stick for the comparative analysis of thixotropic properties of different fluids (Kealy, 2007).

Another method for quantifying the thixotropic property if a fluid is known as the Shear and Recovery Test. It involves the destruction of the internal microstructure of a fluid followed by the non-destructive evaluation of the internal microstructure of a fluid. In order words, a high shear rate is imposed on a fluid sample to destroy its microstructure and the time taken to regain its initial microstructure is measured and analyzed.

2.2.8 Viscoelastic Fluids

Viscoelastic fluids are non-Newtonian fluids that exhibit elastic properties. Some substances exhibit both viscous and elastic effects simultaneously as well. Elasticity is the unique property of a substance to regain its original shape after deformation which is achieved by storing energy. The

elasticity aspect obeys the Hooke's law which states that shear stress (τ) is directly proportional to the strain ($\frac{dx}{dy}$). The coefficient of proportionality is known as the Young's modulus (G).

$$\tau = G\frac{dx}{dy} \tag{2.4}$$

While the viscous property deals with the dissipation of deformation energy. The viscous property obeys the Newton's law which states that shear rate is directly proportional to the shear stress inducing the deformation. It is given in Equation 2.3.

When a fluid is at rest (a state of minimum energy) gets deformed, thermodynamic forces act to return the fluid to its original state. This is analogous with a spring which returns to its original state after being stretched. Both these processes are due to a form of energy called storage energy trying to reproduce the original state of the fluid. In order to understand these intrinsic properties, mechanical models are used.

The dashpot and spring models are physical mechanical models used to describe viscous and elastic effects properly (Figure 2.5). A spring is a simple mechanical model which represents a linear elastic element that follows the Hooke's law (Equation 2.4). In the same way, the dashpot is a mechanical model representing the linear viscous response (Equation 2.3). If the spring and dashpot are connected in series we obtain the simplest representation of a viscoelastic fluid which is called the Maxwell Model (Figure 2.4). If the spring and dashpot are connected in parallel we obtain the simplest representation of a viscoelastic solid which is the kelvin Voigt Model. The combination of these models in series give the Burgers model (Barnes, 2000).

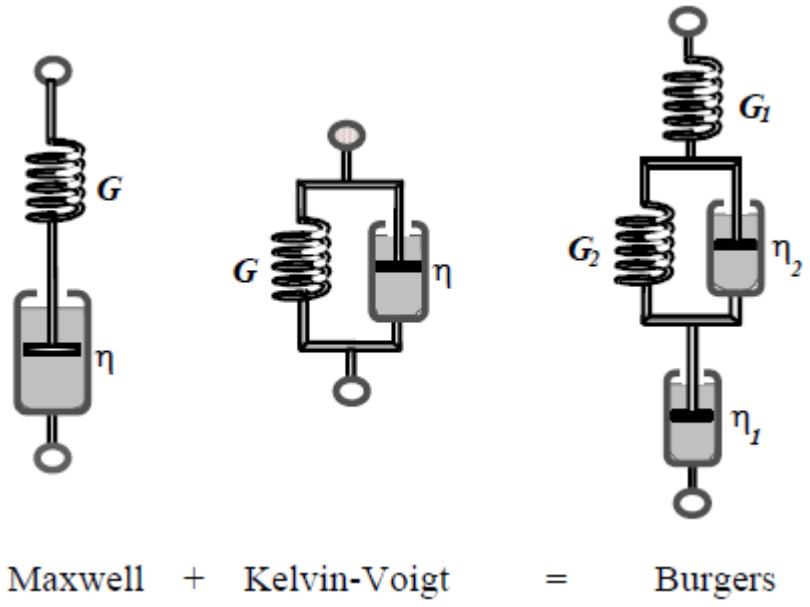

Figure 2.5: Mechanical Models Depicting Linear Elastic and Viscous Responses (Barnes, 2000)

In summary, elastic elements represents any physical system in the microstructure that can store energy (Storage modulus) and viscous elements represents any physical system that can dissipate energy (Loss modulus) which is lost due to internal friction. They are represented by G'' and G' respectively which is used to determine the longest relaxation time used to quantify elasticity.

2.2.8.1 The Longest Relaxation Time

Barnes (2000) stated that the G' and G'' based on the Maxwell model can be mathematically given as;

$$G' = \frac{G(\omega\lambda)^2}{1 + (\omega\lambda)^2} \tag{2.5}$$

$$G'' = \frac{\mu\omega}{1 + (\omega\lambda)^2} \tag{2.6}$$

Where λ is relaxation time given and ω is the frequency. Oscillatory frequency sweep tests are sued to quantify elastic properties in a fluid since both G' and G" are functions of frequency (Arnipally, 2017). An example of a frequency sweep test result is shown below in Figure 2.5

The frequency at which When $G' = G''$ is very significant. The longest relaxation time, λ (sec) which is the inverse of the crossover angular frequency between the elastic modulus and viscous modulus. It signifies the time needed for a material to regain its original structure after any deformation or disturbance. It is used to quantify the elasticity of a fluid (Choi, 2008; Malhotra and Sharma, 2012; Arnipally and Kuru, 2018)

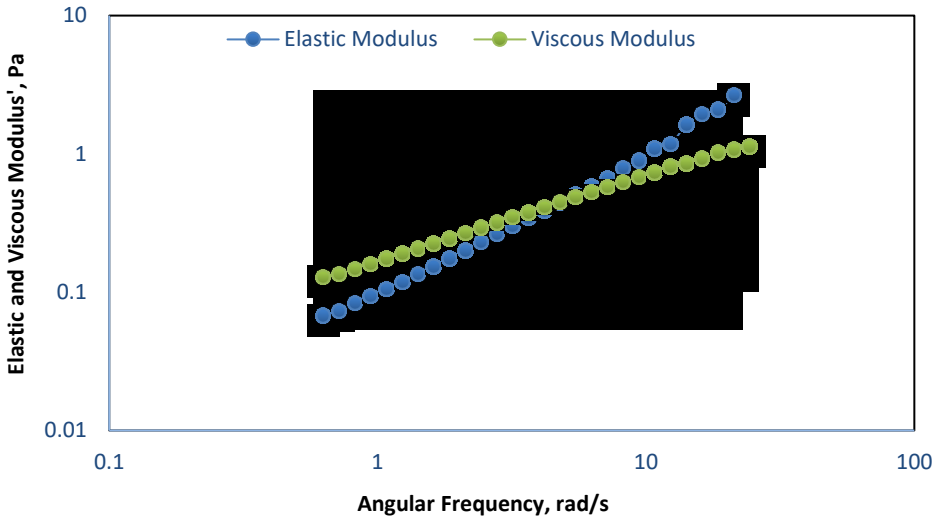

Figure 2.6: Sample Oscillation Test Result

At low frequencies the experimental time scale is longer hence the loss modulus is greater than the elastic modulus (G''>G') and liquid character is exhibited. However at higher frequencies, the experimental time scale is shorter and storage modulus becomes greater than loss modulus (G'>G'') solid like or gel character dominates due to the prevalence of elasticity.

2.3 Yield Stress Phenomena

When it comes to fluid rheology, no topic is widely debated than the yield stress phenomena. Controversies on its definition, dynamics, measurements and existence still subsists till this very day (Møller, Mewis and Bonn, 2006; Ovarlez *et al.*, 2013; Dinkgreve *et al.*, 2016). The yield stress is defined as the minimum stress that can be applied to a fluid before it can undergo a permanent irreversible deformation. It is often symbolized by τ_y. Substances possessing the so called yield stress can exhibit both solid and liquid properties depending on the magnitude of the applied stress. For stress levels lower than the yield stress, the substances behave like a solid and if the applied stress is greater than the yield stress they behave like a liquid. The yield stress is of high pragmatic importance because it is used to determine minimum pumping to initiate flow in slurries, drilling fluids and other pipeline operations. It is also used to know the stiffness of viscoplastics and determine if bubbles will remain trapped during sophisticated cementing operations (Møller, Mewis and Bonn, 2006; Dinkgreve *et al.*, 2016). The idea of the yield stress phenomena was first introduced by Bingham and his colleagues who tried to draw a technical similarity between yield stress and plastic yielding in metals (Bingham, 1922; Dinkgreve *et al.*, 2016). Even after its introduction, controversies and debates surrounding the existence of a "true" yield still linger with some researchers still doubting while some others have experimentally or otherwise proven its

existence (Barnes and Walters, 1985; Barnes, 1999; Moller *et al.*, 2009; Møller, Fall and Bonn, 2009; Husband, Aksel and Gleissle, 2002; Tabuteau, Coussot and de Bruyn, 2007; Ovarlez *et al.*, 2013; Dinkgreve *et al.*, 2016).

The yield stress can be seen as a measure of strength of the internal structure which resists deformation until the stress applied can disintegrate the internal structure making it act flow like a liquid. Although macroscopically, an under-deformed yield stress fluids (viscoplastics) can act similarly to a solid however their microscopic mechanisms are quite disparate. For solid matter reorganization of constituent particles resists deformation while for gels, polymer chains and particles stick together and form a mesh like structure thereby resisting deformation (Møller, Mewis and Bonn, 2006).

Yield stress can be categorized into two major categories. The simple yield stress and the thixotropic yield stress (Møller, Mewis and Bonn, 2006; Moller *et al.*, 2009; Dinkgreve *et al.*, 2016). For the simple yield stress materials, the viscosity is time independent and depends solely on the shear rate while that of thixotropic yield stress materials depend and shear history of the substance. Dinkgreve et al (2016) indicated that the rheological behavior in these thixotropic yield stress materials depends on the competition between aging (microstructure buildup and viscosity increase) and shear rejuvenation (microstructure breakdown and viscosity decrease).

2.3.1 Complexities of the Yield Stress

The convolution associated with the Yield stress is even more compounded with regards to its measurements. There are so many factors that complicates the measurement of yield stress which all deal with the accepted definition.

This conundrum is schematically represented in figure below;

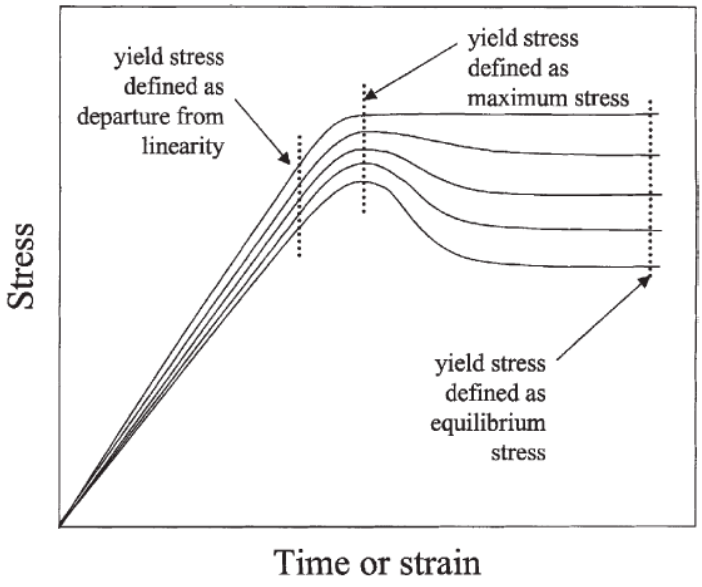

Figure 2.7: Different Definitions of the Yield Stress (Møller, Mewis and Bonn, 2006)

Some researchers have suggested that the stress at the end of the linear elastic region should be taken as the yield stress while others suggest the maximum stress or the equilibrium stress beyond peak should be the yield stress. Apart from the lack of unison in the accepted definition, further complications arise from the devices used to make measurements. Several authors have attested to the fact that multiple devices depending on their respective sensitivities give different values for yield stress. In fact, even the method of approach used and measurement geometry selected for the same equipment can give different ambiguous values of yield stress with difference reaching several orders of magnitude. (Barnes, 1999; Chhabra, 2006; Møller, Mewis and Bonn, 2006; Maxey, Hughes and Fluids, 2007; Moller *et al.*, 2009; Møller, Fall and Bonn, 2009; Dinkgreve *et al.*, 2016). Furthermore, the values of yield stress obtained from measurements may be insufficient

and actually fail to depict what conditions actually initiate flow or manner of flow in industrial applications (Møller, Mewis and Bonn, 2006).

Theoretically, there is meant to be one single value of yield stress, which is the stress that initiates flow within the duration of the experiment. This is rather ambiguous because the value of the yield stress may change depending on the experimental time, equipment utilized and approach followed. The usual explanation is that different methods probe into different property or structure of yield stress fluids or obtain a different definition of yield stress (Møller, Mewis and Bonn, 2006). This leads to the concept of variable yield stress that is antithetical to the theoretical yield stress engendering further lengthy discussions and debates. In fact, these are some of the reasons why many authors conclude that Yield stress is a not a material constant (Mezger, 2006).

Another major problem associated with the yield stress is the concept of shear localization (shear banding) (Møller, Mewis and Bonn, 2006; Dinkgreve *et al.*, 2016). When a macroscopic shear rate is applied to a fluid, the shear rate is not uniformly distributed across the fluid. In fact only a small region moves and the speed of the layers decreases farther from the region of applied shear rate and even some parts are static or solid which leads to the misinterpretation of rheological data. It is more interesting to think about it this way, If some fluids are static while others are moving; this means that the applied stress is greater than the yield stress in some region and lower than the yield stress in other regions. Conflating global shear rate to be uniform across the fluids can lead to erroneous estimation of the yield stress. Shear banding is even experienced in cone-plane geometry which are designed for uniform shear rate application (Møller, Mewis and Bonn, 2006; Moller *et al.*, 2009; Møller, Fall and Bonn, 2009).

2.3.2 Relationship between Yield Stress and Thixotropy

The core of these problems can be related to another phenomenon known as the thixotropy. Thixotropy is defined as the reversible decrease in the viscosity of a material with time when exposed to a constant shear rate. Although entirely different concepts, thixotropy and yield stress are similar and related in their mechanisms. While yield stress is caused by the innate microstructure of a fluid resisting deformation and reorganization, thixotropy is caused by the breakdown of that microstructure.

When a thixotropic material is exposed to a constant shear rate, the viscosity decreases. This viscosity then builds up when it is at rest or a very low shear rate is applied. Thixotropy gives rise to two different concepts known as aging and shear rejuvenation. As explained earlier, viscosity increase of a thixotropic substance at rest is known as aging while viscosity decrease due to time under shear is known as shear rejuvenation (Møller, Mewis and Bonn, 2006). The inter-relation between Yield stress and thixotropy can be experimentally illustrated using the avalanche inclined plane test which involves a fluid on an adjustable inclined plane. The test shows that flow starts at certain angle due to yield stress and viscosity decrease is possible at that fixed angle due to thixotropy. (Møller, Mewis and Bonn, 2006; Moller *et al.*, 2009; Møller, Fall and Bonn, 2009).

Several researchers have attempted to model thixotropy and yield stress phenomena in fluids. Most models make use of the structural parameter, λ that describes the local degree of interconnection or strength of the fluids microstructure. The structural parameter is maximum when the fluid is at rest and decreases with applied shear (Galindo-Rosales and Rubio-Hernández, 2006; Møller, Mewis and Bonn, 2006; Gumulya *et al.*, 2011)

2.3.3 Measurements of the Yield Stress

There are several ways to measure the yield stress each with their associated advantage and limitation. Mezger (2006) and Dinkgreve *et al.*, (2016) made a comprehensive review of different protocols to measure yield stress for interested readers.

The several methods to measure yield stress range from facile to extremely complex depending on the measuring device. A simple standard method for measuring yield stress in a Bingham Plastic fluid was presented by the American Petroleum Institute (API). It involved the use of a simple viscometer. The Yield stress is given by the difference in the R_{300} reading and the Plastic Viscosity. Where the plastic viscosity is given by R_{600} - R_{300} (API, 2006). Another simple method involves the use of the inclined plane test in which the angle the fluid begins to flow is used to depict the yield as explained in the previous section(Mezger, 2006; Møller, Mewis and Bonn, 2006).

For more technical and accurate measurements, advanced rheometers are used to estimate the yield stress. The yield stress can be estimated from viscometric flow curve tests in various ways. Extrapolating the Shear stress to zero shear rate (where flow begins) can be adjudicated as the yield stress. Also curve fitting of the obtained flow curve to the Herschel Bulkley model can be used to get reasonable value of the yield stress.

Another flow curve method known as the tangent method involve a Controlled Shear Stress (CSS) ramp. If the test is carried out one decade below the expected yield stress and a decade above it, the yield stress can be seen as the point of deviation from the linear-elastic deformation range. During the linear elastic deformation range, the fluid still obeys Hooke's law and hence all deformation are reversible; however, after this range is exceeded, the fluid becomes irreversibly

deformed and the yield stress, τ_y is exceeded. Extremely high sensitive rheometers are required to carry out this test because low shear rates may be required. A single tangent or double tangent can be used to carry out this test. A descriptive image of the tangent method is shown below.

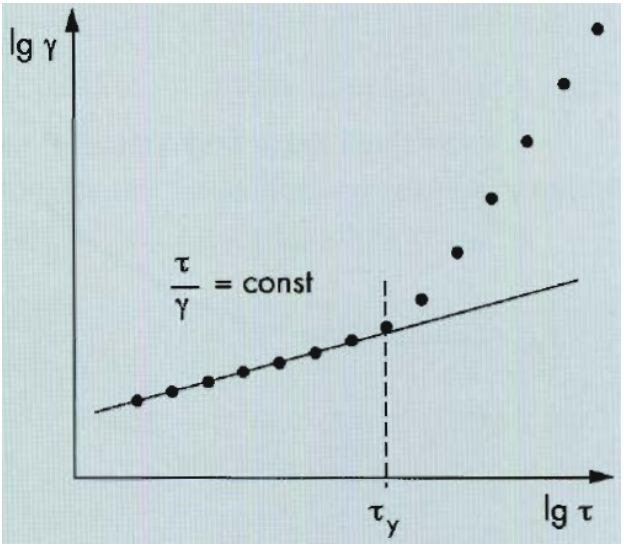

Figure 2.8: Tangent Method for Determining Yield Stress (Mezger, 2006).

Amplitude sweep is another technical and sophisticated method for determining yield stress. Amplitude tests are oscillatory tests performed at different amplitudes while keeping frequency constant. From the amplitude test, a plateau known as the Linear Viscoelastic (LVE) range is clearly observed. It signifies the range of shear stress by which the fluid undergoes reversible deformation and the internal microstructure is still intact.

The yield point or yield stress is given by the shear stress where the loss modulus G" deviates from the linear viscoelastic (LVE) range. It should not be conflated with the flow point (τ_f) which is indicated by the shear stress where the loss modulus equals the storage modulus.

The yield stress or yield point (τ_y) denotes the stress where the internal microstructure is irreversibly destroyed and the flow point (τ_f) is the stress in which flow initiates. They are both two different concepts although similar. For the fluid to flow, its internal microstructure would have been destroyed and reorganized earlier which occurs at the yield point (Mezger, 2006; Dinkgreve *et al.*, 2016). A descriptive image of the process is shown below;

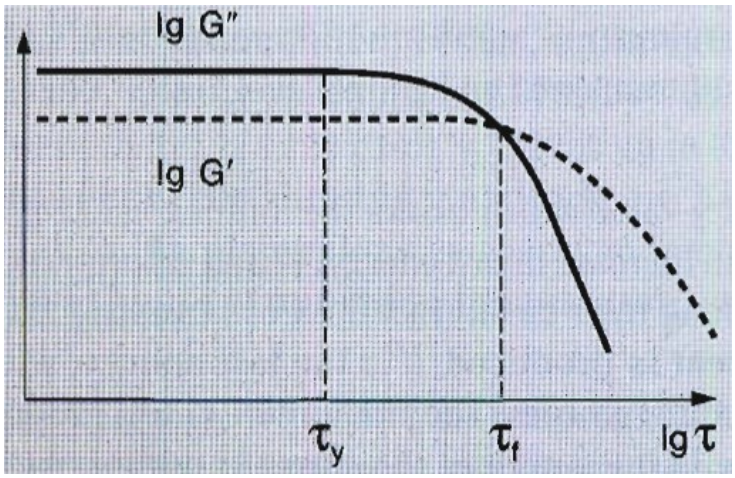

Figure 2.9: amplitude Test Result showing the Yield Point (τ_y) and Flow Point (τ_f)

2.4 The Settling Behavior of Particles

A comprehensive review on the previous literature regarding work done on the settling of particles in Newtonian and non-Newtonian fluids both experimental and theoretical are presented in this section. But first, the Terminal Settling velocity and drag coefficient must be defined.

2.4.1 Terminal Settling Velocity and Drag Force

A free falling particle in a Newtonian fluid is subject to three forces namely gravity, buoyancy and drag forces. Particle motion may initially accelerate but since the drag force increases with velocity (Rhodes, 2008), at some point the net force becomes zero and the particle continues falling with a

constant velocity (Shokrollahzadeh, 2015). Terminal velocity is defined as the constant velocity attained by a particle falling through a fluid when the upward force (drag force and buoyancy) is in equilibrium with the downward force (weight) as shown in 2.6 below. These three parameters determine settling velocity (weight, drag force and buoyancy).

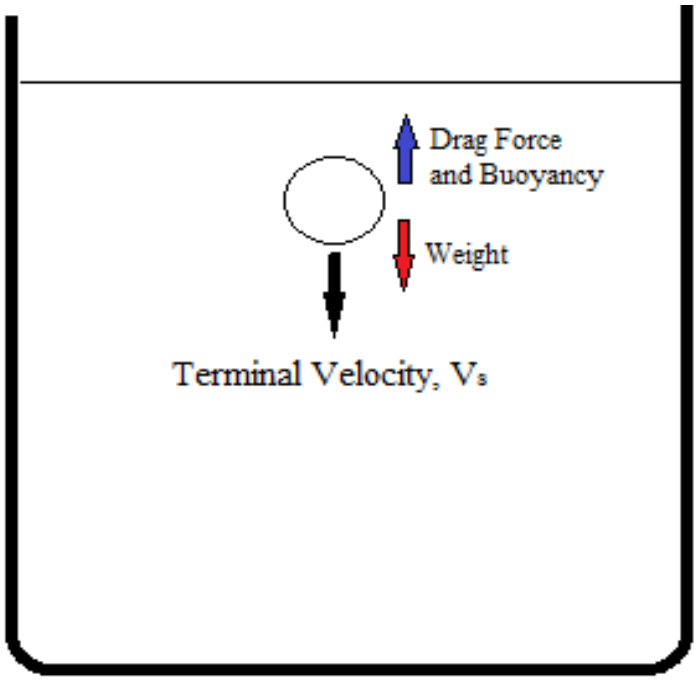

Figure 2.10: Schematic description of terminal velocity.

Describing settling behavior primarily entails the determination of the terminal settling velocity drag coefficient and settling velocity; which is the fundamental hydrodynamic characteristic of the particle motion falling through a fluid (Machač, Ulbrichová, Elson, & Cheesman, 1995). The drag coefficient (C_D) defined as the ratio of the viscous drag force to the kinetic energy acting on the particle (Rushd et al., 2018)

The equations for the three parameters described above are

$$Weight, W = \frac{\pi d^3 \rho_s g}{6} \tag{2.7}$$

$$Buoyancy, F_B = \frac{\pi d^3 \rho g}{6} \tag{2.8}$$

$$Drag\ Force, F_D = \frac{C_D \rho {V_s}^2 A}{2} \tag{2.9}$$

When terminal velocity is attained (Weight = Buoyancy + Drag Force), the settling velocity can be obtained by making V_s subject of formula. The force balance becomes

$$V_s = \sqrt{\frac{4gd}{3C_D}\left(\frac{\rho_s - \rho}{\rho}\right)} \tag{2.10}$$

Where d is the diameter of particle, g is the acceleration due to gravity, A is area, C_D is drag coefficient, ρ_s is the density of solid and ρ is density of fluid. It is necessary to note that a particle immersed in a fluid does not attain terminal velocity (as shown in Figure 2.11 below) immediately but with time depending on the fluid properties and weight of particles In order to obtain accurate results, it is imperative to measure the instantaneous velocity when the constant velocity is attained and not just an average over time.

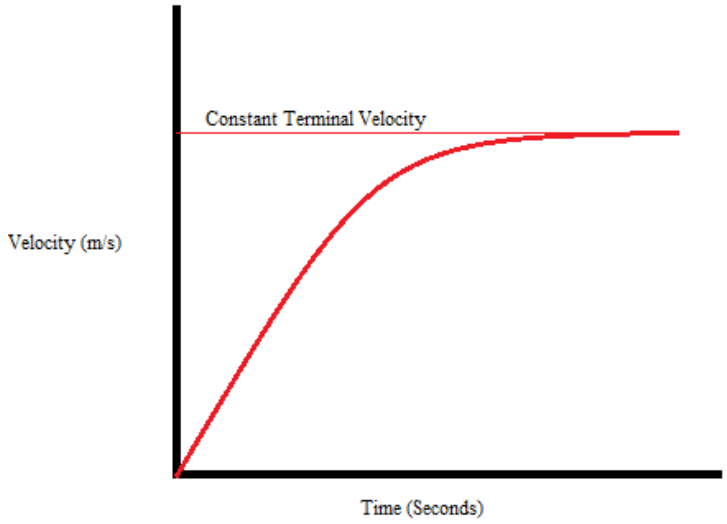

Figure 2.11: A graphical description of terminal velocity.

2.4.2 Settling Behavior of Particles in Newtonian Fluids

In anteceding decades, many efforts have been made by researchers to understand and predict the motion of solid particles in Newtonian fluids (Stokes, 1905; Clift, Grace and Weber, 1978; McCabe and Harriot, 1987; Richardson, Harker and Backhurst, 2002; Chhabra, 2006; Morrison, 2013). The behavior of rigid spherical particles in Newtonian fluids has been accurately dealt with and demystified by various authors (McCabe and Harriot, 1987; Richardson, Harker and Backhurst, 2002; Wilson *et al.*, 2003; Morrison, 2013).

As earlier stated, describing the settling behavior primarily entails the determination of the drag coefficient; which is the fundamental hydrodynamic characteristic of the particle motion falling through a fluid (Machač *et al.*, 1995). The drag coefficient (C_D) defined as the ratio of the viscous

drag force to the kinetic energy acting on the particle (Rushd *et al.*, 2018) and can also be expressed mathematically as:

$$C_D = \frac{4(\rho_s - \rho_f)dg}{3V_t^2\rho_f} \quad 2.11$$

Where d is diameter of the particle, ρ_f is the fluid density, ρ_s is the solid particle density and g is acceleration due to gravity. All things being equal, the drag coefficient determines the particle settling velocity (or vice versa) and consequently the particle Reynolds number, all three of which are interwoven. Due to the difficulty in developing analytical solutions, empirical correlations and experimental methods are employed in the determination of C_D (Machač *et al.*, 1995; Kesely and Matoušek, 2016; Arnipally and Kuru, 2017). The solution method involves the development of a drag coefficient and particle Reynolds number correlation. The particle Reynolds number Re_p is defined as the ratio of inertial forces to viscous forces experienced by the particle (Chhabra, 2006) and is also expressed mathematically as follows:

$$Re_p = \frac{\rho_f V_t d}{\mu} \quad 2.12$$

Where μ is Newtonian viscosity of the fluid medium. If the drag coefficient can be accurately determined with the aid of C_D-Re_p correlation, predicting the settling velocity iteratively becomes relatively easier. Considerable efforts have been made to develop expressions that relate C_D to Re_p with the pioneering work carried out by Sir George Stokes in the 19th century (Stokes, 1905). He proposed the following relationship for Newtonian fluids at laminar condition ($Re_p < 0.3$):

$$C_D = \frac{24}{Re_p} \quad 2.13$$

Over the years, researchers have modified and produced several other Newtonian C_D-Re_p correlations for spherical (Turton and Levenspiel, 1986; Dedegil, 1987; Richardson, Harker and Backhurst, 2002; Brown and Lawler, 2003; Cheng, 2009) and non-Spherical particles (Haider and Levenspiel, 1989; Chien, 1994; Song *et al.*, 2017). A comparative comprehensive review of various correlations was carried out by Chhabra (2006) for interested readers. A universal standard drag curve for Newtonian fluids is shown in figure below.

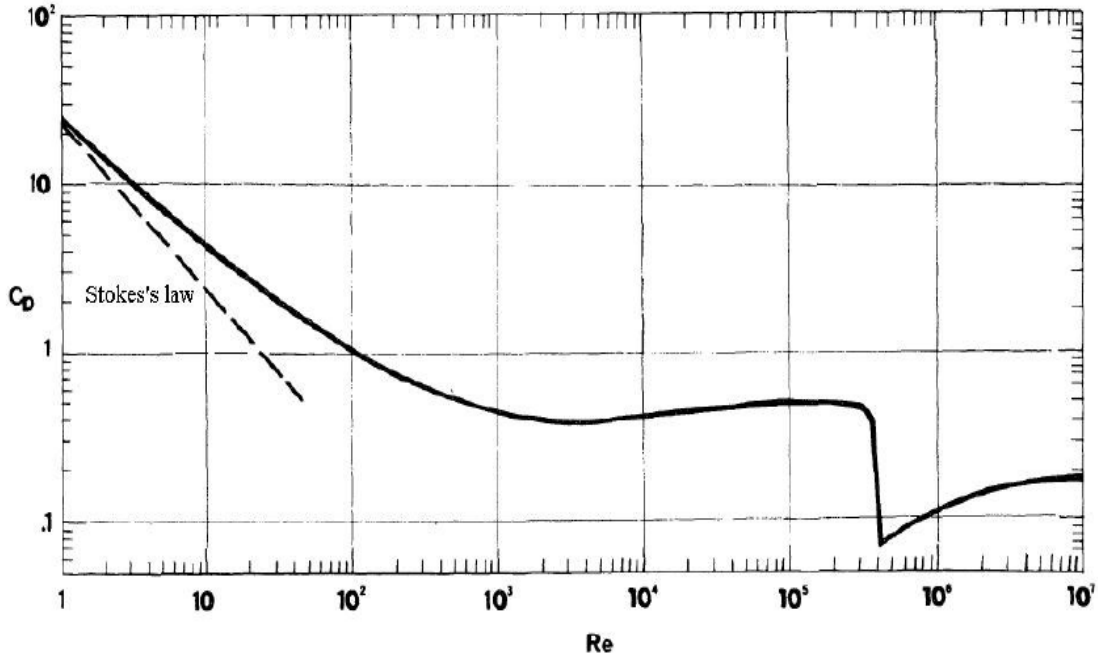

Figure 2.12: Universal Newtonian Drag Curve (Clift, Grace and Weber, 1978)

2.4.3 Prediction of Settling Velocity in Newtonian Fluids

Wilson et al (2003) presented an approach for the direct prediction of settling velocity of spherical particles in Newtonian fluids. His approach was based on pipe flow analysis with which he developed empirical equations based on shear velocity (V*) and shear Reynolds number (Re*).

In pipe flow, shear velocity ($U*$) is the square root of the ratio of the shear stress at the pipe wall to the fluid density and shear Reynolds number ($Re*$) is calculated based on $U*$. One major

difference between the pipe-flow analysis and the flow around a falling particle is that the stress distribution around the particle is not uniform (Wilson and Thomas, 1985; Wilson *et al.*, 2003) .In order to represent the characteristic shear stress of this process, the mean surficial stress ($\bar{\tau}$) of a falling particle was chosen, where $\bar{\tau}$ represents the immersed weight of the particle divided by its total surface area:

$$\bar{\tau} = \frac{dg\ (\rho_s - \rho_f)}{6} \qquad 2.14$$

The shear velocity V* is given by:

$$V^* = \sqrt{\frac{\bar{\tau}}{\rho_f}} = \sqrt{\frac{dg\ (\rho_s - \rho_f)}{6\rho_f}} \qquad 2.15$$

And the shear Reynolds number Re* is given by:

$$Re^* = \frac{d\rho_f V^*}{\mu} \qquad 2.16$$

The authors then transformed the correlations based on the available experimental data in the literature from C_D vs Re_p to V_t/V versus Re^*, thereby producing a "new" standard curve for a sphere falling in a Newtonian fluid. This curve has three distinct regions as shown in Figure below.

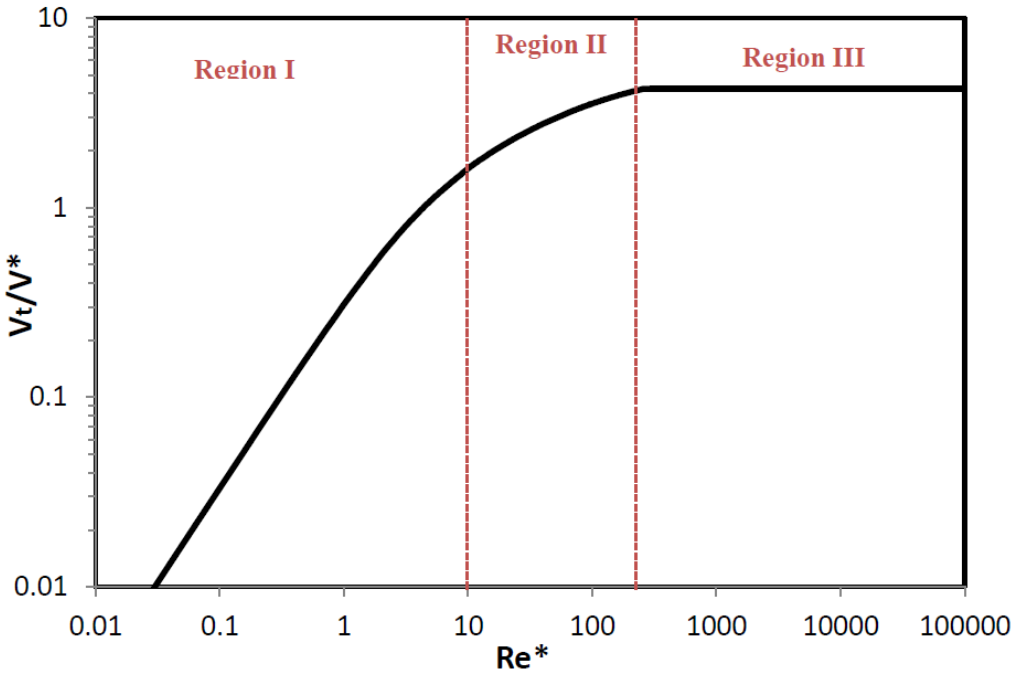

Figure 2.13: Standard Curve for a Sphere falling in a Newtonian Fluid (Wilson *et al.*, 2003; Shokrollahzadeh, 2015)

In Region I, for $Re*$<10, the fitting equation is:

$$\frac{v_t}{v^*} = \frac{Re^*}{3(1+0.08Re^{*1.2})} + \frac{2.80}{(1+3{,}0{,}000Re^{*-3.2})} \qquad 2.17$$

In Region II, for (10<$Re*$<260), the fitting equation is:

$$\frac{v_t}{v^*} = 10^y \qquad 2.18$$

$$y = 0.2069 + 0.050x - 0.158x^{1.72} \quad 2.19$$

$$x = \log\left(\frac{Re^*}{10}\right) \quad 2.20$$

In Region III, for ($Re*$>260), the fitting equation is:

$$\frac{v_t}{v^*} = 4.24 \quad 2.21$$

Region III ($Re*$>260) corresponds to particle Reynolds numbers larger than 1100, where the drag coefficient can be taken as approximately constant, at C_D=0.445. This corresponds to $Vt/V*$=4.24 in the direct method of Wilson et al. (2003). Using this innovative approach, settling velocity of spherical particles in non-Newtonian fluids can be predicted.

2.4.4 Settling Behavior of Particles in non-Newtonian Viscoplastic Fluids

The accurate description of particle settling behavior in non-Newtonian fluid is paramount for the design, analysis, and optimization of a wide spectrum of industrial processes such as pipeline transport of slurries, sand transport in oil and gas production lines, rock cuttings transport in oil and gas well drilling as well as proppant transport in hydraulic fracturing operation.

Throughout the last century, tangible research efforts have been made by researchers to understand and predict the motion of solid particles in Newtonian and non-Newtonian fluids (Stokes, 1905; Valentik and Whitmore, 1965; Ansley and Smith, 1967; Beris *et al.*, 1985; Dedegil, 1987; Atapattu, Chhabra and Uhlherr, 1995; Blackery and Mitsoulis, 1997; Wilson *et al.*, 2003;

Kelessidis and Mpandelis, 2004; Chafe and de Bruyn, 2005; Chhabra, 2006; Gumulya, Horsley and Wilson, 2007; Tabuteau, Coussot and de Bruyn, 2007; Prashant and Derksen, 2011; Gumulya *et al.*, 2011; Arabi and Sanders, 2016; Kesely and Matoušek, 2016; Arnipally and Kuru, 2017; Rushd *et al.*, 2018).

While the behavior of rigid spherical particles in Newtonian fluids has been accurately dealt with by some authors (McCabe and Harriot, 1987; Richardson, Harker and Backhurst, 2002; Wilson *et al.*, 2003; Morrison, 2013), the behavior and motion of rigid particles in non-Newtonian fluids especially in viscoplastic fluids has not been fully demystified due to complexities in particle physical properties and disparities in fluid rheological modelling compounded by the presence of the hard-to-measure yield stress (Chhabra, 2006).

Expounding settling behavior primarily involves the determination of the terminal settling velocity and drag coefficient; which is the fundamental hydrodynamic characteristic of the particle motion falling through a fluid (Machač *et al.*, 1995). The drag coefficient (C_D) defined as the ratio of the viscous drag force to the kinetic energy acting on the particle (Rushd *et al.*, 2018). The drag coefficient is acknowledged to be affected by the particle and the fluid properties (McCabe and Harriot, 1987; Arnipally and Kuru, 2017). Even particle roughness is acknowledged to affect drag coefficient and settling speed (Chhabra, 2006; Tabuteau, Coussot and de Bruyn, 2007; Holenberg *et al.*, 2012). Several studies have also suggested the existence of elasticity effects on drag coefficient especially in Power Law non-Newtonian fluids (Chhabra, 2006; Malhotra and Sharma, 2012; Arnipally and Kuru, 2017).

All things being equal, the drag coefficient determines the particle settling velocity and consequently the particle Reynolds number, all three of which are intertwined. Due to the difficulty

in developing analytical solutions, empirical correlations and experimental methods are employed in the determination of C_D (Machač *et al.*, 1995; Kesely and Matoušek, 2016; Arnipally and Kuru, 2017). The solution method involves the development of a drag coefficient and particle Reynolds number correlation. The particle Reynolds number Re_p is defined as the ratio of inertial forces to viscous forces experienced by the particle (Chhabra, 2006). If the drag coefficient can be accurately determined with the aid of C_D-Re_p correlation, predicting the settling velocity iteratively becomes relatively easier.

Considerable efforts have been made to develop expressions that relate C_D to Re_p with the pioneering work carried out by Sir George Stokes in the 19th century (Stokes, 1905) as shown in the previous subsection. Over the years, researchers have modified and produced several other Newtonian C_D-Re_p correlations for spherical (Turton and Levenspiel, 1986; Dedegil, 1987; Richardson, Harker and Backhurst, 2002; Brown and Lawler, 2003; Cheng, 2009) and non-Spherical particles (Haider and Levenspiel, 1989; Chien, 1994; Song *et al.*, 2017). A comparative comprehensive review of various correlations was carried out by Chhabra (2006) for interested readers.

2.4.5 Prediction of Settling Velocity in non-Newtonian Viscoplastic Fluids

With respect to the settling velocity in non-Newtonian fluids, considerable amount of research efforts have been undertaken resulting in several numerical solutions as well as empirical correlations each with their associated limitations. Although useful, majority of the numerical analysis (Beris *et al.*, 1985; Briscoe *et al.*, 1992; Blackery and Mitsoulis, 1997; Prashant and Derksen, 2011; Kesely and Matoušek, 2016) were implicit and focused on creeping (laminar) flow conditions, hence inapplicable for predicting settling velocities at high practical Reynolds number

(Arabi and Sanders, 2016; Rushd *et al.*, 2018). An empirical approach involved relating drag coefficient to specific dimensionless numbers based on rheological models to predict the settling velocity (Andres, 1961; Valentik and Whitmore, 1965; Ansley and Smith, 1967; Tabuteau, Coussot and de Bruyn, 2007). According to Arabi and Sanders (2016), a major constraint with this approach apart from being model specific is the poor predictability if the fluid exhibits a near Newtonian behavior.

An alternative empirical approach involves modifying the definition of apparent viscosity (i.e. viscosity of the fluid under the shear rate induced by a falling particle) or Reynolds number such that the results of the viscoplastic settling tests coincide with the standard Newtonian drag curve (Ito and Kajiuchi, 1969; Saha, Purohit and Mitra, 1992; Atapattu, Chhabra and Uhlherr, 1995; Machač *et al.*, 1995; Dolejš, Doleček and Šiška, 1998; Chhabra, 2006). This approach not only ensures uniformity for various Newtonian and non-Newtonian fluids but also provides ease for predicting settling velocity since a single C_D-Re_p curve is utilized.

Earlier classic work by Metzner and Reed (1955) developed the modified Reynolds number for Power Law non-Newtonian fluids. Similarly, Machač *et al.* (1995*)* modified the definition of the particle Reynolds number in equation 2 for two rheological viscoplastic models (Bingham Plastic and Herschel Bulkley Models) to collapse their drag coefficient values to the standard Newtonian curve. They proposed the following equations respectively:

$$Re_{pB} = \frac{\rho_f (V_t) d}{\mu_B + \tau_B \left(\frac{d}{V_t}\right)} \qquad 2.22$$

$$Re_{pHB} = \frac{\rho_f (V_t)^{2-n} d^n}{\tau_{HB} \left(\frac{d}{V_t}\right)^n + k} \quad 2.23$$

In equation 4, Re_{pB} is the modified Bingham particle Reynolds number, μ_B is the Bingham Plastic viscosity and τ_B is the Bingham Yield. In equation 5, Re_{pHB} is the modified Herschel Bulkley particle Reynolds number, k is the Consistency index and n is the power law index. The key limitation with this alternative approach apart from requiring complex iteration is its lack of applicability across a wide range of Reynolds number (Arabi and Sanders, 2016). Owing to the difficulty in cumbersome iterations there was a need for a direct explicit approach, which occludes the aforementioned limitations.

In 2003, Wilson et al. presented a direct method that was able to provide reasonable predictions of the terminal settling velocity of a sphere in a viscoplastic fluids. Their method utilized the mean surficial stress $\bar{\tau}$ (i.e. stress resulting from the fall of a particle through a fluid) to determine the shear velocity (V*) and consequently the shear Reynolds number (Re*). They developed a Newtonian plot that correlated the settling velocity, V_t (made dimensionless using the shear velocity V*) to the shear Reynolds number (Re*).

In order to extend their Newtonian plot (Vt/V* vs Re*) to non-Newtonian viscoplastic fluids they introduced an equivalent Newtonian viscosity parameter by calibrating the mean surficial stress,$\bar{\tau}$. The calibrating factor was estimated to be 0.3 based on their experimental data ($\tau = 0.3\ \bar{\tau}$)

However, this method is limited in applicability in that;

- If the fluid yield stress is greater than the calculated reference shear stress ($\tau_y > 0.3\,\bar{\tau}$), the correlation cannot produce a prediction of terminal settling velocity. (Wilson and Thomas, 1985; Wilson *et al.*, 2003; Gumulya, Horsley and Wilson, 2007; Arabi and Sanders, 2016);

- Poor prediction at low shear Reynolds number (Re* < 100). The average absolute error is 75 % for 62 experimental points (Wilson *et al.*, 2003; Arabi and Sanders, 2016);

- Furthermore, a meticulous review of the Wilson et al. (2003) model revealed that the model was developed based on the Turton and Levenspiel (1986) C_D-Re_p relationship, which has undergone recent modifications (Chhabra, 2006; Cheng, 2009; Morrison, 2013).

Arabi and Sanders (2016) carried out an empirical and statistical study to improve the Wilson et al. (2003) model by modifying the equivalent viscosity parameter. Although their model was better and produced relatively more accurate than the original Wilson et al. model, their data was model specific (Casson and Bingham Model) and the experimental results obtained from their study showed poor prediction at laminar regime (low shear Reynolds numbers Re* < 10). Kesely and Matoušek (2016) also presented a model based on the Wilson et al. (2003) method to predict the laminar settling velocity. However, their method is implicit and requires iteration.

Recently, Rushd *et al.* (2018) modified the definition of the shear Reynolds number used in the Wilson et al. (2003) model with the model specific Reynolds number presented by Machač *et al* (1995). However, their approach was model specific and was not tested with other viscoplastic models (Rushd *et al.*, 2018). Based on the review of the prior literature, we conclude that there is

still a need for a universal predictive model that offers versatility in application by occluding the practical constraints listed above and yields relatively more accurate results.

2.4.6 Influence of Elasticity on Particle Settling Behavior in non-Newtonian Viscoelastic Fluids

Current conventional approach to predict settling velocity has a fundamental problem by not accounting for the elastic property of the fluids. Most C_D-Rep correlations do not have any parameter that accounts for elasticity. A study conducted by Arnipally and Kuru (2018) showed that settling velocity could be overestimated by up to 50 times if the effect of elasticity is not considered. Such large margin of error is unacceptable for most models where the particle settling velocity is required as an input for optimization and design calculations. Nonetheless, elasticity is sometimes not considered in some drilling and fracturing operations which can affect operational efficiency (Bui *et al.*, 2012; Arnipally and Kuru, 2018).

Several studies have attested to the influence of elasticity on a particle's settling behavior. While using Weissenberg number as a measure for elasticity, Chhabra et al. (1980) reported a reduction in drag at high Weissenberg numbers with Boger fluids (elastic fluids with constant viscosity). While Acharya (1986) in his study of viscoelastic fracturing fluids posited that the influence of elasticity on settling behavior is dependent on the Reynolds number region. He stated that at low Reynolds number region, settling velocity of proppant particles is influenced by the fluid's viscous property, while in the intermediate or transitional region settling velocity increases with elasticity. In contradictory reports, Van den Brule et al. (1993) however observed an apparent reduction in settling velocity as a result of elasticity in viscoelastic shear thinning fluids. Walters and Tanners (1992) carried out an experimental study on Boger fluids and concluded that elasticity causes a

reduction in drag at low Weissenberg number and a contrasting increase of drag at higher Weissenberg number. This drag increase (reduction in settling velocity) at high elasticity is in agreement with various experimental studies (Malhotra and Sharma, 2012; Arnipally and Kuru, 2018).

Despite contrasting reports, it is a consensus that elasticity plays a significant role in the settling behavior of particles in fluids. Even after obtaining the elastic description of the viscoelastic fluid with the aid of advanced rheometers, the eventual influence of the elasticity on settling behavior is still shrouded in mystery and has not yet been fully expounded, especially in terms of predicting the settling velocity in such viscoelastic fluids. Although, Malhotra and Sharma (2012) presented a correlation for predicting settling velocity in viscoelastic fluids from their experimental study of surfactant-based Shear thinning viscoelastic fluids; however their model was implicit and required complex iteration to determine the particle Reynolds number (and consequently the settling velocity). Malhotra and Sharma (2012)'s model was also based on a very limited relaxation time range of 0.18 – 0.32 seconds (relaxation time is used to quantify the elasticity of a fluid) which is an application constraint.

Based on the review of the literature, we conclude it is necessary to develop an accurate and versatile model that quantifies the effect of elasticity on particle settling in a wide range of elastic relaxation time and is applicable to diverse fluid properties as well as particle physical properties.

2.4.7 Effect of Elasticity and Viscosity on the Flow field and Shape of Yielded Regions surrounding a Settling Particle in a non-Newtonian Viscoplastic Fluid.

Another important aspect of settling behavior, is the Flow field induced by the settling particle as well as the regions surrounding it. When a particle falls through a Newtonian fluid, the flow field

surrounding the particle theoretically expands (Shokrollahzadeh, 2015). The shear stress exerted by the particle decreases monotonically away from particle and a fore-aft symmetry is observed in the flow field (Harlen, 2002; Gueslin et al., 2006; Holenberg et al., 2012). The flow field in non-Newtonian viscoplastic fluid is quite disparate. Many authors have reported fore-aft symmetry being broken in non-Newtonian viscoplastic fluids (Arigo and Mckinley, 1998; Harlen, 2002; Gueslin et al., 2006; Holenberg et al., 2012) and existence of a plug like flow in front of the settling particle (Putz et al., 2008).

If the stress exerted by the settling particle is below the fluid's yield stress the fluid acts as an elastic solid and the particle would not settle (Wilson et al., 2003; Shokrollahzadeh, 2015). This results in the formation of different regions around a settling particle. A cogent knowledge of the shape and dimension of these surrounding regions is salient because it is intertwined with and also determines the magnitude of the particle settling velocity in a viscoplastic fluid (Prashant and Derksen, 2011).

In 1953, Volarich and Gutkin were among the first proponents of the existence of a sheared (yielded) region and an unsheared (unyielded) region surrounding a settling particle in a Viscoplastic fluid. Over the years several shapes and dimensions of the sheared and unsheared regions have been posited by different authors. Valentik and Whitmore (1965) proposed a method for estimating the size of the unsheared shell region surrounding the settling particle by assuming Newtonian fluid laws apply. In 1967, Ansley and Smith suggested the existence of an envelope of toroidal shape sheared region surrounding the settling particle based on the slip line theory of solid mechanics. Yoshioka et al. (1971) identified the existence of stagnant polar cap regions in the sheared region and also showed the extent of the sheared zone using variational principles. Using

a numerical method, Beris et al., (1985) identified the sheared and unsheared regions surrounding a settling particle. Figures of postulated shapes are shown below

A – Ansley and Smith (1967) B – Yoshioka et al. (1971) C – Beris et al. (1985)

Figure 2.14 : Postulated shapes of the sheared envelope surrouding a sphere in creeping motion in Viscoplastic (Chhabra, 2006)

The result from their study showed that the dimensions and shape of the sheared region depend appreciably on the yield stress which in extension determines the speed of the settling particle. Their result agrees with numerical studies by Blackery and Mitsoulis (1997) as well as Prashant and Derksen (2011).

As the yield stress increases, the unsheared region expands which reduces the sheared region drastically as well the particle settling velocity (Prashant and Derksen, 2011). In 2012, Holenberg et al. utilized Particle Image Shadowgraphy (PIS) to determine shape of the yielded zone produced by smooth and rough spheres settling in Carbopol polymers. The shape obtained depended on the speed of the settling particle (peach-like shape for slow particles and bulb shape for faster particles). Although their results did not capture the stagnant polar caps posited by Yoshioka et al. (1971), however their experimental results were accurately predicted by recent numerical study by Fraggedakis, Dimakopoulos and Tsamopoulos (2016).

Apart from the existence of sheared and unsheared regions, there have also been reports concerning the existence of negative wakes in non-Newtonian fluids. Negative wakes refer to the upward movement (opposite direction to the settling particle) of fluid in the settling particle's wake. The existence of a negative wake has been the focus of various debates as regards its underlying mechanism. By changing the composition of the experimental fluids (ratio of water to corn syrup), Bush (1993) was able to obtain various fluid flow behaviors from obtaining negative wakes to extended wakes (downward fluid movement in the same direction of the settling particle).

In 2002, Harlen reported that negative wakes are caused by elastic recoil due to shear stresses generated near the side of the spheres giving rise to a flow directed away from the sphere. He also stated that extended wake is due to extensional stresses generated by extensional flow at the rear of the sphere which drives a flow towards the sphere. The balance between these determines the relative magnitude of both wake and negative wake as well as the position of the stationary point (inflexion point of zero velocity along the axis of the settling particle). His conclusion on two competing viscoelastic forces has been supported by various authors (Bush, 1994; Arigo and Mckinley, 1998; Frank and Li, 2006; Gueslin et al., 2006; Fraggedakis, Dimakopoulos and Tsamopoulos, 2016). This shows that the existence of elasticity in complex fluids can prominently affect flow fields and in extension shape of sheared region in viscoplastic fluids.

It was reported that at low Weissenberg numbers, an increase in elasticity leads to drag reduction on settling particles and vice versa at higher Weissenberg numbers (Walters and Tanner, 1992). This was later confirmed by Malhotra and Sharma (2012) through particle settling experiments in shear thinning fluids. A study by Arnipally and Kuru, 2018 aimed at isolating the individual effects of viscosity and elasticity showed that increasing elasticity at a constant viscosity reduces settling

velocity in shear thinning viscoelastic fluids (Hydrolyzed Polyacrylamide polymer). Elasticity in this study was characterized using longest relaxation time. A more recent study with the same viscoelastic experimental fluids showed that more elastic fluids have stagnation points closer to the settling particle than less elastic fluids for the same shear viscosity under controlled conditions (Arnipally, Bizhani and Kuru, 2019). Some authors have also reported that increasing inertia (speed of the particle) leads to the downstream movement of the stationary point (zero velocity) and negative wake away from the particle (Arigo and Mckinley, 1998; Gueslin et al., 2006; Fraggedakis, Dimakopoulos and Tsamopoulos, 2016).

Based on the literature review it is revealed that both elasticity and viscosity affect flow fields surrounding a settling particle in a viscoplastic fluid. However, there is little or no experimental work in literature that isolates viscous effects and elastic effects in order to ascertain which plays a prominent influential role on the shape of sheared region as well as the vector velocity profile in Viscoplastic fluids.

2.5 Particle Image Shadowgraphy (Literature Review)

A meticulous literature review on the technique (Particle Image Shadowgraphy) used in this study is carried out in this section. The main reason for its selection and advantages of the method are highlighted in this section. The main technique itself is discussed in the next chapter.

2.5.1 Techniques used for measuring Terminal Settling Velocity in Literature.

The settling velocity is an important parameter in the study of solid-liquid interaction and must be properly investigated. A lot of research work has been into this over the years. Briscoe et al (1992) monitored the fall of spheres through bentonite clay dispersions using an ultrasound

technique. In this experiment an ultrasound longitudinal wave was used to monitor the progress of a sphere in bentonite and record distance covered as a function of time. The terminal velocity was calculated by dividing the distance and time.

Similarly, Tabuteau, Coussot and de Bruyn, (2007) and other researchers studied the motion of spheres moving through suspensions of Carbopol using a high-speed video camera with frame rates typically in the range of 60–250 frames/s. The position of the bottom edge of the sphere in each frame was measured with a digital cross hair and converted from pixel units to true distance. The sphere position in each frame was used to measure the terminal velocity.

Smiths and Friedrichs (2012) carried out a field experiment to quantify settling velocities, aggregate states and flocculation within a hopper dredge plume. The Settling velocities and suspended particle sizes were quantified through sampling with the Particle Imaging Camera System (PICS) and automated image processing routines. This simply involved a high speed video camera that records the motion of a particle through a calibrated column to determine settling velocity. Some of the techniques listed above may actually provide good measurements depending on their experimental conditions; however they do not give an instantaneous measurement of settling velocity rather an average value over a wide range, which may lead to errors in some cases.

Shivam and Kuru (2014) investigated the settling velocity of industrial sand particles in various fluids using Particle Image Shadowgraphy. Their experiment made used of a high speed camera and a double pulsed laser. His extensive research demonstrated the reliability of the particle image shadowgraphy in particle sizing and settling velocity determination by cross correlating results obtained with standard theoretical plots (universal drag coefficient versus particle Reynolds number curve).

In 2017, Sumanth Arnipally used the Particle Image Shadowgraphy technique to analyze settling velocity of spherical particles in viscoelastic fluids. His research bolstered the consistency of image shadowgraphy by obtaining similar results of particle size and terminal velocity compared with industrial standards and theoretical correlations although different fluids were used from Shivam's experiment. The major advantage of these latter techniques is that their velocity measurement is instantaneous and gives a higher accuracy than taking an average overtime. The downside of the PIS involves the inability to plot the velocity-time graph as shown in figure 2.11 above from a single experiment since it gives only a single instantaneous velocity.

2.5.2 Particle Image Shadowgraphy: History and Underlying Physics

There are different optical techniques used in the visualizing particle in fluid motion, however image shadowgraphy stands a relatively accurate and powerful technique. Over the years, shadowgraphy has been used to qualitatively study the dynamics of fluids through flow visualization and recording of flow streamlines (Castrejon-Garcia *et al.*, 2011). Flow measurement technique dates back to 1864 when a German physicist August Toepler used it to study supersonic motion and it has evolved over the years to a standard flow visualization technique (Wikipedia, 2003).

Image shadowgraphy is defined as a non-intrusive flow visualization technique that works on the basic optical principle that light cannot pass through an opaque solid object. Since light cannot penetrate solid opaque objects, it refracts or bends around the object forming shadows, which can be recorded. The physics behind this technique is simple, light is sensitive to changes in density of the medium through which it travels and any disparity always result in the formation of shadows.

This technique requires a source of light and an image recording device as shown in **Error! R eference source not found.**5 below.

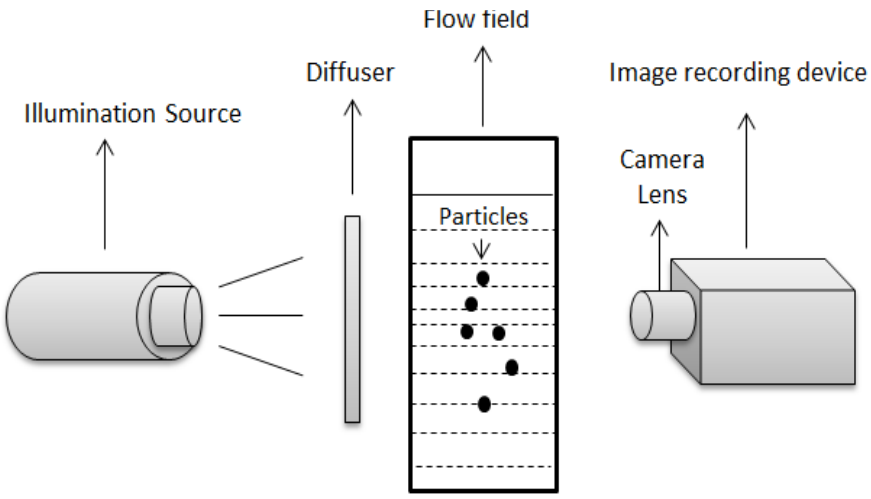

Figure 2.15: Schematic of the operating principle of image shadowgraphy

The aim of the light source arrangement is to provide light which is refracted by the opaque object and to obtain a homogeneous background at the recording sensor. The image recording device must have the ability to capture an image of the objects shadow. The light source can be pulsed laser, spark generator or LED and a CCD camera can be used as recording element. It is ideal for a transparent medium (water or air).

In the presence of back illumination, the light which does not interact with the object produces a bright background while those that interact with the opaque appear dark which are captured by the device (Castrejón-García et al, 2011). The end result is a bright background and with shadows of

the representing regions of different densities. Analysis of these resulting shadowgraph images can help determine a lot of parameters including terminal velocity.

There are a lot of factors that affect image quality (contrast, sharpness and brightness) and accuracy of the resulting data analysis. These parameters include magnification, light sensitivity, field of view, depth of field and focal length of the optical system. Some variables can be manipulated to improve the quality of the image while some are beyond the influence. For example, the size of the particles being investigated determines the optical magnification hence cannot be controlled by the scientific investigator. Some variables like optical length, working distance field of view can be manipulated to enhance image quality and ameliorate the experimental process (Castrejón-García et al, 2011).

Particle Image Shadowgraphy (PIS) is independent of particle shape, opacity and size when using the appropriate imaging system and light source. The computer software selected for this experiment is the Davis 8.3 Software. The camera and light source depend on the experimental setup. Using a short laser pulse as illumination it is possible to freeze motions of more than 100m/s (LaVision, 2010). Particle Image Shadowgraph follows algorithms described in the next chapter to measure size and velocity. A double-pulse laser combined with a double frame camera enables the investigation of particle velocities.

2.5.3 Other Applications of Particle Image Shadowgraphy

Image shadowgraphy is a very versatile fluid flow measurement technique and its application cuts across various fields. Castrejon-Garcia *et al.*, (2011) stated other uses of image shadowgraphy other than measuring terminal velocity. They include but are not limited to:

- Determination of the dynamic surface tension and surface profiles of modulated jets in Rayleigh regime.
- Determination of the droplet size distribution of sprays.
- Measurement of the inclination of jetted droplets
- Quantifying the effects of nozzle defects on directions of jetted droplets.

2.5.4 Advantages of Image Shadowgraphy Over Other Measurement Techniques

This subsection seeks to answer why Particle Image Shadowgraphy was selected despite the availability of several other techniques? The reasons are highlighted below.

- Particle Image Shadowgraphy gives an instantaneous velocity measurement rather than an average over time thereby avoiding errors associated with Pre-terminal velocity.
- Image shadowgraphy has advantages over other flow measurement techniques because it is non-intrusive measuring technique hence it does not interrupt with flow or fluid properties.
- Image shadowgraphy allows the simultaneous measurement of several characteristics, such as interface speed and direction of motion, and object sizes (Brenn et al, 2000).
- In 2017, Arnipally stated that in a literature survey conducted by various researchers, it was concluded that the most advantageous methodology of measuring particle sizing and settling is to employ settling columns equipped with image-capturing facility for recording and software to examine the recorded images.
- This imaging technique is independent of particle shape, opacity and size when using the appropriate imaging system and light source.

- From the literature review carried out, it can be clearly seen that PIS has been proven to be more efficient and used extensively to measure settling velocities of interested objects in the past (Nobbs, Tang and Raper, 2002; Fountain *et al.*, 2012; Shahi and Kuru, 2016; Arnipally and Kuru, 2018).

2.6 References

Acharya, A. (Ruma). (1986). Particle Transport in Viscous and Viscoelastic Fracturing Fluids.pdf. *SPE Production Engineering*, *34*(March), 104–110. https://doi.org/10.2118/13179-PA

Ansley, R. W., & Smith, T. N. (1967). Motion of spherical particles in a Bingham plastic. *AIChE Journal*, *13*(6), 1193–1196. https://doi.org/10.1002/aic.690130629

API. (2006). API Recommended Practice 13D, Recommended Practice on the Rheology and Hydraulics of Oil-Well Drilling Fluids, (5th ed.).

Arabi, A. S., & Sanders, R. S. (2016). Particle terminal settling velocities in non-Newtonian viscoplastic fluids. *Canadian Journal of Chemical Engineering*, *94*(6), 1092–1101. https://doi.org/10.1002/cjce.22496

Arnipally, S. K., & Kuru, E. (2017). Settling Velocity of Particles in Viscoelastic Fluids: A Comparison of the Shear Viscosity vs Elasticity Effect. In SPE Annual Technical Conference and Exhibition held in San Antonio, Texas, 9-11 October 2017.

Arnipally, S. K., & Kuru, E. (2018). Settling Velocity of Particles in Viscoelastic Fluids : A Comparison of the Shear-Viscosity and Elasticity Effects. SPE Journal, (October 2018), 1689–1705

Atapattu, D. D., Chhabra, R. P., & Uhlherr, P. H. T. (1995). Creeping sphere motion in Herschel-Bulkley fluids: flow field and drag. *Journal of Non-Newtonian Fluid Mechanics*, *59*(2–3), 245–265. https://doi.org/10.1016/0377-0257(95)01373-4

Barnes, H. A. (1999). The yield stress—a review or ‘παντα ρ ι’—everything flows? *Journal of Non-Newtonian Fluid Mechanics*, *81*(May 1998), 81(1-2), 133–178.

Barnes, H. A. (2000). *A handbook of elementary rheology*. *Science* (Vol. 331). https://doi.org/10.1126/science.1201543

Beris, A. N., Tsamopoulos, J. A., Armstrong, R. C., & Brown, A. (1985). Creeping Motion of a Sphere through a Bingham plastic Fluid. Journal of Fluids Mechanics, 158, 218–244.Bingham, E. C. (1922). *Fluidity and Plasticity*. McGraw-Hill Book Company, Inc.

Blackery, J., & Mitsoulis, E. (1997). Creeping motion of a sphere in tubes filled with a Bingham plastic material. *Journal of Non-Newtonian Fluid Mechanics*, *70*(1–2), 59–77. https://doi.org/10.1016/S0377-0257(96)01536-4

Briscoe, B. J., Glaese, M., Luckham, P. F., & Ren, S. (1992). The falling of spheres through Bingham fluids. *Colloids and Surfaces*, *65*(1), 69–75. https://doi.org/10.1016/0166-6622(92)80176-3

Brown, P. P., & Lawler, D. F. (2003). Sphere Drag and Settling Velocity Revisited. *Journal of Environmental Engineering*, *129*(3), 222–231. https://doi.org/10.1061/(ASCE)0733-9372(2003)129:3(222)

Bui, B., Saasen, A., Maxey, J., & Ozbayoglu, M. (2012). Viscoelastic Properties of Oil-Based Drilling Fluids. *Annual Transactions of the Nordic Rheology Society*, *20*, 33–47.

Castrejon-Garcia, R., Castrejon-Pita, J. R., Martin, G. D., & Hutchings, I. M. (2011). The Shadowgraphy Imaging Technique and its Modern Application to Fluid Jets and Drops, *57*(3),

266–275. Retrieved from http://search.proquest.com/technologycollection/docview/878341405/2C1FD9CBFB468EPQ/6?accountid=28155#

Chafe, N. P., & de Bruyn, J. R. (2005). Drag and relaxation in a bentonite clay suspension. *Journal of Non-Newtonian Fluid Mechanics*, *131*(1–3), 44–52. https://doi.org/10.1016/j.jnnfm.2005.08.010

Cheng, N. S. (2009). Comparison of formulas for drag coefficient and settling velocity of spherical particles. *Powder Technology*, *189*(3), 395–398. https://doi.org/10.1016/j.powtec.2008.07.006

Chhabra, R. (2006). *Bubbles, Drops, and Particles in Non-Newtonian Fluids, Second Edition* (Vol. 113). https://doi.org/10.1201/9781420015386

Chhabra, R. P. (1983). Some remarks on "Drag coefficients of a slowly moving sphere in Non-Newtonian fluids." *Journal of Non-Newtonian Fluid Mechanics*, *13*(2), 225–227. https://doi.org/10.1016/0377-0257(83)80018-4

Chhabra, R. P., Uhlherr, P. H. ., & Boger, D. . V. (1980). The Influence of Fluid Elasticity on the Drag Coeeficient for Creeping Flow Around a Sphere. *Journal of Non-Newtonian Fluid Mechanics*, *6*, 187–199.

Chien, S.-F. (1994). Settling Velocity of Irregularly Shaped Particles. *SPE Drilling & Completion*, *9*(04), 281–289. https://doi.org/10.2118/26121-PA

Clift, R., Grace, J.R. and Weber, M.E. (1978) Bubbles, Drops and Particles. Academic Press,

New York.

Dedegil, M. Y. (1987). Drag coefficient and settling velocity of particles in non-Newtonian suspensions. *Journal of Fluids Engineering*, *109*(3), 319–323. https://doi.org/10.1115/1.3242667

Dinkgreve, M., Paredes, J., Denn, M. M., & Bonn, D. (2016). On different ways of measuring "the" yield stress. *Journal of Non-Newtonian Fluid Mechanics*, *238*, 233–241. https://doi.org/10.1016/j.jnnfm.2016.11.001

Dolejš, V., Doleček, P., & Šiška, B. (1998). Drag and fall velocity of a spherical particle in generalized newtonian and viscoplastic fluids. *Chemical Engineering and Processing: Process Intensification*, *37*(2), 189–195. https://doi.org/10.1016/S0255-2701(97)00054-8

Fountain, M. S., Blanchard, J., Erikson, R. L., Kurath, D. E., Howe, D. T., Adkins, H., & Jenks, J. (2012). Design of a Particle Shadowgraph Velocimetry and Size (PSVS) system to Determine Particle Size and Density Distributions in Hanford Nuclear Tank Wastes. In *Waste Management-Tucson, Phoenix, Arizona, USA.* (Vol. 1, p. 0). https://doi.org/10.24200/tjer.vol1iss1pp0-0

Galindo-Rosales, F. J., & Rubio-Hernández, F. J. (2006). Structural breakdown and build-up in bentonite dispersions. *Applied Clay Science*, *33*(2), 109–115. https://doi.org/10.1016/j.clay.2006.03.011

Gumulya, M. M., Horsley, R. R., & Wilson, K. C. (2007). The settling of consecutive spheres in viscoplastic fluids. *International Journal of Mineral Processing*, *82*(2), 106–115. https://doi.org/10.1016/j.minpro.2006.11.005

Gumulya, M. M., Horsley, R. R., Wilson, K. C., & Pareek, V. (2011). A new fluid model for particles settling in a viscoplastic fluid. *Chemical Engineering Science*, *66*(4), 729–739. https://doi.org/10.1016/j.ces.2010.11.037

Haider, A., & Levenspiel, O. (1989). Drag coefficient and terminal velocity of spherical and nonspherical particles. *Powder Technology*, *58*(1), 63–70. https://doi.org/10.1016/0032-5910(89)80008-7

Hemphill, T., Campos, W., & Pilehvari, A. (1993). Yield-power law model more accurately predicts mud rheology.pdf. *Oil and Gas Journal*, *91*(34), 34. Retrieved from https://search-proquest-com.manchester.idm.oclc.org/docview/274440935?accountid=12253&rfr_id=info%3Axri%2Fsid%3Aprimo

Holenberg, Y., Lavrenteva, O. M., Shavit, U., & Nir, A. (2012). Particle tracking velocimetry and particle image velocimetry study of the slow motion of rough and smooth solid spheres in a yield-stress fluid PROCEDURE, *066301*, 1–6. https://doi.org/10.1103/PhysRevE.86.066301

Husband, D. M., Aksel, N., & Gleissle, W. (2002). The existence of static yield stresses in suspensions containing noncolloidal particles. *Journal of Rheology*, *37*(2), 215–235. https://doi.org/10.1122/1.550442

Ito, S., & Kajiuchi, T. (1969). Drag Force On A Sphere Moving in Plastic Fluid. *Journal of Chemical Engineering of Japan*, *2*(1), 19–24. https://doi.org/10.1252/jcej.2.19

Kealy, T. (2007). How To Measure Thixotropy for Pharmaceutical and Cosmetic Industries.

Rheology Solutions, 1–17.

Kelessidis, V. C., & Mpandelis, G. (2004). Measurements and prediction of terminal velocity of solid spheres falling through stagnant pseudoplastic liquids. *Powder Technology*, *147*(1–3), 117–125. https://doi.org/10.1016/j.powtec.2004.09.034

Kesely, M., & Matoušek, V. (2016). Laminar Settling of Glass Beads in Visco-Plastic Liquids. *Stavební Obzor - Civil Engineering Journal*, *25*(1). https://doi.org/10.14311/CEJ.2016.01.0001

Machač, I., Ulbrichová, I., Elson, T. P., & Cheesman, D. J. (1995). Fall of spherical particles through non-Newtonian suspensions. *Chemical Engineering Science*, *50*(20), 3323–3327. https://doi.org/10.1016/0009-2509(95)00168-5

Malhotra, S., & Sharma, M. M. (2012). Settling of spherical particles in unbounded and confined surfactant-based shear thinning viscoelastic fluids: An experimental study. *Chemical Engineering Science*, *84*(January), 646–655. https://doi.org/10.1016/j.ces.2012.09.010

Maxey, J., Hughes, B., & Fluids, D. (2007). AADE-07-NTCE-37 Thixotropy and Yield Stress Behavior in Drilling Fluids.

McCabe, W., & Harriot, P. (1987). Unit Operations Of Chemical Engineering, 5th Ed, McCabe And .pdf. https://doi.org/10.1016/j.eplepsyres.2011.07.014

Metzner, A. B., & Reed, J. C. (1955). Flow of Non-Newtonian Fluids-Correlation of the Laminar , Transition , and Turbulent-flow Regions, (4). https://doi.org/10.1002/aic.690010409

Mezger, T. G. (2006). *The Rheology Handbook*.

Møller, P. C.F., Fall, A., & Bonn, D. (2009). Origin of apparent viscosity in yield stress fluids below yielding. *Epl*, *87*(3). https://doi.org/10.1209/0295-5075/87/38004

Moller, P., Fall, A., Chikkadi, V., Derks, D., & Bonn, D. (2009). An attempt to categorize yield stress fluid behaviour. *Philosophical Transactions of the Royal Society A: Mathematical, Physical and Engineering Sciences*, *367*(1909), 5139–5155. https://doi.org/10.1098/rsta.2009.0194

Møller, Peder C.F., Mewis, J., & Bonn, D. (2006). Yield stress and thixotropy: On the difficulty of measuring yield stresses in practice. *Soft Matter*, *2*(4), 274–283. https://doi.org/10.1039/b517840a

Morrison, F. A. (2013). Data Correlation for Drag Coefficient for Spheres. *Cambridge University Press, New York*, *10*(November), 1–2.

Nobbs, D., Tang, P., & Raper, J. . (2002). The Design, Construction and Commissioning of a Low-Cost Optical Particle Size Analyser Specifically for Measuring of Settling Velocities and Size of Flocs. *Measurement Science and Technology*, *29*, 1–3.

Ovarlez, G., Cohen-Addad, S., Krishan, K., Goyon, J., & Coussot, P. (2013). On the existence of a simple yield stress fluid behavior. *Journal of Non-Newtonian Fluid Mechanics*, *193*, 68–79. https://doi.org/10.1016/j.jnnfm.2012.06.009

Prashant, & Derksen, J. (2011). Direct simulations of spherical particle motion in Bingham liquids. *Computers and Chemical Engineering*, *35*(7), 1200–1214.

https://doi.org/10.1016/j.compchemeng.2010.09.002

Richardson, J. F., Harker, J. H., & Backhurst, J. R. (2002). Chemical engineering Voulume 2. *Chemical Engineering Science*, *2*. https://doi.org/10.1016/0009-2509(60)80030-9

Rushd, S., Hassan, I., Sultan, R. A., Kelessidis, V. C., Rahman, A., Hasan, H. S., & Hasan, A. (2018). Terminal settling velocity of a single sphere in drilling fluid. *Particulate Science and Technology*, *0*(0), 1–10. https://doi.org/10.1080/02726351.2018.1472162

Saha, G., Purohit, N. K., & Mitra, A. K. (1992). Spherical particle terminal settling velocity and drag in Bingham liquids. *International Journal of Mineral Processing*, *36*(3–4), 273–281. https://doi.org/10.1016/0301-7516(92)90049-3

Shahi, S. (2014). *An Experimental Investigation of Settling Velocity of Spherical and Industrial Sand Particles in Newtonian and Non Newtonian Fluids using Particle Image Shadowgraph*. University of Alberta.

Shokrollahzadeh, A. (2015). Terminal Settling Velocity of a Sphere in a non-Newtonian Fluid. https://doi.org/10.7939/R3Q23R76B

Song, X., Xu, Z., Li, G., Pang, Z., & Zhu, Z. (2017). A new model for predicting drag coefficient and settling velocity of spherical and non-spherical particle in Newtonian fluid. *Powder Technology*, *321*, 242–250. https://doi.org/10.1016/j.powtec.2017.08.017

Stokes, G. G. (1905). On the Theories of the Internal Friction of Fluids in Motion, and of the Equilibrium and Motion of Elastic Solids. *Mathematical and Physical Papers Vol.1*, 75–129. https://doi.org/10.1017/CBO9780511702242.005

Tabuteau, H., Coussot, P., & de Bruyn, J. R. (2007). Drag force on a sphere in steady motion through a yield-stress fluid. *Journal of Rheology*, *51*(1), 125–137. https://doi.org/10.1122/1.2401614

Turton, R., & Levenspiel, O. (1986). A short note on the drag correlation for spheres. *Powder Technology*, *47*(1), 83–86. https://doi.org/10.1016/0032-5910(86)80012-2

Valentik, L., & Whitmore, R. L. (1965). The terminal velocity of spheres in Bingham plastics. *British Journal of Applied Physics*, *16*(8), 1197–1203. https://doi.org/10.1088/0508-3443/16/8/320

van den Brule, B. H. A. A., & Gheissary, G. (1993). Effects of fluid elasticity on the static and dynamic settling of a spherical particle. *Journal of Non-Newtonian Fluid Mechanics*, *49*(1), 123–132. https://doi.org/10.1016/0377-0257(93)85026-7

Walters, K., & Tanner, R. (1992). The Motion of a Sphere through an Elastic Fluid. *Transport Processes in Bubbles, Drops and Particles*.

Wilson, K. C., Horsley, R. R., Kealy, T., Reizes, J. A., & Horsley, M. (2003). Direct prediction of fall velocities in non-Newtonian materials. *International Journal of Mineral Processing*, *71*(1–4), 17–30. https://doi.org/10.1016/S0301-7516(03)00027-9

Wilson, K. C., & Thomas, A. D. (1985). A new analysis of the turbulent flow of non-newtonian fluids. *The Canadian Journal of Chemical Engineering*, *63*(4), 539–546. https://doi.org/10.1002/cjce.5450630403

CHAPTER 3 : EXPERIMENTAL PROGRAM

The main aim of this chapter is to give a general overview of the experimental setup and equipment used in this research study. A major conundrum arises on how the experiment should be setup, what equipment and apparatus are needed and what exact steps must be carried out to measure terminal velocity or fluid flow field. This chapter aims to answer all these questions.

Details on the experimental materials were also presented and how to obtain them. The detailed experimental procedure was also presented. One of the main reason of this chapter is to provide an outline for enthusiastic researchers to follow if they want to repeat this experimental procedure and obtain similar results. The chapter is concluded by providing mitigating precautions for experimental errors and safety precautions for the experimental procedures.

3.1 Experimental Materials

This subsection provides details on all equipment and devices used in the entire program and where they can be obtained

3.1.1 Glass Spheres

Precision spherical particles of glass, steel, ceramic and Zirconium were used in this experimental study. Their physical properties include a specific gravity ranging from 2.5 – 7.7 and diameters ranging from 1.09 - 4.00 mm.These particles were obtained from Corpuscular's Glass Spacers Millibeads Glass Inc. The settling velocities of these particles were measured in various polymer fluids to obtain a massive experimental database.

The particles were precisely cut and were smooth to reduce drag to barest minimum as well as the fluid particle contact due to reduced surface area. The Physical properties of these opaque particles used for settling experiments are listed in the Table below;

Table 3.1: Physical Properties of the Spherical Particles

Item	Diameter (mm)	Material	Specific Gravity
1	1.18	Glass	2.51
2	1.50	Glass	2.51
3	2.00	Glass	2.51
4	3.00	Glass	2.51
5	3.50	Glass	2.51
6	4.00	Glass	2.51
7	1.85	Ceramic	3.86
8	2.18	Ceramic	3.86
9	2.58	Ceramic	3.86
10	1.09	Zirconium Oxide Yttrium	5.90
11	1.29	Zirconium Oxide Yttrium	5.90
12	1.55	Zirconium Oxide Yttrium	5.90
13	2.4-2.5	Steel	7.70

3.1.2 Fluid Column

The fluid particle column serves as the cuboidal container for the viscoplastic fluid. The fluid particle column is a transparent cuboidal column of height 70 cm made of plexiglass. The length and breadth of the cuboidal container is 15cm by 15cm. This 15cm is more than ideal for the field of view required for the optical measurements The fluid column dimensions were designed by considering the minimum size required to avoid the wall effects (Atapattu, Chhabra and Uhlherr, 1990). An image of the fluid column is shown below;

Figure 3.1: Fluid Column

3.1.3 Calibration Target

In order to calibrate the Imaging system, a plastic replica calibration target is needed to help convert pixel space in physical space. This target is made up of uniform gridlines of known spacing dimensions. The software can use then use this spacing dimensions as a baseline physical reference for scaling future images to be captured.

Equipment calibration is carried out by inserting the calibration target sheet (a sheet having 0.8 mm printed circles spaced 1.5 mm apart) in the column and taking a focused image of the sheet.

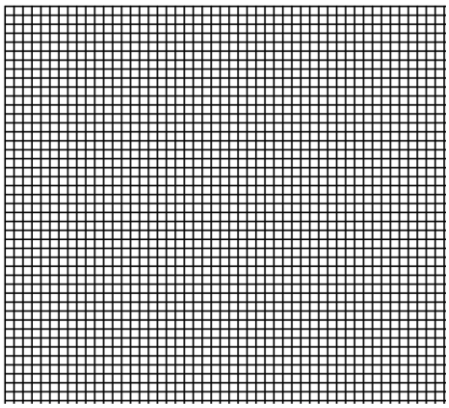

Figure 3.2: Calibration sheet used to calibrate the PIS and PIV Measurements

3.1.4 Polymers

The experimental fluids used in this study form a major component of the experimental setup and materials. The various polymers used in this study include

3.1.4.1 Carbopol® (ETD 2020 and 940)

Carbopol® is a high molecular weight crosslinked polyacrylic acid polymer family. The Chemical formula for Polyacrylic acid is $(C_3H_4O_2)_n$.

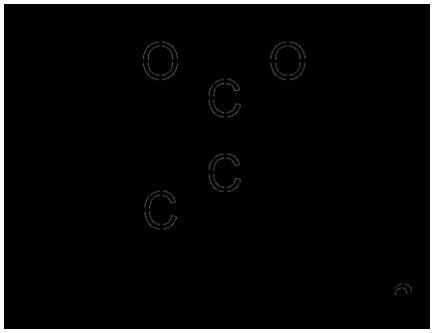

Figure 3.3: Molecular Chain Structure of Polyacrylic Acid (Wikipedia, 2019).

The main variances among the carbopol family stem from the crosslinker type and the density as well as the solvent used to synthesize the polymer (Lubrizol, 2010). The polymer is a low-wettability fine white powder. It is mildly acidic when dissolved in an aqueous and expands upon neutralization to form a transparent gel. The Carbopol ETD 2020 and Carbopol 940 were polymers utilized as test fluids in this study. The white carbopol powders were obtained from Lubrizol™. It is an efficient rheology modifier which acts to enhance viscosity. Products with the Carbopol® Family can achieve viscosities as high as 77,000 cP (Lubrizol, 2010). For carbopol polymers, viscosity alteration can also be easily achieved by meticulously adjusting the fluid's pH till desired rheological property is achieved. Carbopol ETD 2020 has a lower elasticity than Carbopol 940 due to its lower average molecular mass and was used in the study of viscoplastic fluids with negligible elasticity (Chapter 4 and 6), while Carbopol 940 was used in the study of Viscoplastic fluid exhibiting elastic properties (Chapter 6).

3.1.4.2 Hydrolyzed Polyacrylamide (HPAM)

Hydrolyzed Polyacrylamide (HPAM) is an elastic polymer formed from the monomers of acrylamide and acrylic acid. The main physical properties of the polymer are determined

by its degree of hydrolysis while the degree of its elasticity depends on the average molecular weight. The average molecular weight of the polymer ranges from 2 to 20 million (Sorbie, 1992; Arnipally and Kuru, 2018).

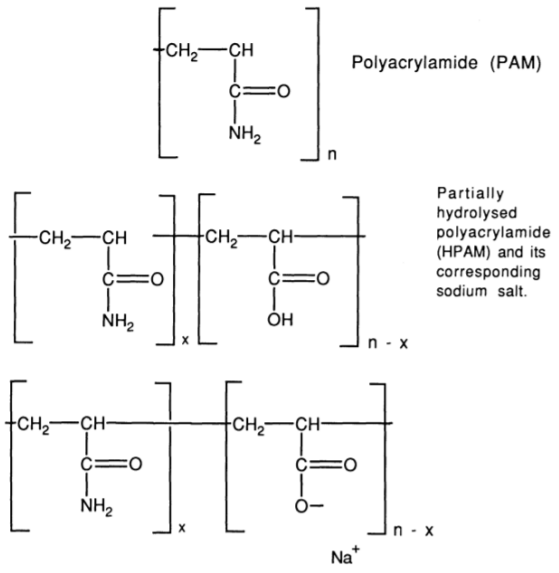

Figure 3.4: The Molecular Chain Structure of HPAM and PAM (Sorbie, 1992)

The white and odorless powders were obtained from SNF Floerger Company. The property of the HPAM grades utilized in this study are given in the table below including their SNF batch numbers to enable future researchers order similar polymers.

Table 3.2: HPAM Grades and Molecular weights

HPAM grade	Batch lot number	Average molecular weight (g/gmol)
Flopaam 3630S	GJ 1008	20×10^6
Flopaam 3330S	V5054	8×10^6
Flobeads AB005V	BB 2481	0.5×10^6

3.1.4.3 Tylose® (Carboxymethyl Cellulose)

Tylose® (Carboxymethyl Cellulose or CMC) is a Cellulose derivative containing carboxymethyl groups (-CH_2-COOH) and hydroxyl groups. It is produced from the Alkali-catalysed reaction of cellulose with chloroacetic acid

It is used as a viscosfier in many industrial applications even in the drilling operations. It has a very low nominal molecular weight of 700,000 g/mol making it relatively inelastic and ideal in the study of fluids with negligible elastic property. (Reynolds and Jones, 1989; Shah, El-Fadili and Chhabra, 2007; Benchabane and Bekkour, 2008).

Tylose® are soluble, non-ionic and highly etherified carboxymethyl polymers. The solubility of the Tylose is due to the polar carboxyl groups rendering Tylose soluble and chemically reactice (Hollabaugh, Burt and Walsh, 2005) . The odorless white fine powder was supplied by ShinEtsu.

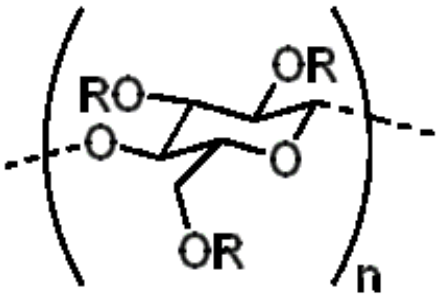

$R = H$ or CH_2CO_2H

Figure 3.5: Molecular Structure of Carboxymethyl (Wikipedia, 2019).

3.2 Polymer Preparation

The detailed steps followed in order to prepare the polymers are discussed in this subsection. If the steps described below are accurately followed, similar results of fluids can be obtained.

3.2.1 Preparation Procedure for Carbopol

The procedure for preparing the Carbopol Test fluids is similar to that utilized by Curran et al., (2002). The procedure is as follows:

- Deionized water of required volume was measured and stirred at a low rpm in a mixing bucket using an overhead mixer. The image of the overhead mixer is shown below. A coated helical stirrer was connected to the mixer. It was coated to prevent corrosive effect of carbopol solution.

Figure 3.6: Overhead Mixer for Preparing Polymer Sample

- The required mass of Carbopol powder was added slowly progressively (not all at once) to the stirring de-ionized water on to the inner sides of the fluid vortex.
- After adding the polymers, the solution was stirred at 150 rpm for 2.5 hours until the low wettability carbopol powders fully dissolve with no visible polymer powder.
- A 10 wt % Sodium hydroxide (NaOH) solution was added in drops to neutralize the polymer solution to about 6.5 or desired rheological property attained. The pH of the polymer solutions were measured by using the Fisherbrand™ accumet AE150 pH benchtop meter. An image of the pH meter is shown below;

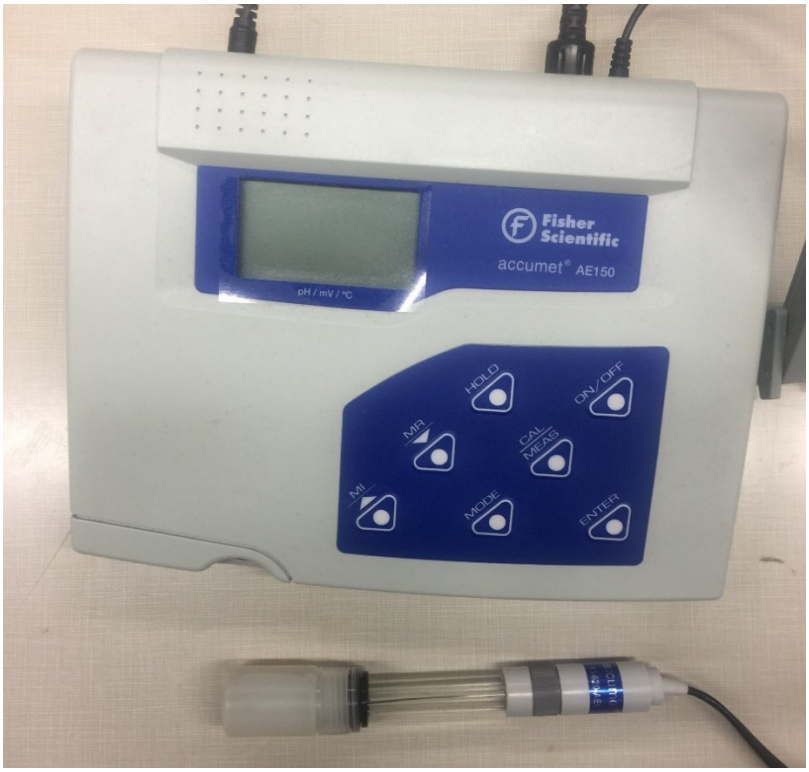

Figure 3.7: pH Benchtop Meter from Fisherbrand™

- After desired rheological property was attained, the fluid was stirred continuously for 1 hour minutes to ensure homogeneity.
- For the Particle Image Velocimetry (PIV) test, an additional step is required which involves the addition of Tracer particles (20ppm concentration) to the polymer fluid. The solution was then stirred for an additional 25 minutes.
- The solution was transferred to the fluid column and allowed to stand still overnight to remove air bubbles. (Filtration was not necessary since the carbopol polymers used were clear and transparent).
- For smaller samples (350mL) used to carry out rheological tests, a magnetic stirrer was utilized to prepare the fluids. The image of the magnetic stirrer is shown below;

Figure 3.8: Magnetic Stirrer for Preparing Smaller Samples of Polymers

3.2.2 Preparation Procedure for Tylose and Hydrolyzed Polyacrylamide (HPAM)

The procedure for preparing the Tylose and HPAM are similar and identical to the procedure followed by Arnipally and Kuru, (2018). The procedure is as follows:

- Deionized water of required volume was stirred at 300 rpm in mixing bucket.
- Based on the desired wt. %, the required mass of polymer powder was added progressively (not all at once) to the stirring de-ionized water on to the inner sides of the fluid vortex.
- After adding the polymers, the solution was stirred at 150 rpm for 3 hours (short time due to low concentration) until the low wettability polymer powders fully dissolve and a completely homogenous fluid is formed.
- The polymer solution was transferred to the fluid column and allowed to stand still overnight to remove air bubbles.

3.3 Rheological and Physical Characterization of Test Fluids

All the equipment used for the measuring and quantifying fluid properties are discussed in this subsection.

3.3.1 Measurement of Fluid Density

The density of the fluids was measured by dividing the weight of the test fluid by the volume using a Pyrex Vista no. 70024 of 10 ml measuring jar. The weight of the test fluid was determined using the sophisticated digital ExplorerPro weighing balance (figure below) obtained

from Ohaus®. The sensitivity of the weighing balance is 0.1mg, while the sensitivity of the measuring Jar is 0.1mL.

Figure 3.9: ExplorerPro Weighing Balance

3.3.2 Rheological Measurements

Two equipment were used for the rheological characterization of experimental test fluids and they are;

3.3.2.1 Fann Viscometer (Model 35A)

Fann Model 35 viscometers are coquette rotational viscometers. In this device, the test fluid is kept in the Viscometer cup and contained in the annular space also known as the shear gap between and outer cylinder and an inner re-attachable bob (Fann Instrument Company, 2016). Viscosity measurements is carried out by imposing a known shear velocity on the experimental fluid and the corresponding resisting viscous drag exerted by the fluid is accurately measured by

the deflection of a precision spring. In other words, it measures the shear stress at a known shear rate. The viscosity is simply the division of the shear stress by the shear rate.

The device has 12 measuring speeds (0.9, 1.8, 3, 6, 30, 60, 90, 100, 180, 200, 300 and 600 RPM). RPM is the unit acronym for Rotations Per Minute. The shear stress is measured by the dial deflection which is converted to pascal by a conversion factor 0.511. Similarly, the shear rate which is measured in RPM can be converted to s^{-1} with a conversion factor of 1.703. The image of the device and its schematic are shown in the figures below.

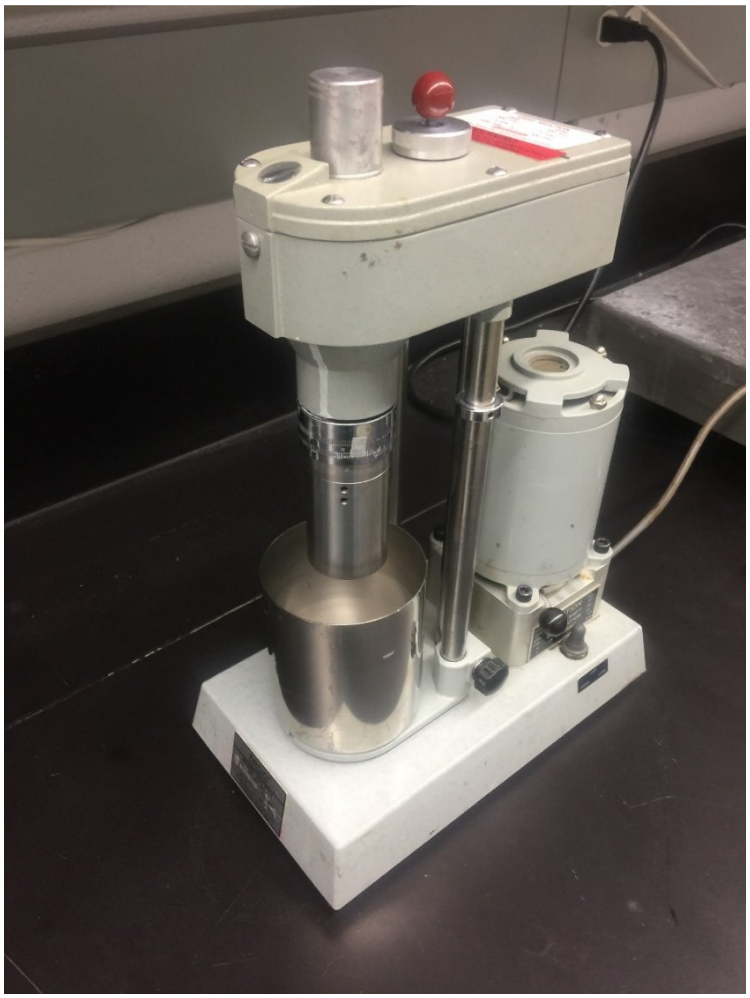

Figure 3.10: Fann Viscometer

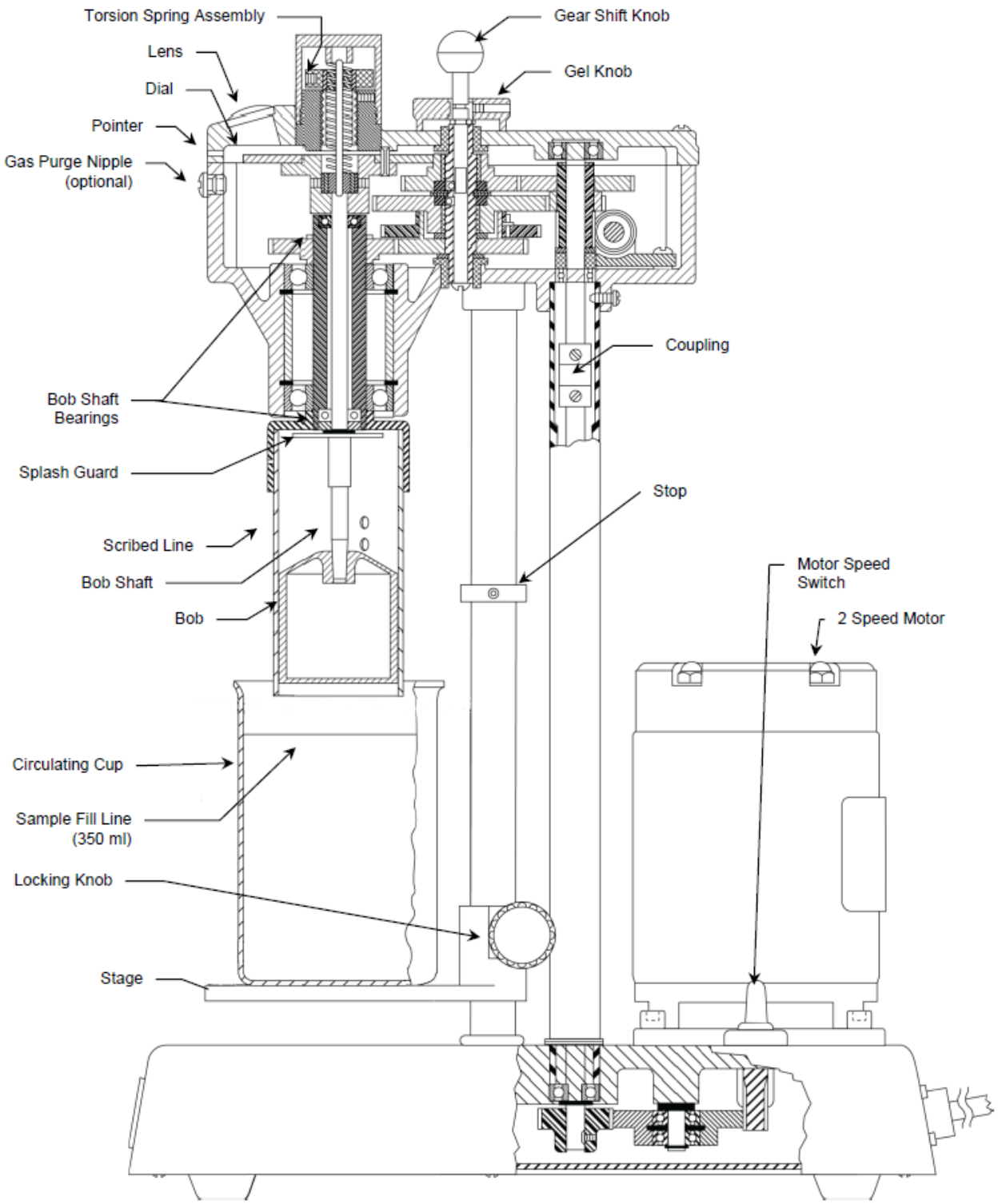

Figure 3.11: Fann Viscometer Model 35A Schematic

3.3.2.2 Bohlin Rheometer

Rheological measurements were performed with the C-VOR cone and plate type rheometer from Bohlin Instruments. The 40mm and 4° cone and plate geometry was used. The diameter of the fixed bottom plate was 6cm (60 mm) and a gap of 150 microns was selected between the cone and plate. The measurements were conducted at room temperature (25°C). An image of the viscometer is shown in the figure below.

Figure 3.12: Bohlin Rheometer

3.4 Rheological Measurements

In this experimental study, the test experimental test fluids were characterized based on their rheology. The Fann Viscometer and Bohlin Rheometer were used to carry out the rheological characterizations. The major tests carried out include the Shear Viscometry tests for the viscous properties of the fluid and Oscillation Frequency Sweep test for elastic property of the fluid.

3.4.1 Shear Viscometry Tests

These are tests carried out on test fluids to determine viscosity and yield stress. It involves imposing a selected shear stress on a fluid and measuring the corresponding shear rate (or vice versa). The viscosity is then calculated by dividing the shear stress by the shear rate. The Fann viscometer and Bohlin rheometer were both used to carry out these tests. In these tests, shear rates ranged from 0.5 s^{-1} to 1000 s^{-1}. While only 6 data points were obtained from the Bohlin Rheometer, a flow curve plot could be obtained from the Bohlin Rheometer. An example shown below;

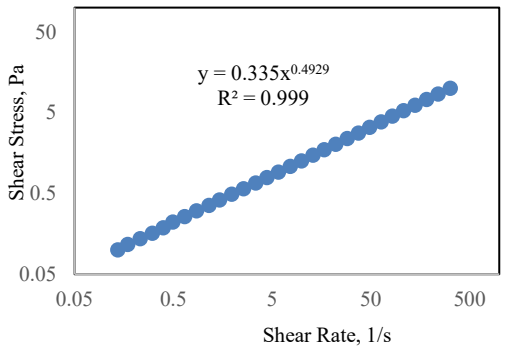

Figure 3.13: Shear Stress Vs Shear Rate

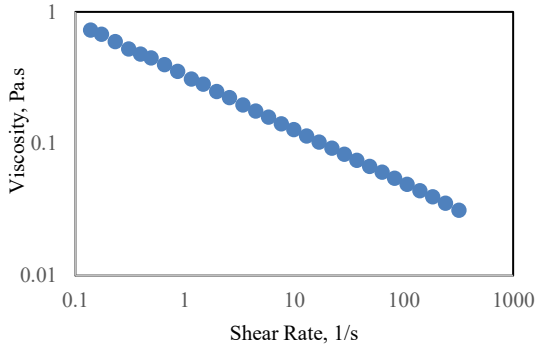

Figure 3.14: Shear Viscosity Vs Shear Rate

3.4.2 Oscillation Frequency Sweep Test

Oscillatory frequency sweep tests involve the sinusoidal application of low values of stress on a material at various angular frequencies and recording how the material responds. Low values or strains are used because elastic properties will be dominant on flow behavior and avoiding the destruction of the materials microstructure (Barnes, 2000; Mezger, 2006). The elastic and viscous properties of the material are determined by measuring the sinusoidal response in each cycle.

For an ideal solid, the sinusoidal strain response will be in a perfect phase unison with the applied sinusoidal stress. The phase angle δ which represents the angle representing the disparity in phases will be 0° for an ideal solid (completely stiff). An ideal solid obeys the Hooke's law hence strain will be directly proportional to sinusoidal stress. This is also known as elastic behavior. For an ideal liquid, the sinusoidal strain response will be totally out of phase with the applied sinusoidal stress. The phase angle will be 90° as stress is not proportional to strain rate for pure liquids.

The phase angle will always be between 0° and 90° for viscoelastic material, the lower the phase angle the more elastic the viscoelastic material and vice versa. In oscillation measurements, the instantaneous ratio of the sinusoidal stress to sinusoidal strain is termed complex modulus (G*). In practical terms, the G* can be used to indicate the rigidity of the material (Mezger, 2006). It is the combination of both the elastic modulus (G') and viscous modulus (G"). The mathematical relationship between G*, G' and G" is given below.

$$G' = G^* cos\delta \quad 3.1$$

$$G'' = G^* sin\delta \quad 3.2$$

The oscillation sweep test is used to determine elastic property of the experimental fluids. An example of a frequency sweep test result is shown below in Figure 2.5

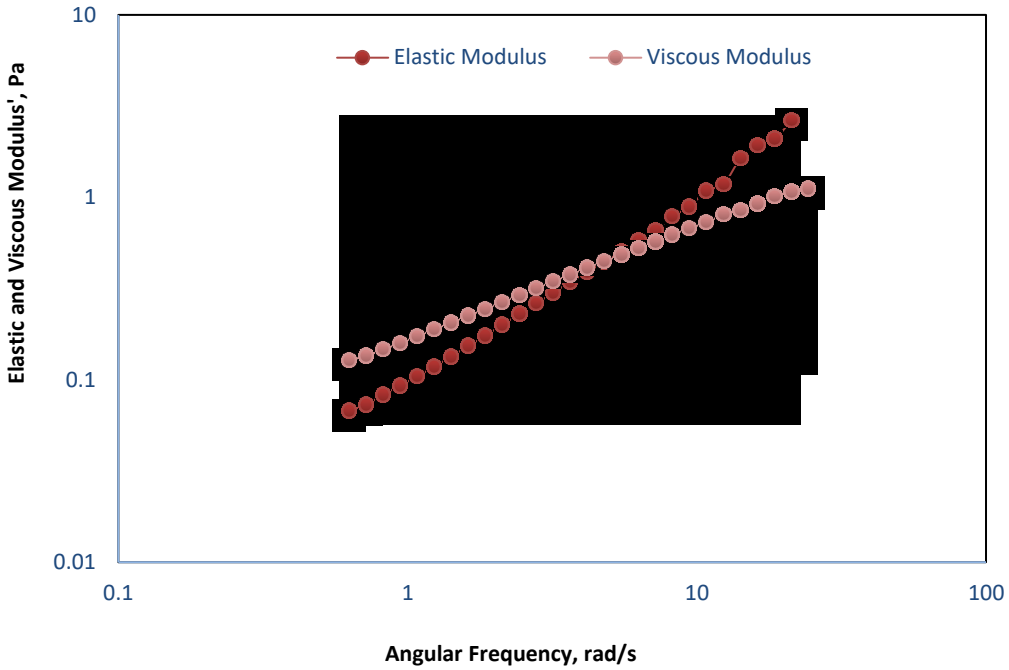

Figure 3.15: Sample Oscillation Test Result

The frequency at which When $G' = G''$ is very significant. The longest relaxation time, λ (sec) which is the inverse of the crossover angular frequency between the elastic modulus and viscous modulus. It signifies the time needed for a material to regain its original structure after any deformation or disturbance. It is used to quantify the elasticity of a fluid (Choi, 2008; Malhotra and Sharma, 2012; Arnipally and Kuru, 2018)

3.5 Particle Image Shadowgraphy

The settling velocities of the spherical particles in various polymer solutions were measured using Particle Image Shadowgraphy (PIS) technique. This section provides a complete description of the Particle Image Shadowgraphy technique. It includes the experimental setup and equipment used to carry out the experiment

3.5.1 The Mechanism and Technique of Particle Image Shadowgraphy

Particle Image Shadowgraphy is a non-intrusive flow visualization technique that works on the basic optical principle that light is sensitive to changes in density of the medium through which it travels and any disparity always result in the formation of shadows. Image Shadowgraphy has advantages over some flow measurement techniques because it is non-intrusive measuring technique hence it does not interrupt the flow or alter the fluid property thereby avoiding errors. It also allows the simultaneous measurement of several other characteristics, such as the interface speed and the direction of motion, and the object size.

This technique requires a source of light and an image acquisition device as shown by experimental setup in the next subsection. The aim of the light source arrangement is to provide light which is refracted by the opaque object and to obtain a homogeneous background at the recording sensor. The image recording device must have the ability to capture an image of the objects shadow. The light source can be pulsed laser, spark generator or LED and a CCD camera can be used as recording element. It is ideal for a transparent medium (water or air). In the presence of back illumination, the light which does not interact with the object produces a bright background while those that interact with the opaque appear dark which are captured by the device (Castrejon-Garcia *et al.*, 2011). The end result is a bright background and with shadows of the representing regions

of different densities. Analysis of these resulting shadowgraph images can help determine a lot of parameters including terminal velocity. Particle Image Shadowgraphy (PIS) is independent of particle shape, opacity and size when using the appropriate imaging system and light source. The camera and light source depend on the experimental setup. Using a short laser pulse as illumination it is possible to freeze motions of more than 100m/s (LaVision, 2003).

3.5.2 The Experimental Setup and Equipment of the Particle Image Shadowgraphy Experiment

The schematic below shows the experiment setup for investigating settling velocity in the Polymer fluids

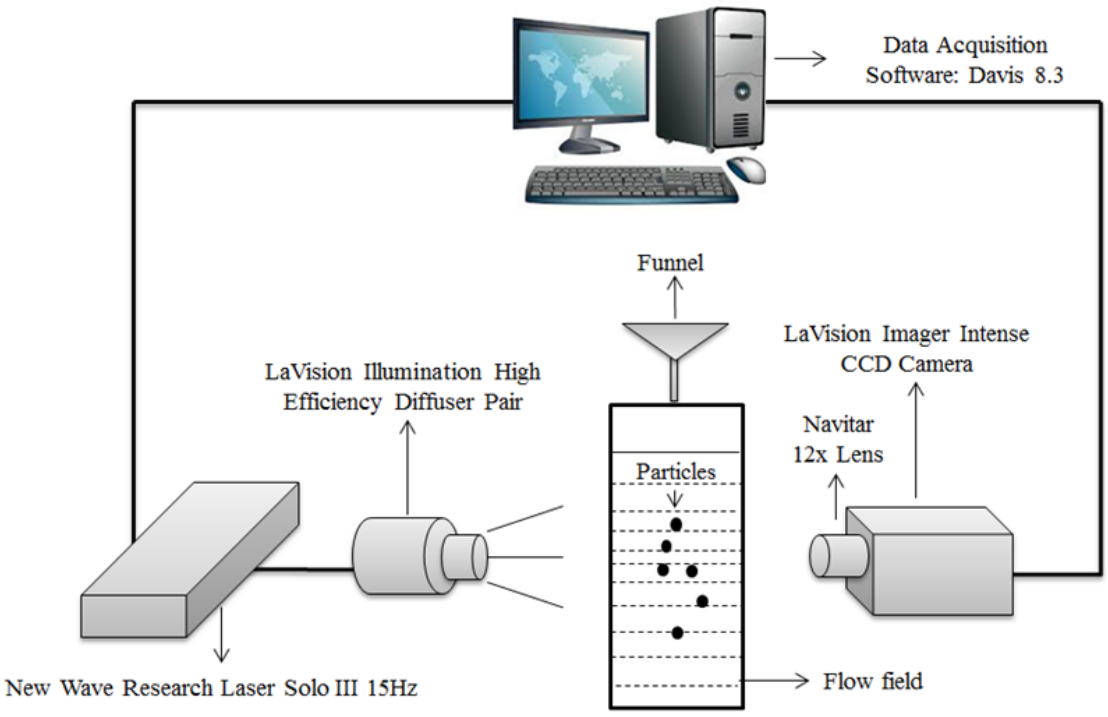

Figure 3.16: Experimental Setup of Particle Image Shadowgraphy

The experimental setup was composed of the light source, which was provided by the New Wave Research Laser Solo III; an Nd-YAG double pulsed laser with a 532 nm wavelength and a frequency of 15 Hz. The laser was coupled with the LaVision circular diffuser pair for greater efficiency and background illumination. The image acquisition was provided by the LaVision Image Intense Camera with a 12x Navitar Lens. This double framed (capable of capturing quick successive images at two different exposure times in as short as 500ns) high resolution camera had a CCD sensor of 1376×1040 pixels capable of capturing 5 frames per sec and a capacity to convey 12-bit digital images. The captured images would result in futility, if they cannot be processed and analyzed to produce data. The Data Acquisition (DAQ) and processing software used was the LaVision Davis 8.3 software.

The ParticleMaster Shadow Project of the Davis 8.3 software follows algorithms to measure the size and the velocity. The algorithm measures the size by first locating the particles in the area of general interest (field of view of the camera) and analyzing the particles for size, shape and position. The recognition and analyzing algorithm is based on the intensity variation of the image. After sizing and locating the particles in the first frame, the algorithm then measures the terminal velocity by correlating the first frame with the successive frame to determine position shift (displacement) of the particle. The displacement and Δt (time difference between frames) can be simultaneously used to determine the velocity. If this measurement is carried out after the constant velocity was achieved by the particle, then this methodology gives an accurate instantaneous measurement of the terminal velocity. The equipment in the experimental setup will be discussed in detail in the next subsection

3.5.2.1 Image Acquisition Device - The LaVision Imager Intense CCD Camera

The LaVision Imager Intense camera is a double frame high-resolution camera with a CCD sensor of 1376x1040 pixels and with a framing rate of 5 frames per second (LaVision, 2003). The CCD sensor helps convert photons to electric charge based on the photoelectric effect. The sensor height is 17mm (LaVision, 2003). The double frame ability of this camera allows it to capture two different exposures in successive frame rates within an infinitesimal time limit of about 500ns. This double frame capturing must be synchronized with the light source. This camera meets the requirement of tracking particles due to its double frame ability, short inter frame time and resolution.

Figure 3.17: The LaVision Imager Intense CCD Camera

3.5.2.2 Camera Lens – 12x Navitar Lens

A camera lens is an optical device that is used in conjunction with a camera to capture images. It determines a lot of the working parameters like working distance, focal length and field of view. The Navitar lens is selected for the experimental setup. It is mounted on the camera, and this lens is suitable for a working distance of 32mm-341mm with a maximum magnification of 12x. The field of view of the current experimental setup is 50mm x 50mm thereby making this lens suitable for carrying out the experiment.

Figure 3.18: 12x Navitar Lens

3.5.2.3 Light source - A Double Pulse Solo III Laser

A double pulsed Nd:YAG solo laser from New Wave Inc. is selected as the illumination source for shadowgraph experiments. The laser is capable of emitting two pulses of light in adjustable assigned time period. The wavelength of the laser light is 532 nm with 15 Hz frequency. The laser is connected to the LaVision circular diffuser at the end. Using short

double pulses from this laser as illumination; it is possible to freeze motions of more than 100m/s (LaVision, 2003, 2008). The image of the laser is shown below

Figure 3.19: Double Pulse Solo III Laser from New Wave Research

3.5.2.4 Diffuser – A LaVision High Efficiency Circular Diffuser Pair

A diffuser is used to spread to increase the size of a beam by spreading out the light. The double pulsed laser is coupled to the diffuser. The diffuser is used to widen the region

which light travels, this improves background illumination and reduces its energy density. The schematic describing the action of a diffuser is shown below.

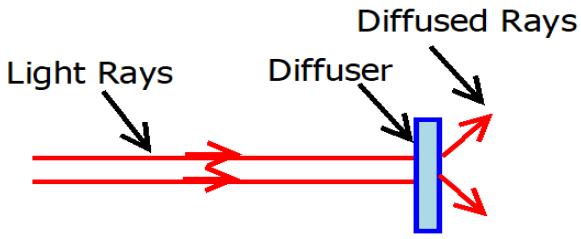

Figure 3.20: The Action of a Diffuser.

The input and output apertures of this diffuser are 9 mm and 120 mm respectively. 100 mJ is the minimum recommended laser power for this diffuser and 20 ns as the duration of pulse (LaVision, 2013). Placing the diffuser at a far distance from the absorber (fluid column) would result in scattering. Hence a maximum spacing distance of 100mm should be employed (Shahi, 2014)

Figure 3.21: Diffuser

Figure 3.22: High Efficiency Diffuser

3.5.2.5 Data Acquisition (DAQ) Software – Davis 8.3 software

Captured images would result in futility if they cannot be processed and analyzed to produce data. This data acquisition and analysis is carried out by the Davis 8.3 software. The ParticleMaster Shadow Project of the Davis 8.3 software follows algorithms to measure size and velocity. The algorithm measures the size by first locating the particles in the area of general interest (field of view of the camera) and analyzing the particles for size, shape and position.

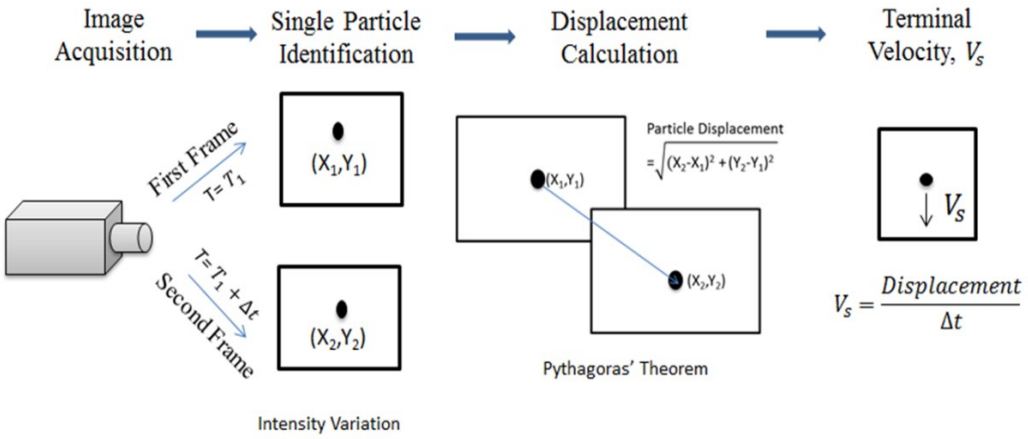

Figure 3.23: Schematic of the Software algorithm to determine terminal velocity

The recognition and analyzing algorithm is based on the intensity variation of the image. After sizing and locating the particles in the first frame; the algorithm then measures terminal velocity by correlating the first frame with the successive frame to determine position shift of the particle. The position shift and Δt (time difference between frames) can be simultaneously used to determine the velocity. If this measurement is carried out after the constant velocity was achieved by the particle, then this methodology gives an

accurate instantaneous measurement of the terminal velocity. The schematic below in Figure 3.23 shows the general algorithm followed to calculate terminal velocity by the software

In other to determine the particle size, Davis 8.3 models each particle as an ellipse and quantifies the major and minor axis. The output diameter is derived from pixel color recognition of the captured particle.

3.5.3 Camera Position

The selection is of experimental equipment step is succeeded by system optimization of the setup to obtain accurate results. This section determines the best positions and dimensions of experimental equipment to obtain accurate experimental results. Due to the complex nature of Viscoplastic fluids, there are no literatures that explicitly define the specific point when the buoyant and drag forces become in equilibrium with the weight force (attainment of terminal velocity). It is however intuitive to place cameras close to the base of the fluid column to obtain the very accurate due to the following reasons

i. As earlier stated, particles do not attain terminal velocity immediately but gradually transit into it as all forces acting on the particle balance out. So placing the cameras close to the top of the column would result in measuring pseudo settling velocity or pre-settling velocity which is inaccurate.

ii. From understanding of basic physics, the time taken to attain settling velocity depends on the buoyancy and drag force both of which have higher values in a polymer than water.

Hence, attaining terminal velocity would take a shorter time in a polymer than a Newtonian fluid for the same mass of particle. In other words, for a 50cm fluid column, 25cm from the base would be more than sufficient to attain terminal velocity for the same mass of particles used. A lower safety value of 15cm should be adopted to ensure that particles would attain terminal velocity before they are captured by the camera. The measurement can similarly be carried out at a different height to ensure that a similar velocity value is obtained. An image depicting the right position for the camera is shown below.

3.5.4 Determination of Maximum Working Distance for Camera

As earlier stated the optics of the camera determines the working distance. The selected lens (12x Navitar Lens) has a versatile focal length range of 32mm-324mm. This creates a variety of options for the working distance. Although th horizonatal field of view is fixed based on the dimensions of the fluid volume (150mm), For an optimum selected focal length of 40mm, the working distance of the camera is calculated to be 353mm. The calculations are attached below. Also Shahi (2014) Claimed that a maximum spacing distance of 100mm should be adopted between column and diffuser for better illumination and less scattering of light source. The schematic shown in 3.21 and 3.22 combines every detail to give correct positions and working distance.

Horizontal Field of View = 150mm (Based on fluid column dimensions)

Focal length of lens = 40mm (Selected focal length of Navitar 12x Lens)

Length of camera sensor= 17mm (LaVision product manual)

$$Working\ Distance = \frac{Horizontal\ field\ of\ view\ x\ Focal\ length}{Sensor\ Height}$$

$$Working\ Distance = \frac{150mm\ x\ 40mm}{17mm}$$

$$Working\ Distance = 352.9\ mm$$

This represents the optimum working distance of the LaVision Camera from the point of interest

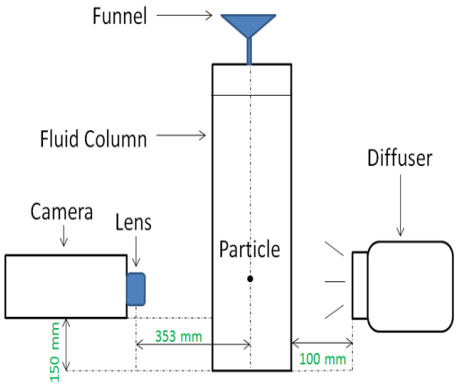

Figure 3.24: Correct position and working distance

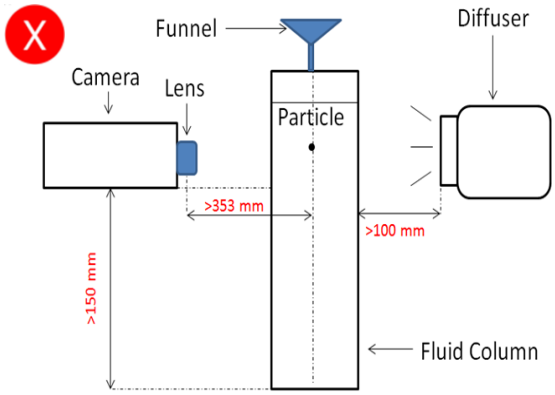

Figure 3.25: Wrong position and working distance.

3.5.5 Particle Image Shadowgraphy System Calibration

Camera calibration is meticulous process of converting pixel space to physical process. According to several authors, accurate calibration and orientation procedures are the most crucial steps to extract precise and reliable data from images (Remondino and Fraser, 2006; Arnipally, 2017). Physical calibration is the most commonly used method for calibrating cameras and was utilized in this study. The physical calibration process involves assigning a pre-known distance

value is assigned between two points, and the captured image is scaled accordingly. At the time of calibration and image acquirement, the position of camera should be fixed and undisturbed (Wieneke, 2005; Adrian, 2005; and Arnipally 2017).

Figure 3.26: Calibration Target

The calibration target sheet is shown in **Error! Reference source not found.**. The gridlines a re 1.5mm spaced. A picture of the grid is captured while placed in the fluid particle column. The image is imported to the Davis 8.3 software under ParticleMaster Shadow project on the computer. After which two known points at an appreciable distance on the horizontal axis are selected with known physical distance between them. From the pixel option in the software, a number of pixels between these two points are calculated to be “p” say. Then one pixel should be equal to d/p mm.

By this way, the image is mapped from pixel space to physical space (Shahi, 2014; Arnipally, 2017). An image depicting the image calibration I shown in figure below.

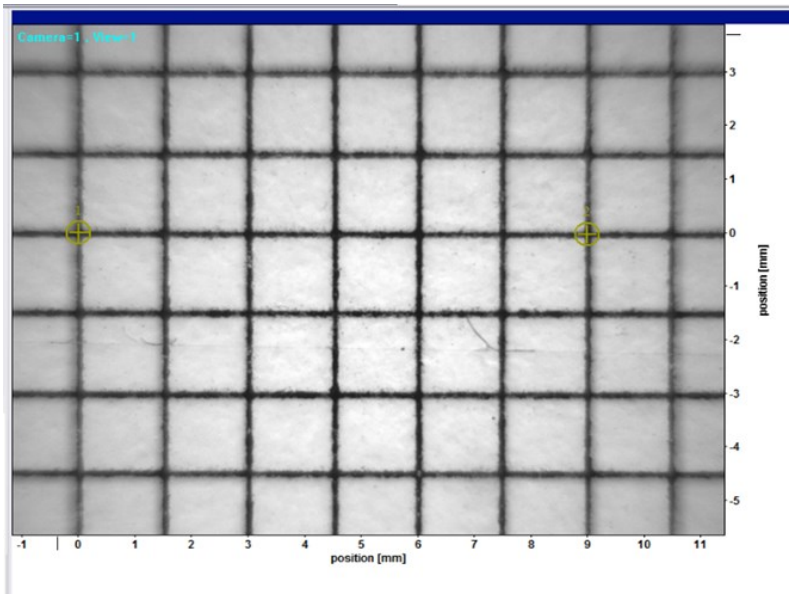

Figure 3.27: The process of System Calibration in Davis 8.3 software (Arnipally, 2017)

3.5.6 Experimental Procedure to Measure Particle Settling Velocity

The experimental procedure follows similar steps employed by Shahi (2015) and Arnipally (2017). The first aspect of the procedure involves the preparation of the physical experimental setup as described in Section 3.2 above. Once the fluid is prepared, it is transferred to plexiglass fluid column and is left unperturbed overnight to expel bubbles (which affect image quality and analysis) and to ensure the polymer regenerates its natural un-sheared state. Equipment calibration is carried out by inserting the calibration target sheet (a sheet having 0.8 mm printed circles spaced 1.5 mm apart) in the column and taking a focused image of the sheet.

The spacing dimensions of the sheet helps the Davis 8.3 software convert pixel dimensions into physical dimensions. The calibrated plane of focus would be marked at the top. It serves as the funnel position and the dropping point of spherical particles. Reference images are captured and averaged to serve as a reference background for the experimental images. The experimental images can now be captured. The spherical particles are to be dropped with the aid of a funnel, to ensure uniformity in landing positions. This improves the accuracy of the results. When the spherical particles pass through the plane of focus, they appear as dark spots on Davis 8.3 software because of the differences in intensity as explained in the experimental section. The software follows a specific algorithm to determine the particle size and the terminal velocity.

Repeatability of the experiment is checked by carrying out at least 5 trials and the averaging of 5 trials gives an accurate measure of the settling velocity. The velocity measurements is performed at two different heights (15cm and 10cm) from the base to ensure that the particle had attained its terminal settling velocity.

A detailed step by step procedure is given below;

- The fluid particle column is filled with the experimental fluid. The test fluid is left unperturbed for 24 hours to expel bubbles (which affect image quality and analysis) and to ensure the polymer regenerates its natural un-sheared state.
- The fluid column should be left partially closed to prevent evaporation which can change the property and mass concentration of test fluid.
- Backlighting illumination is provided by the Nd:YAG laser-diffuser pair placed on the opposite side of the fluid column and the double framed CCD camera.

- The camera temperature should be less than -11°C before turning on the laser. The external connection buttons of the lasers are pressed down to switch controls to the DAQ software. The laser is turned on
- Davis 8.3 software is run by clicking on its icon on the computer, and a new file created under the project type of ParticleMaster Shadowgraph.
- Laser power selected to be not more than 25% with a 4% difference between power 1A and power 1B in device settings on the DAQ. The timing between the two images is chosen within the range of 500 to 3000 nanoseconds, according to the particle sizes.
- Calibration is carried out by inserting the calibration target sheet in the column and taking a focused image of the sheet. The procedures described in section 3.5.3 are then followed. The position of the plane of focus that is calibrated would be marked at the top. It serves as the position where the funnel is placed. It serves as the dropping point of the spherical particles.
- Reference images are captured and averaged to serve as a reference background for the experimental images. Reference image Recording process consist of 15 images that are captured by using Start & Stop buttons.
- The spherical particles are to be dropped with the aid of a funnel (not by hand), to ensure uniformity in landing position and the experimental images can now be captured (recorded). This improves the accuracy of the results. An example of the captured image is shown below in Figure 3.28.
- When the spherical particles pass through the plane of focus, they appear as dark spots on Davis 8.3 software because of the differences in intensity as explained earlier. The

software follows algorithm in section 3.5.2.5 to calculate particle sizing and terminal velocity.

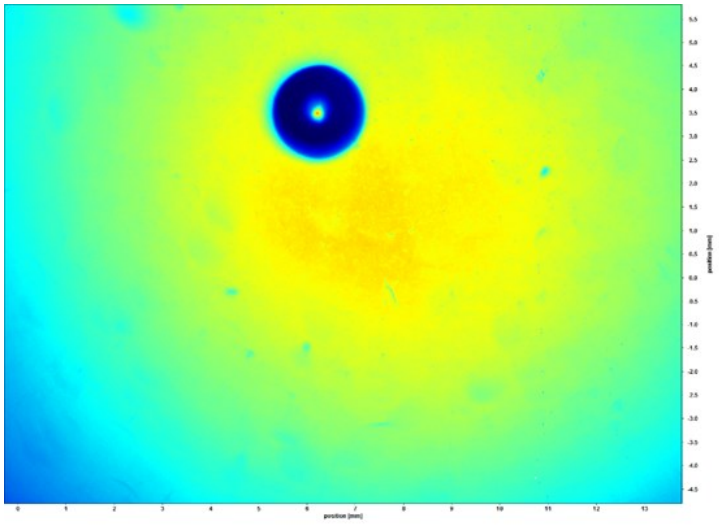

Figure 3.28: Experimental Image of Settling Particle Captured in the DaVis 8.3 Software

- The image processing scheme used by Arnipally (2017) would be adopted in the experimental setup. The particle sizing option under Shadowgraph operation is used to process the images. Smoothing option would not be selected in the image preprocessing steps so as to not interfere with result output. The background reference image is selected as the reference image against which the experimental images would be compared.
- Appropriate values are assigned to the low-level threshold, global threshold, high-level threshold and AOI expansion to get the best output data. Finally, the outliers are filtered using velocity parameters. The output result obtained from the Davis 8.3 software is shown below;

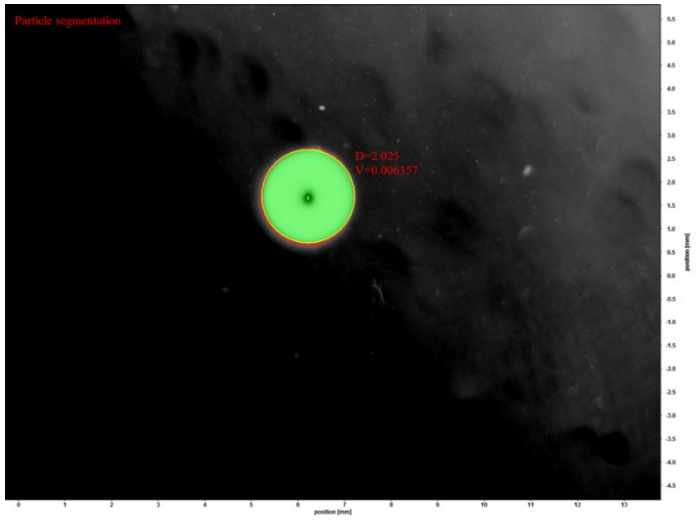

Figure 3.29: Davis 8.3 Processed Output Image after Particle Sizing Function (Shahi, 2014)

- Repeatability of experiment is carried out at least 5 trials and the average of 5 trials gives an accurate measure of the settling velocity.
- The velocity measurements should be performed at two different heights (15cm and 10cm) from the base to ensure that the particle had attained its terminal settling velocity.
- During the experimental process, only one particle at a time was dropped to measure settling velocity then 25 minutes of waiting time were kept to ensure that the fluid had regained its original microstructure to prevent thixotropic effects and enhance accuracy.

3.5.7 Verification of Particle Image Shadowgraphy Measurements.

Using the universal Newtonian drag curve for spheres, the PIS experimental setup is calibrated and tested to authenticate the veracity of results. The test is carried out by measuring

settling velocity of the 4 spherical balls (0.71mm,1.18mm,1.50mm and 2.00mm) in water (standard fluid). The measured settling velocity of the spherical particles is used in determining particle Reynolds number (Equation 2.2) and consequently the drag coefficient of spherical balls using the correlation (Equation 3.3) proposed by Morrison (2013).

$$C_D = \frac{24}{Re_p} + \frac{2.6\left(\frac{Re_p}{5}\right)}{1+\left(\frac{Re_p}{5}\right)^{1.52}} + \frac{0.411\left(\frac{Re_p}{263000}\right)^{-7.94}}{1+\left(\frac{Re_p}{263000}\right)^{-8.00}} + \frac{0.25\left(\frac{Re_p}{10^6}\right)}{1+\left(\frac{Re_p}{10^6}\right)} \qquad 3.3$$

The drag coefficients from the experimental measurements were found to be within 3.5 % of the theoretical values, hence bolstering the reliability of the experimental setup. Furthermore, some authors have previously authenticated the experimental setup used in this study (Shahi and Kuru, 2015; Arnipally and Kuru, 2017).

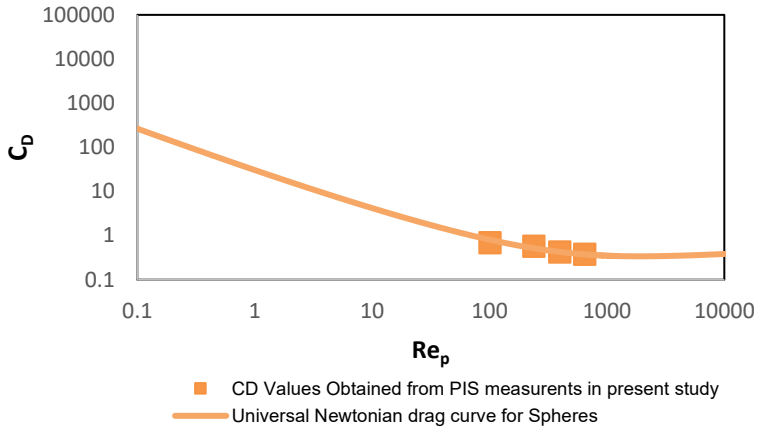

Figure 3.30: C_D vs Re_p Plot for the Verification of the PIS Measurements

To further bolster the accuracy of the technique, the measured diameters for the glass beads were also compared with the particle specification data provided by the manufacturers.

Table 3.3: Verification of PIS Measurements based on Measured Diameters

Glass Bead Specified Diameter	Measured Diameter
0.71 ± 0.02	0.70 ± 0.030
1.18 ± 0.02	1.184 ± 0.016
1.50 ± 0.03	1.55 ± 0.020
2.00 ± 0.04	1.99 ± 0.025

3.6 Particle Image Velocimetry (PIV)

The flow field of the spherical particles in various polymer solutions were measured using Particle Image Velocimetry (PIV) technique. A detailed review of the Particle Image Velocimetry technique is presented here which includes the experimental setup, equipment and procedures used to carry out the experiment.

3.6.1 The Mechanism and Technique of Particle Image Velocimetry (PIV)

Particle Image velocimetry is an optical measurement technique that describes the flow field by tracking light buoyant particles seeded in the fluid. It simply involves the determination of the displacement of these seeded particles thereby obtaining information about the fluid flow. In order to do this, the technique requires the determination a particle position at an initial time t_0 and at a subsequent time t_1 by taking two different pictures at two different times. The particle is located in the first image and its position in the second image is also determined by statistical

analysis, the difference in the position and the time between the two frames can be used to find the displacement and velocity. Hence, the flow field can be fully described.

The PIV Davis 8.3 software follows algorithms to measure displacement and the velocity magnitude. The algorithm divides the captured images into small interrogation windows. During the time interval the tracer particles move by a displacement ds which is determined by cross correlating the same interrogation windows in consecutive images using sophisticated statistical techniques. The velocity is then determined by dividing the displacement (ds) by the time interval (dt). The displacement vectors and velocity of each interrogation window are used to form velocity map result as shown in Figure 3.28 below.

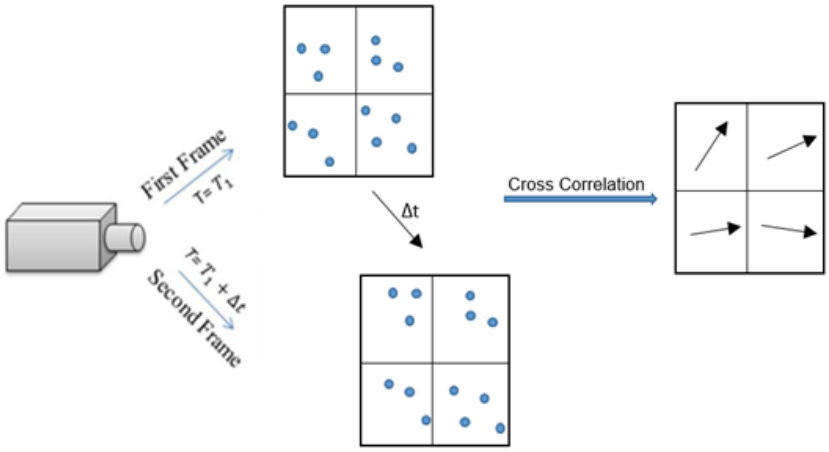

Figure 3.31: A Schematic of the PIV Processing Algorithm

The shape of the yielded region are obtained from processing the PIV images. The PIV images are processed using the PIV processing function of Davis 8.3.

3.6.2 The Experimental Setup and Equipment of the Particle Image Velocimetry Experiment

The flow field behind settling spherical particles in Carbopol solutions were measured using Particle Image Velocimetry (PIV) technique. Particle Image Velocimetry (PIV) is a non-intrusive flow visualization technique that allows capturing instantaneous velocity data of whole flow fields (Raffel *et al.*, 2007)The fluid is seeded with very light buoyant particles (tracer particles) that do not affect flow properties and the major assumption is that these particles move in unison with the flow field and are also descriptive of the fluid flow field. These particles are illuminated by means of a laser light source which are detected by light scattering and their instantaneous positions recorded with an image acquisition device (Camera).

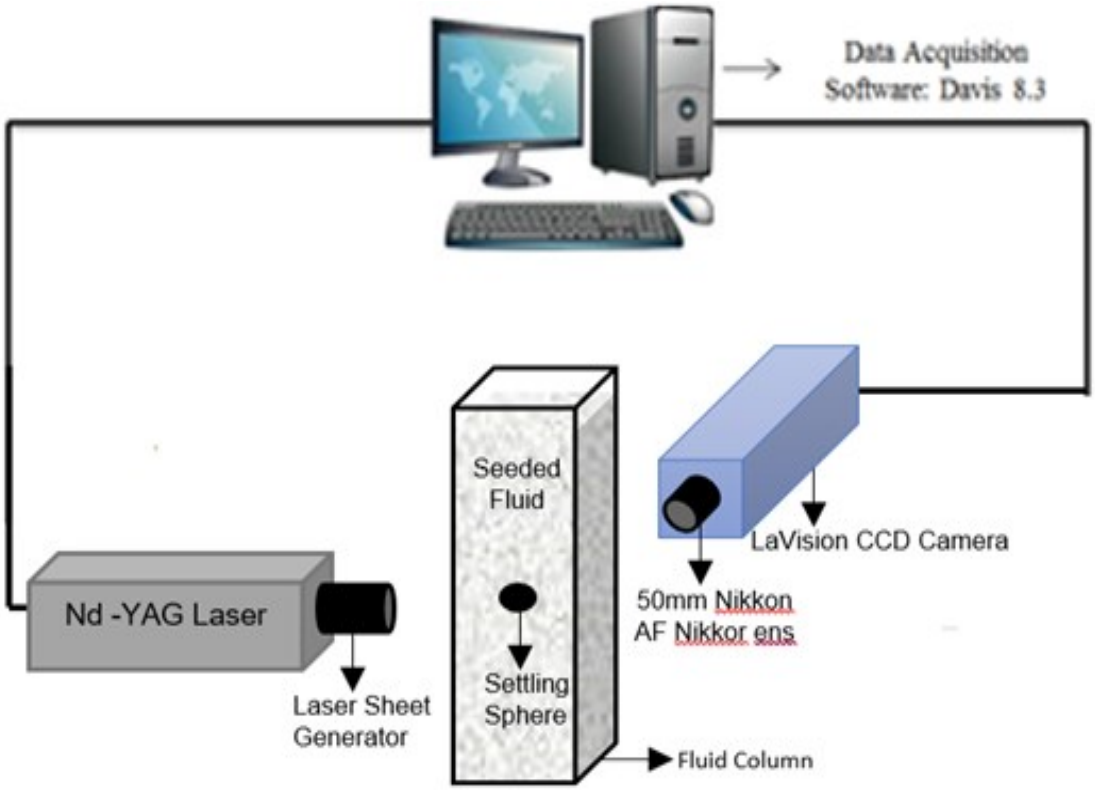

Figure 3.32: PIV Experimental Setup

The magnitude of the fluid flow and their direction are determined using particle position in the captured images. Two successive images are captured at a predetermined time interval (dt). The displacement (ds) and in extension magnitude of velocity is determined using deviation in particles' positions in recorded images by sophisticated Statistical algorithm. The experimental setup is shown below:

The PIV setup (Figure 3.32) was composed of the light source, which was provided by the New Wave Research Laser Solo III; an Nd-YAG double pulsed laser with a 532 nm wavelength and a frequency of 15 Hz. The laser was coupled with the LaVision laser generation sheet for greater efficiency and background illumination. The image acquisition device used was the LaVision Image Intense Camera. This double framed (can capture quick consecutive images at two different exposure times in as short as 10ns) high resolution camera had a Charge-Coupled Device (CCD) sensor of 1376×1040 pixels capable of capturing 5 frames per sec and a capacity to convey 12-bit digital images. A 50 mm Nikon AF Nikkor lens of 1.4 mm aperture was used to capture broader field of View, and it was coupled with the CCD Camera with means of a 12-mm long extension tube. The captured images were processed with the LaVision Davis 8.3 software which was the data acquisition and processing software. Majority of the equipment used are similar to the ones used for the Particle Image Shadowgraphy, so they will not be discussed again.

3.6.3 The Experimental Procedure to Determine Fluid Flow Field Using PIV

The experimental procedure follows similar steps employed by Arnipally, Bizhani and Kuru (2019). The first step involves the preparation of the experimental fluid as outlined above. The experiment was setup similar to Figure 3.28 above with the double pulsed Laser and double framed camera at right angles to each other both connected to the Computer on which Davis 8.3 software

was installed. After ensuring all the equipment are properly set up and 50mm Nikon Lens is mounted on the camera. The double pulsed laser (with the sheet generating diffuser attached) is switched on. The maximum energy of the laser was selected and the laser power of the first and second pulse were adjusted to about 30% and 20% respectively.

Equipment calibration is carried out by inserting a calibration target sheet in the fluid column and taking a focused image of the sheet. The calibration sheet had a grid pattern. The grids were at distance of 1.5 mm from each other; they were printed in black color on a white background. An image of the calibration sheet is shown below.

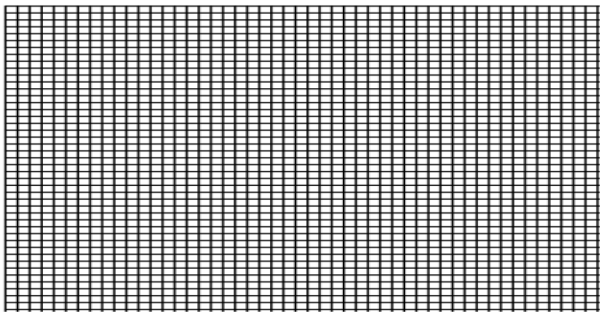

Figure 4: Calibration Sheet

The spacing dimensions of the sheet helps the Davis 8.3 software convert pixel dimensions into physical dimensions. The position of the calibrated sheet is marked so it serves as the position where spheres are dropped to ensure they fall on the focal plane.

After calibration, the PIV images can now be captured by dropping the 2mm and 3mm spherical particles at the marked focal plane decision. A time gap of 30 minutes was maintained between successive ball drops to ensure fluid network build up to original state. Several experimental images were recorded to bolster accuracy and ensure reproducibility.

The experimental images were processed using the Davis 8.3 Software to obtain velocity flow field behind the settling particle and the shape of sheared region as well. The multi-pass interrogation window sizes for cross correlation were chosen to be 256 x 256 pixels and 96 x 96 pixels respectively. The universal outlier detection setting was then finally utilized in post processing to improve experimental results. The Davis 8.3 software has special functions to visualize region of sheared shapes based on vector movement. The optical bit shift function of the PIV processing was used to automatically generate images that showed the sheared regions based on the intensity of velocity vector maps.

3.7 Sources of Errors and Mitigating Precautions to Prevent Them.

As with many other experiments, there would always be errors arising from procedures. This experiment is no exception. Major error sources and controls are listed below and divided into two major sections;

3.7.1 Error Sources in Experimental Fluid Preparation and Rheological Measurements

- Polymer powders should be added progressively and not all at once to the shoulder of the vortex to prevent agglomeration and aid the mixing procedure.
- Mixing the polymers at very high speed could engender mechanical degradation which can affect polymer's rheological property. Hence, an optimum speed of 150 RPM is recommended to obtain the best results for the Polymers.
- After preparing viscoplastic fluid, bubbles are usually entrained in the fluid. Bubbles affect the quality of images captured and result in noise. Hence, the fluids should be left undisturbed for 24 hours for the all the bubbles to be expelled.

- Rheological measurements should be carried out on a fresh sample every time to prevent thixotropic effects which may affect measurement results.
- Rheological measurements should be carried out uniformly at room temperature. Higher temperatures can degrade polymer properties and would lack unison with the temperature at which settling experiments are carried out leading to experimental errors (Arnipally, 2017).

3.7.2 Error Sources in PIS and PIV Experimental Setup and Procedure

- If particles are dropped out of plane of focus, the resulting images would appear blurred. Hence it necessary to use a funnel held with masking tapes to ensure spherical particles fall in the calibrated plane of focus.
- Improper balance of camera gives errors in captured images. The camera should be balanced with spirit level to eliminate inclination errors.
- Over exposure of light can potentially damage the camera sensor and saturate the camera. Hence, the laser power should be gradually increased meticulously from low to high.
- A maximum spacing of 100mm should be applied between diffuser and fluid column. A farther distance would result in scattering of laser light which is not desirable in the project.
- Cameras must be cooled and kept below -11°C to prevent damage from laser. The camera's interaction with the laser always results in temperature increase which may damage the camera (Arnipally, 2017).

- Repeatability of measurements should be carried out to bolster veracity of experimental results. Carrying out experiments in less than 10 trials for a single measurement could lead to errors. Hence a sufficient number of experimental images should be captured.
- Wrong reference images could adversely affect experimental results.

3.8 Safety Practices during Experiment

Lasers are extremely dangerous devices that pose serious threat to lives and properties. From an accident data survey carried out from 1964-1998, students and scientists form a combined total 31.4% of laser accident casualties (Anibarro, 2012). Although most accidents may not be fatal, but avoidable injuries and damages may result.

Based on this, appropriate safety measures must not just be superficially adopted but intrinsically inculcated as habits to avoid accidents associated with lasers while carrying out experiments. Below are some safety practices that must be strictly adhered to while working with lasers.

- Before carrying out any laser experiment, the student or investigator must first enroll and take laser safety course.
- Wear appropriate laser protective eye wear: From a survey carried out in 1999, it was shown that 71% of total laser injuries are eye related injuries (Anibarro, 2012). Viewing laser with a naked eye is definitely a bad idea and can lead to serious eye injuries.
- Total lack or improper use of Personal Protective Equipment (PPE) is equally dangerous and must be put on to avoid accidents.

- Enclose (or indicate) the beam path for the laser system: If the laser beam is confined by a protective covering, risk of human contact is greatly reduced.
- Proper housekeeping must be carried out in laboratories to afford trip hazards.
- Read and understand the instruction manual of the particular type of laser (Nd:YAG Laser) being used for the project.
- Update Standard Operating Procedures (SOPs) for lasers regularly.
- Before operating any laser, the laser safety officer or technician must be contacted.
- Avoid using reflective tools, clothing or accessories while working with lasers.
- Report all laser accidents and near misses to the department's Safety Officer.
- Operate the laser at the lowest beam intensity possible.
- Avoid blocking the output beam or reflections with any part of the body. Use beam dumps to avoid reflections from the target (LaVision, 2008)
- Declare a controlled access area for laser operation. Limit access to trained personnel only.
- Never operate the laser in a room where laser light can escape through windows or doors. (LaVision, 2008)

3.9 References

Anibarro, G. (2012). *Laser Safety: Hazards, Bioeffects, and Control Measures*. Laser Institute of America https://docplayer.net/20891945-Laser-safety-hazards-bioeffects-and-control-measures.html

Arnipally, S. K., Bizhani, M., & Kuru, E. (2018). Experimental Investigation Of Flow Field Past A Spherical Particle Settling In Viscoelastic Fluids Using Particle Image Velocimetry. In ASME 2018 37th International Conference on Ocean, Offshore and Arctic Engineering (OMAE 2018) (pp. 1–10).

Arnipally, S. K., & Kuru, E. (2017). Settling Velocity of Particles in Viscoelastic Fluids: A Comparison of the Shear Viscosity vs Elasticity Effect. In SPE Annual Technical Conference and Exhibition held in San Antonio, Texas, 9-11 October 2017.

Atapattu, D. D., Chhabra, R. P., & Uhlherr, P. H. T. (1990). Wall Effects for Spheres falling at Small Reynolds Number in a Viscoplastic Medium. *Journal of Non-Newtonian Fluid Mechanics*, *38*, 31–42.

Barnes, H. A. (2000). *A handbook of elementary rheology*. *Science* (Vol. 331). https://doi.org/10.1126/science.1201543

Castrejon-Garcia, R., Castrejon-Pita, J. R., Martin, G. D., & Hutchings, I. M. (2011). The Shadowgraphy Imaging Technique and its Modern Application to Fluid Jets and Drops, *57*(3), 266–275. Retrieved from

http://search.proquest.com/technologycollection/docview/878341405/2C1FD9CBFB468EPQ/6?accountid=28155#

Curran, S. J., Hayes, R. E., Afacan, A., Williams, M. ., & Tanguy, P. A. (2002). Properties of Carbopol Solutions as Models for Yield-Stress Fluids. https://doi.org/http://dx.doi.org/10.1016/j.placenta.2014.11.006

Fann Instrument Company. (2016). *FANN 35 instruction manual* (Vol. 207198). Retrieved from http://www.fann.com/fann/products/oil-well-cement-testing/viscosity/visc-model35.page

Hollabaugh, C. B., Burt, L. H., & Walsh, A. P. (2005). Carboxymethylcellulose. Uses and Applications. *Industrial & Engineering Chemistry*, *37*(10), 943–947. https://doi.org/10.1021/ie50430a015

LaVision. (2003). Imager Intense, (0). https://doi.org/10.1007/0-387-29360-4_42

LaVision. (2008). Nd : YAG Laser Systems. *Nd : YAG Laser Systems*. (Reprint)

LaVision. (2013). DaVis 8.1 Software. *Product-Manual for DaVis 8.1*. (Reprint)

Lubrizol. (2010). Technical Data Sheet; Viscosity of Carbopol ® * Polymers in Aqueous Systems.

Mezger T. G., "Rheology Handbook," 2nd Edition, Vincentz Network, Hannover, 2006.

Morrison, F. A. (2013). Data Correlation for Drag Coefficient for Spheres. *Cambridge University Press, New York*, *10*(November), 1–2.

Raffel, M., Willert, C., Wereley, S., & Kompenhans, J. (2007). *Particle image velocimetry. [electronic resource] : a practical guide.* Retrieved from https://search.ebscohost.com/login.aspx?direct=true&db=cat00164a&AN=cran.553115&site=eds-live

Remondino, F., & Fraser, C. (2006). Digital Camera Calibration Methods : In *ISPRS Commission V Symposium "Image Engineering and Vision Metrology"* (pp. 266–272).

Shahi, S. (2014). *An Experimental Investigation of Settling Velocity of Spherical and Industrial Sand Particles in Newtonian and Non Newtonian Fluids using Particle Image Shadowgraph*. University of Alberta.

Shahi, S., & Kuru, E. (2015). An experimental investigation of settling velocity of natural sands in water using Particle Image Shadowgraph. *Powder Technology*, *281*, 184–192. https://doi.org/10.1016/j.powtec.2015.04.065

Sorbie, K. . (1992). *Polymer-Improved Oil Recovery*. *International Journal of Qualitative Studies in Education* (Vol. 5). Blackie and Son Ltd. https://doi.org/10.1080/0951839920050110

CHAPTER 4 : GENERALIZED MODELS FOR PREDICTING THE DRAG COEFFICIENT AND SETTLING VELOCITY OF RIGID SPHERES IN VISCOELASTIC AND VISCOINELASTIC POWER-LAW FLUIDS

4.1 Abstract

The design and optimization of several fluid-particle transport systems often require the determination of particle settling velocity in non-Newtonian fluids. These fluid-particle transport systems are encountered in a wide variety of industrial processes including drill cuttings transport in oil and gas well drilling operations and proppant transport in hydraulic fracturing operations. Current conventional approaches to estimate settling velocity in these non-Newtonian fluids often exclude the effect of elasticity on particle settling which can lead to erroneous estimation. It is therefore imperative to devise an accurate means to mathematically account for the fluid elasticity in particle settling in viscoelastic fluids. An experimental study was conducted to measure the settling velocity of spherical particles in viscoelastic and viscoinelastic power-law type fluids. Using a semi-mechanistic approach, explicit mathematical models were developed for estimating drag coefficient and particle settling velocity in viscoelastic fluids and viscoinelastic fluids. The main objectives of the study were: i.) To measure the terminal settling velocity of particles in various viscoelastic and viscoinelastic power-law type fluids intended at augmenting the present corpus of experimental data in literature. ii.) To develop new drag coefficient and particle Reynolds number correlations that are applicable to viscoelastic and viscoinelastic power-law type fluids and, iii.) To present a general explicit approach for predicting settling velocities of particles in viscoelastic and viscoinelastic fluids.

Particle Image Shadowgraphy (PIS) was used to measure the settling velocities of the spherical particles (Specific gravity 2.5 – 7.7; Diameters: 0.71 - 4.00 mm) in Hydrolyzed Polyacrylamide and Tylose solutions of varying elastic properties. Rheological characterization of the fluids was carried out using the C-VOR Bohlin Rheometer. Experimental results from this

study were combined with various data published in the literature to create an extensive database and widen the scope for empirical analysis. The database had a consistency index (k) range of 0.012-6.773 $Pa.s^n$ and a fluid behavior index (n) range of 0.370 – 0.940. New drag coefficient and Reynold number correlations for particles settling in viscoelastic and viscoinelastic power-law fluids were developed by using a semi- mechanistic approach, which also included the fluid elasticity effect quantified in terms of the longest relaxation time. The newly developed correlations and an advanced statistical modeling program (OriginPro 9.0) were used to mathematically create explicit models that can be used for predicting particle settling velocity in viscoelastic and viscoinelastic fluids.

Comparative analysis showed that an increase in the fluid elasticity gave a corresponding decrease in the particle Reynolds number and dampened the particle settling velocity in viscoelastic fluids. This dampening effect can be attributed to the unique ability of elastic fluids to partially or fully regain their original structure after deformation. Furthermore, statistical analysis showed that the presented new models predict settling velocity accurately with a very low with a Percentage Mean Absolute Error (MAPE) of 7.5% and 11% for viscoinelastic and viscoelastic fluids respectively. The proposed models also exhibited very low Root Mean Square Error (RMSE) values of 0.04m/s and 0.03m/s for viscoinelastic and viscoinelastic fluids respectively. The paper is concluded by presenting practical examples to calculate the terminal velocity of a spherical particle in viscoelastic and viscoinelastic fluids using the models.

The knowledge of particle settling velocity in viscoelastic fluids is essential for the optimization of fluid-particle transport systems like cuttings transport in oil and gas well drilling and proppant transport in hydraulic fracturing operations. This study supplements and provides

vital particle settling velocity data that can be used for modeling relevant transport processes that involve viscoelastic power-law type fluids. The experimental data obtained from this experimental study can also provide the basis for the optimized design of engineering transport viscoelastic and viscoinelastic fluids for a variety of conditions. Based on the statistical analyses of the entire database, we have developed a versatile drag correlation as well as a novel predictive model for particle terminal velocity in viscoelastic and viscoinelastic fluids thereby explicitly quantifying the elastic effect. For the first time in literature, fluid elasticity effect on the particle settling is being explicitly accounted for and precisely modeled.

4.2 Introduction

The accurate estimation of particle settling velocity in non-Newtonian fluids is imperative for the design and optimization of fluid-particle transport systems. These systems are encountered in various processes including drill cuttings transport in oil and gas well drilling operations and proppant transport in hydraulic fracturing operations. The knowledge of particle settling behavior in fracturing fluid is vital in estimating fracture closure and fracture conductivity which are used in ameliorating well productivity (Shah, El-Fadili and Chhabra, 2007). This knowledge is also useful in optimizing hole cleaning in drilling operations (Kelessidis and Mpandelis, 2004); which makes it a very significant.

Despite the fact that particle settling behavior in Newtonian fluids has been fully elucidated by several authors (Clift, Grace and Weber, 1978; Turton and Levenspiel, 1986; Chhabra, 2006); however settling behavior in non-Newtonian has not been fully demystified (Shah, El-Fadili and Chhabra, 2007; Arnipally and Kuru, 2018). These non-Newtonian fluids are of prime importance because most of the fluids described in the operations above are shear thinning non-Newtonian

fluids. Understanding settling behavior in these fluids can be further complicated with the additional presence of elasticity i.e. viscoelastic non-Newtonian fluids. Viscoelastic fluids are currently being used in several oil and gas operations (Bui *et al.*, 2012; Werner, Myrseth and Saasen, 2017) and are prime focus of this study.

In order to fully understand the settling behavior of a particle, the drag coefficient which is the fundamental hydrodynamic characteristic of the particle motion in the fluid must be determined (Machač *et al.*, 1995). The drag coefficient is simply a dimensionless number that quantifies the ratio of viscous forces acting on a particle settling through a fluid to the particle's inertia (velocity). It is mathematically expressed as;

$$C_D = \frac{4(\rho_s - \rho_f)dg}{3V_t^2\rho_f} \tag{4.1}$$

Where d is diameter of the particle, ρ_f is the fluid density, ρ_s is the solid particle density and g is acceleration due to gravity. The drag coefficient is crucial because it determines a particle's settling velocity and in extension the Reynolds number. The drag coefficient is influenced by the particle's physical properties as well as the surrounding fluid's rheological properties which convolutes analytical modelling.

Due to this difficulty in developing analytical solutions, empirical correlations and experimental methods are utilized in the determination of C_D (Machač *et al.*, 1995; Kesely and Matoušek, 2016). This involves developing a drag coefficient and Reynolds number correlation through experimental data. The particle Reynolds number, Re_p which is another significant hydrodynamic

dimensionless number that describes the ratio is kinetic forces to viscous forces experienced by the settling particle. It is expressed mathematically as;

$$Re_p = \frac{\rho_f V_t d}{\mu} \tag{4.2}$$

Where μ is Newtonian viscosity of the fluid medium. If the drag coefficient can be accurately determined with the aid of C_D-Re_p correlation, predicting the settling velocity can be achieved iteratively. In order to simplify the task, Some investigators have altered the definition of Reynolds number (or apparent viscosity) and the drag coefficient to facilitate the estimation of particle settling velocity with reasonable accuracy or so that the results of the non-Newtonian settling test coincides with the standard Newtonian curve (Metzner and Reed, 1955; Lali *et al.*, 1989; Machač *et al.*, 1995; Miura *et al.*, 2001; Wilson *et al.*, 2003; Chhabra, 2006; Shah, El-Fadili and Chhabra, 2007). However, this conventional approach possess a fundamental problem by not accounting for the elastic property of the fluids. A study conducted by Arnipally and Kuru (2018) showed that settling velocity could be overestimated by up to 50 times if the effect of elasticity is not considered. Such large margin of error is unacceptable for most models where the particle settling velocity is required as an input for optimization and design calculations. Nonetheless, elasticity is sometimes not considered in some drilling and fracturing operations which can affect operational efficiency (Bui *et al.*, 2012; Arnipally and Kuru, 2018).

Several studies have attested to the influence of elasticity on a particle's settling behavior. While using Weissenberg number as a measure for elasticity, Chhabra et al. (1980) reported a reduction in drag at high Weissenberg numbers with Boger fluids (elastic fluids with constant viscosity).

While Acharya (1986) in his study of viscoelastic fracturing fluids posited that the influence of elasticity on settling behavior is dependent on the Reynolds number region. He stated that at low Reynolds number region, settling velocity of proppant particles is influenced by the fluid's viscous property, while in the intermediate or transitional region settling velocity increases with elasticity. In contradictory reports, Van den Brule et al. (1993) however observed an apparent reduction in settling velocity as a result of elasticity in viscoelastic shear thinning fluids. Walters and Tanners (1992) carried out an experimental study on Boger fluids and concluded that elasticity causes a reduction in drag at low Weissenberg number and a contrasting increase of drag at higher Weissenberg number. This drag increase (reduction in settling velocity) at high elasticity is in agreement with various experimental studies (Malhotra and Sharma, 2012; Arnipally and Kuru, 2018).

Despite contrasting reports, it is a consensus that elasticity plays a significant role in the settling behavior of particles in fluids. Even after obtaining the elastic description of the viscoelastic fluid with the aid of advanced rheometers, the eventual influence of the elasticity on settling behavior is still shrouded in mystery and has not yet been fully expounded, especially in terms of predicting the settling velocity in such viscoelastic fluids. Although, Malhotra and Sharma (2012) presented a correlation for predicting settling velocity in viscoelastic fluids from their experimental study of surfactant-based Shear thinning viscoelastic fluids; however their model was implicit and required complex iteration to determine the particle Reynolds number (and consequently the settling velocity). Malhotra and Sharma (2012)'s model was also based on a very limited relaxation time range of 0.18 – 0.32 seconds (relaxation time is used to quantify the elasticity of a fluid) which is an application constraint. To the best of our knowledge, there is currently no versatile explicit

model available that has been tested with external experimental data and that provides a direct prediction of settling velocity in shear thinning viscoelastic fluids. This study seeks to fill in this knowledge gap in the literature.

Based on the review of the literature, we conclude it is necessary to develop an accurate and versatile model that quantifies the effect of elasticity on particle settling in a wide range of elastic relaxation time and is applicable to diverse fluid properties as well as particle physical properties. In this study, the results of an experimental and empirical study is presented. The main aims of the study were to measure the terminal settling velocity of particles in various viscoelastic fluids to augment the present corpus of experimental data in literature and develop a general explicit approach for predicting drag coefficient and settling velocities of particles in viscoelastic fluids for a wide range of relaxation time.

4.3 Experimental Materials and Methodology

4.3.1 Test Materials.

Precision spherical particles of glass, steel, ceramic and Zirconium were used in this experimental study. These particles were obtained from Corpuscular Inc. The Physical properties of the particles used for experiments are listed in the Table 4.1 below

Table 4.1: Physical Properties of Spherical Particles

S/N	Diameter (mm)	Material	Specific Gravity
1	1.18	Glass	2.51
2	1.50	Glass	2.51
3	2.00	Glass	2.51

4	3.00	Glass	2.51
5	3.50	Glass	2.51
6	4.00	Glass	2.51
7	1.85	Ceramic	3.86
8	2.18	Ceramic	3.86
9	2.58	Ceramic	3.86
10	1.09	Zirconium Oxide Yttrium	5.90
11	1.29	Zirconium Oxide Yttrium	5.90
12	1.55	Zirconium Oxide Yttrium	5.90
13	2.4-2.5	Steel	7.70

The fluid column was made out of a transparent plexiglass cuboidal column of 70 cm height. The dimensions of the cuboidal container are 15cm by 15cm by 70cm. The fluid column dimensions were designed to avoid all wall effects as specified in the study carried out by Atapattu, Chhabra, & Uhlherr (1990).

4.3.2 Experimental Fluids

Two family of polymers (Hydrolyzed Polyacrylamide and Tylose) with contrasting elastic properties were utilized in this experimental study:

i. Hydrolyzed Polyacrylamide (HPAM) is an elastic polymer formed from the monomers of acrylamide and acrylic acid. The main physical properties of the polymer are determined by its degree of hydrolysis while the degree of its elasticity depends on the

average molecular weight. The average molecular weight of the polymer ranges from 2 to 20 million. (Arnipally and Kuru, 2018)

ii. Tylose (Carboxymethyl Cellulose or CMC) is a Cellulose derivative containing Caboxymethyl groups (-CH_2-COOH) and hydroxyl groups. It is used as a viscosfier in many industrial applications. It has a very low nominal molecular weight of 700,000 g/mol making it relatively inelastic and ideal in the study of fluids with negligible elastic property. (Reynolds and Jones, 1989; Shah, El-Fadili and Chhabra, 2007; Benchabane and Bekkour, 2008)

The experimental fluids were meticulously prepared as follows;

- Deionized water of required volume was stirred at 300 rpm in mixing bucket.
- Based on the desired wt. %, the required mass of polymer powder was added progressively (not all at once) to the stirring de-ionized water on to the inner sides of the fluid vortex.
- After adding the polymers, the solution was stirred at 150 rpm for 3 hours (short time due to low concentration) until the low wettability polymer powders fully dissolve and a completely homogenous fluid is formed.
- The polymer solution was transferred to the fluid column and allowed to stand still overnight to remove air bubbles.

4.3.3 Rheological Measurements and Characterizations.

Viscometry and oscillatory measurements were performed with the C-VOR cone and plate type rheometer from Bohlin Instruments to determining viscoelastic properties. The 40mm and 4° cone

and plate geometry was used. The measurements were conducted at room temperature (25°C) using the controlled shear stress function. Example of the test results are shown in Figure 4-7. The density of the fluids was measured by dividing the weight of the test fluid by the volume using a Pyrex Vista no. 70024 of 10 ml measuring jar.

4.3.4 Experimental Setup.

Particle Image Shadowgraphy (PIS) technique was used to measure settling velocity of spherical particles in Hydrolyzed Polyacrylamide and Tylose solutions. Particle Image Shadowgraphy is a non-intrusive flow visualization technique that leverages on the optical properties of light. When light travels through a medium and encounters an opaque obstruction or change in density, it always results in shadow formations.

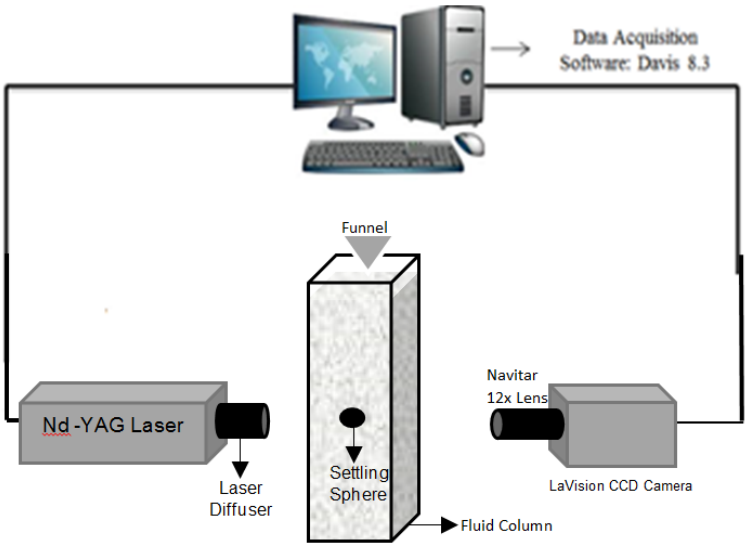

Figure 4.1: Particle Image Shadowgraphy (PIS) Experimental Setup Used in the Current Study

Particle Image Shadowgraphy also allows the simultaneous measurements of several other characteristics; such as the interface speed, the direction of motion, and the object size. The experimental setup and procedure is identical to that in a recent study by Okesanya and Kuru (2019). A light source and an image recording device are required for this technique. The experimental setup is comprised of the light source, which was provided by the New Wave Research Laser Solo III; an Nd-YAG double pulsed laser with a 532 nm wavelength and a frequency of 15 Hz.

The laser was connected to a LaVision circular diffuser pair for greater efficiency and background illumination. LaVision Image Intense Camera with a 12x Navitar Lens was used to capture images. This double framed (capable of capturing quick successive images in as short as 500ns) high resolution camera had a CCD sensor of 1376×1040 pixels capable of capturing 5 frames per sec and a capacity to convey 12-bit digital images. Data processing and analysis was carried out by LaVision Davis 8.3 software.

The ParticleMaster Shadow Project of the Davis 8.3 software follows mathematical and graphic algorithms to measure the size and the velocity. This is achieved by first locating the particles in the field of view and analyzing the particles for size, shape and position. Analysis is based on the intensity variation of the image. After sizing and locating the particles in the first frame, the algorithm then measures the terminal velocity by correlating the first frame with the successive frame to determine the displacement of the particle. The displacement and Δt (time difference between frames) can be simultaneously used to determine the velocity. This technique gives an accurate instantaneous measurement of the terminal velocity (Okesanya and Kuru, 2019). Figure

4.2 shows the schematic of the general algorithm followed by the software to calculate the terminal velocity.

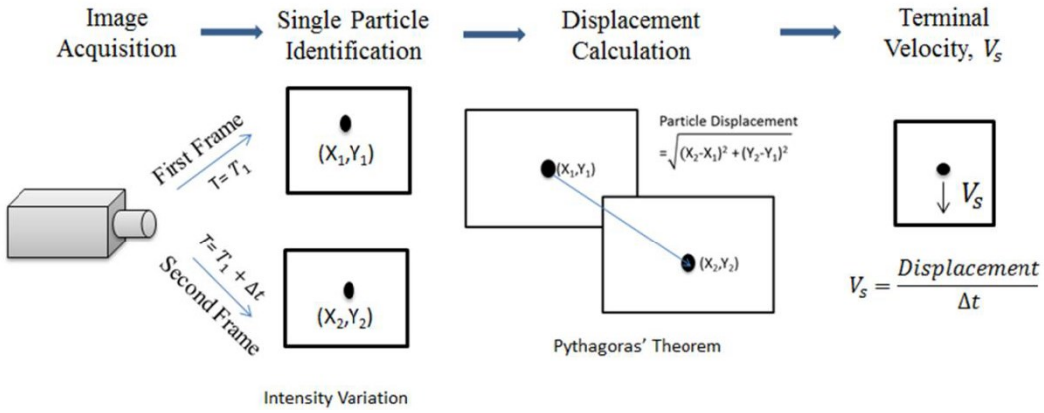

Figure 4.2: Schematic of the Davis 8.3 software algorithm to determine terminal settling velocity (Okesanya and Kuru, 2019)

4.3.5 Verification of Particle Image Shadowgraphy Measurements.

In order to verify the PIS technique, settling tests were carried out in a standard Newtonian fluid (Water) and the test results adjudicated with the universal drag curve. The measured settling velocity of the spherical particles is used in determining the particle Reynolds number (Equation 4.2) and consequently the drag coefficient of spherical balls using the correlation (Equation 4.3) proposed by Morrison (2013).

$$C_D = \frac{24}{Re_p} + \frac{2.6\left(\frac{Re_p}{5}\right)}{1+\left(\frac{Re_p}{5}\right)^{1.52}} + \frac{0.411\left(\frac{Re_p}{263000}\right)^{-7.94}}{1+\left(\frac{Re_p}{263000}\right)^{-8.00}} + \frac{0.25\left(\frac{Re_p}{10^6}\right)}{1+\left(\frac{Re_p}{10^6}\right)} \quad (5.3)$$

The drag coefficients from the experimental measurements were found to be within 3.5 % of the theoretical values, hence bolstering the reliability of the experimental setup. Furthermore, some authors have previously authenticated the experimental setup used in this study (Okesanya and Kuru, 2019; Arnipally & Kuru, 2017; Shahi & Kuru, 2015).

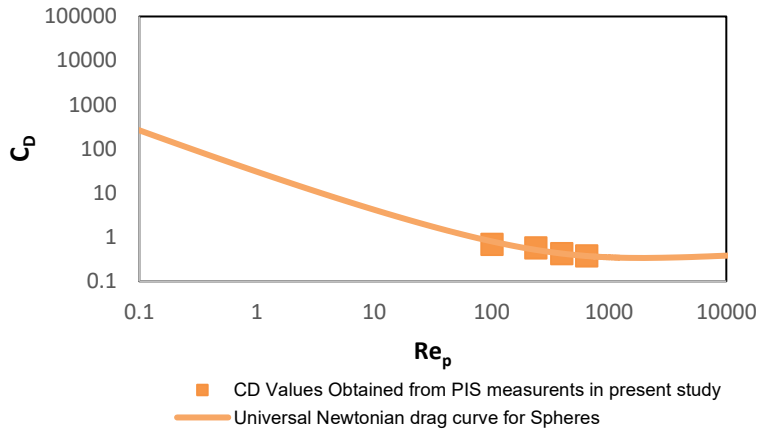

Figure 4.3: C_D vs Re_p Plot for the Verification of the PIS Measurements

4.3.6 Experimental Procedure.

The experimental procedure follows similar steps employed by Arnipally and Kuru (2018) and Okesanya and Kuru (2019). The polymer fluid is prepared and transferred to the fluid column left unperturbed overnight. This was done to remove air bubbles which can affect image quality. The experimental equipment were connected and setup as shown in Figure 1. The fluid column was placed in between the LaVision laser diffuser and the double frame camera which were placed on opposite sides. The Nd:YAG laser was turned on and when the camera temperature was below -11°C and the laser power was adjusted to 25% and 3% respectively for both pulses. The time interval was dependent on particle sizes which ranged from 50ns to 1000ns. The experimental setup is calibrated by inserting a calibration target sheet (Figure 4.4) in the column and taking a

focused image of the sheet. The spacing dimensions (i.e. grids spaced 1.5 mm apart) of the sheet helps the Davis 8.3 software convert pixel dimensions into physical dimensions. The image of the calibration sheet is shown below

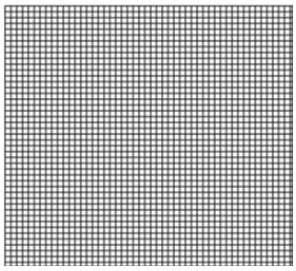

Figure 4.4: Calibration Sheet

The calibrated plane's position would be marked at the top. It serves as the funnel position and the dropping point of spherical particles. Reference images are captured and averaged to serve as a reference background for the experimental images. The spherical particles are to be dropped with the aid of a funnel (not by hand), to ensure uniformity in landing position and the experimental images can now be captured (recorded). When the spherical particles pass through the plane of focus, they appear as dark spots on Davis 8.3 software because of the differences in intensity as explained in the experimental section. The software follows a specific algorithm as shown in Figure 4.2 to determine the particle size and the terminal velocity as explained above. Repeatability of the experiment is checked by carrying out at least 5 trials and the averaging the 5 trials to obtain an accurate value of the settling velocity. The velocity measurements are performed at two different heights (15cm and 10cm) from the base to ensure that the particle attained its constant terminal settling velocity. During the experimental process, only one particle at a time was dropped to measure settling velocity after which 25 minutes of waiting time was observed to ensure that

the fluid had regained its original microstructure to prevent thixotropic effects and enhance accuracy.

4.4 Analysis and Discussion

Over 25 polymer samples with varying elastic properties were utilized in the settling test experiments. Different conditions with respect to the particle size and density were tested. The results of the settling tests and experimental conditions are presented in Appendix A.

4.4.1 Fluid Properties

The results of the viscometry and oscillatory tests which describe the rheological property of two of the experimental test fluids used in this study are presented in this section. The two polymer families utilized were Tylose and Hydrolyzed Polyacrylamide (HPAM) of various concentrations to ensure a wide range of viscometric and elastic property.

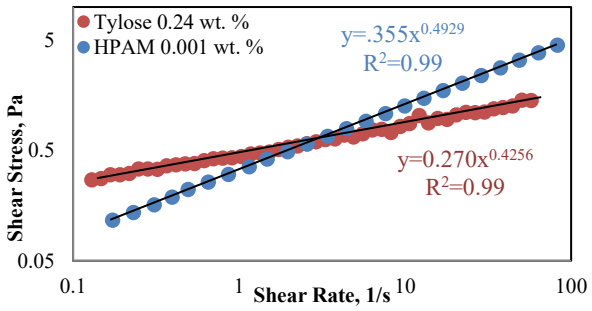

Figure 4.5: Shear Stress Vs Shear Rate plots for Tylose (0.24 wt. %) and HPAM (0.075 wt. %)

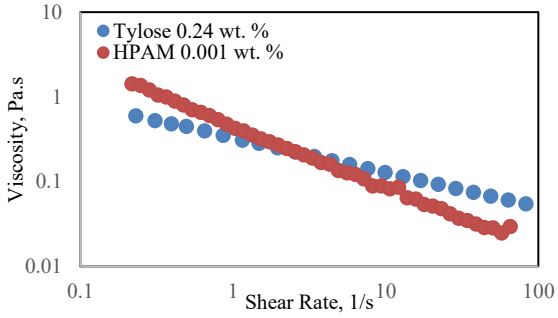

Figure 4.6: Viscosity Vs Shear Rate plots for Tylose (0.24 wt. %) and HPAM (0.075 wt. %)

Viscometry Controlled Shear Stress (CSS) tests were carried out on each test fluid to determine the fluid flow curve and power-law parameters (K and n) for each fluid which will be

used during modeling. The power-law parameters were determined using linear Trendline function of Microsoft excel and they depict the shear stress and shear rate relationship of the test fluids. Examples of viscometry test results are shown below.

Figure 4.5 shows the shear stress vs shear rate plot obtained from the CSS test for two of the experimental fluids (Tylose 0.24wt. % and HPAM 0.01 wt. %); while Figure 4.6 shows the Viscosity vs Shear Rate plot obtained from the CSS test for the same experimental fluids as well. All the fluids used in this study did not exhibit yield stress and exhibited a power-law pseudoplastic behavior. For the experimental fluids (Tylose 0.24wt. % and HPAM 0.075 wt. %) above in Figure 4.5, The Power-law consistency factor (k) were 0.335 Pa.S^n and 0.270 Pa.S^n respectively, while the flow behavior index (n) were 0.4949 and 0.4256 respectively. These parameters depict the flow behavior of a typical power-law non-Newtonian fluid.

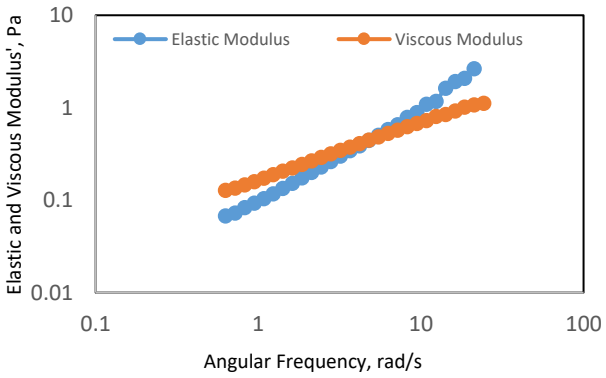

Figure 4.7: Oscillation Test Result for Tylose (0.24 wt.%)

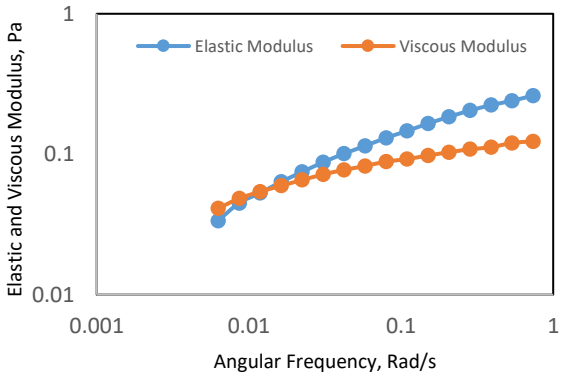

Figure 4.8: Oscillation Test Result for HPAM (0.075 wt. %)

Oscillatory tests were carried out on each test fluid to determine the elastic property and relaxation time of each fluid. Figure 4.7 and Figure 4.8 represent the results of the oscillation test for two of the experimental fluids (Tylose 0.24wt. % and HPAM 0.075 wt. %). Figure 9 is the

oscillation result for Tylose 0.24 wt. % while Figure 10 represents the oscillation test result for HPAM 0.001 wt%.

The longest relaxation time, λ (sec) which is the inverse of the crossover angular frequency between the elastic modulus and viscous modulus. It signifies the time needed for a material to regain its original structure after any deformation or disturbance. It is used to quantify the elasticity of a fluid (Choi, 2008; Malhotra and Sharma, 2012; Arnipally and Kuru, 2018). In the figure above, Tylose (0.24 wt.%) had a low relaxation time of 0.18 seconds. This indicates a very low elastic property. Similar to all the Tylose polymers used in this experimental study irrespective of their concentration. As earlier stated, Tylose is a cellulose derivative and has a very low average molecular wright making it exhibit negligible elastic properties (Benchabane and Bekkour, 2008). While the HPAM (0.075 wt. %) had a relaxation time of 90 seconds demonstrating a very high elastic property, also similar to other HPAM polymers used in this study.

4.4.2 Quantifying non-Newtonian Power-law Viscosity.

A major conundrum associated with non-Newtonian fluids is their shear rate dependent viscosities, which complicates all the modeling efforts. Recently, an experimentally proven approach has been recommended to quantify the apparent non-Newtonian viscosity based on the mean surficial stress concept (Wilson *et al.*, 2003; Arabi and Sanders, 2016; Kesely and Matoušek, 2016). The mean surficial stress, $\bar{\tau}$ is defined as the ratio of the submerged weight force divided by the total surface area (Wilson and Thomas, 1985). Mathematically, it is formulated as follows;

$$\bar{\tau} = \frac{dg\ (\rho_s - \rho_f)}{6} \tag{4.4}$$

The mean surficial stress depicts the stress imposed on the fluid by the settling particle. This stress induces a corresponding shear rate, which can be obtained by using the Power-law Model.

$$\bar{\tau} = k\dot{\gamma}^n \tag{4.5}$$

$$\dot{\gamma} = \left(\frac{\bar{\tau}}{k}\right)^{\frac{1}{n}} \tag{4.6}$$

The corresponding viscosity, μ is simply the ratio of the mean surficial stress ($\bar{\tau}$) to the shear rate ($\dot{\gamma}$) induced.

$$\mu = \frac{\bar{\tau}}{\dot{\gamma}} \tag{4.7}$$

4.4.3 Developing the Predictive Model for Viscoinelastic Power-law Fluids

An extensive database of particle settling information in viscoinelastic fluids was obtained from experimental data acquired from settling test results from the present study (i.e. particle

settling tests in Tylose fluid) coupled with data available from the literature. The settling data obtained across various experimental studies in literature were strictly from viscoinelastic fluids as they were explicitly stated in their respective papers (Reynolds and Jones, 1989; Miura *et al.*, 2001; Pinelli and Magelli, 2001; Kelessidis, 2003; Kelessidis and Mpandelis, 2004; Mohammed, 2013). Furthermore, the experimental fluids utilized in most of the papers were obtained from Carboxymethyl Cellulose (CMC) which has negligible to no elastic property (Shah, El-Fadili and Chhabra, 2007; Benchabane and Bekkour, 2008). Fluids with low relaxation times below 0.9 seconds follow the viscoinelastic curve due to their very low and negligible elastic property.

Based on the information available from this database, a drag curve for viscoinelastic power-law type fluids was formed by plotting the Re_p vs $\sqrt{C_{D.}}Re_p$ (Figure 9); similarly to approach employed by Chhabra, (1990) and Shah, El-Fadili and Chhabra, (2007). Where $\sqrt{C_{D.}}Re_p$ in this study is defined as follows;

$$\sqrt{C_{D.}}Re_p = \sqrt{\frac{4(\rho_s - \rho_f)dg}{3V_t^2\rho_f}} * \frac{\rho_f V_t d}{\mu} = \sqrt{\frac{4(\rho_s - \rho_f)d^3 g\rho_f}{3\mu^2}} \tag{4.8}$$

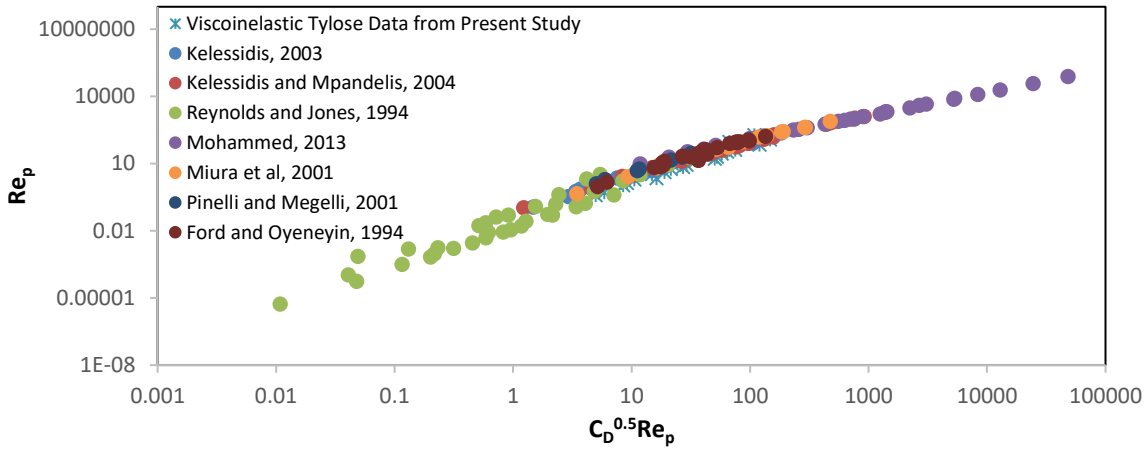

Figure 4.9: Re_p vs $\sqrt{C_D}Re_p$ Plot of Viscoinelastic Power-law Type fluids

Three distinct regions are observed in the plot based on the value of the $\sqrt{C_D}Re_p$. These regions were identified and fitted using Microsoft excel fitting function to develop correlations for each region as shown in Figure 10 below.

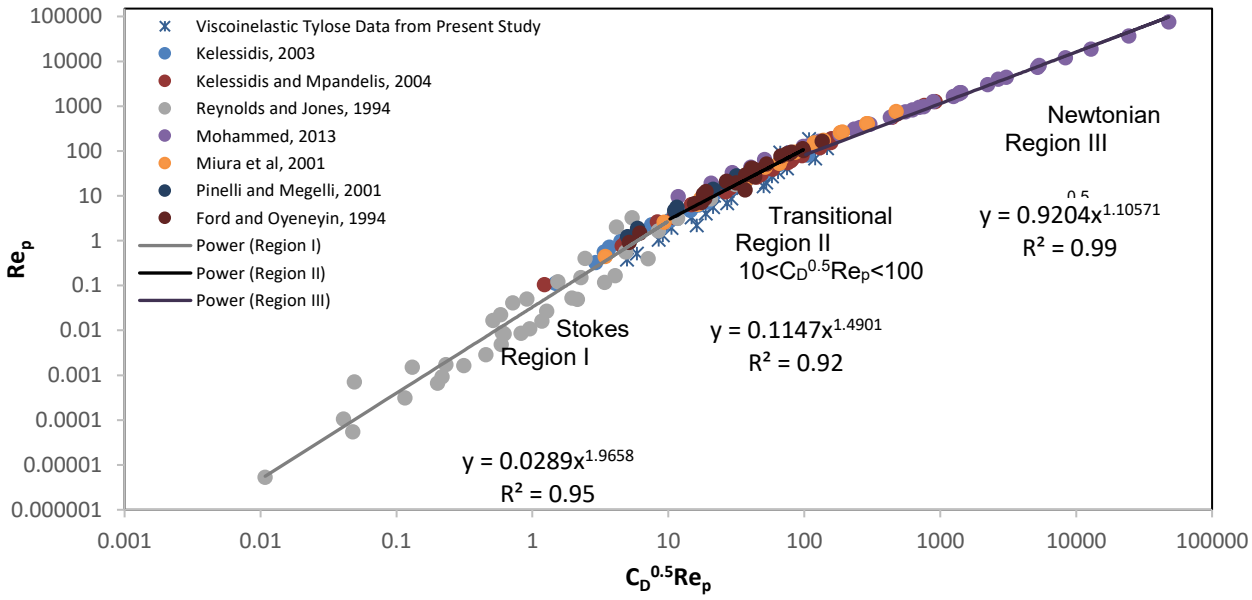

Figure 4.10: Re_p vs $\sqrt{C_D}Re_p$ Plot of Viscoinelastic Power-law Type fluids

The $\sqrt{C_{D.}}Re_p$ value can then be used to determine the viscoinelastic Reynolds number based on the associated region with the use of the following equations obtained from the plot in Figure 4.10.

Region I ($10 > \sqrt{C_{D.}}Re_p$) : $$Re_{p-inelastic} = 0.0289\left(\sqrt{\frac{4(\rho_s-\rho_f)d^3g\rho_f}{3\mu^2}}\right)^{1.9658} \quad (4.9)$$

Region II ($10 < \sqrt{C_{D.}}Re_p < 100$): $$Re_{p-inelastic} = 0.1147\left(\sqrt{\frac{4(\rho_s-\rho_f)d^3g\rho_f}{3\mu^2}}\right)^{1.490} \quad (4.10)$$

Region III ($\sqrt{C_{D.}}Re_p > 100$): $$Re_{p-inelastic} = 0.9204\left(\sqrt{\frac{4(\rho_s-\rho_f)d^3g\rho_f}{3\mu^2}}\right)^{1.05} \quad (4.11)$$

4.4.4 Prediction of Particle Settling Velocity in Viscoinelastic Fluids

After obtaining the particle Reynolds number (using Eqns. 9-10), the settling velocity in viscoinelastic fluids can then be calculated by using Eqn.4.12.

$$V_t = \frac{\mu Re_p}{\rho_f d} \quad (4.12)$$

The predicted settling velocity obtained using this approach are presented in Table A-1 in the Appendix section including the actual measured velocity and the fluid property.

4.4.5 Statistical Evaluation of the Accuracy of the Model Developed for Prediction of the Settling Velocity in Viscoinelastic Power-law Fluids

Statistical parameters were used to further validate the presented model based on the data from the entire viscoinelastic database which includes experimental data presented in Table A-1 and the viscoinelastic database obtained from literature identified in Figure 4.9 above. The

Percentage Mean Absolute Error (PMAE) and Root Mean Square Error (RMSE) were the statistical parameters selected. The Percentage Mean Absolute Error (PMAE) expresses the mean absolute error in percentage. It depicts the expected percentage error associated with a specific model. Hence the lower the value, the more accurate the model. Its equation is shown below.

$$PMAE = \frac{\frac{1}{n}\sum_1^n |V_{tm} - V_{tp}|}{\frac{1}{n}\sum_1^n |V_{tm}|} * 100 \tag{4.13}$$

The Root Mean Square Error (RMSE), which expresses the aberration between the actual and predicted values of the model. It indicates the error of the associated model. The lower the value of the RMSE is, the more accurate the model will be.

$$RMSE = \sqrt{\frac{\sum_1^n (V_{tp} - V_{tm})^2}{n}} \tag{4.14}$$

Where V_tm represents measured settling velocity and V_tp predicted settling velocity. Using statistical analyses, we have found that PMAE and RMSE values were 7.5% and 0.04 m/s, respectively for the Viscoinelastic database.

The above results from the statistical evaluation of the entire database (data from literature and experimental results) indicate the accuracy of the proposed model. An average error of about 0.04m/s (4cm/s) is expected to be associated with the model, which can be deemed negligible depending on the operation required.

A plot of the predicted settling velocity (V_{tp}) and the measured settling velocity (V_{tm}) is shown in Figure 4.11 which includes experimental data presented in Table A-1 and the viscoinelastic database obtained from literature identified in Figure 4.9 above

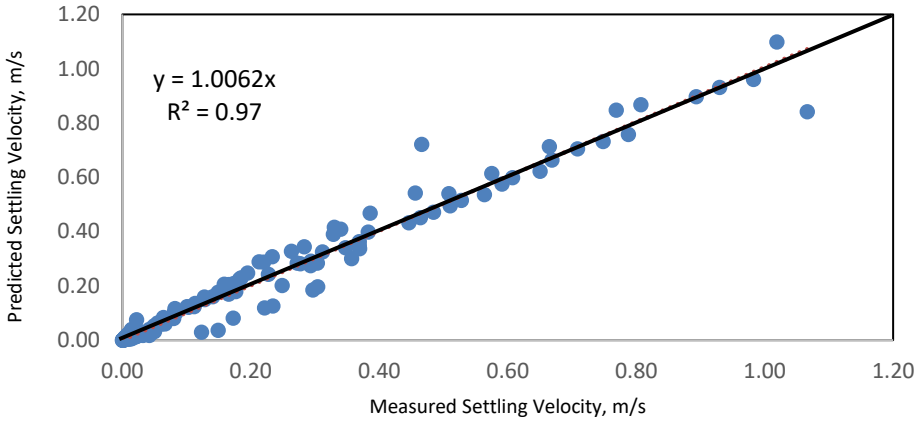

Figure 4.11: A plot of Predicted Settling Velocity vs. Measured Settling Velocity for the Viscoinelastic Power-law Type Fluids

The comparative plot had an R^2 value of 0.97 with a linear equation of $V_{tp} = 1.0062\ V_{tm}$. The coefficient of determination (R^2) is used to depict the accuracy and precision of the model fit with actual measured data. It shows the deviations of the measured and predicted values. Higher R^2 values portray less scatter and deviation from the predicted values of a specific model and further bolsters the accuracy of the proposed model.

4.4.6 Developing the Predictive Model for Viscoelastic Power-law Fluids

We have also generated a database for particle settling velocity in viscoelastic power-law fluids by gathering the data from the literature Arnipally and Kuru(2017), Mohammed (2013) as well as from the experiments conducted in this study (using viscoelastic polyacrylamide polymer-

based fluid). The polyacrylamide polymer fluids are very elastic in nature with relaxation time reaching up to 150 secs. (Mohammed, 2013; Arnipally and Kuru, 2018). The experimental data for viscoelastic fluids are summarized in Table A-2 shown in the Appendix Section. We have then added these data into the Re_p vs $\sqrt{C_D}Re_p$ plot of the viscoinelastic fluid (Figure 4.9). The combined viscoelastic and inelastic fluid data are shown in Fig 4.12.

The disparate trend was observed when the viscoelastic and viscoinelasatic data were plotted on the same Re_p vs $\sqrt{C_D}Re_p$ graph (Figure 4.12).

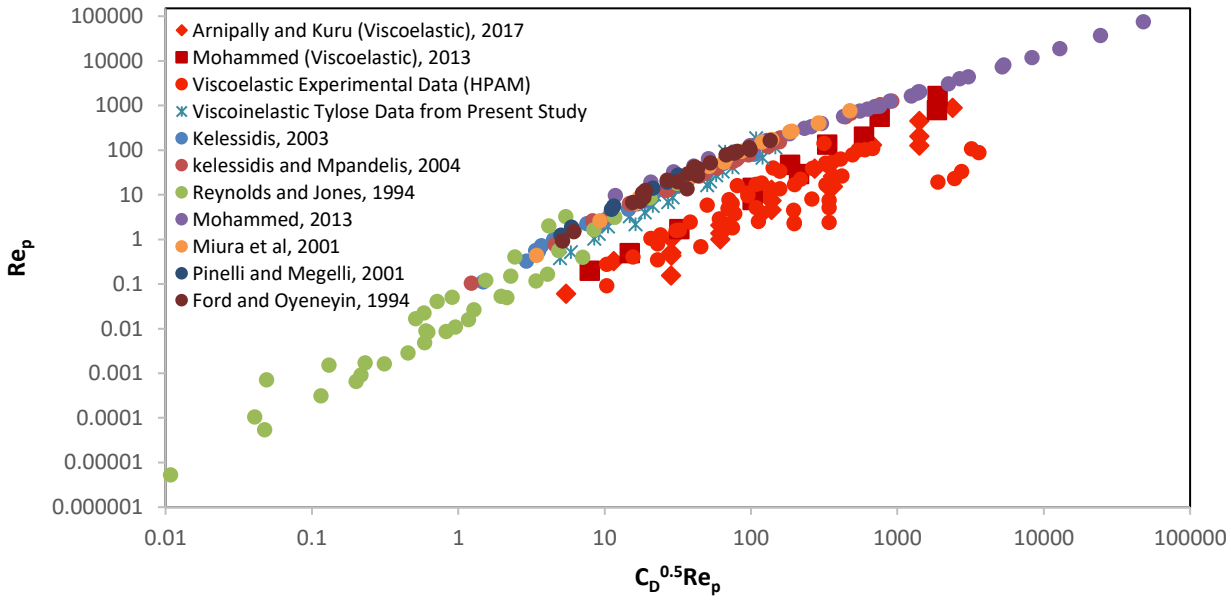

Figure 4.12: $\sqrt{C_D}Re_p$ vs Re_p Plot Based on the Available Data for Particle Settling Velocity in Viscoelastic and Viscoinelastic Power-law Type Fluids

The $\sqrt{C_D}Re_p$ vs Re_p plot of the viscoelastic fluid test data shows an apparent downward shift (several orders) from the general trend of the similar data obtained from viscoinelastic fluid

tests. This apparent decrease can be attributed to the elasticity effect. These results highlight the major contribution of elasticity in the reduction of the particle settling velocity (as a result of increasing effective drag forces), which also translates to a reduction in the particle Reynolds number.

Elastic fluids have a high storage modulus, which depicts their unique ability to store energy during deformation that can be used for regaining their original structure after deformation ends. This energy resists the shear induced by a settling particle and eventually leading to an increase in drag, which dampens the settling velocity. This dampening effect of elasticity is in agreement with various experimental studies (van den Brule and Gheissary, 1993; Malhotra and Sharma, 2012; Arnipally and Kuru, 2018). All things being equal, the magnitude of this dampening depends on the elasticity of the fluid, which will be further illustrated. Data shown in Figure 4.12 indicate that the range of Reynolds number values ($0.001 < Re_p > 5{,}000$) in viscoelastic fluids is rather limited compared to the range of the data obtained for viscoinelastic fluids ($10^{-5} < Re_p > 10^5$). It should be noted, however, that the range of viscoelastic fluid data presented here is within the range of the data with practical significance in the drilling industry as reported by the Zamora, Roy and Slater, (2005).

A drag curve for viscoelastic power-law type fluids alone was formed by plotting the Re_p vs $\sqrt{C_{D.}}Re_p$ with multiple data obtained from literature combined with particle settling experiments carried out using viscoelastic polyacrylamide polymer fluids (Figure 4.13). A trend was observed for the viscoelastic database with a single region. However, it had a relatively low R^2 value (0.72) compared with the 0.95 average value for viscoinelastic fluids indicating a large

scatter from the model predicted value. The low R^2 value and scatter can lead to erroneous estimation of the settling velocity in these viscoelastic fluids.

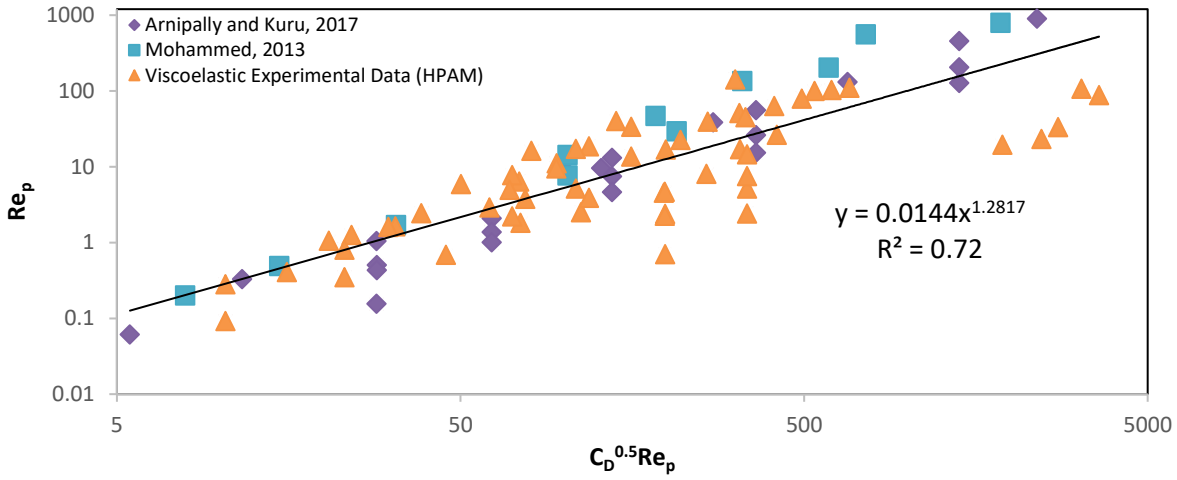

Figure 4.13: Re_p vs $\sqrt{C_D}Re_p$ Plot based on the Available Data for Particle Settling Velocity in Viscoelastic Power-law Type Fluids

The cause of this scatter can be attributed to the presence of elasticity. The two terms (Re_p and $\sqrt{C_D}Re_p$) used to generate the plot lack any parameter that accounts for the elasticity. An earlier study by Arnipally and Kuru (2018) revealed that settling velocity could be overestimated by up to 50 times if the effect of elasticity is not considered. Such a large margin of error is intolerable for most design models, where the terminal settling velocity is required as an input for model calculations. Hence, the approach used for the viscoinelastic fluids can not be utilized for the viscoelastic fluids.

In an attempt to account for the effect of elasticity and predict the settling velocity of spherical particles in viscoelastic power-law fluids; a new explicit correlation is proposed here,

which relates the particle Reynolds number for viscoelastic fluids to particle Reynolds number for the viscoinelastic fluids (i.e., Equations 4.9 - 4.11). The suggested correlation of particle Reynolds number for particles settling viscoelastic fluids is shown in Equation 4.15.

$$Re_{p-elastic} = \frac{Re_{p-inelastic}}{(1+Ⱪ)^{0.689}} \tag{4.15}$$

Where Ⱪ (Elasticity Factor) is a function of $\sqrt{C_D}Re_p$ and the dimensionless Weissenberg Number, Wi which is equal to the product of shear rate, $\dot{\gamma}$ and the longest relaxation time, λ. Therefore, Ⱪ approaches zero as relaxation time approaches zero indicating a near inelastic property, which then equates the $Re_{p\text{-elastic}}$ to $Re_{p\text{-inelastic}}$. Ⱪ was determined by using curve fitting functions of the statistical analysis software, OriginPro 9.0.

$$Ⱪ = \frac{3.03782Wi^{0.5064267}}{\sqrt{\frac{4(\rho_s - \rho_f)d^3 g\rho_f}{3\mu^2}}^{0.78936}} \tag{4.16}$$

After obtaining the particle Reynolds number, $Re_{p\text{-elastic}}$, for viscoelastic fluids, the settling velocity can then be calculated by using Equation 4.12. This approach is applicable for viscoelastic power-law fluids with relaxation time above 0.9 seconds. The database for viscoelastic fluids is presented in Table A-2 in the Appendix section.

4.4.7 Statistical Evaluation of the Accuracy of the Model Developed for Prediction of the Settling Velocity in Viscoelastic Power-law Fluids

Statistical parameters were used to further authenticate the presented model for the viscoelastic fluids' database. The database is presented in Table A-2 in the Appendix section. The

Percentage Mean Absolute Error (PMAE) and Root Mean Square Error (RMSE) were the statistical parameters again selected. Using statistical analyses, we have found that PMAE and RMSE values were 11% and 0.03 m/s respectively for viscoelastic fluids. An average error of about 0.03 m/s (3 cm/s) is expected to be associated with the viscoelastic model, which can also be deemed negligible depending on the operation required.

A plot of the predicted settling velocity (V_{tp}) and the measured settling velocity (V_{tm}) is shown in Fig.14, which includes experimental data presented in Table A-2 and data obtained from Arnipally and Kuru (2018). The relaxation time of the fluids used by Mohammed (2013) was not stated hence data was not utilized for statically analysis.

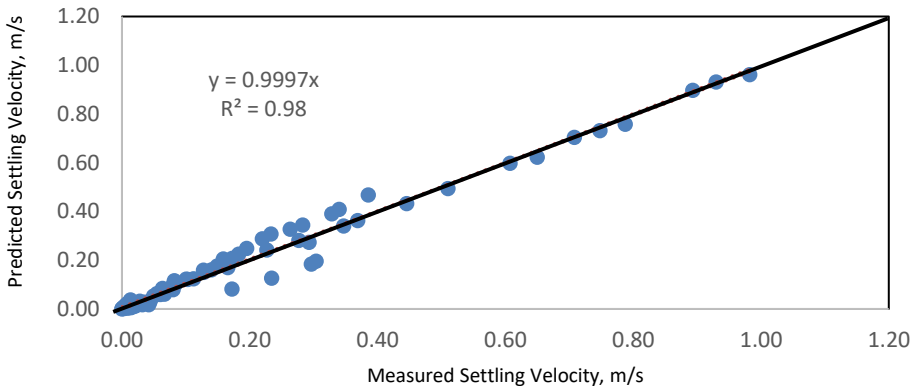

Figure 4.14: A plot of Predicted Settling Velocity vs. Measured Settling Velocity for Viscoelastic Fluids

The comparative plot had an R^2 value of 0.97 with a linear equation of $V_{tp} = 0.9997\ V_{tm}$. The coefficient of determination (R^2), which depicts the accuracy of the model fit with actual measured data. It shows the deviations of the measured and predicted values. Higher R^2 values portray less scatter and deviation from the predicted values of a specific model and further bolsters the accuracy of the proposed model.

4.5 Conclusions

An experimental and empirical modeling study was carried out to describe the settling behavior of spherical particles in both viscoinelastic and viscoelastic power-law fluids with emphasis placed on quantifying the effect of the fluid elasticity. Polymer samples with varying viscoelastic properties were prepared and settling velocities of the particles with variable size and densities were measured in these fluids. The experimental results were combined with results from the literature to create a comprehensive database for viscoinelastic and viscoelastic fluids separately. Characteristic drag coefficient ($\sqrt{C_D}Re_p$) versus particle Reynolds number curves (Re_p) were developed for describing settling behavior of rigid spherical particles in both viscoinelastic and viscoelastic power-law fluids applicable to consistency index (k) range of 0.012-6.773 Pa.s^n and fluid behavior index (n) range of 0.370 – 0.940.

Comparative analysis showed that an increase in the elasticity gave a corresponding decrease in the particle Reynolds number and settling velocity for a specific$\sqrt{C_D}Re_p$. This dampening effect is due to the unique ability of elastic fluids to regain their original structure after deformation. This dampening effect can be leveraged upon in many technical operations where particle suspension is desired.

Explicit models were proposed to quantify and predict the particle settling behavior in viscoinelastic fluid as well as to account for the elasticity effects on the drag and settling velocity; thereby, accurately predict settling velocity of a particle falling through a viscoelastic fluid or viscoinelastic fluid.

Statistical analysis showed that the proposed models were indeed accurate and could predict the settling velocity of particles in viscoinelastic and viscoelastic power-law type fluids with a Percentage Mean Absolute Error (PMAE) of 7.5% and 11%, respectively. Root Mean Square Error values of 0.04m/s and 0.03m/s were also obtained for predicting the settling velocity of particles in viscoinelastic and viscoelastic power-law fluids, respectively. Plots of the predicted settling velocity (Vtp) versus the measured settling velocity (Vtm) gave high R2 values of 0.97 and 0.98 for viscoinelastic and viscoelastic fluids, respectively with both plots having linear equations of Vtp ≈ Vtm.

Notwithstanding the confident statistical result, supplementary research work is necessary to corroborate and ameliorate the accuracy of the proposed model especially in dynamic conditions not tested in this study. It is also recommended to investigate the influence of wall effects on the viscoelastic fluids.

4.6 Acknowledgment

This research is financially supported by the funds available from the Natural Sciences and Engineering Research Council of Canada (NSERC RGPIN-2016-04647 KURU).

4.7 Nomenclature

Symbol	Description	Unit
C_D	Drag coefficient	-
V_t	Terminal settling velocity	m/s
V_{tm}	Measured settling velocity	m/s
V_{tp}	Predicted terminal settling velocity	m/s
α	Fluid Calibration Constant	-
Ƙ	Elasticity Factor	-
$\dot{\gamma}$ or γ	Shear rate	s^{-1}
μ	Viscosity	Pa.s
R	Coefficient of Determination	-
Re_p	Reynolds Particle Number	-
d	Particle Diameter	m
ρ_s	Particle (sphere) density	kg/m^3
ρ_f	Fluid density	kg/m^3
τ	Shear Stress	Pa
$\bar{\tau}$	Mean Surficial Stress	Pa
k	Power-law consistency index	$Pa.S^n$
n	Power-law flow behavior index	-
g	Acceleration due to gravity	m/s^2
λ	Longest Relaxation Time	s

Appendix A – Experimental Results

The experimental results obtained in this study are presented in this section. Table A-1 represents data for viscoinelastic fluids (Tylose) and Table A-2 represents data for viscoelastic fluids (HPAM).

Table A-1: Viscoinelastic Experimental Database

No.	Fluid	d (m)	ρ_f (kg/m^3)	ρ_s (kg/m^3)	K (Pa.S^n)	n	Relaxation Time (Sec/Rad)	V_{tm} (m/s)	V_{tp} (m/s)
1	Tylose (0.040 wt. %)	0.002	996	2510	0.012	0.832	0.5	0.30	0.24
2		0.0015	996	2510	0.012	0.832		0.24	0.20
3	Tylose (0.080 wt. %)	0.00071	998	2510	0.026	0.776	0.4	0.03	0.04
4		0.00118	998	2510	0.026	0.776		0.07	0.09
5		0.0015	998	2510	0.026	0.776		0.12	0.12
6	Tylose (0.120 wt. %)	0.00118	1000	2510	0.066	0.646	0.3	0.07	0.08
7		0.0015	1000	2510	0.066	0.646		0.07	0.11
8		0.002	1000	2510	0.066	0.646		0.10	0.18
9		0.003	1000	2510	0.066	0.646		0.20	0.30
10	Tylose (0.150 wt. %)	0.00118	1002	2510	0.099	0.608	0.3	0.03	0.07
11		0.0015	1002	2510	0.099	0.608		0.04	0.10
12		0.002	1002	2510	0.099	0.608		0.06	0.16
13		0.003	1002	2510	0.099	0.608		0.14	0.25

14	Tylose (0.180 wt. %)	0.00118	1003	2510	0.198	0.546	0.2	0.02	0.03
15		0.0015	1003	2510	0.198	0.546		0.04	0.07
16		0.002	1003	2510	0.198	0.546		0.06	0.12
17		0.003	1003	2510	0.198	0.546		0.13	0.23
18	Tylose (0.210 wt. %)	0.00118	1005	2510	0.282	0.513	0.2	0.01	0.02
19		0.0015	1005	2510	0.282	0.513		0.03	0.06
20		0.002	1005	2510	0.282	0.513		0.05	0.10
21		0.003	1005	2510	0.282	0.513		0.11	0.20
22	Tylose (0.240 wt. %)	0.00118	1005	2510	0.335	0.493	0.2	0.01	0.02
23		0.0015	1005	2510	0.335	0.493		0.03	0.04
24		0.002	1005	2510	0.335	0.493		0.04	0.10
25		0.003	1005	2510	0.335	0.493		0.09	0.19
26	Tylose (0.270 wt. %)	0.002	998	2510	0.026	0.776	0.4	0.16	0.18
27		0.003	998	2510	0.026	0.776		0.27	0.30

Table A-2: Viscoelastic Experimental Database

No.	Fluid	d (m)	ρ_f (kg/m^3)	ρ_s (kg/m^3)	K (Pa.S^n)	n	Relaxation Time (Sec/Rad)	V_{tm} (m/s)	V_{tp} (m/s)
1	HPAM (0.085 wt. %)	0.00129	1002	5900	0.520	0.370	52	0.003	0.003
2		0.00155	1002	5900	0.520	0.370		0.005	0.005
3	HPAM (0.120 wt. %)	0.00129	1002	5900	0.520	0.420	143	0.001	0.002
4		0.00155	1002	5900	0.520	0.420		0.002	0.003
5	HPAM (0.060 wt. %)	0.00129	997	5900	0.250	0.420	55	0.003	0.003
6		0.00155	997	5900	0.250	0.420		0.007	0.005
7	HPAM (0.120 wt. %)	0.00129	997	5900	0.330	0.400	143	0.007	0.010
8		0.00155	997	5900	0.330	0.400		0.013	0.013
9	HPAM (0.080 wt. %)	0.0015	1002	2510	0.410	0.440	52	0.005	0.002
10		0.002	1002	2510	0.410	0.440		0.007	0.005
11		0.003	1002	2510	0.410	0.440		0.027	0.014
12		0.0035	1002	2510	0.410	0.440		0.042	0.022
13		0.004	1002	2510	0.410	0.440		0.060	0.026
14	HPAM (0.130 wt. %)	0.0015	1002	2510	0.630	0.370	144	0.002	0.002
15		0.002	1002	2510	0.630	0.370		0.003	0.003
16		0.003	1002	2510	0.630	0.370		0.008	0.010
17		0.0035	1002	2510	0.630	0.370		0.012	0.015
18		0.004	1002	2510	0.630	0.370		0.024	0.019
19	HPAM (0.040 wt. %)	0.00118	997	2510	0.270	0.430	52	0.004	0.003
20		0.0015	997	2510	0.270	0.430		0.009	0.005

21		0.002	997	2510	0.270	0.430		0.014	0.011
22		0.003	997	2510	0.270	0.430		0.025	0.024
23		0.0035	997	2510	0.270	0.430		0.035	0.029
24		0.004	997	2510	0.270	0.430		0.045	0.035
25	HPAM (0.075 wt. %)	0.003	997	2510	0.270	0.420	112	0.037	0.019
26		0.0035	997	2510	0.270	0.420		0.041	0.023
27		0.004	997	2510	0.270	0.420		0.048	0.028
28	HPAM (0.040 wt. %)	0.00185	1002	3860	0.520	0.370	52	0.006	0.018
29		0.0022	1002	3860	0.520	0.370		0.007	0.023
30		0.00258	1002	3860	0.520	0.370		0.016	0.029
31		0.00185	1002	3860	0.520	0.420		0.004	0.009
32		0.0022	1002	3860	0.520	0.420		0.007	0.014
33	HPAM (0.100 wt. %)	0.00258	1002	3860	0.520	0.420	55	0.010	0.022
34		0.00185	997	3860	0.250	0.420		0.008	0.022
35		0.00218	997	3860	0.250	0.420		0.018	0.027
36		0.00258	997	3860	0.250	0.420		0.051	0.034
37	HPAM (0.055 wt. %)	0.00185	997	3860	0.330	0.400	143	0.023	0.014
38		0.00218	997	3860	0.330	0.400		0.045	0.018
39		0.00258	997	3860	0.330	0.400		0.058	0.023
40	HPAM (0.045 wt. %)	0.0015	1002	2510	0.020	0.892	66	0.009	0.004
41		0.002	1002	2510	0.020	0.892		0.013	0.007
42		0.003	1002	2510	0.020	0.892		0.021	0.013
43		0.0035	1002	2510	0.020	0.892		0.031	0.018
44		0.004	1002	2510	0.020	0.892		0.044	0.023

45		0.0218	1002	3860	0.020	0.892		0.011	0.008
46		0.0258	1002	3860	0.020	0.892		0.024	0.011
47	HPAM (0.065 wt. %)	0.0015	1005	2510	0.017	0.949	70	0.009	0.003
48		0.002	1005	2510	0.017	0.949		0.010	0.006
49		0.003	1005	2510	0.017	0.949		0.012	0.011
50		0.0035	1005	2510	0.017	0.949		0.013	0.015
51		0.004	1005	2510	0.017	0.949		0.028	0.019
52		0.0218	1005	3860	0.017	0.949		0.009	0.006
53		0.0258	1005	3860	0.017	0.949		0.009	0.009
54		0.02263	1005	7700	0.017	0.949		0.047	0.048
55	HPAM (0.080 wt.%)	0.00118	1000	2510	0.030	0.681	47	0.018	0.006
56		0.0015	1000	2510	0.030	0.681		0.035	0.010
57		0.002	1000	2510	0.030	0.681		0.056	0.017

Appendix B – Settling Velocity Calculation Procedure and Example

Steps in Calculating Terminal Settling Velocity

I. Calculate the mean surficial stress, $\bar{\tau}$

II. Using $\bar{\tau}$, calculate shear rate and viscosity based on the Power-law model.

III. Calculate $\sqrt{\frac{4(\rho_s - \rho_f)d^3 g\rho_f}{3\mu^2}}$ and use it to determine the viscoinelastic Reynolds number based on the associated Region.

IV. For inelastic fluids ($\lambda < 0.9$), the settling velocity can be calculated from the inelastic Reynolds number using equation 14.

V. If the fluid is elastic ($\lambda > 0.9$), calculate the elasticity factor (~~K~~) and use it to determine the elastic Reynolds number.

VI. The settling velocity in the elastic fluid can now be calculated using equation 14.

Example Calculation of Particle Settling Velocity in a Viscoinelastic Fluid

Data

Diameter of Particle, d = 1.29 mm = 0.00129 m

Density of Particle, ρ_s = 5900 kg/m^3

Density of Fluid, ρ_f= 1002 kg/m^3

Relaxation time, λ = 0.1 (Viscoinelastic)

k = 0.33 Pa.s^n

n = 0.40

Steps

- $Mean\ Surficial\ Stress,\ \bar{\tau} = \frac{dg\ (\rho_s - \rho_f)}{6} = 10.33\ Pa$
- $Shear\ rate, \dot{\gamma} = \left(\frac{\bar{\tau}}{k}\right)^{\frac{1}{n}} = 5483.15\ 1/s$
- $Viscosity, \mu = \frac{\bar{\tau}}{\dot{\gamma}} = 0.002\ Pa.s$
- $\sqrt{C_{D.}}Re_p = \sqrt{\frac{4(\rho_s - \rho_f)d^3 g\rho_f}{3\mu^2}} = 197.032$
- Region III ($C_D^{0.5}Re_p$>100), therefore, $Re_{p-inelastic} = 0.9204\sqrt{\frac{4(\rho_s - \rho_f)d^3 g\rho_f}{3\mu^2}}^{1.0571} = 245.2$

  Since fluid is inelastic ($\lambda < 0.9$)
- $Predicted\ Settling\ Velocity = \frac{\mu Re_p}{\rho_f d} = 0.379\ m/s$

Example Calculation of Particle Settling Velocity in a Viscoelastic Fluid

Data

Diameter of Particle, d = 1.29 mm = 0.00129 m

Density of Particle, ρ_s = 5900 kg/m^3

Density of Fluid, ρ_f= 1002 kg/m^3

Relaxation time, λ = 52 Seconds/Rad (324.38 Seconds)

k = 0.33 Pa.s^n

n = 0.40

Steps

- $Mean\ Surficial\ Stress,\ \bar{\tau} = \frac{dg\ (\rho_s - \rho_f)}{6} = 10.33\ Pa$
- $Shear\ rate, \dot{\gamma} = \left(\frac{\bar{\tau}}{k}\right)^{\frac{1}{n}} = 5483.15\ 1/s$
- $Viscosity, \mu = \frac{\bar{\tau}}{\dot{\gamma}} = 0.002\ Pa.s$
- $\sqrt{C_{D.}}Re_p = \sqrt{\frac{4(\rho_s - \rho_f)d^3 g\rho_f}{3\mu^2}} = 197.032$
- Region III ($C_D^{0.5}Re_p$>100), therefore, $Re_{p-inelastic} = 0.9204\sqrt{\frac{4(\rho_s - \rho_f)d^3 g\rho_f}{3\mu^2}}^{1.0571} = 245.2$

  Since fluid is elastic (λ > 0.9)

- $\text{Ƙ} = \frac{3.03782Wi^{0.5064267}}{\sqrt{\frac{4(\rho_s - \rho_f)d^3 g\rho_f}{3\mu^2}}^{0.78936}} = 68.6364$

  (Where $Wi = \dot{\gamma} * \lambda$)

- $Re_{p-elastic} = Re_{p-inelastic}(1 + \text{Ƙ})^{-0.689} = 2.304$
- $Predicted\ Settling\ Velocity = \frac{\mu Re_p}{\rho_f d} = 0.003\ m/s$

  Measured Settling Velocity = 0.003m/s

References

Acharya, A. (Ruma) (1986) 'Particle Transport in Viscous and Viscoelastic Fracturing Fluids.pdf', *SPE Production Engineering*, 34(March), pp. 104–110. doi: 10.2118/13179-PA.

Arabi, A. S. and Sanders, R. S. (2016) 'Particle terminal settling velocities in non-Newtonian viscoplastic fluids', *Canadian Journal of Chemical Engineering*, 94(6), pp. 1092–1101. doi: 10.1002/cjce.22496.

Arnipally, S. K., & Kuru, E. (2017). Settling Velocity of Particles in Viscoelastic Fluids: A Comparison of the Shear Viscosity vs Elasticity Effect. In SPE Annual Technical Conference and Exhibition held in San Antonio, Texas, 9-11 October 2017.

Benchabane, A. and Bekkour, K. (2008) 'Rheological properties of carboxymethyl cellulose (CMC) solutions', *Colloid and Polymer Science*, 286(10), pp. 1173–1180. doi: 10.1007/s00396-008-1882-2.

van den Brule, B. H. A. A. and Gheissary, G. (1993) 'Effects of fluid elasticity on the static and dynamic settling of a spherical particle', *Journal of Non-Newtonian Fluid Mechanics*, 49(1), pp. 123–132. doi: 10.1016/0377-0257(93)85026-7.

Bui, B. *et al.* (2012) 'Viscoelastic Properties of Oil-Based Drilling Fluids', *Annual Transactions of the Nordic Rheology Society*, 20, pp. 33–47.

Chhabra, R. (2006) *Bubbles, Drops, and Particles in Non-Newtonian Fluids, Second Edition*. doi: 10.1201/9781420015386.

Chhabra, R. P., Uhlherr, P. H. . and Boger, D. . V. (1980) 'The Influence of Fluid Elasticity on the Drag Coeeficient for Creeping Flow Around a Sphere', *Journal of Non-Newtonian Fluid Mechanics*, 6, pp. 187–199.

Choi, S. K. (2008) 'p H Sensitive Polymers for Novel Conformance Control and Polymer Flooding Applications', *PhD Thesis, University of Texas, Austin*.

Clift, R., Grace, J. R. and Weber, M. E. (1978) *Bubbles, Drops, and Particles*.

Kelessidis, V. (2003) 'Terminal velocity of solid spheres falling in newtonian and non newtonian liquids', *Tech. Chron. Sci.*, (1–2), pp. 43–45.

Kelessidis, V. C. and Mpandelis, G. (2004) 'Measurements and prediction of terminal velocity of solid spheres falling through stagnant pseudoplastic liquids', *Powder Technology*, 147(1–3), pp. 117–125. doi: 10.1016/j.powtec.2004.09.034.

Kesely, M. and Matoušek, V. (2016) 'Laminar Settling of Glass Beads in Visco-Plastic Liquids', *Stavební obzor - Civil Engineering Journal*, 25(1). doi: 10.14311/CEJ.2016.01.0001.

Lali, A. M. *et al.* (1989) 'Behaviour of solid particles in viscous non-newtonian solutions: Settling velocity, wall effects and bed expansion in solid-liquid fluidized beds', *Powder Technology*, 57(1), pp. 39–50. doi: 10.1016/0032-5910(89)80102-0.

Machač, I. *et al.* (1995) 'Fall of spherical particles through non-Newtonian suspensions', *Chemical Engineering Science*, 50(20), pp. 3323–3327. doi: 10.1016/0009-2509(95)00168-5.

Malhotra, S. and Sharma, M. M. (2012) ‘Settling of spherical particles in unbounded and confined surfactant-based shear thinning viscoelastic fluids: An experimental study’, *Chemical Engineering Science*, 84(January), pp. 646–655. doi: 10.1016/j.ces.2012.09.010.

Metzner, A. B. and Reed, J. C. (1955) ‘Flow of Non-Newtonian Fluids-Correlation of the Laminar , Transition , and Turbulent-flow Regions’, (4). doi: 10.1002/aic.690010409.

Miura, H. *et al.* (2001) ‘Bed expansion in liquid-solid two-phase fluidized beds with Newtonian and non-Newtonian fluids over the wide range of Reynolds numbers’, *Powder Technology*, 117(3), pp. 239–246. doi: 10.1016/S0032-5910(00)00375-2.

Mohammed, M. A. R. (2013) ‘Studying the Factors Affecting the Settling Velocity of Solid Particles in Non-Newtonian Fluids Terminal Settling Velocity ’:, 16(1), pp. 41–50.

Morrison, F. A. (2013) ‘Data Correlation for Drag Coefficient for Spheres’, *Cambridge University Press, New York*, 10(November), pp. 1–2.

*Okesanya, T.O and Kuru, E. (2019) 'SPE-196104-MS A New Generalized Model for Predicting Particle Settling Velocity in Viscoplastic Fluids' Accepted to be Presented at the ATCE, Calgary 2019.

Pinelli, D. and Magelli, F. (2001) ‘Solids settling velocity and distribution in slurry reactors with dilute pseudoplastic suspensions’, *Industrial and Engineering Chemistry Research*, 40(20), pp. 4456–4462. doi: 10.1021/ie0010518.

Reynolds, P. A. and Jones, T. E. R. (1989) ‘An experimental study of the settling velocities of single particles in non-Newtonian fluids’, *International Journal of Mineral Processing*, 25(1–2), pp. 47–77. doi: 10.1016/0301-7516(89)90056-2.

Shah, S. N., El-Fadili, Y. E. and Chhabra, R. P. (2007) ‘New model for single spherical particle settling velocity in power law (viscoinelastic) fluids’, 33, pp. 51–66. doi: 10.1016/j.ijmultiphaseflow.2006.06.006.

Shahi, S. and Kuru, E. (2015) ‘An experimental investigation of settling velocity of natural sands in water using Particle Image Shadowgraph’, *Powder Technology*. Elsevier B.V., 281, pp. 184–192. doi: 10.1016/j.powtec.2015.04.065.

Turton, R. and Levenspiel, O. (1986) ‘A short note on the drag correlation for spheres’, *Powder Technology*, 47(1), pp. 83–86. doi: 10.1016/0032-5910(86)80012-2.

Walters, K. and Tanner, R. (1992) ‘The Motion of a Sphere through an Elastic Fluid’, *Transport Processes in Bubbles, Drops and Particles*.

Werner, B., Myrseth, V. and Saasen, A. (2017) ‘Werner, B., Myrseth, V., & Saasen, A. (2017). Viscoelastic properties of drilling fluids and their influence on cuttings transport. Journal of Petroleum Science and Engineering. http://doi.org/10.1016/j.petrol.2017.06.063scoelastic properties of drilling ’, *Journal of Petroleum Science and Engineering*. doi: 10.1016/j.petrol.2017.06.063.

Wilson, K. C. *et al.* (2003) 'Direct prediction of fall velocities in non-Newtonian materials', *International Journal of Mineral Processing*, 71(1–4), pp. 17–30. doi: 10.1016/S0301-7516(03)00027-9.

Wilson, K. C. and Thomas, A. D. (1985) 'A new analysis of the turbulent flow of non-newtonian fluids', *The Canadian Journal of Chemical Engineering*, 63(4), pp. 539–546. doi: 10.1002/cjce.5450630403.

CHAPTER 5 : A NEW GENERALIZED MODEL FOR PREDICTING THE DRAG COEFFICIENT AND SETTLING VELOCITY OF RIGID SPHERES IN VISCOPLASTIC FLUIDS[1]

[1] The major results and discussions of the chapter has been submitted and accepted as Temitope Okesanya and Ergun Kuru, "A New Generalized Model for Predicting Particle Settling Velocity in Viscoplastic Fluids." with paper number SPE-196104-MS for presentation at the 2019 SPE Annual Technical Conference and Exhibition to be held 30 September – 2 October 2019 in Calgary, Canada.

5.1 Abstract

An experimental study was conducted to measure the settling velocity of spherical particles in viscoplastic fluids exhibiting inelastic and elastic behavior. Using a mechanistic model based on the balance of the forces acting on the settling particle and detailed statistical analyses of the experimental results, a generalized model for predicting settling velocity of spherical particles in such yield stress fluids (elastic and inelastic) was developed.

The main objectives of the study were: i.) To measure the terminal settling velocity of particles in various elastic and inelastic yield stress fluids intending to expand the present database of experimental data ii.) To develop a new Drag coefficient-particle Reynolds number (C_D-Re_p) correlation that is applicable to both Newtonian and non-Newtonian viscoplastic fluids iii.) To present a general non-iterative approach for predicting settling velocities of particles in Newtonian and non-Newtonian viscoplastic (elastic and inelastic) fluids irrespective of their rheological models (Casson Model, Herschel Bulkley Model, and Bingham Model etc.).

The settling velocities of the spherical particles (Specific gravity ranging from 2.5 – 7.7; Diameters: ranging from 1.09 - 4.00 mm) in various Carbopol polymer solutions of varying elastic properties were measured using Particle Image Shadowgraphy (PIS). Rheological characterization of the fluids was carried out using the world class C-VOR Bohlin Rheometer. The experimental results were combined with experimental data published in the literature to broaden the range and applicability of the database. The database had a yield stress range of 0 - 6.6 Pa, consistency index (k) range of 0.15 -2.1 $Pa.s^n$ and a fluid behavior index (n) range of 0.4 – 0.9 for Herschel Bulkley fluids and a yield stress range of 1 – 60 Pa for Bingham and Casson fluids. Advanced statistical analysis programs (OriginPro 9.0 and MATLAB r2018b) were utilized together with the extensive

database to develop a new C_D-Re_p correlation. In this study, a new modified shear Reynolds number (Re_T^*) was introduced, which physically quantifies the effects of non-Newtonian fluid rheological properties on the settling velocity. The newly developed C_D-Re_p correlation and the modified shear Reynolds number were incorporated into the Wilson *et al.* (2003) model to develop a generalized model that can be used for predicting particle settling velocity in all viscoplastic fluids.

The settling velocities of the spherical particles (Specific gravity ranging from 2.5 – 7.7; Diameters: ranging from 1.09 - 4.00 mm) in various Carbopol polymer solutions of varying elastic properties were measured using Particle Image Shadowgraphy (PIS). Rheological characterization of the fluids was carried out using the world class C-VOR Bohlin Rheometer. The experimental results were combined with experimental data published in the literature to broaden the range and applicability of empirical analysis. Advanced statistical analysis programs (OriginPro 9.0 and MATLAB r2018b) were utilized together with extensive experimental data to develop a new CD-Rep correlation. In this study, a new modified shear Reynolds number (Re_T^*)was introduced, which physically quantifies the effects of non-Newtonian fluid rheological properties on the settling velocity. The newly developed CD-Rep correlation and the modified shear Reynolds number were incorporated into the Wilson et al. (2003) model to develop a generalized model that can be used for predicting particle settling velocity in all viscoplastic fluids.

We have shown that presented new model predicts settling velocity better and yielded relatively more accurate results than existing models. Statistical comparative analysis showed that the generalized model gives the lowest approximate Percentage Mean Absolute Error (PMAE) of 24.5 % for all data points. In addition to enhanced prediction accuracy, this new model occludes

application constraints and offers prediction versatility that is lacking in current existing models by being valid for diverse rheological models of non-Newtonian viscoplastic fluids.

The proposed new model was further evaluated with elastic yield stress fluids in order to investigate the effects of elasticity on the settling behavior and to assess its prediction performance. Experimental results showed that generalized model was able to provide settling velocity prediction for the elastic yield stress fluids with reasonable accuracy achieving a very low Percentage Mean Absolute Error (PMAE) of 30.15 % and Root Mean Square Error (RMSE) of 0.02 m/s. While elasticity reduces the settling velocity in certain non-Newtonian fluids; however in viscoplastic fluids the presence of a yield stress may eclipse the elastic property of the fluid leading to uniformity in settling behavior which can be predicted with the generalized model. The paper is concluded by presenting illustrative examples to calculate the terminal velocity of a spherical particle in non-Newtonian viscoplastic fluids using the presented generalized model.

The knowledge of particle settling velocity in viscoplastic fluids is indispensable for the design, analysis, and optimization of a wide spectrum of industrial processes such as cuttings transport in oil and gas well drilling and proppant transport in hydraulic fracturing operations. By augmenting the current corpus of experimental data; we have provided much-needed particle settling velocity database that can be used for modeling of relevant transport processes (i.e. cuttings and/or proppants transport). Finally, by combining a mechanistic model describing the forces acting on the settling particles with the newly developed CD-Rep correlation, we have presented a new generalized predictive model of particle settling velocity in viscoplastic fluids that can be used for the optimization of particle transport in oil and gas well drilling and hydraulic fracturing operations.

5.2 Introduction

The accurate prediction of terminal settling velocity of solids in viscoplastic fluids (i.e. non-Newtonian fluids that undergo no permanent deformation unless the applied shear stress exceeds the minimum yield stress of the fluid) is paramount for the design, analysis, and optimization of a wide spectrum of industrial processes such as pipeline transport of slurries, sand transport in oil and gas production lines, rock cuttings transport in oil and gas well drilling as well as proppant transport in hydraulic fracturing operation. The Terminal Settling velocity (V_t) is defined as the constant and unhindered free falling velocity attained by a particle settling in a fluid when all the forces acting on the particle are balanced (i.e. under equilibrium). The settling velocity is termed hindered settling if the falling particle is obstructed by other particles or a neighboring wall (McCabe & Harriot, 1987), which is ubiquitous in industrial processes. Conversely, the hindered settling velocity is reportedly related to free terminal particle settling velocity (Kelessidis & Mpandelis, 2004; Rushd et al., 2018); hence ensuing the priority for the estimation of free particle settling velocity.

In anteceding decades, many efforts have been made by researchers to understand and predict the motion of solid particles in Newtonian and non-Newtonian fluids (Ansley & Smith, 1967; Arabi & Sanders, 2016; Arnipally & Kuru, 2017; Atapattu, Chhabra, & Uhlherr, 1995; Beris, Tsamopoulos, Armstrong, & Brown, 1985; Blackery & Mitsoulis, 1997; Chafe & de Bruyn, 2005; Chhabra, 2006; Dedegil, 1987; Gumulya, Horsley, & Wilson, 2007; Gumulya, Horsley, Wilson, & Pareek, 2011; Kelessidis & Mpandelis, 2004; Kesely & Matoušek, 2016; Prashant & Derksen, 2011; Rushd et al., 2018; Stokes, 1905; Tabuteau, Coussot, & de Bruyn, 2007; Valentik & Whitmore, 1965; Wilson, Horsley, Kealy, Reizes, & Horsley, 2003). While the behavior of rigid

spherical particles in Newtonian fluids has been accurately dealt with by some authors (McCabe & Harriot, 1987; Morrison, 2013; Richardson, Harker, & Backhurst, 2002; Wilson et al., 2003), the behavior and motion of rigid particles in non-Newtonian fluids especially in viscoplastic fluids has not been fully demystified due to complexities in particle physical properties and disparities in fluid rheological modelling compounded by the presence of the hard-to-measure yield stress (Chhabra, 2006). Describing settling behavior primarily entails the determination of the drag coefficient; which is the fundamental hydrodynamic characteristic of the particle motion falling through a fluid (Machač, Ulbrichová, Elson, & Cheesman, 1995). The drag coefficient (C_D) defined as the ratio of the viscous drag force to the kinetic energy acting on the particle (Rushd et al., 2018) and can also be expressed mathematically as:

$$C_D = \frac{4(\rho_s - \rho_f)dg}{3V_t^2\rho_f} \qquad 5.1$$

Where d is diameter of the particle, ρ_f is the fluid density, ρ_s is the solid particle density and g is acceleration due to gravity. The drag coefficient is acknowledged to be affected by the particle and the fluid properties (Arnipally & Kuru, 2017; McCabe & Harriot, 1987). Several studies have also suggested the existence of elasticity effects on drag coefficient especially in Power Law non-Newtonian fluids (Arnipally & Kuru, 2017; Chhabra, 2006; Malhotra & Sharma, 2012). It is also possible for yield stress (viscoplastics) fluid to exhibit elastic properties which may settling behavior of particles (Fraggedakis, Dimakopoulos and Tsamopoulos, 2016).

All things being equal, the drag coefficient determines the particle settling velocity (or vice versa) and consequently the particle Reynolds number, all three of which are interwoven. Due to the

difficulty in developing analytical solutions, empirical correlations and experimental methods are employed in the determination of C_D (Arnipally & Kuru, 2017; Kesely & Matoušek, 2016; Machač et al., 1995). The solution method involves the development of a drag coefficient and particle Reynolds number correlation. The particle Reynolds number Re_p is defined as the ratio of inertial forces to viscous forces experienced by the particle (Chhabra, 2006) and is also expressed mathematically as follows:

$$Re_p = \frac{\rho_f V_t d}{\mu} \tag{5.2}$$

Where μ is Newtonian viscosity of the fluid medium. If the drag coefficient can be accurately determined with the aid of C_D-Re_p correlation, predicting the settling velocity iteratively becomes relatively easier.

Considerable efforts have been made to develop expressions that relate C_D to Re_p with the pioneering work carried out by Sir George Stokes in the 19th century (Stokes, 1905). He proposed the following relationship for Newtonian fluids at laminar condition ($Re_p < 0.3$):

$$C_D = \frac{24}{Re_p} \tag{5.3}$$

Over the years, researchers have modified and produced several other Newtonian C_D-Re_p correlations for spherical (Brown & Lawler, 2003; Cheng, 2009; Dedegil, 1987; Richardson et al., 2002; Turton & Levenspiel, 1986) and non-Spherical particles (Chien, 1994; Haider & Levenspiel,

1989; Song, Xu, Li, Pang, & Zhu, 2017). A comparative comprehensive review of various correlations was carried out by Chhabra (2006) for interested readers.

With respect to the settling velocity, considerable amount of research efforts have been undertaken resulting in several numerical solutions as well as empirical correlations each with their associated limitations. Although useful, majority of the numerical analysis (Beris et al., 1985; Blackery & Mitsoulis, 1997; Briscoe, Glaese, Luckham, & Ren, 1992; Kesely & Matoušek, 2016; Prashant & Derksen, 2011) were implicit and focused on creeping (laminar) flow conditions, hence inapplicable for predicting settling velocities at high practical Reynolds number (Arabi & Sanders, 2016; Rushd et al., 2018). An empirical approach involved relating drag coefficient to specific dimensionless numbers based on rheological models to predict the settling velocity (Andres, 1961; Valentik and Whitmore, 1965; Ansley and Smith, 1967; Tabuteau, Coussot and de Bruyn, 2007). According to Arabi and Sanders (2016), a major constraint with this approach apart from being model specific is the poor predictability if the fluid exhibits a near Newtonian behavior.

An alternative empirical approach involves modifying the definition of apparent viscosity (i.e. viscosity of the fluid under the shear rate induced by a falling particle) or Reynolds number such that the results of the viscoplastic settling tests coincide with the standard Newtonian drag curve (Atapattu et al., 1995; Chhabra, 2006; Dolejš, Doleček, & Šiška, 1998; Ito & Kajiuchi, 1969; Machač et al., 1995; Saha, Purohit, & Mitra, 1992). This approach not only ensures uniformity for various Newtonian and non-Newtonian fluids but also provides ease for predicting settling velocity since a single C_D-Re_p curve is utilized. Earlier classic work by Metzner and Reed (1955) developed the modified Reynolds number for Power Law non-Newtonian fluids. Similarly, Machač *et al.* (1995*)* modified the definition of the particle Reynolds number in equation 5.2 for two rheological

viscoplastic models (Bingham Plastic and Herschel Bulkley Models) to collapse their drag coefficent values to the standard Newtonian curve. They proposed the following equations respectively:

$$Re_{pB} = \frac{\rho_f (V_t) d}{\mu_B + \tau_B \left(\frac{d}{V_t}\right)} \quad 5.4$$

$$Re_{pHB} = \frac{\rho_f (V_t)^{2-n} d^n}{\tau_{HB} \left(\frac{d}{V_t}\right)^n + k} \quad 5.5$$

In equation 4, Re_{pB} is the modified Bingham particle Reynolds number, μ_B is the Bingham Plastic viscosity and τ_B is the Bingham Yield. In equation 5, Re_{pHB} is the modified Herschel Bulkley particle Reynolds number, k is the Consistency index and n is the power law index. The key limitation with this alternative approach apart from requiring complex iteration is its lack of applicability across a wide range of Reynolds number (Arabi & Sanders, 2016). Owing to the difficulty in cumbersome iterations there was a need for a direct explicit approach, which occludes the aforementioned limitations.

In 2003, Wilson et al. presented a direct method that was able to provide reasonable predictions of the terminal settling velocity of a sphere in a viscoplastic fluids. Their method utilized the mean surficial stress $\bar{\tau}$ (i.e. stress resulting from the fall of a particle through a fluid) to determine the shear velocity (V*) and consequently the shear Reynolds number (Re*). Where ;

The mean surficial stress $\bar{\tau}$ is given by:

$$\bar{\tau} = \frac{dg\ (\rho_s - \rho_f)}{6} \qquad 5.6$$

The shear velocity V* is given by:

$$V^* = \sqrt{\frac{\bar{\tau}}{\rho_f}} = \sqrt{\frac{dg\ (\rho_s - \rho_f)}{6\rho_f}} \qquad 5.7$$

And the shear Reynolds number Re* is given by:

$$Re^* = \frac{d\rho_f V^*}{\mu} \qquad 5.8$$

They developed a Newtonian plot that correlated the settling velocity, V_t (made dimensionless using the shear velocity V*) to the shear Reynolds number (Re*). In order to extend their Newtonian plot (Vt/V* vs Re*) to non-Newtonian viscoplastic fluids they introduced an equivalent Newtonian viscosity parameter by calibrating the mean surficial stress,$\bar{\tau}$. The calibrating factor was estimated to be 0.3 based on their experimental data ($\tau = 0.3\ \bar{\tau}$)

However, this method is limited in applicability in that; i-) If the fluid yield stress is greater than the calculated reference shear stress ($\tau_y > 0.3\ \bar{\tau}$), the correlation cannot produce a prediction of terminal settling velocity. (Arabi & Sanders, 2016; Gumulya et al., 2007; Wilson et al., 2003; Wilson & Thomas, 1985); ii-) Poor prediction at low shear Reynolds number (Re* < 100). The average absolute error is 75 % for 62 experimental points (Arabi & Sanders, 2016; Wilson et al.,

2003); iii.) Furthermore, a meticulous review of the Wilson et al. (2003) model revealed that the model was developed based on the Turton and Levenspiel (1986) C_D-Re_p relationship, which has undergone recent modifications (Cheng, 2009; Chhabra, 2006; Morrison, 2013).

Arabi and Sanders (2016) carried out an empirical and statistical study to improve the Wilson et al. (2003) model by modifying the equivalent viscosity parameter. Although their model was better and produced relatively more accurate than the original Wilson et al. model, their data was model specific (Casson and Bingham Model) and the experimental results obtained from their study showed poor prediction at laminar regime (low shear Reynolds numbers $Re^* < 10$). Kesely and Matoušek (2016) also presented a model based on the Wilson et al. (2003) method to predict the laminar settling velocity. However, their method is implicit and requires iteration. Recently, Rushd *et al.* (2018) modified the definition of the shear Reynolds number used in the Wilson et al. (2003) model with the model specific Reynolds number presented by Machač *et al* (1995). However, their approach was model specific and was not tested with other viscoplastic models (Rushd et al., 2018).

Based on the review of the prior literature, we conclude that there is still a need for a universal predictive model that offers versatility in application by occluding the practical constraints listed above and yields relatively more accurate results. The main objectives of this study is to conduct settling velocity measurements of spherical particles in viscoplastic fluids intended at augmenting the present database of experimental data, which will be used in developing a new generalized Drag coefficient-Reynolds number (C_D-Re_p) curve that is applicable to both Newtonian and non-Newtonian viscoplastic fluid models. Furthermore, this study seeks to develop a general non-iterative approach for predicting settling velocities of particles in Newtonian and non-Newtonian

viscoplastic fluids irrespective of their rheological models based on the experimental results from this study and other published data.

5.3 Experimental Materials and Methodology

5.3.1 Experimental Setup.

The settling velocities of the spherical particles in various Carbopol solutions were measured using Particle Image Shadowgraphy (PIS) technique. Particle Image Shadowgraphy is a non-intrusive flow visualization technique that works on the basic optical principle that light is sensitive to changes in density of the medium through which it travels and any disparity always result in the formation of shadows.

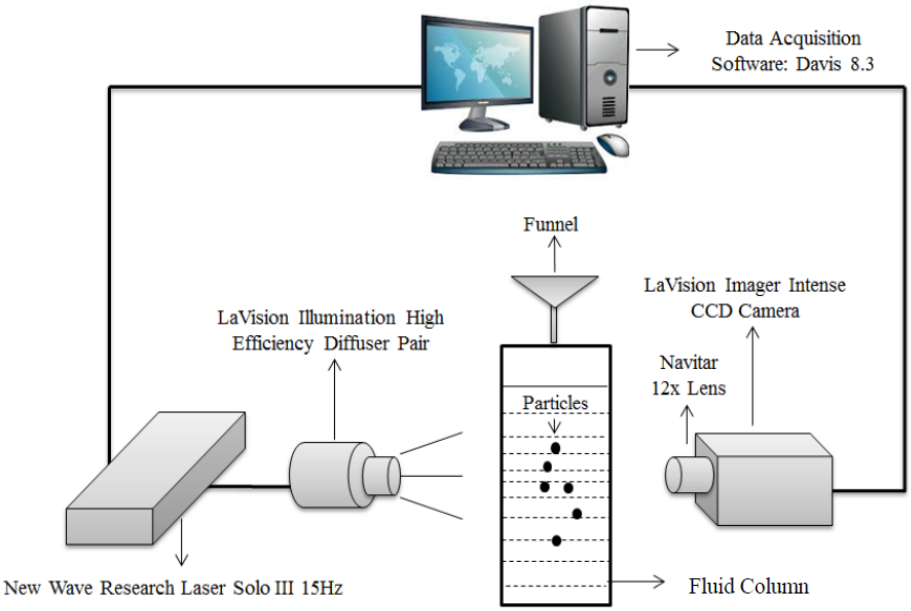

Figure 5.1 Particle Image Shadowgraphy (PIS) Experimental Setup Used in the Current Study

Image Shadowgraphy has advantages over some flow measurement techniques because it is non-intrusive measuring technique hence it does not interrupt the flow or alter the fluid property

thereby avoiding errors. It also allows the simultaneous measurement of several other characteristics, such as the interface speed and the direction of motion, and the object size. This technique requires a source of light and an image acquisition device as shown by experimental setup in Figure 5.1. The experimental setup was composed of the light source, which was provided by the New Wave Research Laser Solo III; an Nd-YAG double pulsed laser with a 532 nm wavelength and a frequency of 15 Hz. The laser was coupled with the LaVision circular diffuser pair for greater efficiency and background illumination. The image acquisition was provided by the LaVision Image Intense Camera with a 12x Navitar Lens. This double framed (capable of capturing quick successive images at two different exposure times in as short as 500ns) high resolution camera had a CCD sensor of 1376×1040 pixels capable of capturing 5 frames per sec and a capacity to convey 12-bit digital images. The captured images would result in futility, if they cannot be processed and analyzed to produce data. The Data Acquisition (DAQ) and processing software used was the LaVision Davis 8.3 software.

The ParticleMaster Shadow Project of the Davis 8.3 software follows algorithms to measure the size and the velocity. The algorithm measures the size by first locating the particles in the area of general interest (field of view of the camera) and analyzing the particles for size, shape and position. The recognition and analyzing algorithm is based on the intensity variation of the image. After sizing and locating the particles in the first frame, the algorithm then measures the terminal velocity by correlating the first frame with the successive frame to determine position shift (displacement) of the particle. The displacement and Δt (time difference between frames) can be simultaneously used to determine the velocity. If this measurement is carried out after the constant velocity was achieved by the particle, then this methodology gives an accurate

instantaneous measurement of the terminal velocity. Figure 5.2 shows the schematic of the general algorithm followed by the software to calculate the terminal velocity.

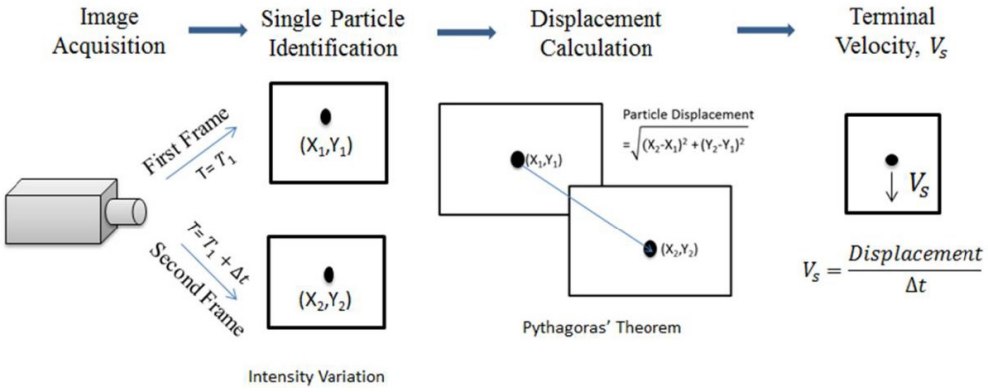

Figure 5.2: Schematic of the Davis 8.3 software algorithm to determine terminal settling velocity

The container for the viscoplastic fluid column is made out of a transparent plexiglass cuboidal column of 70 cm height. The dimensions of the cuboidal container are 15cm by 15cm by 70cm. The fluid column dimensions were designed by considering the minimum size required for avoiding the wall effects (Atapattu, Chhabra, & Uhlherr, 1990).

5.3.2 Verification of Particle Image Shadowgraphy Measurements.

Using the universal Newtonian drag curve for spheres, the PIS experimental setup is calibrated and tested to authenticate the veracity of results. The test is carried out by measuring settling velocity of the 4 spherical balls (0.71mm,1.18mm,1.50mm and 2.00mm) in water (standard fluid). The measured settling velocity of the spherical particles is used in determining particle Reynolds number (Equation 5.2) and consequently the drag coefficient of spherical balls using the correlation (Equation 5.9) proposed by Morrison (2013).

$$C_D = \frac{24}{Re_p} + \frac{2.6\left(\frac{Re_p}{5}\right)}{1+\left(\frac{Re_p}{5}\right)^{1.52}} + \frac{0.411\left(\frac{Re_p}{263000}\right)^{-7.94}}{1+\left(\frac{Re_p}{263000}\right)^{-8.00}} + \frac{0.25\left(\frac{Re_p}{10^6}\right)}{1+\left(\frac{Re_p}{10^6}\right)} \quad (5.9)$$

The drag coefficients from the experimental measurements were found to be within 3.5 % of the theoretical values, hence bolstering the reliability of the experimental setup. Furthermore, some authors have previously authenticated the experimental setup used in this study (Arnipally & Kuru, 2017; Shahi & Kuru, 2015).

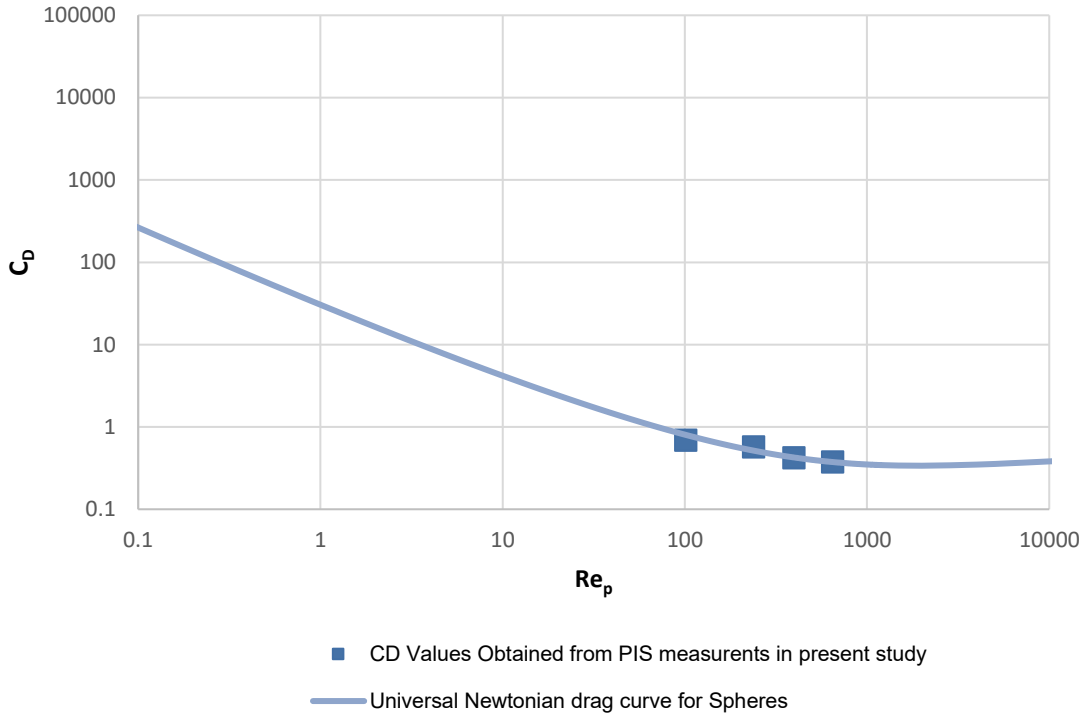

Figure 5.3: C_D vs Re_p Plot for the Verification of the PIS Measurements

5.3.3 Test Materials.

In this study, precision spherical particles of glass, steel, ceramic and Zirconium were used. Physical properties of the particles used for experiments are listed in the Table 5.1.

Table 5.1: Physical Properties of Spherical Particles

S/N	Diameter (mm)	Material	Density (kg/m^3)
1	1.18	Glass	2510
2	1.50	Glass	2510
3	2.00	Glass	2510
4	3.00	Glass	2510
5	3.50	Glass	2510
6	4.00	Glass	2510
7	1.85	Ceramic	3860
8	2.18	Ceramic	3860
9	2.58	Ceramic	3860
10	1.09	Zirconium Oxide Yttrium	5900
11	1.29	Zirconium Oxide Yttrium	5900
12	1.55	Zirconium Oxide Yttrium	5900
13	2.4-2.5	Steel	7700
14	2.00	Marble	2711

The Carbopol ETD 2020 was used to prepare the test fluids. Carbopol® is a high molecular weight crosslinked polyacrylic acid polymer. The main variances among the carbopol family stem from the crosslinker type and the density as well as the solvent used to synthesize the polymer

(Lubrizol, 2010). The Carbopol polymers expand upon neutralization in aqueous medium and form a transparent gel. 13 different fluids were utilized in the settling velocity tests. The white carbopol powders were obtained from Lubrizol™. The concentration (wt%) of the carbopol polymers was varied within the range of 0.03–0.06. The procedure for preparing the test fluids is similar to that described by Curran *et al.*, 2002. The procedure is outlined below:

- Deionized water of required volume was measured and stirred at 300 rpm in mixing bucket.
- Based on the desired wt%, the required mass of Carbopol powder was added slowly progressively (not all at once) to the stirring de-ionized water on to the inner sides of the fluid vortex.
- After adding the polymers, the solution was stirred at 150 rpm for 3 hours (short time due to low concentration <0.075%) until the low wettability carbopol powders fully dissolve and a completely homogenous fluid is formed with no visible polymer powder.
- A 10 wt % Sodium hydroxide (NaOH) solution was then added in drops to raise the uniform pH of polymer to about 6.5. The pH of the polymer solutions were measured by using the Fisherbrand™ accumet™ AE150 pH benchtop meter.
- The Fluid was then stirred for an additional 1 hour to ensure uniformity.
- The solution was allowed to stand still overnight to remove air bubbles. (Note that Filtration was not necessary since the carbopol polymers used were clear and transparent).

5.3.4 Rheological Measurements and Characterizations.

Rheological measurements were performed with the C-VOR cone and plate type rheometer from Bohlin Instruments Bohlin Instruments. The 40mm and 4° cone and plate geometry was used. The measurements were conducted at room temperature (25°C) using the controlled shear stress function. An example of a measured flow curve is shown in Figure 4. The density of the fluids was measured by dividing the weight of the test fluid by the volume using a Pyrex Vista no. 70024 of 10 ml measuring jar.

There are several rheological models (Bingham plastic model, Casson Model, Herschel Bulkley Model, Sisko Model, Carreau Model, Quemada-Casson model, and so on) used for modelling viscoplastic fluids (Khalili Garakani et al., 2011; Rao, 2014). The Table 5.2 shows the mathematical equations for some of the popular rheological viscoplastic models.

Table 5.2: Mathematical Equations for some popular viscoplastic models

Rheological Model	Equations	
Bingham Plastic Model	$\tau = \tau_B + \mu_B \dot{\gamma}$	5.10
Casson Model	$\tau^{0.5} = {\tau_c}^{0.5} + (\mu_c \dot{\gamma})^{0.5}$	5.11
Herschel Bulkley	$\tau = \tau_{HB} + k\dot{\gamma}^n$	5.12

The Herschel Bulkley model is chosen for this experimental study because it has been reported by multiple authors to be the relatively accurate description of the drilling fluid rheology (Hemphill, Campos, & Pilehvari, 1993; Rushd et al., 2018). The Herschel Bulkley model require three parameters τ_{HB}, k and n for rheological characterization.

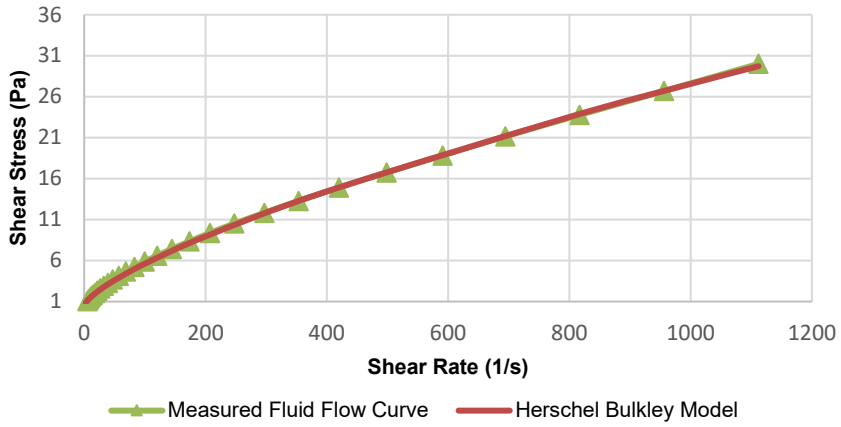

Figure 5.4: Shear stress vs shear rate diagram of a selected Carbopol solution.

These three parameters are determined using the numerical technique procedure outlined in API Recommended Practice 13D (API, 2006). The model was always matched with measured data from rheometer to ensure the accuracy as shown by the Figure 5.4. Average R^2 value was 0.99.

5.3.5 Experimental Procedure.

The experimental procedure follows similar steps employed by Shahi (2015). The first aspect of the procedure involves the preparation of the physical experimental setup as described in experimental section above. Once the fluid is prepared, it is transferred to plexiglass fluid column and is left unperturbed overnight to expel bubbles (which affect image quality and analysis) and to ensure the polymer regenerates its natural un-sheared state. Equipment calibration is carried out by inserting the calibration target sheet (a sheet having 0.8 mm printed circles spaced 1.5 mm apart) in the column and taking a focused image of the sheet. An image of the calibration sheet is shown in Figure 5.5.

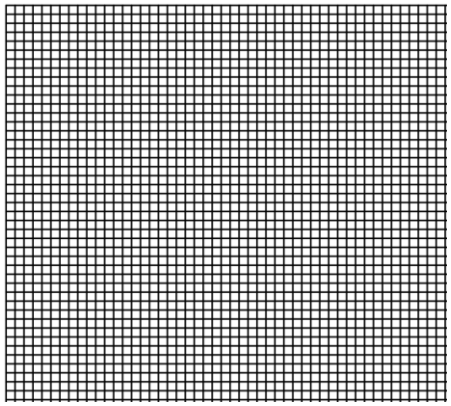

Figure 5.5: Calibration sheet used to calibrate the camera

The spacing dimensions of the sheet helps the Davis 8.3 software convert pixel dimensions into physical dimensions. The calibrated plane of focus would be marked at the top. It serves as the funnel position and the dropping point of spherical particles. Reference images are captured and averaged to serve as a reference background for the experimental images. The experimental images can now be captured. The spherical particles are to be dropped with the aid of a funnel, to ensure uniformity in landing positions.

This improves the accuracy of the results. When the spherical particles pass through the plane of focus, they appear as dark spots on Davis 8.3 software because of the differences in intensity as explained in the experimental section. The software follows a specific algorithm as shown in Figure 5.2 to determine the particle size and the terminal velocity (the processing scheme is described below). Repeatability of the experiment is checked by carrying out at least 5 trials and the averaging of 5 trials gives an accurate measure of the settling velocity. The velocity measurements is performed at two different heights (15cm and 10cm) from the base to ensure that the particle had attained its terminal settling velocity.

5.4 Analysis and Discussion

Overall, 17 different Carbopol polymer solutions were prepared of varying viscous and elastic properties. Over 90 different conditions were tested during settling experiments. The settling velocity results as well as the physical properties of fluid particle systems tested are presented in Appendix A to augment the current corpus of experimental data for future researchers.

5.4.1 Fluid Properties

The results of the viscometry and oscillatory tests which describe the rheological property of two of the experimental test fluids used in this study are presented in this section. The two polymer families utilized were Carbopol ETD 2020 and Carbopol 940; which were prepared in various concentrations to ensure a wide range of viscometric and elastic property.

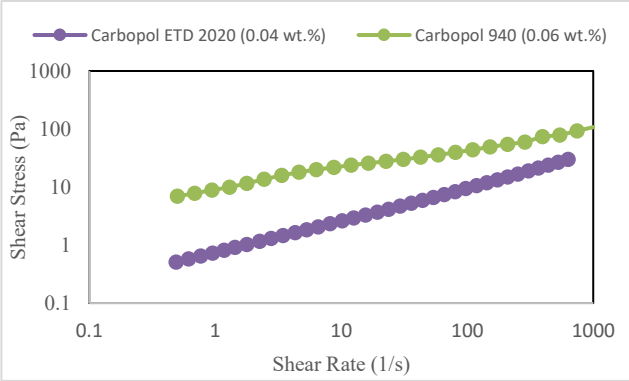

Figure 5.6: Shear Stress Vs Shear Rate plots for Carbopol ETD 2020 (0.04 wt. %) and Carbopol 940 (0.06 wt. %)

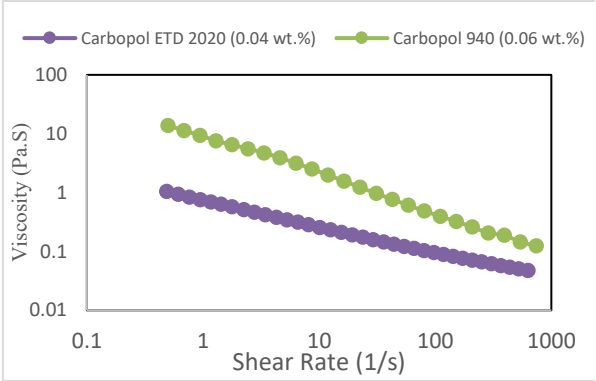

Figure 5.7: Viscosity Vs Shear Rate plots for Carbopol ETD 2020 (0.04 wt. %) and Carbopol 940 (0.06 wt. %)

Viscometry Controlled Shear Stress (CSS) tests were carried out on each test fluid to determine viscous property. The yield stress and fluid parameters were determined using the Fann Viscometer by adhering to procedures outlined in the API Recommended Practice 13D (API, 2006). Examples of viscometry test results are shown above.

Figure 5.6 shows the shear stress vs shear rate plot obtained from the CSS test for two of the experimental fluids Carbopol ETD 2020 (0.04 wt. %) and Carbopol 940 (0.06 wt. %); while Figure 5.7 shows the Viscosity vs Shear Rate plot obtained from the CSS test for the same set of experimental fluids as well. All the fluids used in this study exhibited yield stress as shown by the Fann Viscometer Measurements in the Table 5.3 below. As earlier stated, the fluid parameters τ_y, k and n were obtained adhering to numerical procedures outlined in the API Recommended Practice 13D (API, 2006). A complete list of fluids rheological property obtained from the Fann viscometer is presented in Table A-0 in the Appendix.

Table 5.3: Fluid Rheological Properties Measured by the Fann Viscometer

RPM (Revolutions Per Minute)	Fann Viscometer Dial Readings (° Deflection)	
	Fluid 1L - Carbopol ETD 2020 (0.04 wt. %)	Fluid B2 - Carbopol 940 (0.06 wt. %)
600 (1022 sec^{-1})	48.5	64
300 (511 sec^{-1})	32.5	44
200 (341 sec^{-1})	26	36
100 (170 sec^{-1})	18	25
6 (10 sec^{-1})	5.5	8
3 (5 sec^{-1})	3.5	6.5
Calculated Properties		
Plastic Viscosity →R600-R300 (cP)	16	20
Yield Stress → R300-Plastic Viscosity ($lb/100ft^2$)	16.5	24
τ_y (Pa)	1.089	1.881
K (Pa.s)	0.347	0.569
n	0.609	0.658

For the experimental fluids Carbopol ETD 2020 (0.04 wt. %) and Carbopol 940 (0.06 wt. %) above in Figure 6 and Figure 7, the power law consistency factor (k) were 0.601 $Pa.S^n$ and 0.569 $Pa.S^n$ respectively, while the flow behavior index (n) were 0.556 and 0.658 respectively. The yield stress τ_y obtained were 1.089 Pa amd 1.881 Pa respectively. These parameters depict the flow behavior of a typical viscoplastic fluid.

Oscillatory tests were carried out on each test fluid to determine the elastic property and relaxation time of each fluid. Figure 9 and Figure 10 represent the results of the oscillation test for two of the experimental fluids (0.04 wt. % Carbopol ETD 2020 and 0.06 wt. % Carbopol 940).

Figure 9 is the oscillation result for 0.04 wt. % Carbopol ETD 2020 while Figure 10 represents the oscillation test result for 0.06 wt. % Carbopol 940.

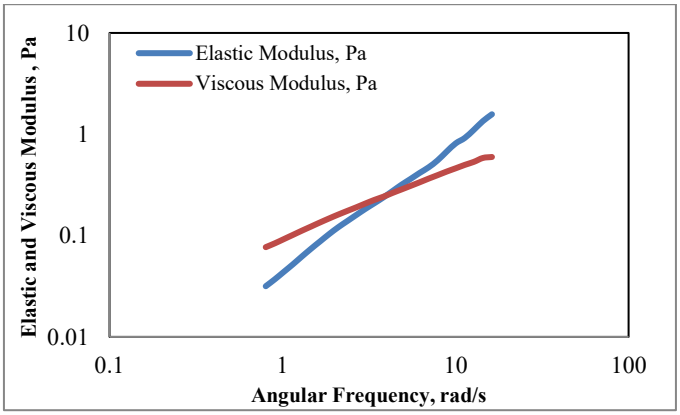

Figure 5.8: Oscillation Test Result for Carbopol ETD 2020 (0.04 wt. %)

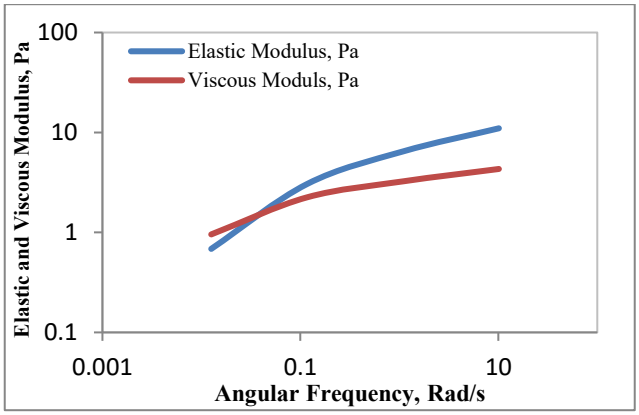

Figure 5.9: Oscillation Test Result for Carbopol 940 (0.06 wt. %)

The longest relaxation time, λ (sec) which is the inverse of the crossover angular frequency between the elastic modulus and viscous modulus. It signifies the time required for a material to regain its original structure after any deformation or disturbance. It is used to quantify the elasticity of a fluid (Choi, 2008; Malhotra and Sharma, 2012a; Arnipally and Kuru, 2018). In the figure above, Carbopol ETD 2020 (0.04 wt.%) had a low relaxation time of 0.20 seconds. This indicates a very low elastic property. Similar to all the Carbopol ETD 2020 polymers used in this experimental study irrespective of their concentration (Table A-1 in Appendix). While the Carbopol 940 (0.06wt. %) had a relaxation time of 40 seconds demonstrating a very high elastic property, also similar to other Carbopol 940 polymers used in this study. Although both fluids are viscoplastic (possess a yield stress) in nature, however only Carbopol 940 exhibits significant elastic property with relaxation time reaching 240s in some cases (Table A-2 in Appendix). Apart

from neutralizing, the viscous and elastic property of the Carbopol 940 polymers can also be altered by mixing with Carbopol Ultrez at different concentrations.

5.4.2 Drag Curve for Viscoplastic Fluids.

The experimental results from this study were combined with other experimental data published in the literature to broaden the range and applicability of the empirical model developed in this study. In order to obtain a universal drag curve, modified Reynolds number (equation 4 and 5) that collapse drag values to the standard Newtonian curve are utilized. As earlier stated, this approach not only ensures uniformity for various Newtonian and non-Newtonian fluids but also provides ease for predicting settling velocity. However for Casson fluids, a new modified Reynolds is presented in this study for collapsing settling tests on the Newtonian curve.

$$Re_{pC} = \frac{\rho_f (V_t) d}{\mu_c + 1.205 \tau_c \left(\frac{d}{V_t}\right)} \qquad 5.13$$

The equation was developed by correlating the Casson yield stress values and Bingham yield stress values for the same fluid available in the literature. The C_D-Re_p values of the entire database (experimental and literature) is plotted and matched with the Turton - Levenspiel Newtonian drag curve as shown in Figure 5.5. The Turton-Levenspiel curve was chosen because it was used in the development for Wilson et al. predictive model.

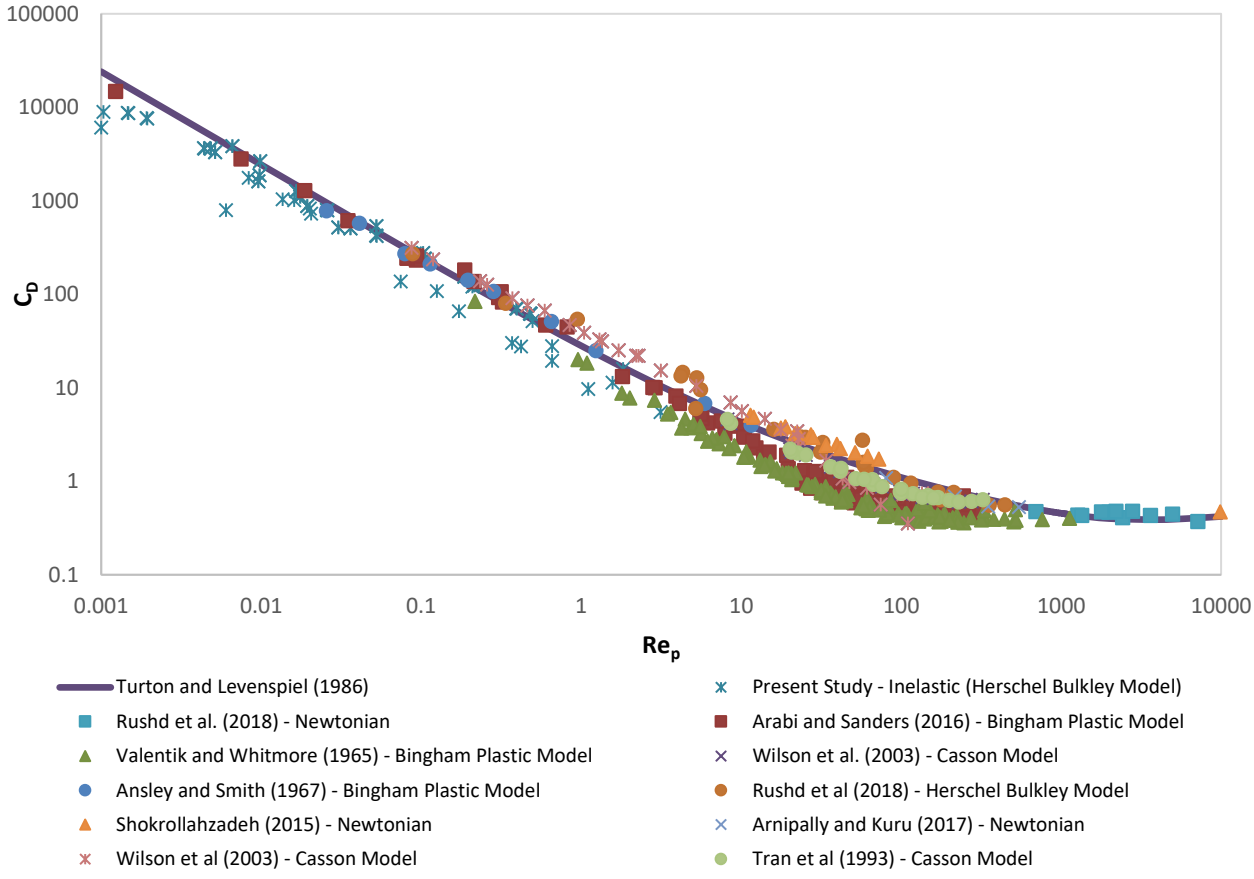

Figure 5.10: Plot of drag coefficient (C_D) vs particle Reynolds number (Re_p) with the Turton-Levenspiel Curve

A deviation from the Turton-Levenspiel curve is observed after Re_p value of 5. Usage of the Turton-Levenspiel curve in this approach would generate errors especially at high particle Reynolds number values. In order to circumvent this conundrum, a new correlation is presented based on the Cheng's five parameter C_D-Re_p correlation model for Newtonian fluids (Cheng, 2009).

$$C_D = \frac{24}{Re_p}(1 + ARe_p)^B + C(1 - \exp(-DRe_p{}^E)) \qquad 5.14$$

The constant parameters were determined using the Curve Fitting Toolbox from MATLAB (r2018b). The resulting equation becomes:

$$C_D = \frac{24}{Re_p}(1 + 0.12Re_p)^{0.35} + 0.398(1 - \exp(-0.01Re_p{}^{0.9282}) \qquad 5.15$$

Plotting the entire C_D-Re_p database with this proposed correlation results into the plot shown in Figure 5.11.

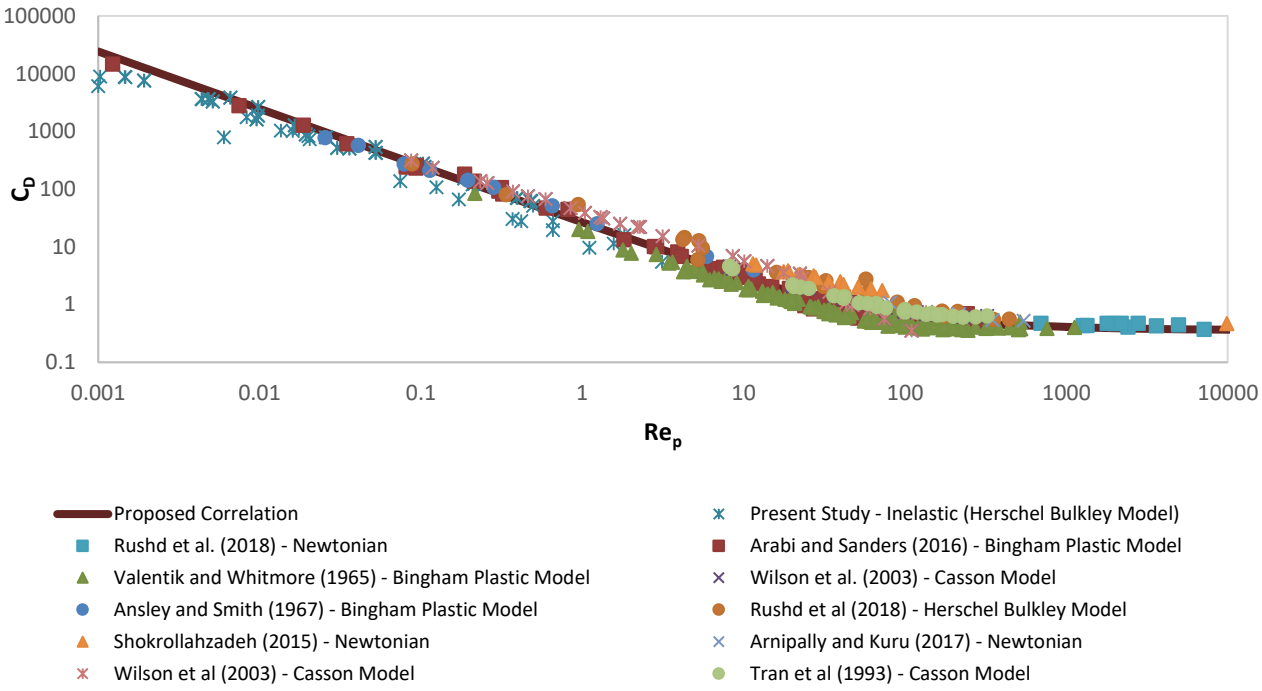

Figure 5.11: Plot of drag coefficient (C_D) vs particle Reynolds number (Re_p) with the New Correlation Curve Proposed by this Study

The Sum Squared of Errors (SSE) was the statistical parameter chosen to evaluate the C_D-Re_p curve based on each rheological model. The sum of Sum of Squared Errors (SSE) is a statistical parameter used to quantify errors associated with a particular model. It measures the variation between data and model prediction with lower SSE values indicating higher accuracy and model fit to the data. It is mathematically described by Equation 5.16.

$$SSE = \frac{\sum_1^n (C_{D_P} - C_{D_m})^2}{\sum_1^n (C_{D_m})^2} \quad 5.16$$

Where $C_{D_P}$the predicted is is drag coefficient and $C_{D_m}$is the measured drag coefficient. The SSE values of the plot (based on the different rheological models) are given in the

Table 5.4: C_D Vs Re_p Statistical Evaluation Results for Proposed Correlation

Rheological Model	SSE
Herschel-Bulkley	0.09
Bingham Plastic	0.89
Casson	0.87
Newtonian	0.48

There is a good match for viscoplastic fluids and Newtonian fluids (especially at high Reynolds number) data with a low average SSE of about 0.58. These low error values further support the potency of the proposed general correlation.

5.4.3 Developing the Generalized Model.

5.4.3.1 Developing the Vt/V* vs Re_T^* Plot.

In order to systematically explain how the new generalized model correlation is developed, the mechanistic fundamentals of particle settling as well as the Wilson *et al.* (2003) approach must be revisited and modified.

Making V_t subject of the formula from equation (5.1) gives:

$$V_t = \sqrt{\frac{4(\rho_s - \rho_f)dg}{3C_D\rho_f}} \tag{5.17}$$

Dividing V_t (Equation 19) by V^* (Equation 7), we have

$$\frac{V_t}{V^*} = \sqrt{\frac{8}{C_D}} \tag{5.18}$$

Note that the conventional particle Reynolds number Re_p (Equation 5.2) is equal to the product of Re* and V_t/V^* (Equations 5.8 and 5.18)

$$Re_p = Re^* * \frac{V_t}{V^*} = \frac{\rho_f V^* d}{\mu} * \frac{V_t}{V^*} = \frac{\rho_f V_t d}{\mu} \tag{5.19}$$

Therefore,

$$Re^* = \frac{Re_p}{\frac{V_t}{V^*}} = \frac{Re_p}{\sqrt{\frac{8}{C_D}}} \quad 5.20$$

Two major modifications are carried out in order to generalize this approach for viscoplastics fluids. The definition for Re* is modified from what Wilson et al. (2003) defined. A new shear Reynolds (Re_T^*) is introduced based on the modified Reynolds number.

$$Re_T^* = \frac{Modified\ Reynolds\ Number}{\frac{V_t}{V^*}} \quad 5.21$$

The equation for Re_T^* depends on the fluid model.

$$Re_{T-Bingham\ Plastic}^* = \frac{\frac{\rho_f (V_t) d}{\mu_B + \tau_B \left(\frac{d}{V_t}\right)}}{\frac{V_t}{V^*}} \quad 5.22$$

$$Re_{T-Casson}^* = \frac{\frac{\rho_f (V_t) d}{\mu_c + 1.205\tau_c \left(\frac{d}{V_t}\right)}}{\frac{V_t}{V^*}} \quad 5.23$$

$$Re^*_{T-HB} = \frac{\frac{\rho_f (V_t)^{2-n} d^n}{\tau_{HB}\left(\frac{d}{V_t}\right)^n + k}}{\frac{V_t}{V^*}} \qquad 5.24$$

While Wilson *et al.* (2003) used the C_D-Re_p correlation proposed by Turton and Levenspiel (1986) in their model, The C_D-Re_p correlation (equation 15) developed in this investigation is used for this model. Therefore the equation 18 becomes,

$$\frac{V_t}{V^*} = \sqrt{\frac{8}{\frac{24}{Re_p}(1 + 0.12Re_p)^{0.35} + 0.378(1 - \exp(-0.01{Re_p}^{0.9282})}} \qquad 5.25$$

The good thing about the C_D-Re_p correlation proposed in this study is that it collapses into the standard Newtonian curve at very high Reynolds numbers occluding the need to define region constants. By inputting various values of Re_p into equations 5.21 and 5.25, a new Vt/V* vs Re^*_T plot is formed shown in Figure 5.12

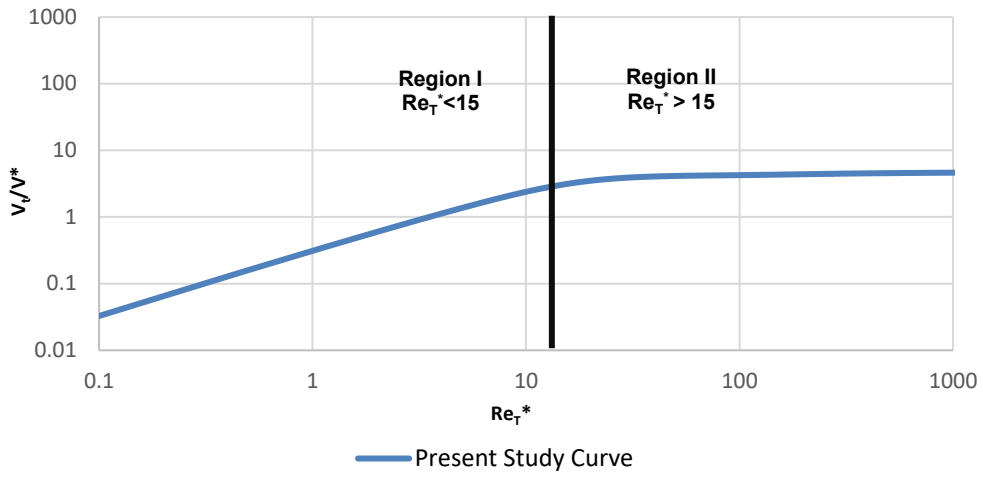

Figure 5.12: V_t/V^* vs Re_T^*

The Non-Linear curve fit function of Origin Pro 9.0 software was used to fit the two regions of the resulting plot.

Region 1

$$\frac{V_t}{V^*} = 5.0286\left[1 - e^{(-0.064Re_T^*)}\right] \quad 5.26$$

Region 2

$$\frac{V_t}{V^*} = e^{\left(1.4962 - \frac{3.741}{Re_T^* - 4.816}\right)} \quad 5.27$$

Plotting the new Vt/V* vs Re_T^* curve with the entire database (Ansley & Smith, 1967; Arabi & Sanders, 2016; Arnipally & Kuru, 2017; Rushd et al., 2018; Shokrollahzadeh, 2015; Valentik & Whitmore, 1965; Wilson et al., 2003) gives the plot shown in Figure 5.13

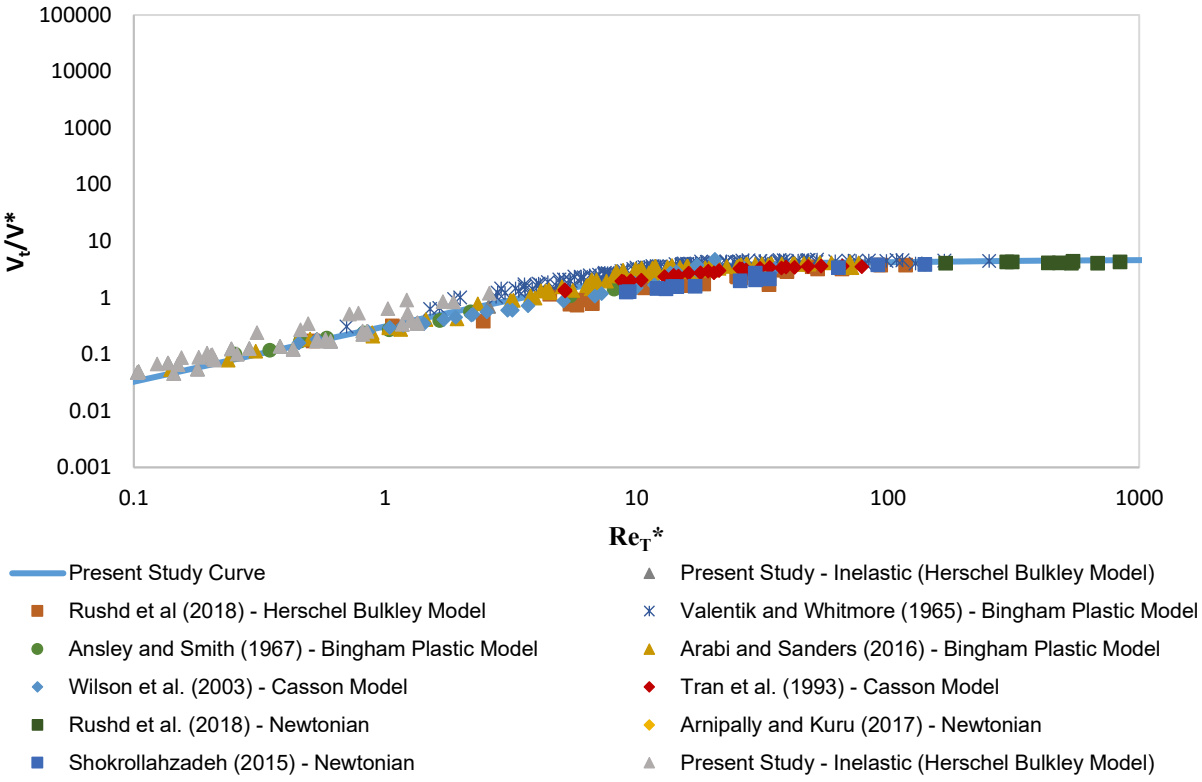

Figure 5.13: V_t/V^* vs Re_T^* with entire data base.

The resulting plot gives a good fit (R^2 values shown in the next section) for entire database of almost 400 points, irrespective of the rheological model of the fluid. This further buttresses the use of Vt/V* vs Re_T^* plot as a universal tool for predicting settling velocity in various models.

5.4.3.2 Direct Method to Predict Velocity

At a glance, the presented model above seems implicit due to the presence of V_t on both axes. However, it was empirically ascertained that Re_T^* is a function of the following V_t exclusive parameters:

Relative characteristic shear stress, ξ: (analogous to wall shear stress, τ_w in Pipe flow), which is defined as the as the ratio of fluid yield stress to the characteristic shear stress of the system. It was introduced by Wilson and Thomas (1985) and it is mathematically defined as;

$$\xi = \frac{\tau_y}{\tau} \tag{5.28}$$

Shape Factor, α: A model independent parameter also introduced by Wilson and Thomas (1985). It is defined as the ratio of the entire area of a fluids rheogram to the area of Newtonian region of that rheogram (Wilson & Thomas, 1985). The shape factor quantifies the Newtonian deviation of a viscoplastic fluid. A schematic is shown in Figure 5.14 below; where α=1 indicates a Newtonian fluid and α = 2 represents a pure plastic solid. It is mathematically defined as;

$$\alpha = 1 + \frac{\tau_y}{\tau} = 1 + \xi \tag{5.29}$$

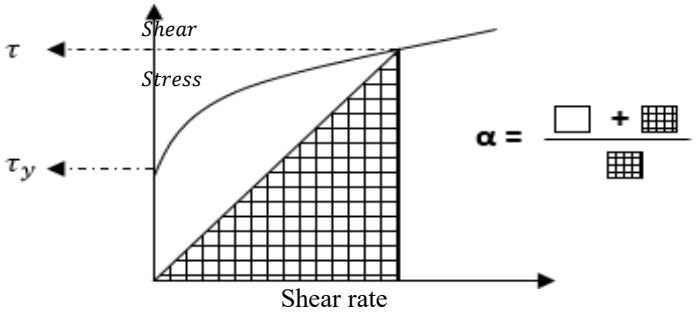

Figure 5.14: Schematic Description of Shape Factor,

A modified shear Reynolds number, Re_G^* presented by Rushd *et al* (2018). They presented a parameter for Herschel Bulkley fluids that involved replacing all the V_t terms by V* in the modified Reynolds number presented by Machač *et al* (1995) in equation (5.5). This is shown for Herschel Bulkley fluid model in the Equation 30 below.

$$Re_{G-HB}^* = \frac{\rho_f (V^*)^{2-n} d^n}{\tau_{HB} \left(\frac{d}{V^*}\right)^n + k} \quad 5.30$$

And also the shear Reynolds number.

$$Re_T^* = f\{Re_G^*, Re^*, \alpha, \xi\} \quad 5.31$$

The Re_T^* quantifies non-Newtonian deviation based on the α and ξ parameters and then with the aid of Re_G^*, collapses this deviation on the Newtonian curve. The regression analysis function from OriginPro 9.0 was utilized to fit a multivariable model and mathematically define Re_T^* based on the value of the fluid's shape factor.

For values of α < 1.3

$$Re_T^* = 0.7015 {Re_G^*}^{1.3692} {Re^*}^{0.2958} \alpha^{-3.2294} \xi^{0.26674} \quad 5.32$$

For values of α > 1.3

$$Re_T^* = 4.1 * 10^{-8} {Re_G^*}^{-0.815} {Re^*}^{0.7579} \alpha^{18.637} \xi^{-8.7519} \quad 5.33$$

The 1.3 boundary was chosen because it was reported by Shokrollahzadeh that significant changes in non-Newtonian fluid behavior were observed as α values become larger than 1.3 (Shokrollahzadeh, 2015). This is also in unison with the simulation results presented by Prashant and Derksen (2011), who reported an increase in unyielded zones or plasticity surrounding a falling particle in a viscoplastic fluid as the yield stress increases; which is analogous with the increase in shape factor α (Arabi & Sanders, 2016). The 1.3 value was further bolstered by empirical and statistical experimental results in this study. Furthermore, a corrective factor of 2.08854 (obtained from data fitting) is used for yield stress and consistency index for parameters in equations 32 and 33 for Herschel Bulkley fluid model only (as shown in Appendix B).

5.4.3 Statistical Evaluation.

Statistical parameters were used for comparative analysis of the two models to further authenticate the accuracy of the presented generalized model. Coefficient of determination (R^2), which depicts the accuracy of the model fit with actual measured data (Eq. 5.34). It shows the deviations of the measured and predicted values. R^2 ranges from 0-1. Higher R^2 values portray less scatter and deviation from the predicted values of a specific model. The results are shown in Table 5.5

$$R^2 = 1 - \frac{\sum_1^n (V_{tp} - V_{tm})^2}{\sum_1^n (V_{tp} - \overline{V_{tm}})^2} \qquad 5.34$$

The Root Mean Square Error (RMSE) which quantifies deviation between measured and predicted values of models. It depicts the error of the associated model. The lower the value of RMSE the more accurate the model. The results are shown in Table 5.6.

$$RMSE = \sqrt{\frac{\sum_1^n (V_{tp} - V_{tm})^2}{n}} \quad 5.35$$

The Percentage Mean Absolute Error (PMAE) expresses the mean absolute error in percentage. It depicts the expected percentage error associated with a specific model. Hence the lower the value, the more accurate the model. Its equation is shown below. The results are shown in Table 5.7.

$$PMAE = \frac{\frac{1}{n}\sum_1^n |V_{tm} - V_{tp}|}{\frac{1}{n}\sum_1^n |V_{tm}|} * 100 \quad 5.36$$

In Equations 5.34 – 5.36, n is the number of data points, V_{tp} is the predicted settling velocity, V_{tm} is the measured settling velocity, $\overline{V_{tm}}$ is the average of measured velocities. The performance of the current model is juxtaposed with other models and the results are presented in Tables 5.5-5.7.

5.5: R^2 Model Comparison

Coefficient of Determination (R^2)	
Wilson et al. (2003)	Present Study
0.84	0.89

5.6: RMSE Model Comparison

Root Mean Square Error (RMSE) – m/s	
Wilson et al. (2003)	Present Study
0.47	0.37

5.7: PMAE Model Comparison

Percentage Mean Absolute Error (PMAE) %	
Wilson et al. (2003)	Present Study
40.0	24.5

5.8: Newtonian Statistical Results

Statistical Parameter	Newtonian Fluids
	Present Study
R^2	0.96
RMSE (m/s)	0.10
PMAE (%)	9.8

From the statistical results presented above, the presented generalized model offered prediction versatility for all three rheological viscoplastic models (Tables 5.5-5.7) and still provides reasonable accuracy for Newtonian fluids (Table 5.8) especially at high Reynolds number as shown in Figure 5.9. For Table 5.5, the generalized model exhibited the better R^2 value indicating good correlation fit. Table 5.6 shows the results of Root Mean Square Error (RMSE) analysis while Table 5.7 shows the results of the Percentage Mean Absolute Error (PMAE) analysis. On an average, the generalized model gave a lower standard error than the other model (Tables 5.5-5.7) and exhibited the lowest average PMAE of about 24.5% (Table 5.6 and 5.7).

Note that the Wilson et al. (2003) model was unable to provide predictions for over 60 fluid particle systems due to $\tau_y > 0.3\,\bar{\tau}$. These fluid particle systems were proficiently handled and predicted using the generalized approach presented in this study. A major constraint from the models listed above was the poor predictability at low shear Reynolds number (laminar settling), which the authors recommended must be further investigated (Arabi & Sanders, 2016; Rushd et al., 2018; Wilson et al., 2003). Using the generalized approach presented in this study, as shown in Figure 5.15 V_t/V^* vs Re_T^* plot can provide relatively accurate predictions of particle settling behavior in viscoplastic fluids even at laminar flow conditions.

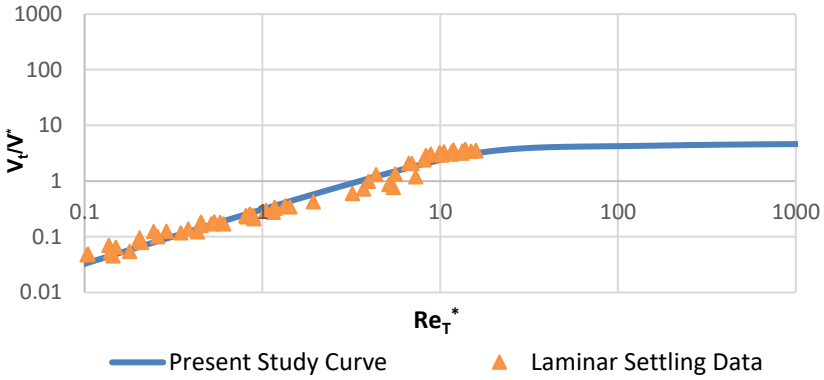

Figure 5.15: V_t/V^* vs Re_T^* for particle settling in viscoplastic fluids under laminar flow conditions.

This good prediction of the generalized model at low shear Reynolds number is as a result of the relatively larger database, developed C_D-Re_p curve coupled with behavior of viscoplastic fluids at laminar conditions. From a rheological perspective, creeping laminar settling occurs in or close to the Stokes region. The effect of inertia is negligible compared to viscosity in this region, hence a relatively simplistic relationship occurs between C_D and Re_p (Chhabra, 2006; Stokes, 1905).

5.4.4 The Settling Behavior of Spheres in Elastic Yield Stress Fluids.

The settling velocity of various spherical particles in elastic yield stress fluids were measured in order to examine the effects of elasticity on the settling behavior of these particles. Multiple Carbopol 940 polymer solutions were prepared, which have been shown in the fluid property section to exhibit elastic property. The results of the settling velocity experiments are presented in Table A-2 of the appendix section, which even include fluids similar elastic property with varying viscous yield properties.

5.4.4.1 Assessing the Generalized Drag Curve's Performance on Elastic Yield-Stress Fluids

The settling velocity data in elastic yield stress fluids from this present study (obtained from the settling velocity experiments in Carbopol 940 presented in Table A-2) were plotted on the drag curve (Figure 5.11) developed in this study in order to observe any deviation or coherence with the presented correlation (Equation 5.15).

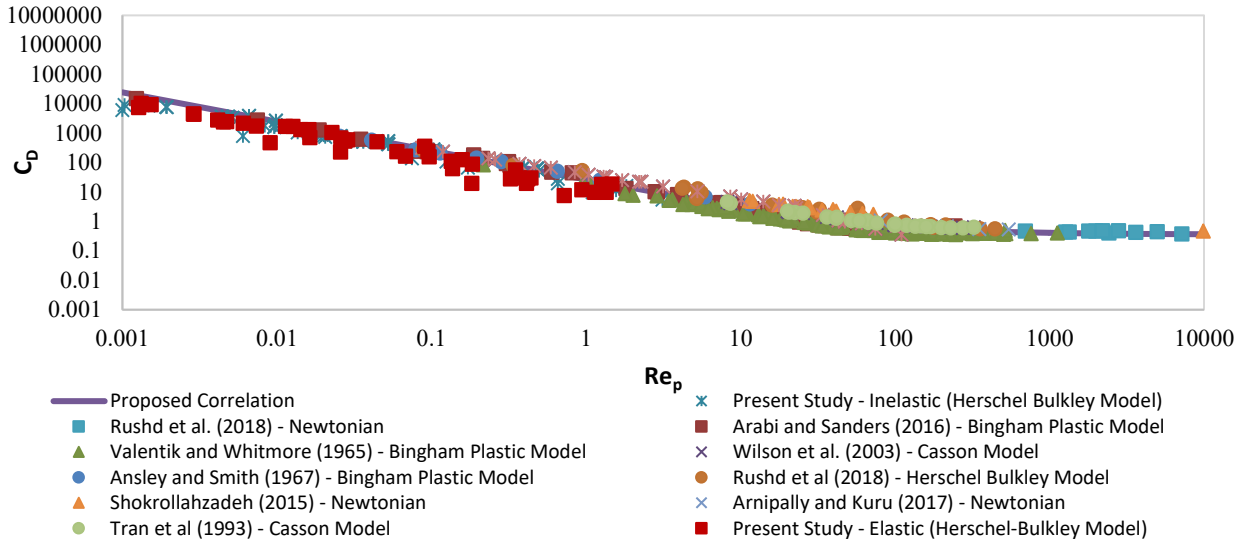

Figure 5.16: Proposed Drag Curve Including Settling Velocity Data in Elastic Yield Stress Fluids.

From Figure 5.16, reasonable match was found between the settling velocity data obtained in the elastic yield stress fluids and our proposed model (Equation 5.15). This further authenticates the potency of the generalized model to offer reasonable drag prediction even for elastic yield stress fluids. Unlike the power-law pseudoplastic fluids where the presence of elasticity is evident in the settling behavior of the particles (van den Brule and Gheissary, 1993; Malhotra and Sharma, 2012a; Arnipally and Kuru, 2018), in viscoplastic fluids the presence of a yield stress may overshadow the elastic property of the fluid leading to uniformity in settling behavior. Statistical

analysis showed that the presented drag curve correlation gave a low Squared Sum of Error (SSE) of 0.1 for the elastic drag curve. In order to prevent the effects of inertia and mainly focus on fluid property effects (Clift, Grace and Weber, 1978; Chhabra, 2006); only low velocity Reynolds number were investigated for the elastic fluids in this study.

5.4.4.2 Assessing the Generalized Vt/V* vs Re_T^* Curve's Performance on Elastic Yield-Stress Fluids

Similar to the proposed drag curve's correlation, the performance of the presented Vt/V* vs Re_T^* plot for predicting settling velocity was also examined on the elastic yield stress fluids. The settling velocity data (Table A-2) were plotted on the Vt/V* vs Re_T^* plot (Figure 5.13) to observe if there is any coherence or disparity and the combined results are shown in Figure 5.17.

Comparable to the proposed drag curve's performance, there was a very reasonable match between the proposed correlation and elastic yield stress fluids' data (Table A-2) as shown in Figure 5.17. The proposed correlation predicted settling velocity in elastic yield stress fluids with good accuracy. Statistical analysis showed that the generalized model gave a Percentage Mean Absolute Error of 30.15 % and Root Mean Square Error (RMSE) of 0.02 m/s for the elastic yield stress fluids.

The generalized correlation curve for predicting settling velocity in viscoplastic fluids can also be applied to elastic yield stress fluids. While it is experimentally proven and factual that elasticity can retard settling velocity in certain non-Newtonian fluids (Chhabra, Uhlherr and Boger, 1980; Walters and Tanner, 1992; Malhotra and Sharma, 2012b; Arnipally and Kuru, 2018), the yield stress may have a more prominent influence than elasticity on the settling behavior of particle if

both forces are acting simultaneously on a particle, which is further bolstered by the data shown in Table A-2, which include particle settling velocity data in fluids with similar elastic property (relaxation time) and varying viscous yield properties (vice versa as well).

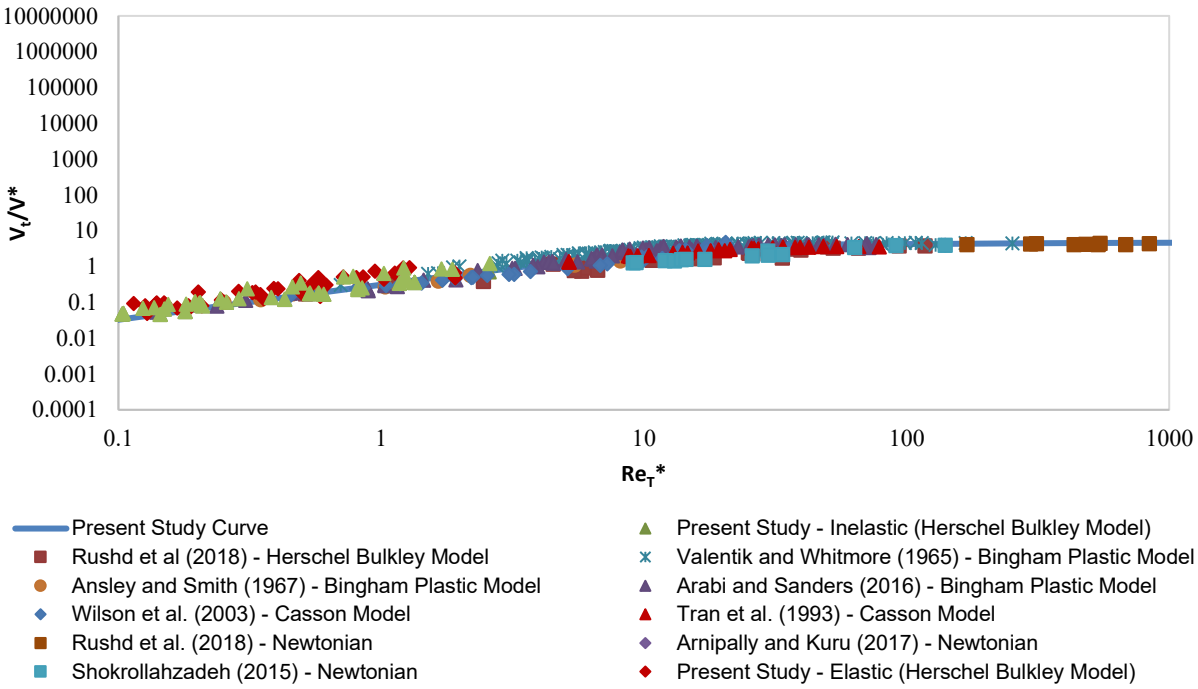

Figure 5.17: V_t/V^* vs Re_T^* curve Including Settling Velocity Data in Elastic Yield Stress Fluids.

The yield stress is related to the strength of the internal structure of the fluid causing it to act stiff or solid-like until the applied force exceeds the strength of the internal structure, thereby, engendering the fluid deformation. This sturdy internal structure of the fluid imposes a drag on the settling particle, which gradually dampens the stress imposed on the fluid by the settling particle and in extension dampens the settling velocity.

5.5 Conclusions

A comprehensive experimental and empirical study was conducted to investigate the settling behavior of spherical particles in elastic and inelastic yield stress fluids using Particle Image Shadowgraphy (PIS). Over 90 different fluid-particle systems were investigated to augment the current corpus of experimental data. The experimental results were amalgamated with published data to produce a versatile C_D-Re_p curve with the aid of MATLAB (r2018b) curve fitting function.

A modified generalized shear Reynolds number Re_T^*, which quantifies the effect of non-Newtonian deviation on settling velocity was introduced and integrated with the developed C_D-Re_p curve to generate an improved universal model for predicting settling velocity based on the Wilson *et al.* (2003) approach. The model is applicable to a yield stress range of 0 - 6.6 Pa, consistency index (k) range of 0.15 - 2.1 Pa.s^n and a fluid behavior index (n) range of 0.4 – 0.9 for Herschel Bulkley fluids and a yield stress range of 1 – 60 Pa for Bingham and Casson fluids.

A statistical juxtaposition between the generalized model and other present models showed that the generalized model exhibited model independent versatility, on an average gave a lower standard error than the other models and exhibited the lowest average PMAE of about 24.5 %. It was also shown that the model provides reasonable prediction for settling velocity in Newtonian fluids with a low Root Mean Square Error of 0.1m/s.

The proposed generalized model was further assessed with elastic yield stress fluids in order to examine the effects of elasticity on the settling behavior of particles and to evaluate its prediction performance. The generalized model was able to provide settling velocity prediction for the elastic yield stress fluids with reasonable accuracy achieving a very low Percentage Mean Absolute Error

of 30.15 % and Root Mean Square Error (RMSE) of 0.02 m/s. While elasticity reduces the settling velocity in certain non-Newtonian fluids; however in viscoplastic fluids the presence of a yield stress may eclipse the elastic inhibiting property of the fluid leading to uniformity in settling behavior which can be predicted with the generalized model.

Regardless of the positive statistical result, additional research is imperative to corroborate and improve the accuracy of the generalized model at extensive conditions including dynamic and hindered settling conditions, which were not tested in this study. It is also recommended to investigate the effect of thixotropic aging on the settling velocity.

5.6 Acknowledgment

This research is financially supported by the funds available from the Natural Sciences and Engineering Research Council of Canada (NSERC RGPIN-2016-04647 KURU).

5.7 Nomenclature

Symbol	Description	Unit
C_D	Drag coefficient	-
Re*	Shear Reynolds number	-
Re_T^*	Present study's modified shear Reynolds number	-
Re_G^*	Rushd et al. modified shear Reynolds number	-
Re_p	Particle Reynolds number	-
V_t	Terminal settling velocity	m/s
$V*$	Particle shear velocity	m/s
V_{tm}	Measured settling velocity	m/s
V_{tp}	Predicted terminal settling velocity	m/s
α	Rheogram shape factor	-
$\dot{\gamma}$ or γ	Shear rate	s^{-1}
C_{DP}	Predicted drag coefficient	-
C_{Dm}	Measured drag coefficient	-
μ	Viscosity	Pa.s
μ_B	Bingham plastic viscosity	Pa.s
μ_c	Casson plastic viscosity	Pa.s
ξ	Relative shear stress	-
ρ_s	Particle (sphere) density	kg/m^3
ρ_f	Fluid density	kg/m^3
τ or τ_y	Shear stress	Pa
$\bar{\tau}$	Mean surficial stress on a falling sphere	Pa
τ_B	Bingham yield stress	Pa
τ_{HB}	Herschel-Bulkley yield stress	Pa
τ_c	Casson yield stress	Pa
k	Herschel-Bulkley consistency index	$Pa.S^n$
n	Herschel-Bulkley flow behaviour index	-
g	Acceleration due to gravity	m/s^2

Appendix A – Experimental Results

The experimental results obtained in this study are presented in this section. Table A-0 represents rheological data obtained from the Fann Viscometer as well as the relaxation times for all experimental test fluids. Table A-1 represents data for inelastic yield stress fluids and Table A-2 represents data for elastic yield stress fluids.

Table A-0: Experimental Fluids' Data (Prefix 1 Signifies Inelastic Yield Stress Fluids While Prefix 2 Signifies Elastic Yield Stress Fluids).

Fluid Samples	Composition	Fann Viscometer Dial Readings (°)						Relaxation Time (s)
		600	300	200	100	6	3	
1A	Carbopol ETD 2020 (0.035 wt. %)	40	27	25	12	2.5	2	0.2
1B	Carbopol ETD 2020 (0.050 wt. %)	72	50.5	41	29	11	6	0.2
1C	Carbopol ETD 2020 (0.046 wt. %)	60.5	41.5	33	23	7	4	0.2
1D	Carbopol ETD 2020 (0.046 wt. %)	55	33	25.5	16	3	2	0.3
1E	Carbopol ETD 2020 (0.050 wt. %)	71.5	44	34	22.5	4.5	3	0.4
1F	Carbopol ETD 2020 (0.051 wt. %)	57.5	40	32	22.5	7	4.5	0.2
1G	Carbopol ETD 2020 (0.045 wt. %)	31.5	20.5	15.5	10	2.5	1.5	0.3
1H	Carbopol ETD 2020 (0.055 wt. %)	99.5	72	59.5	43	16	11	0.5
1I	Carbopol ETD 2020 (0.038 wt. %)	43	28.5	22	14.5	4.5	3	0.2
1J	Carbopol ETD 2020 (0.060 wt. %)	96	69.5	57	41	23	13	0.2
1K	Carbopol ETD 2020 (0.060 wt. %)	96	68	56	40	15	10	0.2
1L	Carbopol ETD 2020 (0.04 wt. %)	48.5	32.5	26	18	5.5	3.5	0.1
2A	Carbopol 940 (0.065 wt. %)	48.5	32.5	26	17.5	5.5	3.5	125
2B	Carbopol 940 (0.060 wt. %)	64	44	36	25	8	6.5	30
2C	Carbopol 940 (0.075 wt. %)	95	63	51	37	15	12	230
2D	Carbopol 940 (0.040 wt. %)	43	28.5	22	14.5	4.5	3	47
2E	Carbopol 940 (0.055wt. %)	47	31.5	25.5	17.5	6	3.5	35

Table A-1: Inelastic Yield Stress Fluids' Experimental Database

No.	Fluid Sample	d (m)	ρ_f (kg/m^3)	ρ_s (kg/m^3)	τ_y (Pa)	K (Pa.S^n)	n	V_{tm} (m/s)	V_{tp} (m/s)	Relaxation Time (s)
1	1A	0.004	999.2	2510	0.048	0.460	0.587	0.023	0.020	0.2
2		0.0035	999.2	2510	0.048	0.460	0.587	0.016	0.014	
3		0.003	999.2	2510	0.048	0.460	0.587	0.011	0.009	
4		0.002	999.2	2510	0.048	0.460	0.587	0.004	0.003	
5		0.00118	999.2	2510	0.048	0.460	0.587	0.003	0.002	
6	1B	0.004	1004.7	2510	0.472	0.999	0.518	0.008	0.009	0.2
7		0.0035	1004.7	2510	0.472	0.999	0.518	0.006	0.006	
8		0.003	1004.7	2510	0.472	0.999	0.518	0.004	0.004	
9	1C	0.004	999.2	2510	0.958	0.580	0.569	0.012	0.013	0.2
10		0.0035	999.2	2510	0.958	0.580	0.569	0.009	0.009	
11		0.003	999.2	2510	0.958	0.580	0.569	0.006	0.005	
12	1D	0.004	998.0	2510	0.520	0.181	0.725	0.034	0.042	0.3
13		0.0035	998.0	2510	0.520	0.181	0.725	0.024	0.029	
14		0.003	998.0	2510	0.520	0.181	0.725	0.016	0.019	
15		0.002	998.0	2510	0.520	0.181	0.725	0.006	0.005	
16		0.0015	998.0	2510	0.520	0.181	0.725	0.003	0.002	
17		0.00118	998.0	2510	0.520	0.181	0.725	0.002	0.003	
18	1E	0.00245	998.0	7700	0.768	0.297	0.691	0.059	0.074	0.4
19		0.004	998.0	2510	0.768	0.297	0.691	0.018	0.021	

20		0.0035	998.0	2510	0.768	0.297	0.691	0.013	0.014	
21		0.003	998.0	2510	0.768	0.297	0.691	0.009	0.009	
22		0.002	998.0	2510	0.768	0.297	0.691	0.003	0.007	
23		0.0015	998.0	2510	0.768	0.297	0.691	0.002	0.002	
24		0.00118	998.0	2510	0.768	0.297	0.691	0.001	0.001	
25		0.00245	998.0	7700	0.768	0.297	0.691	0.059	0.074	
26	1F	0.0013	994.0	5900	1.073	0.601	0.556	0.009	0.006	0.2
27		0.00155	994.0	5900	1.073	0.601	0.556	0.011	0.010	
28		0.00185	994.0	3860	1.073	0.601	0.556	0.006	0.005	
29		0.00218	994.0	3860	1.073	0.601	0.556	0.009	0.009	
30		0.00258	994.0	3860	1.073	0.601	0.556	0.030	0.014	
31	1G	0.00109	995.0	5900	0.399	0.158	0.664	0.016	0.017	0.3
32		0.00129	995.0	5900	0.399	0.158	0.664	0.026	0.027	
33		0.00155	995.0	5900	0.399	0.158	0.664	0.044	0.045	
34		0.00185	995.0	3860	0.399	0.158	0.664	0.050	0.030	
36		0.00218	995.0	3860	0.399	0.158	0.664	0.080	0.050	
37	1H	0.00258	996.0	3860	2.871	1.429	0.507	0.003	0.003	0.5
38		0.004	996.0	2510	2.871	1.429	0.507	0.003	0.003	
39		0.0035	996.0	2510	2.871	1.429	0.507	0.002	0.002	
40		0.0024	996.0	7700	2.871	1.429	0.507	0.017	0.016	
41	1I	0.0020	999	2510	0.879	0.232	0.652	0.06	0.01	0.2
42	1J	0.0020	1000.0	2510	6.488	2.115	0.577	0.009	0.00	0.2

43		0.0030	1000.0	2510	6.488	2.115	0.577	0.0035	0.00	
44	1K	0.004	998.0	2510	6.646	0.783	0.550	0.009	0.001	0.2
45		0.00258	998.0	3860	6.646	0.783	0.550	0.004	0.001	
46		0.0025	998.0	7700	6.646	0.783	0.550	0.040	0.010	
47	1L	0.003	997	2510	1.089	0.347	0.609	0.025	0.015	0.1
48		0.0035	997	2510	1.089	0.347	0.609	0.055	0.020	
49		0.004	997	2510	1.089	0.347	0.609	0.064	0.021	
50		0.00218	997	3860	1.089	0.347	0.609	0.052	0.013	
51		0.00258	997	3860	1.089	0.347	0.609	0.098	0.030	
52		0.0025	997	7700	1.089	0.347	0.609	0.180	0.110	

Table A-2: Elastic Yield Stress Fluids' Experimental Database

No.	Fluid Sample	d (m)	ρ_f (kg/m^3)	ρ_s (kg/m^3)	τ_y (Pa)	K (Pa.S^n)	n	V_{tm} (m/s)	V_{tp} (m/s)	Relaxation Time (Sec)
1	2A	0.0015	999.0	2510	1.089	0.347	0.609	0.002	0.001	125
2		0.0020	999.0	2510	1.089	0.347	0.609	0.004	0.002	
3		0.0030	999.0	2510	1.089	0.347	0.609	0.016	0.015	
4		0.00185	999.0	3860	1.089	0.347	0.609	0.050	0.080	
5		0.00218	999.0	3860	1.089	0.347	0.609	0.052	0.013	
6		0.00258	999.0	3860	1.089	0.347	0.609	0.090	0.030	
7		0.00130	999.0	5900	1.089	0.347	0.609	0.008	0.008	
8		0.00129	999.0	5900	1.089	0.347	0.609	0.007	0.008	
9		0.00155	999.0	5900	1.089	0.347	0.609	0.030	0.020	
10		0.0022	999.0	5900	1.089	0.347	0.609	0.050	0.042	
11		0.0025	999.0	7700	1.089	0.347	0.609	0.110	0.110	
12	2B	0.0015	997.0	2510	1.881	0.569	0.576	0.003	0.001	30
13		0.0020	997.0	2510	1.881	0.569	0.576	0.004	0.001	
14		0.0030	997.0	2510	1.881	0.569	0.576	0.006	0.002	
15		0.0035	997.0	2510	1.881	0.569	0.576	0.009	0.004	
16		0.0040	997.0	2510	1.881	0.569	0.576	0.020	0.010	
17		0.00185	997.0	3860	1.881	0.569	0.576	0.010	0.003	
18		0.00218	997.0	3860	1.881	0.569	0.576	0.008	0.006	
19		0.00258	997.0	3860	1.881	0.569	0.576	0.045	0.020	

20		0.00129	997.0	5900	1.881	0.569	0.576	0.005	0.005	
21		0.00155	997.0	5900	1.881	0.569	0.576	0.010	0.014	
22		0.0022	997.0	5900	1.881	0.569	0.576	0.022	0.020	
23		0.0020	997.0	2711	1.881	0.569	0.576	0.005	0.002	
24		0.0020	997.0	7700	1.881	0.569	0.576	0.070	0.030	
25	2C	0.0040	1006.0	2510	5.225	0.452	0.658	0.003	0.001	230
26		0.00258	1006.0	3860	5.225	0.452	0.658	0.040	0.014	
27		0.00250	1006.0	7700	5.225	0.452	0.658	0.030	0.012	
28		0.0020	1006.0	7700	5.225	0.452	0.658	0.014	0.010	
29		0.0025	1006.0	7700	5.225	0.452	0.658	0.040	0.011	
30		0.0020	1006.0	7700	5.225	0.452	0.658	0.013	0.010	
31	2D	0.0020	999	2510	0.879	0.232	0.652	0.032	0.010	47
32	2E	0.0015	999.0	2510	1.219	0.200	0.677	0.001	0.001	35
33		0.002	999.0	2510	1.219	0.200	0.677	0.003	0.002	
34		0.003	999.0	2510	1.219	0.200	0.677	0.010	0.011	
36		0.0035	999.0	2510	1.219	0.200	0.677	0.020	0.018	
37		0.00185	999.0	3860	1.219	0.200	0.677	0.010	0.010	
38		0.00218	999.0	3860	1.219	0.200	0.677	0.052	0.020	
39		0.00258	999.0	3860	1.219	0.200	0.677	0.020	0.029	
40		0.0013	999.0	5900	1.219	0.200	0.677	0.008	0.011	
41		0.00129	999.0	5900	1.219	0.200	0.677	0.007	0.011	
42		0.00155	999.0	5900	1.219	0.200	0.677	0.014	0.019	

Appendix B – Settling Velocity Calculation Procedure and Example

Steps in Calculating Terminal Settling Velocity

VII. Calculate mean surficial stress, $\bar{\tau}$

VIII. Particle Shear Velocity, V^*

IX. Using $\bar{\tau}$, calculate shear rate and viscosity* based on rheological model.

X. Determine shear Reynolds number and generalized shear Reynolds number

XI. Calculate shape factor and relative characteristics shear stress

XII. Calculate Re_T^* based on the value of shape factor and use it to determine V_t/V^*.

XIII. Finally, multiply Vt/V* by V* calculated in step II to determine the Terminal Settling Velocity.

*Note that if the rheological model has defined its viscosity in a specific way, use that mathematical definition.

Example Calculation of Particle Settling Velocity in Herschel Bulkley Type Fluid (Comparison versus the measured data using present study experimental set-up)

Data

Diameter of Particle, d = 3.5 mm = 0.0035m

Density of Particle, ρ_s = 2510 kg/m^3

Density of Fluid, ρ_f= 1004.67 kg/m^3

Yield Stress, τ_y= 0.4721 Pa (0.9861 lbf/100 ft^2)

k = 0.9989 Pa.S^n (2.0862 lbf•s^n/100 ft^2)

n = 0.5183

Relaxation Time = 0.2 Sec.

Steps

I. $Mean\ Surficial\ Stress,\ \bar{\tau} = \frac{dg\ (\rho_s - \rho_f)}{6} = 8.6143\ Pa$

II. $Particle\ Shear\ velocity, V^* = \sqrt{\frac{\bar{\tau}}{\rho_f}} = 0.0926$

III. $HB\ Shear\ rate, \gamma = \left[\frac{\bar{\tau}-\tau_y}{k}\right]^{\frac{1}{n}} = 57.283\ 1/s$

$HB\ Viscosity, \mu = \frac{\bar{\tau}}{\gamma} = 0.1504\ Pa.s$

IV. $Re^* = \frac{d\rho_f V^*}{\mu} = 2.1652$

$$Re_G^* = \frac{d^n (V^*)^{2-n} \rho_f}{2.08854\left(\tau_y \left(\frac{d}{V^*}\right)^n + K\right)} = 0.6958$$

V. $\xi = \frac{2.08854\tau_y}{\bar{\tau}} = 0.1145$

$\alpha = 1 + \varepsilon = 1.1145$

VI. Since α<1.3

$Re_T^* = 0.7015 Re_G^{*\,1.3692} Re^{*0.2958} \alpha^{-3.2294} \xi^{0.26674} = 0.211$

Using Region I, since $Re_T^* < 15$

$\frac{V_t}{V^*} = 5.0286\left[1 - e^{(-0.064 Re^{T*})}\right] = 0.06742$

VII. Predicted Settling Velocity, Vt $= \frac{V_t}{V^*} * V^* = 0.06742 * 0.0926 = \mathbf{0.00624\ m/s}$

Measured Settling Velocity $= \mathbf{0.00605\ m/s}$

Error = 3.61 %

Example Calculation of Particle Settling Velocity in Bingham Plastic Type Fluid

(Comparison versus the measured data using present study experimental set-up)

Data

Diameter of Particle, d = 19 mm = 0.019m

Density of Particle, ρ_s = 2790 kg/m^3

Density of Fluid, ρ_f= 1303 kg/m^3

Yield Stress, τ_y= 16.9 Pa

μ_p = 0.1 Pa.s

Steps

I. $Mean\ Surficial\ Stress,\ \bar{\tau} = \frac{dg\ (\rho_s - \rho_f)}{6} = 46.194\ pa$

II. $Particle\ Shear\ velocity, V^* = \sqrt{\frac{\bar{\tau}}{\rho_f}} = 0.188$

III. $HB\ Shear\ rate, \gamma = \left[\frac{\bar{\tau} - \tau_y}{\mu_p}\right] = 292.94\ 1/s$

$HB\ Viscosity, \mu = \frac{\bar{\tau}}{\gamma} = 0.158\ Pa.s$

IV. $Re^* = \frac{d\rho_f V^*}{\mu} = 29.560$

$$Re_G^* = \frac{\rho_f (V^*) d}{\mu_B + \tau_B \left(\frac{d}{V^*}\right)} = 2.5819$$

V. $\xi = \frac{\tau_y}{\bar{\tau}} = 0.365851$

$\alpha = 1 + \varepsilon = 1.365851$

VI. Since α>1.3

$Re_T^* = 4.1 * 10^{-8} {Re_G^*}^{-0.815} {Re^*}^{0.7579} \alpha^{18.637} \xi^{-8.7519} = 0.5467$

Using Region I, since $Re_T^* < 15$

$$\frac{V_t}{V^*} = 5.0286\left[1 - e^{\left(-0.064 Re^{T*}\right)}\right] = 0.1728$$

VII. Predicted Settling Velocity, Vt $= \frac{V_t}{V^*} * V^* = 0.1728 * 0.1888 = \mathbf{0.033\ m/s}$

Measured Settling Velocity $= \mathbf{0.035\ m/s}$

Error = 5.71 %

Appendix C – MATLAB Codes for Correlation Development

```
function [fitresult, gof] = createFit(f, g)
%CREATEFIT(F,G)
%  Create a fit.
%
%  Data for 'untitled fit 1' fit:
%      X Input : f
%      Y Output: g
%  Output:
%      fitresult : a fit object representing the fit.
%      gof : structure with goodness-of fit info.
%
%  See also FIT, CFIT, SFIT.

%  Auto-generated by MATLAB on 22-Nov-2018 16:20:00



%% Fit: 'untitled fit 1'.
[xData, yData] = prepareCurveData( f, g );

% Set up fittype and options.
ft = fittype( '((24/x)*(1+(a*x^b)))+(c*(1-exp(-d*x^e)))',
'independent', 'x', 'dependent', 'y' );
opts = fitoptions( 'Method', 'NonlinearLeastSquares' );
opts.Display = 'Off';
opts.Lower = [0.11 0.35 0.35 0.01 0.9282];
opts.Robust = 'Bisquare';
```

```
opts.StartPoint = [0.0851943304994446 0.137730234638915
0.534239479077962 0.01 0.706046088019609];
opts.Upper = [1 0.4 0.358 0.02 0.9282];

% Fit model to data.
[fitresult, gof] = fit( xData, yData, ft, opts );

% Plot fit with data.
figure( 'Name', 'untitled fit 1' );
h = plot( fitresult, xData, yData );
legend( h, 'g vs. f', 'untitled fit 1', 'Location', 'NorthEast'
);
% Label axes
xlabel f
ylabel g
grid on
```

References

Ansley, R. W., & Smith, T. N. (1967). Motion of spherical particles in a Bingham plastic. *AIChE Journal*, *13*(6), 1193–1196. https://doi.org/10.1002/aic.690130629

API. (2006). API Recommended Practice 13D, Recommended Practice on the Rheology and Hydraulics of Oil-Well Drilling Fluids, (5th ed.).

Arabi, A. S., & Sanders, R. S. (2016). Particle terminal settling velocities in non-Newtonian viscoplastic fluids. *Canadian Journal of Chemical Engineering*, *94*(6), 1092–1101. https://doi.org/10.1002/cjce.22496

Arnipally, S. K., & Kuru, E. (2017). Settling Velocity of Particles in Viscoelastic Fluids: A Comparison of the Shear Viscosity vs Elasticity Effect. In SPE Annual Technical Conference and Exhibition held in San Antonio, Texas, 9-11 October 2017.

Atapattu, D. D., Chhabra, R. P., & Uhlherr, P. H. T. (1990). Wall Effects for Spheres falling at Small Reynolds Number in a Viscoplastic Medium. *Journal of Non-Newtonian Fluid Mechanics*, *38*, 31–42.

Atapattu, D. D., Chhabra, R. P., & Uhlherr, P. H. T. (1995). Creeping sphere motion in Herschel-Bulkley fluids: flow field and drag. *Journal of Non-Newtonian Fluid Mechanics*, *59*(2–3), 245–265. https://doi.org/10.1016/0377-0257(95)01373-4

Beris, A. N., Tsamopoulos, J. A., Armstrong, R. C., & Brown, A. (1985). Creeping Motion of a Sphere through a Bingham plastic Fluid. Journal of Fluids Mechanics, 158, 218–244.Blackery,

J., & Mitsoulis, E. (1997). Creeping motion of a sphere in tubes filled with a Bingham plastic material. *Journal of Non-Newtonian Fluid Mechanics*, *70*(1–2), 59–77. https://doi.org/10.1016/S0377-0257(96)01536-4

Briscoe, B. J., Glaese, M., Luckham, P. F., & Ren, S. (1992). The falling of spheres through Bingham fluids. *Colloids and Surfaces*, *65*(1), 69–75. https://doi.org/10.1016/0166-6622(92)80176-3

Brown, P. P., & Lawler, D. F. (2003). Sphere Drag and Settling Velocity Revisited. *Journal of Environmental Engineering*, *129*(3), 222–231. https://doi.org/10.1061/(ASCE)0733-9372(2003)129:3(222)

Chafe, N. P., & de Bruyn, J. R. (2005). Drag and relaxation in a bentonite clay suspension. *Journal of Non-Newtonian Fluid Mechanics*, *131*(1–3), 44–52. https://doi.org/10.1016/j.jnnfm.2005.08.010

Cheng, N. S. (2009). Comparison of formulas for drag coefficient and settling velocity of spherical particles. *Powder Technology*, *189*(3), 395–398. https://doi.org/10.1016/j.powtec.2008.07.006

Chhabra, R. (2006). *Bubbles, Drops, and Particles in Non-Newtonian Fluids, Second Edition* (Vol. 113). https://doi.org/10.1201/9781420015386

Chien, S.-F. (1994). Settling Velocity of Irregularly Shaped Particles. *SPE Drilling & Completion*, *9*(04), 281–289. https://doi.org/10.2118/26121-PA

Curran, S. J., Hayes, R. E., Afacan, A., Williams, M. ., & Tanguy, P. A. (2002). Properties of Carbopol Solutions as Models for Yield-Stress Fluids. https://doi.org/http://dx.doi.org/10.1016/j.placenta.2014.11.006

Dedegil, M. Y. (1987). Drag coefficient and settling velocity of particles in non-Newtonian suspensions. *Journal of Fluids Engineering*, *109*(3), 319–323. https://doi.org/10.1115/1.3242667

Dolejš, V., Doleček, P., & Šiška, B. (1998). Drag and fall velocity of a spherical particle in generalized newtonian and viscoplastic fluids. *Chemical Engineering and Processing: Process Intensification*, *37*(2), 189–195. https://doi.org/10.1016/S0255-2701(97)00054-8

Gumulya, M. M., Horsley, R. R., & Wilson, K. C. (2007). The settling of consecutive spheres in viscoplastic fluids. *International Journal of Mineral Processing*, *82*(2), 106–115. https://doi.org/10.1016/j.minpro.2006.11.005

Gumulya, M. M., Horsley, R. R., Wilson, K. C., & Pareek, V. (2011). A new fluid model for particles settling in a viscoplastic fluid. *Chemical Engineering Science*, *66*(4), 729–739. https://doi.org/10.1016/j.ces.2010.11.037

Haider, A., & Levenspiel, O. (1989). Drag coefficient and terminal velocity of spherical and nonspherical particles. *Powder Technology*, *58*(1), 63–70. https://doi.org/10.1016/0032-5910(89)80008-7

Hemphill, T., Campos, W., & Pilehvari, A. (1993). Yield-power law model more accurately predicts mud rheology.pdf. *Oil and Gas Journal*, *91*(34), 34. Retrieved from https://search-proquest-

com.manchester.idm.oclc.org/docview/274440935?accountid=12253&rfr_id=info%3Axri%2Fsid%3Aprimo

Ito, S., & Kajiuchi, T. (1969). Drag Force On A Sphere Moving in Plastic Fluid. *Journal of Chemical Engineering of Japan*, *2*(1), 19–24. https://doi.org/10.1252/jcej.2.19

Kelessidis, V. C., & Mpandelis, G. (2004). Measurements and prediction of terminal velocity of solid spheres falling through stagnant pseudoplastic liquids. *Powder Technology*, *147*(1–3), 117–125. https://doi.org/10.1016/j.powtec.2004.09.034

Kesely, M., & Matoušek, V. (2016). Laminar Settling of Glass Beads in Visco-Plastic Liquids. *Stavební Obzor - Civil Engineering Journal*, *25*(1). https://doi.org/10.14311/CEJ.2016.01.0001

Khalili Garakani, A. H., Mostoufi, N., Sadeghi, F., Hosseinzadeh, M., Fatourechi, H., Sarrafzadeh, M. H., & Mehrnia, M. R. (2011). Comparison Between Different Models for Rheological Characterization of Activated Sludge. *J . Environ . Health . Sci . Eng*, *8*(3), 255–264. https://doi.org/10.1515/jwld-2017-0053

Lubrizol. (2010). Technical Data Sheet; Viscosity of Carbopol ® * Polymers in Aqueous Systems.

Machač, I., Ulbrichová, I., Elson, T. P., & Cheesman, D. J. (1995). Fall of spherical particles through non-Newtonian suspensions. *Chemical Engineering Science*, *50*(20), 3323–3327. https://doi.org/10.1016/0009-2509(95)00168-5

Malhotra, S., & Sharma, M. M. (2012). Settling of spherical particles in unbounded and confined surfactant-based shear thinning viscoelastic fluids: An experimental study. *Chemical Engineering Science*, *84*(January), 646–655. https://doi.org/10.1016/j.ces.2012.09.010

McCabe, W., & Harriot, P. (1987). Unit Operations Of Chemical Engineering, 5th Ed, McCabe And .pdf. https://doi.org/10.1016/j.eplepsyres.2011.07.014

Metzner, A. B., & Reed, J. C. (1955). Flow of Non-Newtonian Fluids-Correlation of the Laminar , Transition , and Turbulent-flow Regions, (4). https://doi.org/10.1002/aic.690010409

Morrison, F. A. (2013). Data Correlation for Drag Coefficient for Spheres. *Cambridge University Press, New York*, *10*(November), 1–2.

Prashant, & Derksen, J. (2011). Direct simulations of spherical particle motion in Bingham liquids. *Computers and Chemical Engineering*, *35*(7), 1200–1214. https://doi.org/10.1016/j.compchemeng.2010.09.002

Rao, M. A. (2014). *Rheology of Fluid, Semisolid, and Solid Foods*. *Rheology of Fluid, Semisolid, and Solid Foods*. Springer US. https://doi.org/10.1007/978-1-4614-9230-6

Richardson, J. F., Harker, J. H., & Backhurst, J. R. (2002). Chemical engineering Voulume 2. *Chemical Engineering Science*, *2*. https://doi.org/10.1016/0009-2509(60)80030-9

Rushd, S., Hassan, I., Sultan, R. A., Kelessidis, V. C., Rahman, A., Hasan, H. S., & Hasan, A. (2018). Terminal settling velocity of a single sphere in drilling fluid. *Particulate Science and Technology*, *0*(0), 1–10. https://doi.org/10.1080/02726351.2018.1472162

Saha, G., Purohit, N. K., & Mitra, A. K. (1992). Spherical particle terminal settling velocity and drag in Bingham liquids. *International Journal of Mineral Processing*, *36*(3–4), 273–281. https://doi.org/10.1016/0301-7516(92)90049-3

Shahi, S., & Kuru, E. (2015). An experimental investigation of settling velocity of natural sands in water using Particle Image Shadowgraph. *Powder Technology*, *281*, 184–192. https://doi.org/10.1016/j.powtec.2015.04.065

Shokrollahzadeh, A. (2015). Terminal Settling Velocity of a Sphere in a non-Newtonian Fluid. https://doi.org/10.7939/R3Q23R76B

Song, X., Xu, Z., Li, G., Pang, Z., & Zhu, Z. (2017). A new model for predicting drag coefficient and settling velocity of spherical and non-spherical particle in Newtonian fluid. *Powder Technology*, *321*, 242–250. https://doi.org/10.1016/j.powtec.2017.08.017

Stokes, G. G. (1905). On the Theories of the Internal Friction of Fluids in Motion, and of the Equilibrium and Motion of Elastic Solids. *Mathematical and Physical Papers Vol.1*, 75–129. https://doi.org/10.1017/CBO9780511702242.005

Tabuteau, H., Coussot, P., & de Bruyn, J. R. (2007). Drag force on a sphere in steady motion through a yield-stress fluid. *Journal of Rheology*, *51*(1), 125–137. https://doi.org/10.1122/1.2401614

Turton, R., & Levenspiel, O. (1986). A short note on the drag correlation for spheres. *Powder Technology*, *47*(1), 83–86. https://doi.org/10.1016/0032-5910(86)80012-2

Valentik, L., & Whitmore, R. L. (1965). The terminal velocity of spheres in Bingham plastics. *British Journal of Applied Physics*, *16*(8), 1197–1203. https://doi.org/10.1088/0508-3443/16/8/320

Wilson, K. C., Horsley, R. R., Kealy, T., Reizes, J. A., & Horsley, M. (2003). Direct prediction of fall velocities in non-Newtonian materials. *International Journal of Mineral Processing*, *71*(1–4), 17–30. https://doi.org/10.1016/S0301-7516(03)00027-9

Wilson, K. C., & Thomas, A. D. (1985). A new analysis of the turbulent flow of non-newtonian fluids. *The Canadian Journal of Chemical Engineering*, *63*(4), 539–546. https://doi.org/10.1002/cjce.5450630403

CHAPTER 6 : EXPERIMENTAL VISUALIZATION AND ANALYSIS OF ELASTIC AND VISCOUS EFFECTS ON THE FLOW FIELD SURROUNDING A SETTLING PARTICLE IN VISCOPLASTIC FLUIDS USING PARTICLE IMAGE VELOCIMETRY (PIV).

6.1 Abstract

An experimental study was conducted to visualize and evaluate the flow field surrounding the spherical particles settling in viscoplastic fluids exhibiting elastic and inelastic behavior. This study was carried out to obtain a profound understanding of the individual effects of elasticity and viscous yield stress on the settling behavior of spherical particles and shape of induced yielded regions (which illustrates the influence of fluid properties on particle settling behavior) in non-Newtonian fluids. It has been reported that both of these forces affect the settling behavior of particles in non-Newtonian fluids therefore making it imperative to determine which of these two forces play a prominent role especially when transport fluids exhibit both properties simultaneously. This knowledge is essential for the optimized design of engineering fluids for different conditions. The main objectives of this study were;

- To depict and visualize the intrinsic flow field surrounding a settling particle in such fluids,
- To investigate the isolated effects of viscous yield stress and elasticity on the fluid velocity profile and flow field surrounding the settling particle,
- To corroborate valid postulates about the negative wake phenomena and the shape of the yielded region surrounding a settling particle using visual experimental evidence.

Two sets of fluids were prepared using two distinct Carbopol polymers (ETD 2020 and 940). First set of fluids exhibited similar shear viscosity and yield stress but different elastic properties while the second set of fluids had almost identical elasticity but disparate shear viscosity and yield stress. Rheological characterization of the fluids was conducted by the using Bohlin C-

VOR Rheometer and Fann Viscometer. The settling velocities of the spherical particles (Specific gravity ranging from 2.5 – 3.9; Diameters: ranging from 2.00mm - 3.00 mm) in the various Carbopol solutions were measured using Particle Image Shadowgraphy (PIS). The fluid flow field and sheared region surrounding the settling particle was determined by using the Particle Image Velocimetry (PIV) technique.

Experimental results showed that for the same shear viscosity, increasing elasticity can dampen the particle settling velocity and fluid velocity profile significantly, which is beneficial for particle suspension during fluid transport. This inhibiting effect can also be achieved with greater potency by increasing the yield stress as well. Furthermore, experimental images showed that the shape of sheared region depends on the mean surficial stress exerted on the fluid by the settling particle and the physical property of the fluid. The set of fluids with different elastic property (but identical viscous property) gave similar shapes of yielded region when sheared by the same particle however increasing the viscous yield stress reduces the shape of the yielded region and changes the shape of the yielded region. This indicates the prominence of viscous yield stress as a major deciding factor in determining the shape of the yielded region. Finally, the existence of theoretical unyielded regions adjacent to the settling particle were observed experimentally for the first time in this study

The technical knowledge of particle settling in Non-Newtonian fluids is applicable to many operations ranging from hole cleaning in oil and gas drilling operations to slurry transport in mining engineering. By visualizing and investigating the individual effects of yield stress and elasticity, we are able to show how these two rheological properties influence particle settling and its surrounding flow field. The results from this essential study can provide the experimental basis

for the modeling of particle settling in complex fluids which can be utilized for the enhanced manufacturing of engineering transport fluids for a variety of conditions.

6.2 Introduction

Fluid-particle transport systems are ubiquitous in various industrial processes. These industrial processes include hydraulic fracturing where solid proppants are transported to induced fractures by fracturing fluids and drilling operations where solid cuttings are circulated back to the surface by drilling fluids. In the mining industry, some of the processes that deal with slurries likewise involve fluid-particle transport systems. These fluids described above are usually viscoplastic non-Newtonian fluids (fluids that undergo no significant deformation until the applied stress exceeds the minimum yield stress of the fluid) and they are of prime importance due to their vast applicability. The adept understanding of particle behavior and motion in such complex non-Newtonian fluids is paramount for the analysis, modeling and optimization of these fluid-particle transport systems.

Over the past decades, the transport and settling of particles in Non-Newtonian fluids has been subject to various experimental and numerical studies due to its pragmatic versatility. Compared to Newtonian fluids, which have been fully demystified (McCabe & Harriot, 1987; Richardson, Harker, & Backhurst, 2002), the settling behavior of particles in non-Newtonian fluids is convoluted due to complexities in rheological properties compounded by the hard-to-measure yield stress coupled with elasticity in some fluids (Chhabra, 2006). When a particle falls through a Newtonian fluid, the flow field surrounding the particle theoretically expands (Shokrollahzadeh, 2015). The shear stress exerted by the particle decreases monotonically away from particle and a fore-aft symmetry is observed in the flow field (Gueslin, Talini, Herzhaft, Peysson, & Allain, 2006;

Harlen, 2002; Holenberg, Lavrenteva, Shavit, & Nir, 2012). The flow field in non-Newtonian viscoplastic fluid is quite disparate. Many authors have reported fore-aft symmetry being broken in non-Newtonian viscoplastic fluids (Arigo and Mckinley, 1998; Harlen, 2002; Gueslin et al., 2006; Holenberg et al., 2012) and existence of a plug like flow in front of the settling particle (Putz et al., 2008). If the stress exerted by the settling particle is below the fluid's yield stress, the fluid acts as an elastic solid and the particle would not settle (Shokrollahzadeh, 2015; Wilson, Horsley, Kealy, Reizes, & Horsley, 2003). This results in the formation of different regions around a settling particle. A cogent knowledge of the shape and dimension of these surrounding regions is salient because it is interwoven with the settling behavior and also determines the magnitude of the particle settling velocity in a viscoplastic fluid (Prashant & Derksen, 2011).

Volarich and Gutkin (1953) were among the first proponents of the existence of a sheared (yielded) region and an unsheared (unyielded) region surrounding a settling particle in a viscoplastic fluid. Over the years several shapes and dimensions of the sheared and unsheared regions have been posited by different authors. Valentik and Whitmore (1965) proposed a method for estimating the size of the unsheared shell region surrounding the settling particle by assuming Newtonian fluid laws apply. In 1967, Ansley and Smith suggested the existence of an envelope of toroidal shape sheared region surrounding the settling particle based on the slip line theory of solid mechanics. Yoshioka et al. (1971) identified the existence of stagnant polar cap regions in the sheared region and also showed the extent of the sheared zone using variational principles. Using a numerical method, Beris *et al.*, (1985) identified the sheared and unsheared regions surrounding a settling particle. Postulated shapes of the sheared envelope surrounding a sphere are shown in Fig.1.The results of Beris *et al.*, (1985) study showed that the dimensions and shape of the sheared

region depend appreciably on the yield stress, which in extension determines the speed of the settling particle. Their result agrees with numerical studies by Blackery and Mitsoulis (1997) as well as Prashant and Derksen (2011).

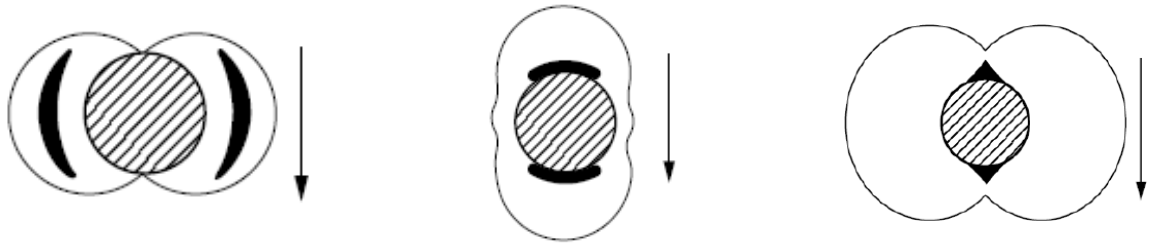

A – Ansley and Smith (1967) B – Yoshioka et al. (1971) C – Beris et al. (1985)

Figure 6.1: Postulated shapes of the sheared envelope surrouding a sphere in creeping motion in Viscoplastic (Chhabra, 2006)

As the yield stress increases, the unsheared region expands, which reduces the sheared region drastically as well as the particle settling velocity (Prashant and Derksen, 2011). Holenberg et al. (2012) utilized Particle Image Shadowgraphy (PIS) to determine shape of the yielded zone produced by smooth and rough spheres settling in Carbopol polymers. The shape obtained depended on the speed of the settling particle (peach-like shape for slow particles and bulb shape for faster particles). Although results of the Holenberg et al. (2012)did not capture the stagnant polar caps posited by Yoshioka et al. (1971), their experimental results were accurately predicted by recent numerical study by Fraggedakis, Dimakopoulos and Tsamopoulos (2016).

Apart from the existence of sheared and unsheared regions, there have also been reports concerning the existence of negative wakes in non-Newtonian fluids. Negative wakes refer to the upward movement (i.e. opposite direction to the settling particle) of fluid in the settling particle's wake. The existence of a negative wake and its underlying mechanism have been the focus of various debates as it regards its underlying mechanism. By changing the composition of the experimental fluids (ratio of water to corn syrup), Bush (1993) was able to obtain various fluid flow behaviors from obtaining negative wakes to extended wakes (i.e. downward fluid movement in the same direction of the settling particle). Harlen (2002) reported that negative wakes are caused by elastic recoil due to shear stresses generated near the side of the spheres giving rise to a flow directed away from the sphere. He also stated that extended wake is due to extensional stresses generated by extensional flow at the rear of the sphere, which drives a flow towards the sphere. The balance between these two, determines the relative magnitude of the both wake and negative wake as well as the position of the stationary point (i.e. inflexion point of zero velocity along the axis of the settling particle). Harlen's conclusion on two competing viscoelastic forces has also been supported by other researchers (Arigo & Mckinley, 1998; Bush, 1994; Fraggedakis, Dimakopoulos, & Tsamopoulos, 2016; Xavier Frank & Li, 2006; Gueslin et al., 2006). This shows that the existence of elasticity in complex fluids can prominently affect flow fields and in extension shape of the sheared region in viscoplastic fluids.

It was reported that at low Weissenberg numbers, an increase in elasticity leads to drag reduction on settling particles and vice versa at higher Weissenberg numbers (Walters and Tanner, 1992). This was later confirmed by Malhotra and Sharma (2012) through particle settling experiments in shear thinning fluids. A study by Arnipally and Kuru (2018) aimed at isolating the

individual effects of the shear viscosity and the elasticity showed that increasing elasticity at a constant viscosity reduces settling velocity in shear thinning viscoelastic fluids (prepared by using Hydrolyzed Polyacrylamide polymer). Elasticity in this study was characterized by using the longest relaxation time. A more recent study with the same viscoelastic experimental fluids showed that more elastic fluids have stagnation points closer to the settling particle than less elastic fluids for the same shear viscosity under controlled conditions (Arnipally, Bizhani, & Kuru, 2019). Other researchers have also reported that increasing inertia (speed of the particle) leads to the downstream movement of the stationary point (zero velocity) and negative wake away from the particle (Arigo & Mckinley, 1998; Fraggedakis et al., 2016; Gueslin et al., 2006).

Based on the literature review, it is revealed that both elasticity and viscosity affect flow fields surrounding a settling particle in a viscoplastic fluid. However, there is little work in the literature that isolates viscous effects and elastic effects in order to ascertain, which plays a prominent influential role on the shape of the sheared region as well as the fluid (vector) velocity profile in viscoplastic fluids. The present study investigates the isolated effects of the elasticity and the viscosity on the fluid velocity profile and flow field surrounding the settling particle in yield stress fluids using Particle Image Velocimetry (PIV) technique. This knowledge is important because it determines which of these properties plays a major inhibitive role in particle suspension and transport. The smaller the size of sheared region, the greater the suspension efficiency of the fluid. The main objectives of this study were: i.) To visualize the intrinsic flow field surrounding a particle settling in complex non-Newtonian fluids exhibiting elastic properties, ii.) To decouple and investigate the isolated effects of viscous yield stress and elasticity on the fluid velocity profile and flow field surrounding the settling particle. This is achieved by using two sets of fluids with

one set having the similar shear viscosity but different elasticity and the other set having almost identical elasticity but different shear viscosity. iii.) To corroborate valid postulates about the negative wake phenomena and the shape of the yielded region surrounding a settling particle using visual experimental evidence.

6.3 Experimental Materials and Methodology

6.3.1 Experimental Materials

In this study, precision spherical particles of glass (Specific gravity 2.51) was used. The diameters of the spheres used were from 2.00mm and 3.00mm. The spheres were obtained from Corpuscular Inc. The fluid column is made out of a transparent plexiglass cuboidal column of 70 cm height. The dimensions of the fluid column are 15cm by 15cm by 70cm. The fluid column dimensions were designed by considering the minimum size required to avoid the wall effects (Atapattu, Chhabra and Uhlherr, 1990).

6.3.2 Experimental Fluids and Preparation Procedure

Carbopol® is a high molecular weight cross-linked polyacrylic acid polymer. The main rheological difference among the carbopol polymers result from the crosslinker type and the density (Lubrizol, 2010). The polymer is a low-wettability fine white powder. It is mildly acidic when dissolved in an aqueous and expands upon neutralization to form a transparent gel.

The Carbopol ETD 2020 and Carbopol 940 were polymers utilized as test fluids in this study. Fluid A (0.0286% Weight) and Fluid B (0.0571% Weight) were prepared from Carbopol ETD 2020 while Fluid C (0.0428% Weight) was prepared from Carbopol 940. The experimentally proven

methodology for decoupling viscosity and elasticity followed by Arnipally and Kuru, 2017 was used in preparing the test fluids in this study. Selfsame polymer yields identical elasticity due to intrinsic equivalent average molecular weight. However, increasing polymer concentration increases viscosity (Arnipally and Kuru, 2017). For carbopol polymers, viscosity alteration can also be easily achieved by meticulously adjusting the fluid's pH till desired rheological property is achieved.

Carbopol polymers were obtained from Lubrizol™. The procedure for preparing the test fluids is similar to that utilized by Curran *et al.*, 2002. The procedure is as follows:

- Deionized water of required volume was measured and stirred at a low rpm in a mixing bucket.
- The required mass of Carbopol powder was added slowly progressively (not all at once) to the stirring de-ionized water on to the inner sides of the fluid vortex.
- After adding the polymers, the solution was stirred at 150 rpm for 2.5 hours until the low wettability carbopol powders fully dissolve with no visible polymer powder.
- A 10 wt % Sodium hydroxide (NaOH) solution was added in drops to neutralize the polymer solution to about 6.5 or desired rheological property attained. The pH of the polymer solutions were measured by using the Fisherbrand™ accumet™ AE150 pH benchtop meter.
- After desired rheological property was attained, the fluid was stirred continuously for 1 hour minutes to ensure homogeneity.

- Tracer glass particles (20ppm concentration) were added to the fluid in preparation for the PIV test. The solution was then stirred for an additional 25 minutes.

- The solution was transferred to the fluid column and allowed to stand still overnight to remove air bubbles. (Filtration was not necessary since the carbopol polymers used were clear and transparent).

6.3.3 Rheological Measurements and Characterizations.

Rheological measurements were performed with the C-VOR cone and plate type rheometer (40mm and 4° cone and plate geometry was used) from Bohlin Instruments Bohlin Instruments and Fann Model 35A Viscometer from the Fann Instrument Company. The measurements were conducted at room temperature (25°C). All fluids were pre-sheared prior to measurements in order occlude aging effect (if it existed). The Controlled Stress viscometry function and Oscillatory measurement function of the rheometer were used to determine the fluid flow curve and elastic properties respectively. The yield stress was determined using the Fann Viscometer by adhering to procedures outlined in the API Recommended Practice 13D (API, 2006)

6.3.4 Experimental Setup

The flow field behind settling spherical particles in Carbopol solutions were measured using Particle Image Velocimetry (PIV) technique. Particle Image Velocimetry (PIV) is a non-intrusive flow visualization technique that allows capturing instantaneous velocity data of whole flow fields (Raffel *et al.*, 2007). The fluid is seeded with very light buoyant particles (tracer particles) that do not affect flow properties and the major assumption is that these particles move in unison with the flow field and are also descriptive of the fluid flow field.

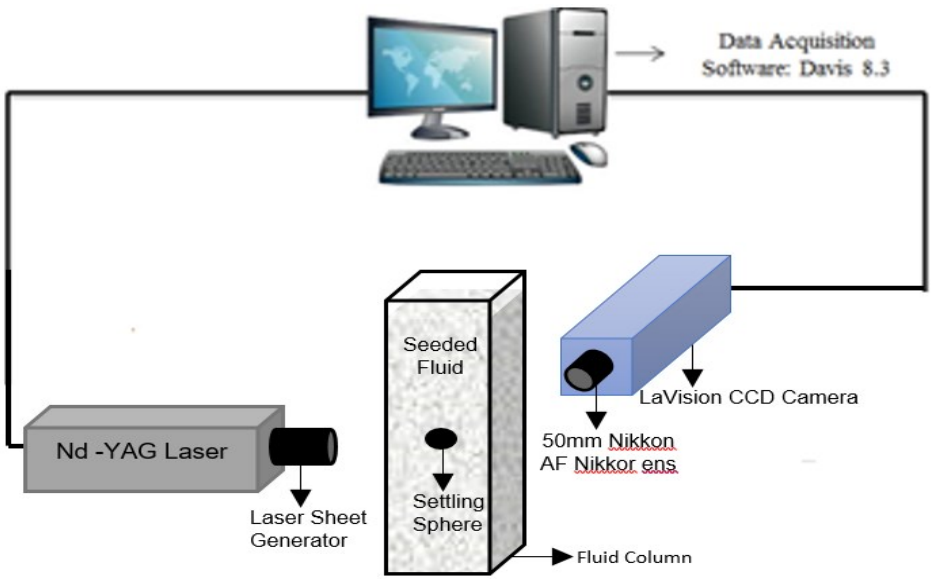

Figure 6.2: PIV Experimental Setup

These particles are illuminated by means of a laser light source which are detected by light scattering and their instantaneous positions recorded with an image acquisition device (Camera). The magnitude of the fluid flow and their direction are determined using particle position in the captured images. Two successive images are captured at a predetermined time interval (dt). The displacement (ds) and in extension magnitude of velocity is determined using deviation in particles' positions in recorded images by sophisticated Statistical algorithm. The experimental setup is shown below:

The PIV setup (Figure 6.2) was composed of the light source, which was provided by the New Wave Research Laser Solo III; an Nd-YAG double pulsed laser with a 532 nm wavelength and a frequency of 15 Hz. The laser was coupled with the LaVision laser generation sheet for greater efficiency and background illumination. The image acquisition device used was the LaVision Image Intense Camera. This double framed (can capture quick consecutive images at two different

exposure times in as short as 10ns) high resolution camera had a Charge-Coupled Device (CCD) sensor of 1376×1040 pixels capable of capturing 5 frames per sec and a capacity to convey 12-bit digital images. A 50 mm Nikon AF Nikkor lens of 1.4 mm aperture was used to capture broader field of View, and it was coupled with the CCD Camera with means of a 12-mm long extension tube. The captured images were processed with the LaVision Davis 8.3 software which was the data acquisition and processing software.

The PIV Davis 8.3 software follows algorithms to measure displacement and the velocity magnitude. The algorithm divides the captured images into small interrogation windows. During the time interval the tracer particles move by a displacement ds which is determined by cross correlating the same interrogation windows in consecutive images using sophisticated statistical techniques. The velocity is then determined by dividing the displacement (ds) by the time interval (dt). The displacement vectors and velocity of each interrogation window are used to form velocity map result as shown in Figure 3 below.

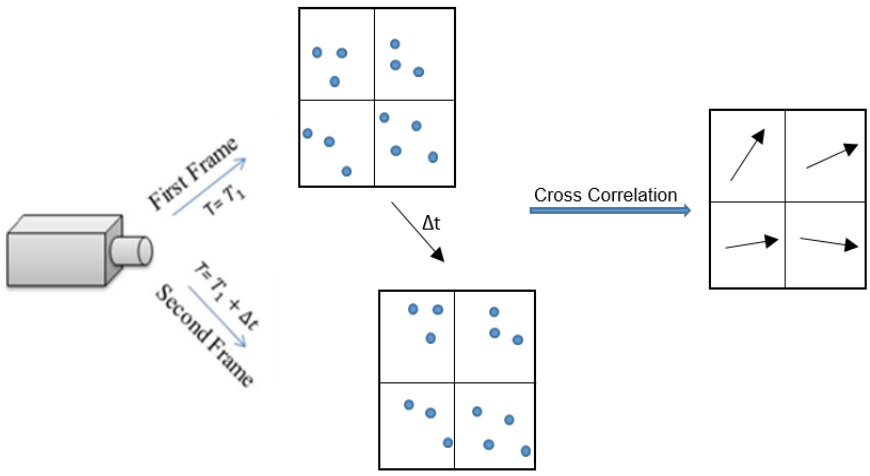

Figure 6.3: A Schematic of the PIV Processing Algorithm

The shape of the yielded region are obtained from processing the PIV images. The PIV images are processed using the PIV processing function of Davis 8.3. An example of processed PIV image is shown in Figure 4.

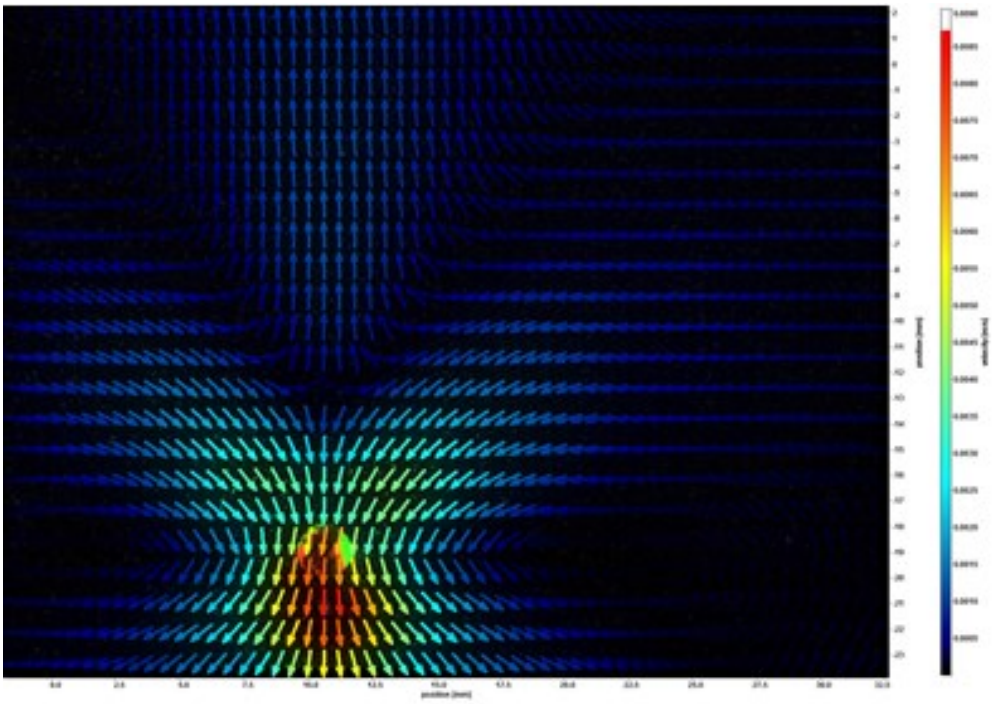

Figure 6.4: Processed PIV Image

6.3.5 Experimental Procedure

The experimental procedure follows similar steps employed by Arnipally, Bizhani and Kuru (2019). The first step involves the preparation of the experimental fluid as outlined above. The experiment was setup similar to Figure 6.2 with the double pulsed Laser and double framed camera at right angles to each other both connected to the Computer on which Davis 8.3 software was installed. After ensuring all the equipment are properly set up and 50mm Nikon Lens is mounted on the camera. The double pulsed laser (with the sheet generating diffuser attached) is switched

on. The maximum energy of the laser was selected and the laser power of the first and second pulse were adjusted to about 30% and 20% respectively.

Equipment calibration is carried out by inserting a calibration target sheet in the fluid column and taking a focused image of the sheet. The calibration sheet had a grid pattern. The grids were at distance of 1.5 mm from each other; they were printed in black color on a white background. An image of the calibration sheet is shown below.

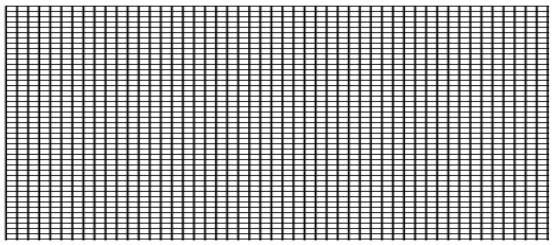

Figure 6.5: Calibration Sheet

The spacing dimensions of the sheet helps the Davis 8.3 software convert pixel dimensions into physical dimensions. The position of the calibrated sheet is marked so it serves as the position where spheres are dropped to ensure they fall on the focal plane.

After calibration, the PIV images can now be captured by dropping the 2mm and 3mm spherical particles at the marked focal plane decision. A time gap of 30 minutes was maintained between successive ball drops to ensure fluid network build up to original state. Several experimental images were recorded to bolster accuracy and ensure reproducibility.

The experimental images were processed using the Davis 8.3 Software to obtain velocity flow field behind the settling particle and the shape of sheared region as well. The multi-pass interrogation window sizes for cross correlation were chosen to be 256 x 256 pixels and 96 x 96

pixels respectively. The universal outlier detection setting was then finally utilized in post processing to improve experimental results. The Davis 8.3 software has special functions to visualize region of sheared shapes based on vector movement. The optical bit shift function of the PIV processing was used to automatically generate images that showed the sheared regions based on the intensity of velocity vector maps.

6.4 Results and Discussions

6.4.1 Test Fluid Properties

Figure 6.6 and Figure 6.7 represents the shear stress and shear viscosity profiles of the respective fluids. Fluid A and Fluid C represent fluids with the same shear viscosity. As shown in the figures, Fluid B is more viscous than Fluid A and Fluid C due to its higher concentration.

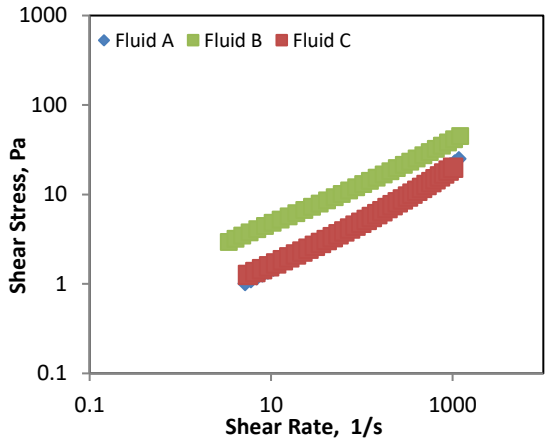

Figure 6.6: Flow Curves for Test Fluids

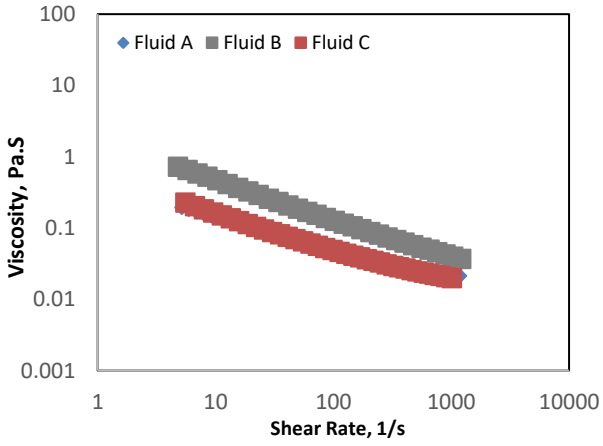

Figure 6.7: Shear Viscosity vs. Shear Rate Profiles of Test Fluids

The equal shear viscosity profile is also bolstered from the test results of the Fann viscometer (Table 1). Similarly, Fluid A and Fluid C exhibited similar shear viscosity and showed nearly identical dial readings. The plastic viscosity and yield stress were estimated using equations specified by the American Petroleum Institute (API, 2006)

Table 6.1: Fluid Property measured by the Fann Viscometer

RPM (Revolutions Per Minute)	**Fann Viscometer Dial Readings (º Deflection)**		
	Fluid A	**Fluid B**	**Fluid C**
600 (1022 sec^{-1})	43.5	96	43.5
300 (511 sec^{-1})	28.5	69.5	28.5
200 (341 sec^{-1})	22	57	22
100 (170 sec^{-1})	14.5	41	14
6 (10 sec^{-1})	4.5	23	4.5
3 (5 sec^{-1})	3	13	3
Calculated Properties			
Plastic Viscosity →R600-R300 (cP)	15	26.5	15
Yield Stress → R300-Plastic Viscosity ($lb/100ft^2$)	13.5	43	13.5

The Herschel Bulkley fluid model ($\tau = \tau_{HB} + k\dot{\gamma}^n$) is chosen for the rheological characterization of the test fluids. The Herschel Bulkley model require three parameters τ_{HB}, k and n for rheological

characterization. These three parameters were determined using the numerical technique procedure outlined in API Recommended Practice 13D (API, 2006).

Table 6.2: Power Law Parameters of fluids

Experimental Fluids	τ_{HB} (lb/100ft^2)	K (lb.S^n /100ft^2)	n
Fluid A	1.836	0.484	0.652
Fluid B	13.55	1.635	0.577
Fluid C	1.836	0.484	0.652

The results of the oscillatory tests and the longest relation time, λ (sec) that describe the elastic properties of the test fluids are shown below in Figures 7-9. The longest relaxation time, λ (sec) which is the inverse of the crossover frequency between the elastic modulus and viscous modulus indicates the time needed for any deformed material to regain its original structure and is used to depict the elasticity of a material (Choi, 2008; Arnipally and Kuru, 2018).

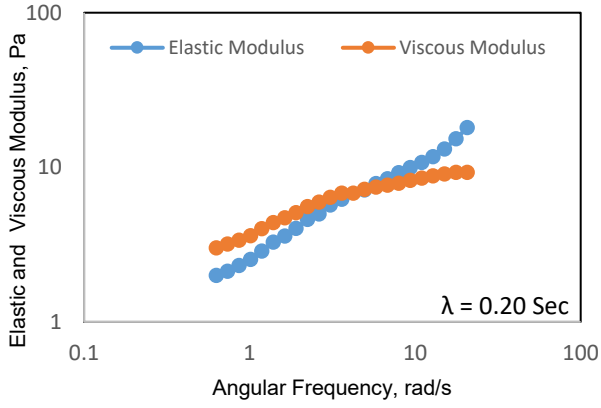

Figure 6.8: Oscillation Frequency Sweep Test Result for Fluid A

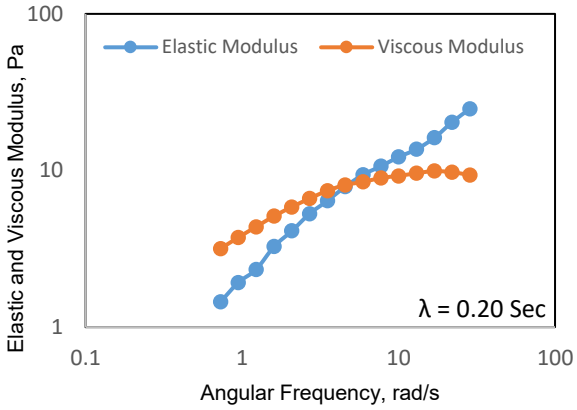

Figure 6.9: Oscillation Frequency Sweep Test Result for Fluid B

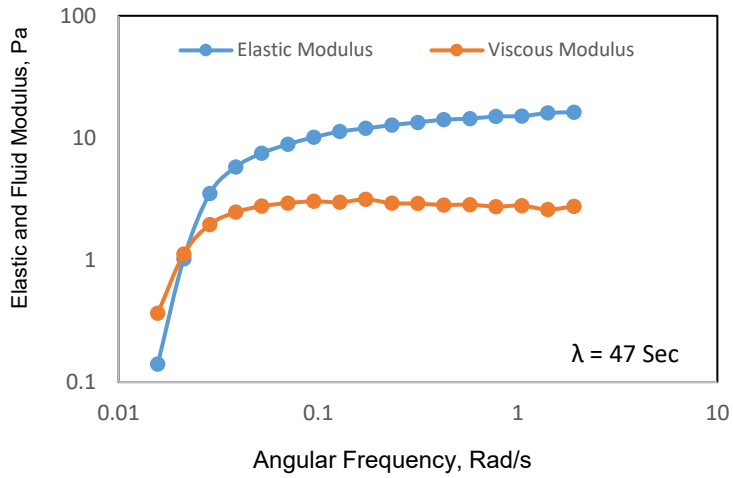

Figure 6.10: Oscillation Frequency Sweep Test Result for Fluid C

Fluids with higher relaxation time are more elastic and vice versa. The elastic modulus represents solid-like behavior indicates energy stored in the material to recover from deformation while viscous modulus indicates the energy dissipated or lost during from deformation. The elastic modulus rises more rapidly than the viscous modulus indicating elastic properties present in the fluids with fluid C being the most elastic with the highest relaxation time of 47 Secs.

In summary, the three test fluids were prepared following the Arnipally and Kuru (2017) methodology in such a way that two fluids (Fluid A and Fluid C) have identical shear viscosity profile but differ in elastic properties and another set of fluids (Fluid A and Fluid B) have similar elastic properties but disparate in shear viscosity profiles.

6.4.2 Velocity Field in a Sample Newtonian Fluid (Water).

Particle Image Velocimetry was used to capture the flow field surrounding a settling particle in water which is a standard Newtonian fluid. The image of the flow field is shown below. The region of interest is isolated and enlarged for emphasis.

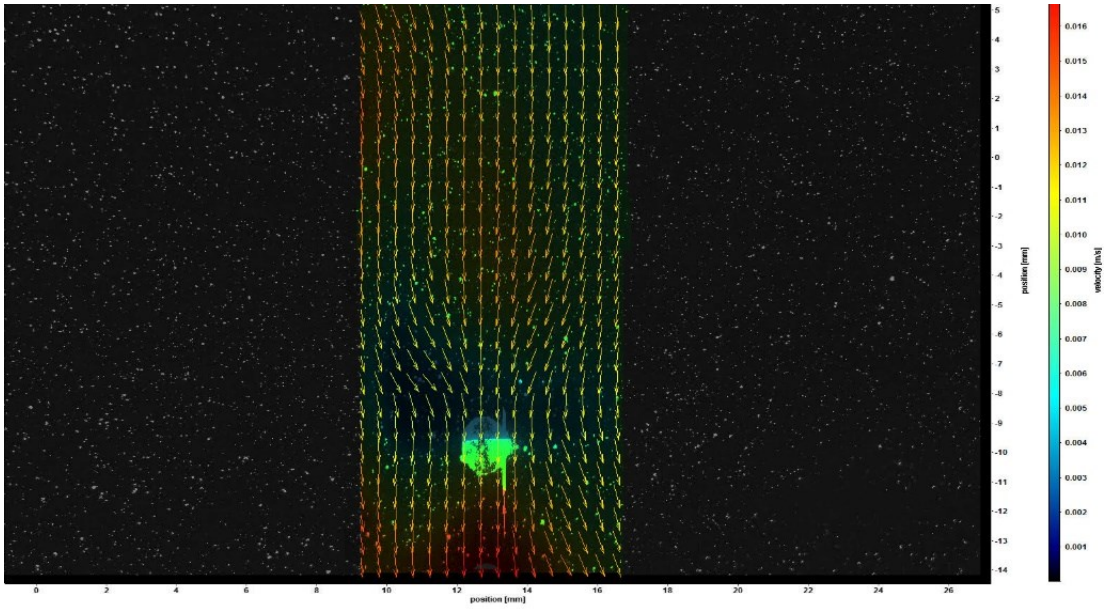

Figure 6.11: Velocity Field induced by 2mm Sphere in Water.

The flow field figures shows a fore-aft symmetry (similar fluid vectors before and after the settling particle). This is a common phenomenon with Newtonian fluids (Fraggedakis et al., 2016; Gueslin et al., 2006; Putz, Burghelea, Frigaard, & Martinez, 2008). There was also an absent of negative wake in the flow field while a partial side recirculation zone was found at the sides of the sphere. This is due to the shear stress exerted by the settling particle on the fluid layers.

6.4.3 Velocity Fields in the Carbopol Solutions

A comparative study of the particle settling velocity by using fluids having similar shear viscosity and different elasticity as well as the similar elasticity and different shear viscosity have been conducted and the results are provided in the following sections.

6.4.3.1 Effect of Fluid Elasticity on the Velocity Field around the Settling Particle

Fluid A and Fluid C represent fluids with the same shear viscosity profile but different elasticity. Fluid C is more elastic than Fluid A. The Velocity flow fields induced by the 2mm glass sphere in Fluid A and Fluid C are shown in the figures 11 and 12, respectively.

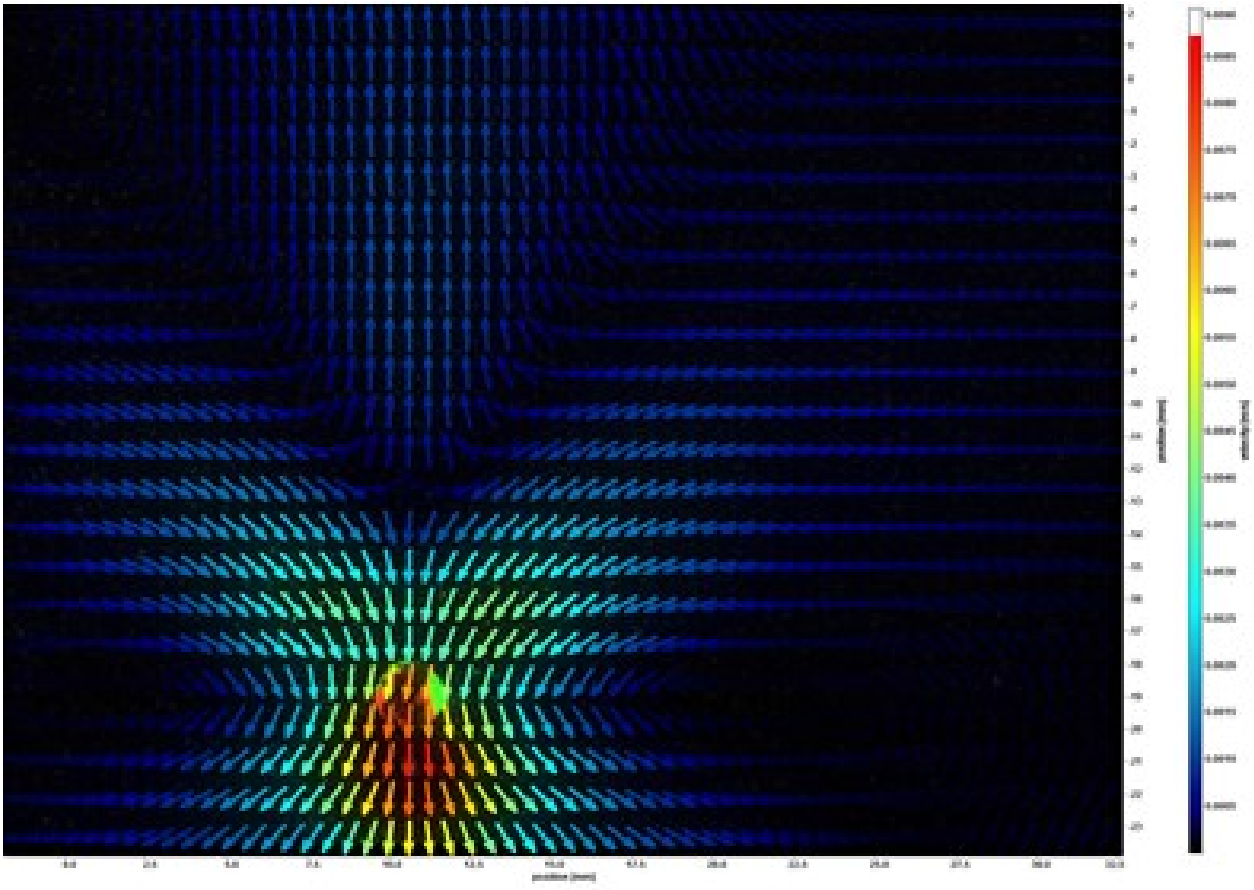

Figure 6.12: Velocity field induced by 2mm sphere in Fluid A

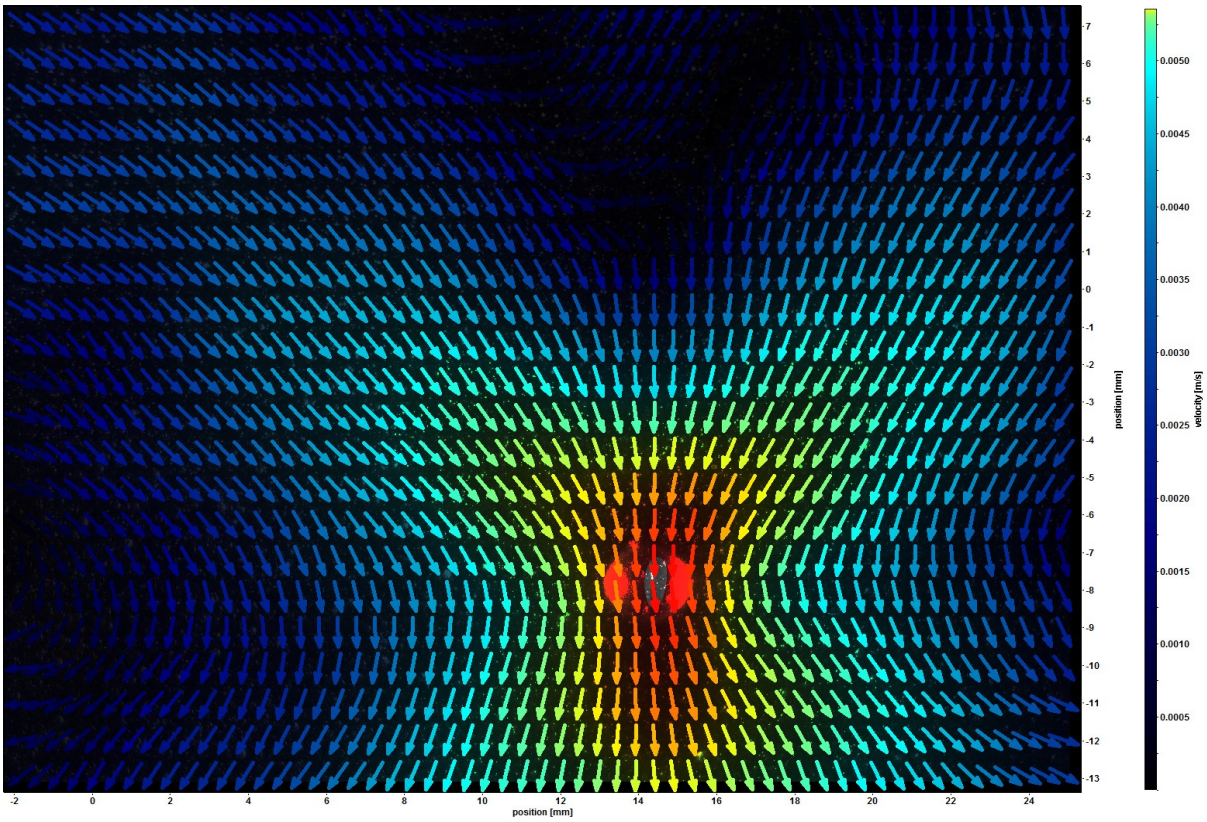

Figure 6.13: Velocity field induced by 2mm sphere in Fluid C

Firstly, the fore-aft symmetry observed in Newtonian fluids is broken in the case of these non-Newtonian viscoplastic fluids, this is in agreement with experimental results present in literature (Gueslin et al., 2006; Holenberg et al., 2012; Putz et al., 2008). The fastest movement of the fluid is observed just below the sphere, where the vector is reddish in color similar to the plug flow observed by Putz et al. (2008). A noticeable difference in both images is the proximity of the recirculation zones to the side of the spheres. The side recirculation zones are closer in the Fluid A than in Fluid C (more elastic fluid). Increasing elasticity shifts these zones farther to sides which

may be due to wall slip effects and the difference in the fluid rheology (Gueslin et al., 2006; Putz et al., 2008) since two different polymers were utilized.

A negative wake (upward) and an extended wake (downward) are also observed in both figures. There are very strong movements of the fluid in the opposite and also in the same directions of the settling sphere, which are also in concordance with various numerical and experimental studies. The extended wake, which is due to the downward settling of the sphere has its magnitude reportedly related to extensional elastic forces (Arigo & Mckinley, 1998; Harlen, 2002; Putz et al., 2008); While the negative wake is attributed to be caused by elastic recoil forces generated at rear of the settling sphere.

Along the sphere's centerline, the magnitude of the extended wake decreases (which is seen as vector color gets darker) monotonically until a point of zero velocity is attained, which indicates the stagnation point, after which the extended wake begins as shown in figure 12 and 13. The "V" shaped stagnation zone is observed in both figures. The V shape cone and it's angle were attributed to a propagation front of lateral viscoelastic wave emitted by the settling sphere (X. Frank, Dietrich, & Li, 2014). Although both flow fields appear rather similar, these little differences confirm that elasticity plays a role in the flow field characteristics.

In order to buttress the effect of increased elasticity, the vector magnitude of the velocity profile along the centerline of the sphere is plotted against distance from the top of the settling sphere for both fluids in Figure 14. The point of 0 m/s signified by a black straight line indicates the stagnation point downstream of the sphere.

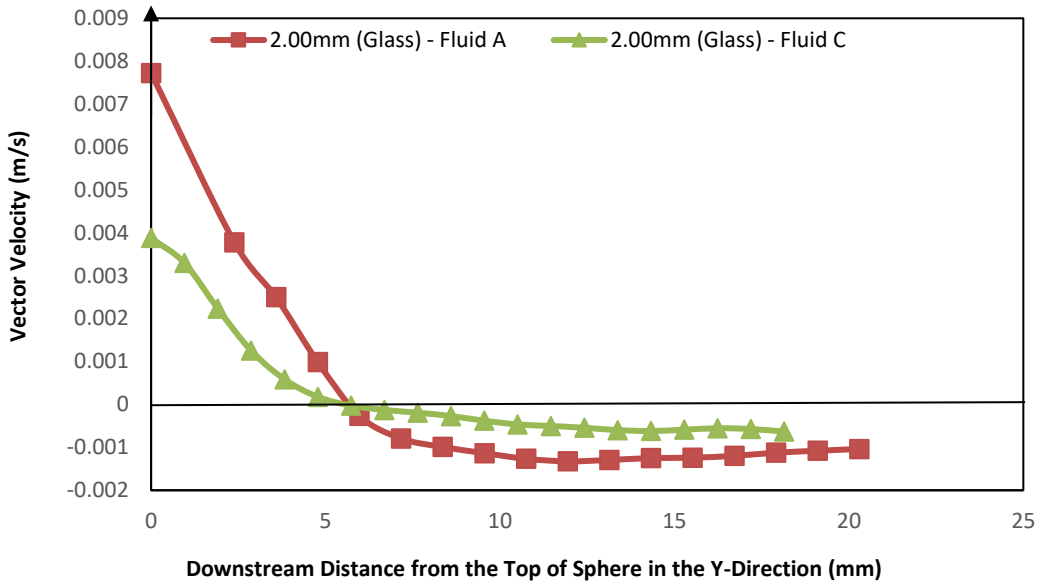

Figure 6.14: Vector Velocity Profile along the Centerline of the Sphere

The results envisaged the damping effect of elasticity. The vector velocity reduces drastically with increase in elasticity. An almost 50% decrease in vector velocity was observed for all positions away from the top of the sphere, even in the negative wake region (negative velocity). According to Mezger (2006), this is due to the unique ability of elastic fluids to resist deformation as a result of their higher storage modulus (energy stored) and a lower loss modulus (energy lost) for the same angular frequency. So they behave more solid like. This unique property is beneficial in many field operations, where particle suspension is desirable. This is also true with respect to the particle settling velocity. The settling velocity of the 2mm glass particles were measured using Particle Image Shadowgraphy. The results are shown below.

Table 6.3: Measured Particle Settling Velocity in Fluid A and Fluid C

Experimental Fluid	Particle Settling Velocity (m/s)
Fluid A	0.061
Fluid C	0.032

6.4.3.2 Effect of Fluid Shear Viscosity and the Yield Stress on the Velocity Field around the Settling Particle

Fluid A and Fluid B represent fluids with similar elastic properties but different shear viscosity profile. Fluid B is more viscous and has a higher yield stress than fluid A. The velocity field induced by 2mm Sphere in Fluid A is shown in Figure 12 while that of Fluid B is shown in Figure 15. The first observation is proximity of the recirculation zones at the sides of the spheres. They are much closer in Fluid B, which is due to the increase in yield stress and viscosity. As the yield stress of a fluid increases, the unsheared region expands closer to the settling particle (Chhabra, 2006; Prashant & Derksen, 2011). Another study claims that the position of the recirculation zone may also be due to thixotropy or aging (Gueslin et al., 2006), however, this is not antithetical because aging equally affects the magnitude of the unsheared region.

Due to the small size of the (2mm) glass sphere coupled with the high viscosity and yield stress of the Fluid B, the vector field induced by the settling sphere was not easily distinguishable from the entire flow field of the fluid because the velocity vectors had relatively similar magnitude

(Figure 15). In order to buttress the effect of increased yield and get a clearer vector image, a larger particle size (3mm) is also used for Fluid B shown in Figure 16.

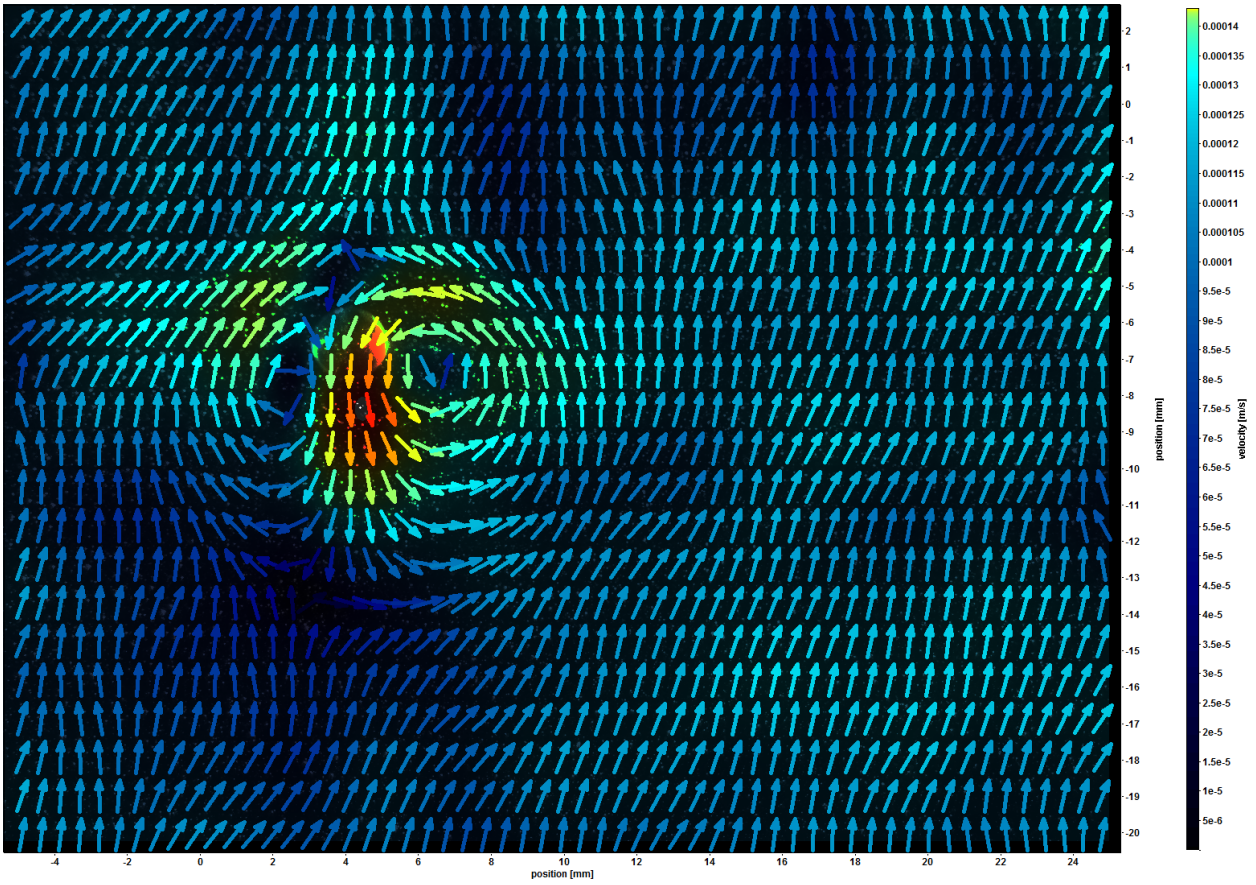

Figure 6.15: Velocity Field Induced by 2mm Sphere in Fluid B

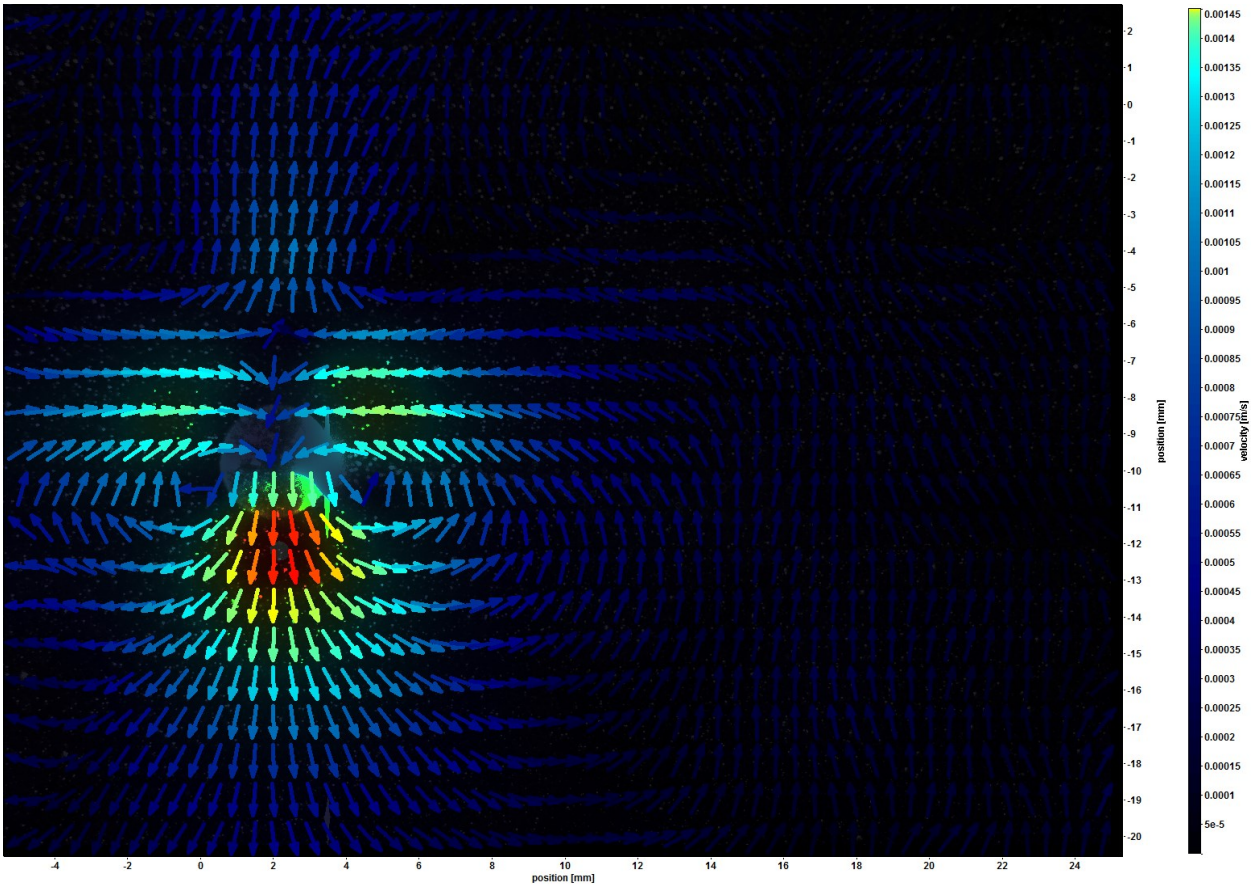

Figure 6.16: Velocity field Induced by 3mm Sphere in Fluid B

The negative wake is also noticeable in both images due to the elastic properties and the stagnation point is much closer to the sphere. The downstream V cone shape disappears with its angle now perpendicular to the centerline axis of the settling sphere. We postulate that these disparities may be due to the reduced settling velocity resulting from increased yield stress and viscosity. The high internal viscous friction resists deformation induced by the settling sphere hence the perpendicularity and close proximity of the stagnation points. The viscosity profile of

both fluids are shown in Figure 7 with Fluid C having the highest viscosity. The yield stress also plays a major role in this phenomenon.

The yield stress is associated with the fortitude of the internal structure of the fluid causing it to act like a solid until the applied stress exerted by the settling particle exceeds the strength of the internal structure causing deformation. The durable internal structure of the fluid imposes a drag on the settling particle which gradually dampens the stress imposed on the fluid by the settling particle. This causes a change in the fluid flow field induced by a particle in a high yield stress compared to a lower yield stress fluid. As a result of this inhibitive effect of the yield stress, the settling velocity is greatly reduced. This reduced speed may lead to an upstream shift of the stagnation point closer to the particle which was posited in the experimental study conducted by Arigo and Mckinley, (1998) and Fraggedakis, Dimakopoulos and Tsamopoulos (2016). The results of the Particle Image Shadowgraphy tests for measuring the particle settling velocity are shown in Table 4.

Table 6.4: Measured Particle Settling Velocity in Fluid A and Fluid B

Experimental Fluid	Particle Settling Velocity (m/s)
Fluid A (2mm Glass Sphere)	0.061
Fluid B (2mm Glass Sphere)	0.009
Fluid B (3mm Glass Sphere)	0.035

From the settling velocity measurement results, it is shown that both the yield stress and the elasticity can reduce the settling velocity. However the yield stress carries out the dampening effect with far greater potency. In order to buttress the effect of increased yield stress, the vector magnitude of the velocity profile along the centerline of the sphere is plotted against distance from the top of the settling sphere for all the fluids in Figure 17; similar to the earlier plot on Figure 14. The point of 0 m/s signified by a black straight line indicates the stagnation point downstream of the sphere.

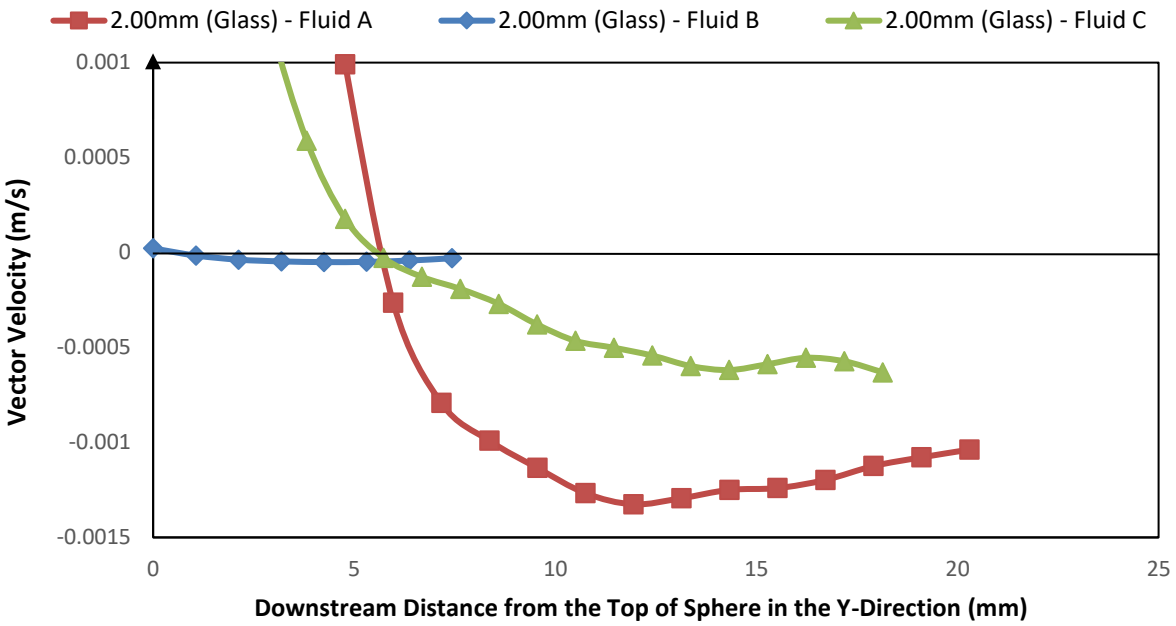

Figure 6.17: Vector Velocity Profile along the Centerline of the Sphere for 2.00mm in Fluid A and Fluid B

The fluid velocity vector profile is nearly non-existent for Fluid B compared to Fluid A and Fluid C. The fluid movement is restricted to the barest minimum with the maximum vector velocity recorded at 5.04 x10^{-5} m/s compared to 1.32 x 10^{-3} m/s of Fluid A and 5.56 x 10^{-4} m/s for Fluid C which are several magnitudes higher. Such low velocity indicate the effectiveness of

increased yield stress in reducing settling velocity thereby aiding particle transport and suspension. However, from the practical point of view it would probably be more efficient to control particle suspension by increasing the fluid elasticity rather than increasing the fluid viscosity and yield stress because fluid with higher yield stress and viscosity may require more hydraulic energy (i.e. increased frictional pressure losses and associated pumping cost to transport more viscous fluids).

6.4.4 Shape of Sheared Region

6.4.4.1 Shape of Sheared Regions Induced by a 2mm Spherical Particle Settling in Fluid A

The results of the shape of the sheared region obtained from processing the PIV images are shown in the followings. Figure 16 shows the shape induced by 2mm particle settling in Fluid A. The blended raw image is attached to the right hand side to show the position of the sphere. Three different sheared regions are showed with the innermost being the most yielded. This is congruent with reports from literature (Chhabra, 2006). The outer region spreads wider downwards with two extended elevated (V shaped) horns at the top. Each of the regions have a different shape.

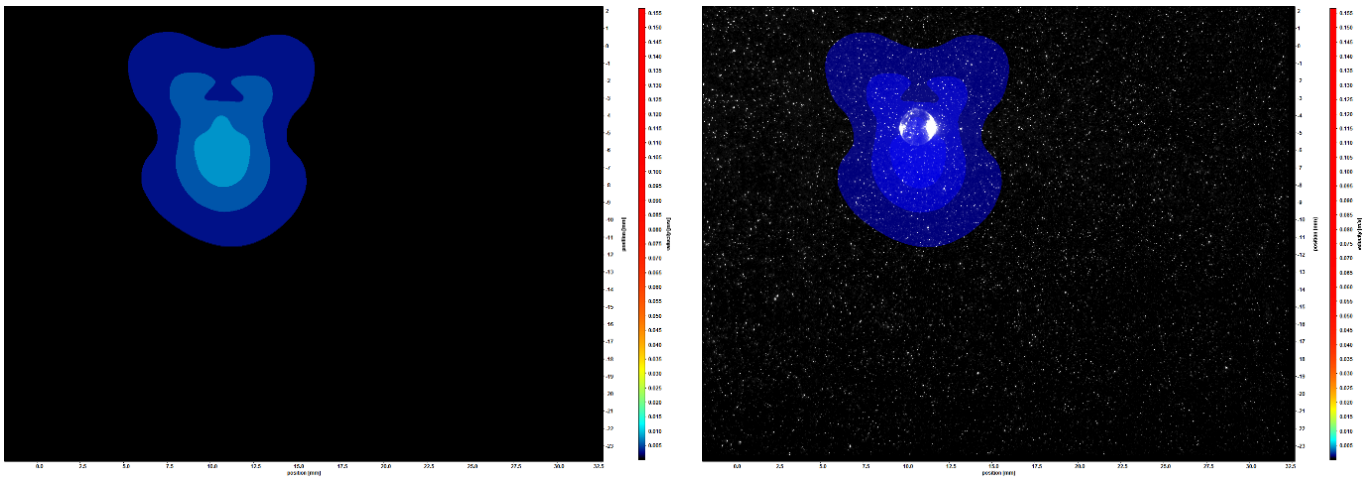

Figure 6.18: Shape of Sheared Regions Induced by a 2mm Spherical Particle Settling in Fluid A (Black represents the unyielded zone and the colored region represents the yielded zones. The blended raw image is attached to the right)

The innermost yielded region is very similar to the pear shape obtained in previous experimental study carried out by Holenberg et al. (2012), which confirms the accuracy of the experimental procedure. The two images are placed side by side for comparison (Figs. 17 and 18). Below the sphere, the wide extension is due to the stress imposed on the fluid by the settling sphere, which generates a plug like flow. This was first postulated by Putz *et al.*, (2008).

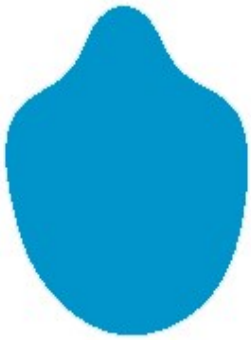

Figure 6.19: Innermost Yielded Region obtained in this current study.

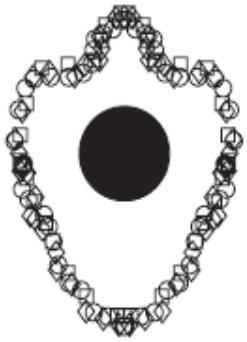

Figure 6.20: Shape of Yielded Region from Holenberg *et al.*, 2012

6.4.4.2 Shape of Sheared Regions Induced by 2mm & 3mm Spherical Particles Settling in Fluid B

Figure 21 represents the shape of the sheared region induced by 2mm sphere settling in Fluid B while Figure 22 represents the shape of the sheared region induced by 3mm sphere settling in Fluid B. Note that Fluid B is more viscous and has a higher yield stress than Fluid A. The

intensity range of the optical bit shift had to be adjusted to capture the low magnitude sheared regions due to the low settling velocity.

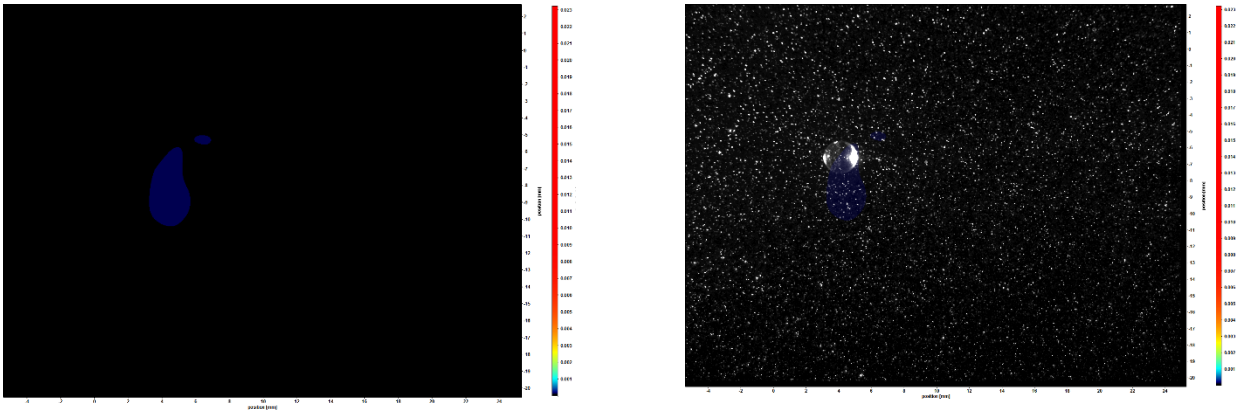

Figure 6.21: Shape of Sheared Regions Induced by a 2mm sphere Settling in Fluid B

(The raw blended image is shown at the right)

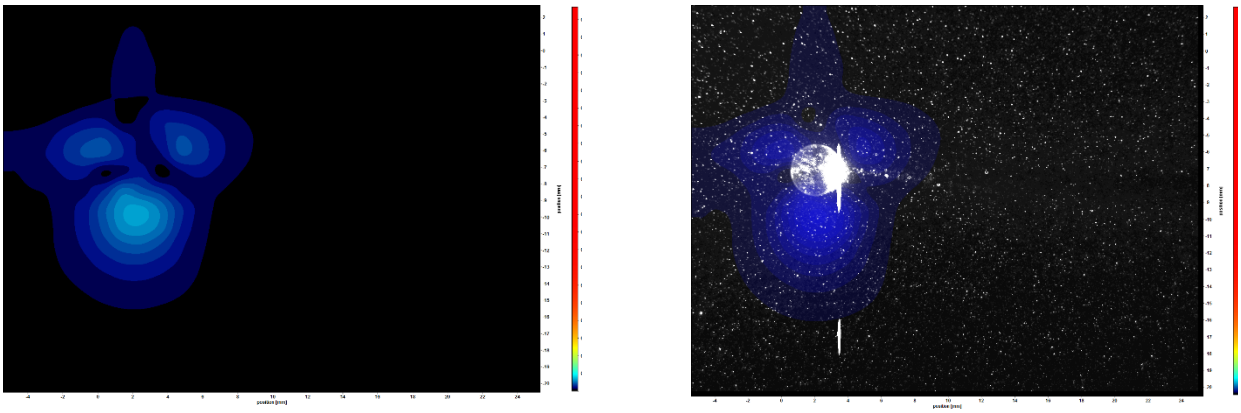

Figure 6.22: Shape of Sheared Regions Induced by a 3mm sphere Settling in Fluid B

(The raw blended image is shown at the right)

The first observation in Figure 21 is the irregular shape of the sheared region which doesn't completely surround the particle. This is due to the low settling velocity of the particle caused by the high yield stress of the fluid hence low quality vector fields were produced. Another observation is the size of the sheared region induced by the 2mm sphere in Fluid B. It is a whole lot smaller that the sheared region induced by the same 2mm spherical particle in Fluid A (Figure 18). As earlier stated, the size of the sheared region depicts the extent of influence a settling particle has on a fluid and it is salient because it indicates the settling behavior and magnitude of the particle settling velocity in a viscoplastic fluid. The smaller the size of sheared region, the greater the suspension efficiency of the fluid. The stress exerted by the 2mm particle in Fluid B is not as immense as that in Fluid A. This further buttresses the effect of increased yield stress on particle settling behavior. Due to the lack of considerable influence of the 2mm spherical particle in Fluid B, a larger sized particle (3mm) was introduced (Figure 22).

The first observation in Figure 22 is the unsheared or unyielded (black) regions located within the sheared regions. Yoshioka et al (1971) were one of the first proponents of the existence of stagnant unyielded regions within the sheared region, however, to the best of our knowledge this has not been confirmed experimentally till date. Our experimental results evinces proof of the existence of the stagnant unyielded zones located at the sides of the sphere as well as the top (Unyielded black zones). While the location of stagnant polar caps postulated by some authors were located at polar positions that is top and bottom (Beris et al., 1985; Yoshioka & Adachi, 1971), other authors have postulated the existence of these stagnant regions at the sides (Ansley & Smith, 1967). The high intensity velocity fields observed at the horns are analogous with images obtained from a similar study carried out by Holenberg et al. (2012). It is expected that sheared

region should become smaller with the increasing yield stress, however, a larger particle size (3mm) used in this case perhaps would induce more shear when settling. This is coherent with the fact that the shape of the sheared region is also factor of the mean surficial stress exerted by the settling particle on the fluid.

6.4.4.3 Shape of Sheared Regions Induced by 2mm Settling in Fluid C

Figure 20 presents the shape induced by a 2mm sphere settling in Fluid C. Fluid C is the more elastic fluid with relaxation time of 47 seconds. Elastic fluids have a high storage modulus, which portrays their distinctive capacity to store energy during deformation that can be used for regaining their original structure after deformation ends. However, the shape obtained is comparable to Fluid A due to their similar shear viscosity. This proves that yield stress and viscosity may play a greater role than elasticity in determining shapes of sheared region when the two forces are simultaneously existing in a fluid. The shape obtained for the Fluid C similarly has elevated horns and extends at the bottom. There are two inner sheared regions with the same intensity located within the outer sheared zone. One of the inner sheared region also takes the pear shape of Fluid A.

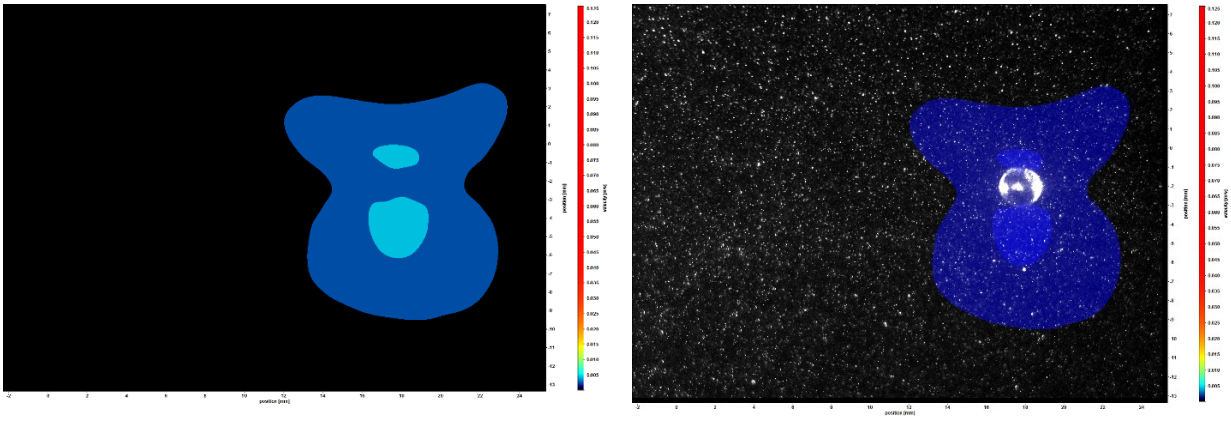

Figure 6.23: Shape of Sheared Regions Induced by a 3mm sphere Settling in Fluid B (The raw blended image is shown at the right)

If all the sheared regions induced by the 2mm spheres settling in the various experimental fluids are juxtaposed (Figures 18, 21 and 23), it is evident that Fluid B stands out in size and shape. The increase in elasticity makes no significant difference to the size of the sheared region (Figure 23) however there is a lack of surrounding layers which was present in Fluid A (Figure 18). Fluid B's exceptionality in shape and size of the sheared region demonstrates the primacy of yield stress in determining settling behavior of particles in viscoplastics fluids even in the presence of elasticity. The images obtained from the three fluids show that shapes of the sheared region are far from the conventional double circles predicted by the numerical models in Figure 1. The shapes of the sheared region observed in this study are eccentric.

6.5 Conclusions

An experimental study was carried out to visualize the flow field surrounding a settling particle in viscoplastic fluids exhibiting elastic and inelastic behaviors. This study was carried out to gain a deeper understanding of the individual effects of elasticity and viscous yield stress on the settling

behavior of spherical particles and shape of sheared region in viscoplastic fluids. It has been reported that both of these forces affect the settling behavior of particles in non-Newtonian fluids therefore making it vital to find out which of these two forces play a prominent role especially when transport fluid exhibit both properties simultaneously. Such knowledge is essential for the optimized design of engineering fluids for a variety of conditions

Experimental results showed that increasing elasticity of a fluid, which has same shear viscosity and yield stress, can dampen particle settling velocity and fluid velocity profile significantly, which is auspicious for fluid-particle transport systems. Elastic fluids have a relatively high storage modulus, which depicts their unique ability to store energy during deformation that can be used for partially or completely regaining of their original structure after deformation ends. This helps to dampen settling velocity as the fluid molecular structure tries to achieve pristine state and conditions. On the other hand, increasing viscosity and yield stress while keeping the elasticity constant can also produce the same effect even with far greater potency, however, more energy is required to transport more viscous fluids making it less efficient. This was evident in the vector velocity profile along the centerline of the sphere in which the fluid with the higher yield stress gave the lowest velocity magnitude and also achieved the lowest particle settling velocity of all three experimental fluids.

Furthermore, analysis of the experimental images showed that the set of fluids with disparate elastic property (but identical viscous property) produced similar shapes and size of the yielded region when sheared by the same particle however increasing the viscous yield stress reduces the shape of the yielded region and changes the shape of the yielded region. This further bolsters the position of the yield stress' primacy over elasticity in determining particle settling behavior in non-

Newtonian fluids. The shape and size of the sheared region indirectly illustrates the influence of a fluid's property on particle settling behavior in a non-Newtonian fluid. Smaller sheared regions indicate the higher resistance to particle sedimentation which is ideal for particle transport and suspension. The fluid with the higher yield stress gave the smallest shape of sheared region.

Finally, for the first time in literature this experimental study was able to visually proof the existence of the theoretically postulated stagnant regions within the sheared region that surrounds the settling particle.

6.6 Nomenclature

Symbol	Description	Unit
V_t	Terminal settling velocity	m/s
τ_{HB}	Herschel-Bulkley yield stress	lb/100ft^2
k	Herschel-Bulkley consistency index	lb.S^n/100ft^2
n	Herschel-Bulkley flow behaviour index	-
λ	Longest Relaxation Time	Sec

References

Ansley, R. W. and Smith, T. N. (1967) 'Motion of spherical particles in a Bingham plastic', *AIChE Journal*, 13(6), pp. 1193–1196. doi: 10.1002/aic.690130629.

API (2006) 'API Recommended Practice 13D, Recommended Practice on the Rheology and Hydraulics of Oil-Well Drilling Fluids', (5th ed.).

Arigo, M. T. and Mckinley, G. H. (1998) 'An experimental investigation of negative wakes behind spheres settling in a shear-thinning viscoelastic fluid', *Rheologica Acta Journal* 327, pp. 307–327.

Arnipally, S. K., Bizhani, M., & Kuru, E. (2018). Experimental Investigation Of Flow Field Past A Spherical Particle Settling In Viscoelastic Fluids Using Particle Image Velocimetry. In ASME 2018 37th International Conference on Ocean, Offshore and Arctic Engineering (OMAE 2018) (pp. 1–10).

Arnipally, S. K., & Kuru, E. (2017). Settling Velocity of Particles in Viscoelastic Fluids: A Comparison of the Shear Viscosity vs Elasticity Effect. In SPE Annual Technical Conference and Exhibition held in San Antonio, Texas, 9-11 October 2017.

Arnipally, S. K., & Kuru, E. (2018). Settling Velocity of Particles in Viscoelastic Fluids : A Comparison of the Shear-Viscosity and Elasticity Effects. SPE Journal, (October 2018), 1689–1705.

Atapattu, D. D., Chhabra, R. P. and Uhlherr, P. H. T. (1990) 'Wall Effects for Spheres falling at Small Reynolds Number in a Viscoplastic Medium', *Journal of Non-Newtonian Fluid Mechanics*, 38, pp. 31–42.

Beris, A. N., Tsamopoulos, J. A., Armstrong, R. C., & Brown, A. (1985). Creeping Motion of a Sphere through a Bingham plastic Fluid. Journal of Fluids Mechanics, 158, 218–244.

Blackery, J. and Mitsoulis, E. (1997) 'Creeping motion of a sphere in tubes filled with a Bingham plastic material', *Journal of Non-Newtonian Fluid Mechanics*, 70(1–2), pp. 59–77. doi: 10.1016/S0377-0257(96)01536-4.

Boardman, G. Whitmore, R.L. "The static measurement of yield stress" Laboratory Practice 10, p782 (1961).

Bush, M. B. (1993) 'The stagnation flow behind a sphere', *Journal of Non-Newtonian Fluid Mechanics*, 49(1), pp. 103–122. doi: 10.1016/0377-0257(93)85025-6.

Bush, M. B. (1994) 'On the stagnation flow behind a sphere in a shear-thinning viscoelastic liquid', *Journal of Non-Newtonian Fluid Mechanics*, 55(3), pp. 229–247. doi: 10.1016/0377-0257(94)80072-3.

Chhabra, R. (2006) *Bubbles, Drops, and Particles in Non-Newtonian Fluids, Second Edition*. doi: 10.1201/9781420015386.

Choi, S. K. (2008) 'p H Sensitive Polymers for Novel Conformance Control and Polymer Flooding Applications', *PhD Thesis, University of Texas, Austin*.

Curran, S. J. *et al.* (2002) 'Properties of Carbopol Solutions as Models for Yield-Stress Fluids'. doi: http://dx.doi.org/10.1016/j.placenta.2014.11.006.

Fraggedakis, D., Dimakopoulos, Y. and Tsamopoulos, J. (2016) 'Yielding the yield-stress analysis: A study focused on the effects of elasticity on the settling of a single spherical particle in simple yield-stress fluids', *Soft Matter*. Royal Society of Chemistry, 12(24), pp. 5378–5401. doi: 10.1039/c6sm00480f.

Frank, X., Dietrich, N. and Li, H. Z. (2014) 'A damping phenomenon in viscoelastic fluids', *Epl*, 105(5). doi: 10.1209/0295-5075/105/54006.

Frank, X. and Li, H. Z. (2006) 'Negative wake behind a sphere rising in viscoelastic fluids: A lattice Boltzmann investigation', *Physical Review E - Statistical, Nonlinear, and Soft Matter Physics*, 74(5), pp. 1–9. doi: 10.1103/PhysRevE.74.056307.

Gueslin, B. *et al.* (2006) 'Flow induced by a sphere settling in an aging yield-stress fluid', *Physics of Fluids*, 18(10). doi: 10.1063/1.2358090.

Gyr, A. and Bewersdorff, H.-W. (1995) 'Drag Reduction of Turbulent Flows by Additives', 32(0), p. 6221. doi: 10.1007/978-94-017-1295-8.

Harlen, O. G. (2002) 'The negative wake behind a sphere sedimenting through a viscoelastic fluid', *Journal of Non-Newtonian Fluid Mechanics*, 108(1–3), pp. 411–430. doi: 10.1016/S0377-0257(02)00139-8.

Holenberg, Y., Lavrenteva, O. M., Shavit, U., & Nir, A. (2012). Particle tracking velocimetry and particle image velocimetry study of the slow motion of rough and smooth solid

spheres in a yield-stress fluid PROCEDURE, 066301, 1–6. https://doi.org/10.1103/PhysRevE.86.066301

Lubrizol (2010) ‘Technical Data Sheet; Viscosity of Carbopol ® * Polymers in Aqueous Systems’.

Malhotra, S. and Sharma, M. M. (2012) ‘Settling of spherical particles in unbounded and confined surfactant-based shear thinning viscoelastic fluids: An experimental study’, *Chemical Engineering Science*, 84(January), pp. 646–655. doi: 10.1016/j.ces.2012.09.010.

McCabe, W. and Harriot, P. (1987) ‘Unit Operations Of Chemical Engineering, 5th Ed, McCabe And .pdf’, pp. 500–528. doi: 10.1016/j.eplepsyres.2011.07.014.

Mezger, T. G. (2006) *The Rheology Handbook*.

Petrie, C. J. S. (2006) ‘Extensional viscosity: A critical discussion’, *Journal of Non-Newtonian Fluid Mechanics*, 137(1–3), pp. 15–23. doi: 10.1016/j.jnnfm.2006.01.011.

Prashant and Derksen, J. (2011) ‘Direct simulations of spherical particle motion in Bingham liquids’, *Computers and Chemical Engineering*. Elsevier Ltd, 35(7), pp. 1200–1214. doi: 10.1016/j.compchemeng.2010.09.002.

Putz, A. M. V. *et al.* (2008) ‘Settling of an isolated spherical particle in a yield stress shear thinning fluid’, *Physics of Fluids*, 20(3). doi: 10.1063/1.2883937.

Raffel, M. *et al.* (2007) *Particle image velocimetry. [electronic resource] : a practical guide.*Availableat:

https://search.ebscohost.com/login.aspx?direct=true&db=cat00164a&AN=cran.553115&site=eds-live.

Richardson, J. F., Harker, J. H. and Backhurst, J. R. (2002) 'Chemical engineering Voulume 2', *Chemical Engineering Science*, 2. doi: 10.1016/0009-2509(60)80030-9.

Shokrollahzadeh, A. (2015) 'Terminal Settling Velocity of a Sphere in a non-Newtonian Fluid'. doi: 10.7939/R3Q23R76B.

Valentik, L. and Whitmore, R. L. (1965) 'The terminal velocity of spheres in Bingham plastics', *British Journal of Applied Physics*, 16(8), pp. 1197–1203. doi: 10.1088/0508-3443/16/8/320.

Volarovich, M. P., Gutkin, A. M. "Theory of flow of a viscoplastic medium." Colloid Journal. USSR, 15, p153 (1953).

Walters, K. and Tanner, R., "The Motion of a Sphere through an Elastic Fluid," in Transport Processes in Bubbles, Drops and Particles, Chhabra, R. P. and De Kee, D., Eds., ed New York: Hemisphere, 1992.

Wilson, K. C. *et al.* (2003) 'Direct prediction of fall velocities in non-Newtonian materials', *International Journal of Mineral Processing*, 71(1–4), pp. 17–30. doi: 10.1016/S0301-7516(03)00027-9.

Yoshioka, N. and Adachi, K. (1971) 'On variational principles for a non-Newtonian fluid', *Journal of Chemical Engineering of Japan*, 4, pp. 41–47. doi: 10.1007/bf01073578.

Yoshika, N., Adachi, K. "On variational principles for a non-Newtonian fluid." J. Chem. Eng. Jpn, 4, p217 (1971).

Zell, A. *et al.* (2009) ‘Is there a Relationship between the Elongational Viscosity and the First Normal Stress Difference in Polymer Solutions?’, pp. 1–22. Available at: http://arxiv.org/abs/0909.2506.

CHAPTER 7 : CONCLUSIONS AND RECOMMENDATIONS.

The chapter provides a comprehensive summary of the entire study. A detailed explanation and discussion of results have been presented in the individual chapters. The major summary and conclusion of this experimental study is presented in this chapter as well as recommendations for subsequent and future experimental study, thereby, providing a direction for enthusiastic researchers. The major conclusions from the study will be highlighted followed by individual conclusions from the three papers that this thesis is comprised of.

7.1 Major Summary and Conclusions of the Entire Study

An experimental study was conducted to further elucidate and describe the settling behavior of spheres in non-Newtonian fluids. The experimented fluids included those viscoelastic and viscoinelastic power law and viscoplastic fluids.

Mathematical models were formulated that describe and predict the settling velocities of particles in such fluids with high precision and accuracy. Furthermore, the fluid flow field surrounding the settling particles were further investigated using Particle Image Velocimetry (PIV).

For the first part of this thesis (Generalized Models for Predicting the Drag Coefficient and Settling Velocity of Rigid Spheres in Viscoelastic and Viscoinelastic Power-Law Fluids); the major summary of the experimental study can be highlighted in following key points.

- Current conventional approaches used for estimating particle settling velocity in power-law non-Newtonian fluids often exclude the effect of the fluid elasticity on the particle settling behavior, which can lead to erroneous estimation.

- It was therefore imperative to devise a means to mathematically and accurately account for elasticity in particle settling in viscoelastic fluids. An experimental study was conducted to measure the settling velocity of spherical particles in viscoelastic power law type fluids.
- Using a semi-mechanistic approach, an explicit mathematical model was developed for estimating drag coefficient and particle settling velocity in viscoelastic power law type fluids.
- A new drag coefficient versus particle Reynolds number correlations for viscoelastic and viscoinelastic power law fluids were developed based on the mechanistic analyses of the forces involved. The elasticity effect was accounted for by using the longest relaxation time.
- The newly developed correlation and an advanced statistical modelling program (OriginPro 9.0) were used to mathematically create an explicit model that can be used for predicting particle settling velocity in viscoelastic and viscoinelastic power-law type fluids.
- Comparative analysis showed that an increase in the fluid elasticity gave a corresponding decrease in the particle Reynolds number and dampened the particle settling velocity in viscoelastic fluids. This dampening effect can be attributed to the unique ability of elastic fluids to partially or fully regain their original structure after deformation.
- Furthermore, statistical analysis showed that the presented new models predict settling velocity accurately with a very low with a Percentage Mean Absolute Error (PMAE) of 7.5% and 11% for viscoinelastic and viscoelastic fluids respectively. The proposed models also exhibited very low Root Mean Square Error (RMSE) values of 0.04m/s and 0.03m/s for viscoinelastic and viscoinelastic fluids respectively.

For the second part of this thesis (A New Generalized Model for Predicting the Drag Coefficient and Settling Velocity of Rigid Spheres in Viscoplastic Fluids); The major summary of this experimental study can be highlighted in following key points.

- An experimental study was conducted to measure the settling velocity of spherical particles in viscoplastic fluids exhibiting elastic and inelastic properties. The fluids utilized were made from inelastic and elastic carbopol polymers.
- A semi-mechanistic model based on the balance of the forces acting on the settling particle and detailed statistical analyses of the experimental results were used to develop a generalized model for predicting settling velocity of spherical particles in viscoplastic fluids. The model was applicable to major types of viscoplastic fluids irrespective of their rheological property.
- This was achieved by measuring the settling velocities of the spherical particles with varying diameters and densities in various Carbopol solutions using Particle Image Shadowgraphy (PIS). The experimental results were combined with experimental data published in the literature to broaden the range and applicability of empirical analysis.
- In this study, a new modified shear Reynolds number (Re_T^*) was introduced, which physically quantifies the effects of non-Newtonian fluid rheological properties on the settling velocity. The newly developed C_D-Re_p correlation and the modified shear Reynolds number were incorporated into the Wilson *et al.* (2003) model to develop a generalized model that can be used for predicting particle settling velocity in viscoplastic fluids.

- The new model was shown to predict settling velocity better and yielded relatively more accurate results than existing models. Statistically speaking, it gave the lowest approximate Percentage Mean Absolute Error (PMAE) of 24.5 % for all data points. In addition to enhanced prediction accuracy, this new model occludes application constraints and offers prediction versatility that is lacking in current existing models by being valid for diverse rheological models of non-Newtonian viscoplastic fluids.
- The proposed generalized model was further assessed with elastic yield stress fluids in order to examine the effects of elasticity on the settling behavior of particles and to evaluate its prediction performance. The generalized model was able to provide settling velocity prediction for the elastic yield stress fluids with reasonable accuracy achieving a very low Percentage Mean Absolute Error of 30.15 % and Root Mean Square Error (RMSE) of 0.02 m/s.

For the final part of this thesis (Experimental Visualization and Analysis of Elastic and Viscous Effects on the Flow Field Surrounding a Settling Particle in Viscoplastic Fluids using Particle Image Velocimetry); the major summary of the experimental study can be highlighted in following key points.

- An experimental study was conducted to visualize and evaluate the flow field surrounding the sedimentation of spherical particles in viscoplastic fluids exhibiting elastic and inelastic behavior.
- Two sets of fluids were formulated from two distinct Carbopol polymers (ETD 2020 and 940). They were formulated in such a way that the first set of fluids exhibited similar

shear viscosity and yield stress but differed in elastic properties while the second set of fluids had almost identical elasticity but disparate shear viscosity and yield stress.

- The settling velocities of the spherical particles with varying diameters and densities in the various Carbopol solutions were measured using Particle Image Shadowgraphy (PIS) while the fluid flow field and sheared region surrounding the settling particle were determined using the advanced Particle Image Velocimetry (PIV) technique.
- The major results of the study showed that for the same shear viscosity, increasing elasticity can dampen the particle settling velocity and vector velocity profile by about 50% which is beneficial for particle suspension during fluid transport. This inhibiting effect can also be achieved with greater potency by increasing the yield stress as well.
- The set of fluids with different elastic property (but identical viscous property) gave similar shapes of yielded region when sheared by the same particle. However increasing the viscous yield stress reduces the shape of the yielded region and changes the shape of the yielded region. This indicates the prominence of viscous yield stress as a major deciding factor in determining the shape of the yielded region.
- Results also showed that the shape of sheared region depends on the mean surficial stress exerted on the fluid by the settling particle and yield stress of the fluid.
- Furthermore, the existence of theoretical unyielded regions adjacent to the settling particle were observed experimentally for the first time.

7.2 Conclusions from "Generalized Models for Predicting the Drag Coefficient and Settling Velocity of Rigid Spheres in Viscoelastic and Viscoinelastic Power-Law Fluids"

An experimental and empirical modeling study was carried out to describe the settling behavior of spherical particles in both viscoinelastic and viscoelastic power-law fluids with emphasis placed on quantifying the effect of the fluid elasticity. Polymer samples with varying viscoelastic properties were prepared and settling velocities of the particles with variable size and densities were measured in these fluids. The experimental results were combined with results from the literature to create a comprehensive database for viscoinelastic and viscoelastic fluids separately. Characteristic drag coefficient ($\sqrt{C_D}Re_p$) versus particle Reynolds number curves (Re_p) were developed for describing settling behavior of rigid spherical particles in both viscoinelastic and viscoelastic power-law fluids.

Comparative analysis showed that an increase in the elasticity gave a corresponding decrease in the particle Reynolds number and settling velocity for a specific$\sqrt{C_D}Re_p$. This dampening effect is due to the unique ability of elastic fluids to regain their original structure after deformation. This dampening effect can be leveraged upon in many technical operations where particle suspension is desired.

Explicit models were proposed to quantify and predict the particle settling behavior in viscoinelastic fluid as well as to account for the elasticity effects on the drag and settling velocity; thereby, accurately predict settling velocity of a particle falling through a viscoelastic fluid or viscoinelastic fluid.

Statistical analysis showed that the proposed models were indeed accurate and could predict the settling velocity of particles in viscoinelastic and viscoelastic power-law type fluids with a percentage mean absolute error of 7.5% and 11%, respectively. Root Mean Square Error values of 0.04m/s and 0.03m/s were also obtained for predicting the settling velocity of particles in viscoinelastic and viscoelastic power-law fluids, respectively. Plots of the predicted settling velocity (Vt_p) versus the measured settling velocity (Vt_m) gave high R^2 values of 0.97 and 0.98 for viscoinelastic and viscoelastic fluids, respectively with both plots having linear equations of Vtp ≈ Vtm

Notwithstanding the confident statistical result, supplementary research work is necessary to corroborate and ameliorate the accuracy of the proposed model especially in dynamic conditions not tested in this study. It is also recommended to investigate the influence of wall effects on the viscoelastic fluids.

7.3 Conclusions from "A New Generalized Model for Predicting the Drag Coefficient and Settling Velocity of Rigid Spheres in Viscoplastic Fluids."

A comprehensive experimental and empirical study was conducted to investigate the settling behavior of spherical particles in elastic and inelastic Yield Stress fluids using Particle Image Shadowgraphy (PIS). Over 90 different fluid-particle systems were investigated to augment the current corpus of experimental data. The experimental results were amalgamated with published data to produce a versatile C_D-Re_p curve with the aid of MATLAB (r2018b) curve fitting function.

A modified generalized shear Reynolds number Re_T^*, which quantifies the effect of non-Newtonian deviation on settling velocity was introduced and integrated with the developed C_D-

Re_p curve to generate an improved universal model for predicting settling velocity based on the Wilson *et al.* (2003) approach.

A statistical juxtaposition between the generalized model and other present models showed that the generalized model exhibited model independent versatility, on an average gave a lower standard error than the other models and exhibited the lowest average PMAE of about 24.5 %. It was also shown that the model provides reasonable prediction for settling velocity in Newtonian fluids with a low Root Mean Square Error of 0.1m/s.

The proposed generalized model was further assessed with elastic yield stress fluids in order to examine the effects of elasticity on the settling behavior of particles and to evaluate its prediction performance. The generalized model was able to provide settling velocity prediction for the elastic yield stress fluids with reasonable accuracy achieving a very low Percentage Mean Absolute Error of 30.15 % and Root Mean Square Error (RMSE) of 0.02 m/s. While elasticity reduces the settling velocity in certain non-Newtonian fluids; however in viscoplastic fluids the presence of a yield stress may eclipse the elastic property of the fluid leading to uniformity in settling behavior which can be predicted with the generalized model.

Regardless of the positive statistical result, additional research is imperative to corroborate and improve accuracy of the generalized model at extensive conditions including dynamic and hindered settling conditions which were not tested in this study. It is also recommended to investigate the effect of thixotropic aging on settling velocity.

7.4 Conclusions from "Experimental Visualization and Analysis of Elastic and Viscous Effects on the Flow Field Surrounding a Settling Particle in Viscoplastic Fluids using Particle Image Velocimetry (PIV)".

An experimental study was carried out to visualize the flow field surrounding a settling particle in viscoplastic fluids exhibiting elastic and inelastic behaviors. This study was carried out to gain a deeper understanding of the individual effects of elasticity and viscous yield stress on the settling behavior of spherical particles and shape of sheared region in viscoplastic fluids. It has been reported that both of these forces affect the settling behavior of particles in non-Newtonian fluids therefore making it vital to find out which of these two forces play a prominent role especially when transport fluid exhibit both properties simultaneously. Such knowledge is essential for the optimized design of engineering fluids for a variety of conditions

Experimental results showed that increasing elasticity of a fluid, which has same shear viscosity and yield stress, can dampen particle settling velocity and fluid velocity profile significantly, which is auspicious for fluid-particle transport systems. Elastic fluids have a relatively high storage modulus, which depicts their unique ability to store energy during deformation that can be used for partially or completely regaining of their original structure after deformation ends. This helps to dampen settling velocity as the fluid molecular structure tries to achieve pristine state and conditions. On the other hand, increasing viscosity and yield stress while keeping the elasticity constant can also produce the same effect even with far greater potency, however, more energy is required to transport more viscous fluids making it less efficient. This was evident in the vector velocity profile along the centerline of the sphere in which the fluid with the higher yield stress gave the lowest velocity magnitude and also achieved the lowest particle settling velocity of all three experimental fluids.

Furthermore, analysis of the experimental images showed that the set of fluids with disparate elastic property (but identical viscous property) produced similar shapes and size of the yielded region when sheared by the same particle however increasing the viscous yield stress reduces the shape of the yielded region and changes the shape of the yielded region. This further bolsters the position of the yield stress' primacy over elasticity in determining particle settling behavior in non-Newtonian fluids. The shape and size of the sheared region indirectly illustrates the influence of a fluid's property on particle settling behavior in a non-Newtonian fluid. Smaller sheared regions indicate the higher resistance to particle sedimentation which is ideal for particle transport and suspension. The fluid with the higher yield stress gave the smallest shape of sheared region.

Finally, for the first time in literature this experimental study was able to visually proof the existence of the theoretically postulated stagnant regions within the sheared region that surrounds the settling particle.

7.5 Recommendations for future study.

Despite the success of this experimental and semi-mechanistic study, additional research is imperative to corroborate and improve accuracy of the proposed models as well as improving the quality of the PIV visualization experiments. Therefore, the following recommendations for the future work of this study are listed below for enthusiastic researchers;

- Additional work is required to carry out settling experiments at extensive conditions not tested in this study including extreme laminar and dynamic conditions.

- It is also necessary to devise a means to mathematically model consecutive and hindered settling of spheres, which was not carried out in this study.
- Inclined settling conditions should also be investigated. Inclined settling which is representative of typical conditions faced in current directional drilling operations in the industry.
- The effect of thixotropy on settling velocity should be investigated and modelled to aid accurate description of particle settling behavior in non-Newtonian fluids. Some non-Newtonian fluids are thixotropic, meaning their rheological properties are time dependent after deformation occurs. This deformation can be induced by shearing or a spherical particle falling through the layers of the fluid. A thixotropic fluid would need time to heal and regenerate to its original form after deformation occurs; if not all measurements carried out on it would not depict its actual property.

REFERENCES

Acharya, A. (Ruma). (1986). Particle Transport in Viscous and Viscoelastic Fracturing Fluids.pdf. *SPE Production Engineering*, *34*(March), 104–110. https://doi.org/10.2118/13179-PA

Agwu, O. E., Akpabio, J. U., Alabi, S. B., & Dosunmu, A. (2018). Settling velocity of drill cuttings in drilling fluids: A review of experimental, numerical simulations and artificial intelligence studies. *Powder Technology*, *339*, 728–746. https://doi.org/10.1016/j.powtec.2018.08.064

Anibarro, G. (2012). Laser Safety: Hazards, Bioeffects, and Control Measures. Laser Institute of America https://docplayer.net/20891945-Laser-safety-hazards-bioeffects-and-control-measures.html

Ansley, R. W., & Smith, T. N. (1967). Motion of spherical particles in a Bingham plastic. *AIChE Journal*, *13*(6), 1193–1196. https://doi.org/10.1002/aic.690130629

API. (2006). API Recommended Practice 13D, Recommended Practice on the Rheology and Hydraulics of Oil-Well Drilling Fluids, (5th ed.).

Arabi, A. S., & Sanders, R. S. (2016). Particle terminal settling velocities in non-Newtonian viscoplastic fluids. *Canadian Journal of Chemical Engineering*, *94*(6), 1092–1101. https://doi.org/10.1002/cjce.22496

Arigo, M. T. and Mckinley, G. H. (1998) 'An experimental investigation of negative wakes behind spheres settling in a shear-thinning viscoelastic fluid', Rheologica Acta Journal 327, pp. 307–327.

Arnipally, S. K., Bizhani, M., & Kuru, E. (2018). Experimental Investigation Of Flow Field Past

A Spherical Particle Settling In Viscoelastic Fluids Using Particle Image Velocimetry. In ASME 2018 37th International Conference on Ocean, Offshore and Arctic Engineering (OMAE 2018) (pp. 1–10).

Arnipally, S. K., & Kuru, E. (2017). Settling Velocity of Particles in Viscoelastic Fluids: A Comparison of the Shear Viscosity vs Elasticity Effect. In SPE Annual Technical Conference and Exhibition held in San Antonio, Texas, 9-11 October 2017.

Arnipally, S. K., & Kuru, E. (2018). Settling Velocity of Particles in Viscoelastic Fluids : A Comparison of the Shear-Viscosity and Elasticity Effects. SPE Journal, (October 2018), 1689–1705.

Atapattu, D. D., Chhabra, R. P., & Uhlherr, P. H. T. (1990). Wall Effects for Spheres falling at Small Reynolds Number in a Viscoplastic Medium. *Journal of Non-Newtonian Fluid Mechanics*, *38*, 31–42.

Atapattu, D. D., Chhabra, R. P., & Uhlherr, P. H. T. (1995). Creeping sphere motion in Herschel-Bulkley fluids: flow field and drag. *Journal of Non-Newtonian Fluid Mechanics*, *59*(2–3), 245–265. https://doi.org/10.1016/0377-0257(95)01373-4

Barnes, H. A. (1999). The yield stress—a review or ‘παντα ρ ι’—everything flows? *Journal of Non-Newtonian Fluid Mechanics*, *81*(May 1998), 81(1-2), 133–178.

Barnes, H. A. (2000). *A handbook of elementary rheology*. *Science* (Vol. 331). https://doi.org/10.1126/science.1201543

Benchabane, A., & Bekkour, K. (2008). Rheological properties of carboxymethyl cellulose (CMC)

solutions. *Colloid and Polymer Science*, *286*(10), 1173–1180. https://doi.org/10.1007/s00396-008-1882-2

Beris, A. N., Tsamopoulos, J. A., Armstrong, R. C., & Brown, A. (1985). Creeping Motion of a Sphere through a Bingham plastic Fluid. Journal of Fluids Mechanics, 158, 218–244.Bingham, E. C. (1922). *Fluidity and Plasticity*. McGraw-Hill Book Company, Inc.

Blackery, J., & Mitsoulis, E. (1997). Creeping motion of a sphere in tubes filled with a Bingham plastic material. *Journal of Non-Newtonian Fluid Mechanics*, *70*(1–2), 59–77. https://doi.org/10.1016/S0377-0257(96)01536-4

Briscoe, B. J., Glaese, M., Luckham, P. F., & Ren, S. (1992). The falling of spheres through Bingham fluids. *Colloids and Surfaces*, *65*(1), 69–75. https://doi.org/10.1016/0166-6622(92)80176-3

Brown, P. P., & Lawler, D. F. (2003). Sphere Drag and Settling Velocity Revisited. *Journal of Environmental Engineering*, *129*(3), 222–231. https://doi.org/10.1061/(ASCE)0733-9372(2003)129:3(222)

Bui, B., Saasen, A., Maxey, J., & Ozbayoglu, M. (2012). Viscoelastic Properties of Oil-Based Drilling Fluids. *Annual Transactions of the Nordic Rheology Society*, *20*, 33–47.

Bush, M. B. (1993). The stagnation flow behind a sphere. *Journal of Non-Newtonian Fluid Mechanics*, *49*(1), 103–122. https://doi.org/10.1016/0377-0257(93)85025-6

Bush, M. B. (1994). On the stagnation flow behind a sphere in a shear-thinning viscoelastic liquid. *Journal of Non-Newtonian Fluid Mechanics*, *55*(3), 229–247. https://doi.org/10.1016/0377-

0257(94)80072-3

Castrejon-Garcia, R., Castrejon-Pita, J. R., Martin, G. D., & Hutchings, I. M. (2011). The Shadowgraphy Imaging Technique and its Modern Application to Fluid Jets and Drops, *57*(3), 266–275. Retrieved from http://search.proquest.com/technologycollection/docview/878341405/2C1FD9CBFB468EPQ/6?accountid=28155#

Chafe, N. P., & de Bruyn, J. R. (2005). Drag and relaxation in a bentonite clay suspension. *Journal of Non-Newtonian Fluid Mechanics*, *131*(1–3), 44–52. https://doi.org/10.1016/j.jnnfm.2005.08.010

Cheng, N. S. (2009). Comparison of formulas for drag coefficient and settling velocity of spherical particles. *Powder Technology*, *189*(3), 395–398. https://doi.org/10.1016/j.powtec.2008.07.006

Chhabra, R. (2006). *Bubbles, Drops, and Particles in Non-Newtonian Fluids, Second Edition* (Vol. 113). https://doi.org/10.1201/9781420015386

Chhabra, R. P. (1983). Some remarks on "Drag coefficients of a slowly moving sphere in Non-Newtonian fluids." *Journal of Non-Newtonian Fluid Mechanics*, *13*(2), 225–227. https://doi.org/10.1016/0377-0257(83)80018-4

Chhabra, R. P., Uhlherr, P. H. ., & Boger, D. . V. (1980). The Influence of Fluid Elasticity on the Drag Coeeficient for Creeping Flow Around a Sphere. *Journal of Non-Newtonian Fluid Mechanics*, *6*, 187–199.

Chien, S.-F. (1994). Settling Velocity of Irregularly Shaped Particles. *SPE Drilling & Completion*, *9*(04), 281–289. https://doi.org/10.2118/26121-PA

Choi, S. K. (2008). p H Sensitive Polymers for Novel Conformance Control and Polymer Flooding Applications. *PhD Thesis, University of Texas, Austin*.

Clift, R., Grace, J.R. and Weber, M.E. (1978) Bubbles, Drops and Particles. Academic Press, New York.

Curran, S. J., Hayes, R. E., Afacan, A., Williams, M. ., & Tanguy, P. A. (2002). Properties of Carbopol Solutions as Models for Yield-Stress Fluids. https://doi.org/http://dx.doi.org/10.1016/j.placenta.2014.11.006

Dedegil, M. Y. (1987). Drag coefficient and settling velocity of particles in non-Newtonian suspensions. *Journal of Fluids Engineering*, *109*(3), 319–323. https://doi.org/10.1115/1.3242667

Dinkgreve, M., Paredes, J., Denn, M. M., & Bonn, D. (2016). On different ways of measuring "the" yield stress. *Journal of Non-Newtonian Fluid Mechanics*, *238*, 233–241. https://doi.org/10.1016/j.jnnfm.2016.11.001

Dolejš, V., Doleček, P., & Šiška, B. (1998). Drag and fall velocity of a spherical particle in generalized newtonian and viscoplastic fluids. *Chemical Engineering and Processing: Process Intensification*, *37*(2), 189–195. https://doi.org/10.1016/S0255-2701(97)00054-8

Fann Instrument Company. (2016). *FANN 35 instruction manual* (Vol. 207198). Retrieved from http://www.fann.com/fann/products/oil-well-cement-testing/viscosity/visc-model35.page

Fountain, M. S., Blanchard, J., Erikson, R. L., Kurath, D. E., Howe, D. T., Adkins, H., & Jenks, J. (2012). Design of a Particle Shadowgraph Velocimetry and Size (PSVS) system to Determine Particle Size and Density Distributions in Hanford Nuclear Tank Wastes. In *Waste Management-Tucson, Phoenix, Arizona, USA.* (Vol. 1, p. 0). https://doi.org/10.24200/tjer.vol1iss1pp0-0

Fraggedakis, D., Dimakopoulos, Y., & Tsamopoulos, J. (2016). Yielding the yield-stress analysis: A study focused on the effects of elasticity on the settling of a single spherical particle in simple yield-stress fluids. *Soft Matter*, *12*(24), 5378–5401. https://doi.org/10.1039/c6sm00480f

Frank, X., Dietrich, N., & Li, H. Z. (2014). A damping phenomenon in viscoelastic fluids. *Epl*, *105*(5). https://doi.org/10.1209/0295-5075/105/54006

Frank, Xavier, & Li, H. Z. (2006). Negative wake behind a sphere rising in viscoelastic fluids: A lattice Boltzmann investigation. *Physical Review E - Statistical, Nonlinear, and Soft Matter Physics*, *74*(5), 1–9. https://doi.org/10.1103/PhysRevE.74.056307

Galindo-Rosales, F. J., & Rubio-Hernández, F. J. (2006). Structural breakdown and build-up in bentonite dispersions. *Applied Clay Science*, *33*(2), 109–115. https://doi.org/10.1016/j.clay.2006.03.011

Gueslin, B., Talini, L., Herzhaft, B., Peysson, Y., & Allain, C. (2006). Flow induced by a sphere settling in an aging yield-stress fluid. *Physics of Fluids*, *18*(10). https://doi.org/10.1063/1.2358090

Gumulya, M. M., Horsley, R. R., & Wilson, K. C. (2007). The settling of consecutive spheres in viscoplastic fluids. *International Journal of Mineral Processing*, *82*(2), 106–115. https://doi.org/10.1016/j.minpro.2006.11.005

Gumulya, M. M., Horsley, R. R., Wilson, K. C., & Pareek, V. (2011). A new fluid model for particles settling in a viscoplastic fluid. *Chemical Engineering Science*, *66*(4), 729–739. https://doi.org/10.1016/j.ces.2010.11.037

Gyr, A., & Bewersdorff, H.-W. (1995). Drag Reduction of Turbulent Flows by Additives, *32*(0), 6221. https://doi.org/10.1007/978-94-017-1295-8

Haider, A., & Levenspiel, O. (1989). Drag coefficient and terminal velocity of spherical and nonspherical particles. *Powder Technology*, *58*(1), 63–70. https://doi.org/10.1016/0032-5910(89)80008-7

Harlen, O. G. (2002). The negative wake behind a sphere sedimenting through a viscoelastic fluid. *Journal of Non-Newtonian Fluid Mechanics*, *108*(1–3), 411–430. https://doi.org/10.1016/S0377-0257(02)00139-8

Hemphill, T., Campos, W., & Pilehvari, A. (1993). Yield-power law model more accurately predicts mud rheology.pdf. *Oil and Gas Journal*, *91*(34), 34. Retrieved from https://search-proquest-com.manchester.idm.oclc.org/docview/274440935?accountid=12253&rfr_id=info%3Axri%2Fsid%3Aprimo

Holenberg, Y., Lavrenteva, O. M., Shavit, U., & Nir, A. (2012). Particle tracking velocimetry and

particle image velocimetry study of the slow motion of rough and smooth solid spheres in a yield-stress fluid PROCEDURE, *066301*, 1–6. https://doi.org/10.1103/PhysRevE.86.066301

Hollabaugh, C. B., Burt, L. H., & Walsh, A. P. (2005). Carboxymethylcellulose. Uses and Applications. *Industrial & Engineering Chemistry*, *37*(10), 943–947. https://doi.org/10.1021/ie50430a015

Husband, D. M., Aksel, N., & Gleissle, W. (2002). The existence of static yield stresses in suspensions containing noncolloidal particles. *Journal of Rheology*, *37*(2), 215–235. https://doi.org/10.1122/1.550442

Ito, S., & Kajiuchi, T. (1969). Drag Force On A Sphere Moving in Plastic Fluid. *Journal of Chemical Engineering of Japan*, *2*(1), 19–24. https://doi.org/10.1252/jcej.2.19

Kealy, T. (2007). How To Measure Thixotropy for Pharmaceutical and Cosmetic Industries. *Rheology Solutions*, 1–17.

Kelessidis, V. (2003). Terminal velocity of solid spheres falling in newtonian and non newtonian liquids. *Tech. Chron. Sci.*, (1–2), 43–45.

Kelessidis, V. C., & Mpandelis, G. (2004). Measurements and prediction of terminal velocity of solid spheres falling through stagnant pseudoplastic liquids. *Powder Technology*, *147*(1–3), 117–125. https://doi.org/10.1016/j.powtec.2004.09.034

Kesely, M., & Matoušek, V. (2016). Laminar Settling of Glass Beads in Visco-Plastic Liquids. *Stavební Obzor - Civil Engineering Journal*, *25*(1). https://doi.org/10.14311/CEJ.2016.01.0001

Khalili Garakani, A. H., Mostoufi, N., Sadeghi, F., Hosseinzadeh, M., Fatourechi, H., Sarrafzadeh, M. H., & Mehrnia, M. R. (2011). Comparison Between Different Models for Rheological Characterization of Activated Sludge. *J . Environ . Health . Sci . Eng*, *8*(3), 255–264. https://doi.org/10.1515/jwld-2017-0053

Lali, A. M., Khare, A. S., Joshi, J. B., & Nigam, K. D. P. (1989). Behaviour of solid particles in viscous non-newtonian solutions: Settling velocity, wall effects and bed expansion in solid-liquid fluidized beds. *Powder Technology*, *57*(1), 39–50. https://doi.org/10.1016/0032-5910(89)80102-0

LaVision. (2003). Imager Intense, (0). https://doi.org/10.1007/0-387-29360-4_42

LaVision. (2008). Nd : YAG Laser Systems. *Nd : YAG Laser Systems*.

LaVision. (2013). DaVis 8.1 Software. *Product-Manual for DaVis 8.1*.

Lubrizol. (2010). Technical Data Sheet; Viscosity of Carbopol ® * Polymers in Aqueous Systems.

Machač, I., Ulbrichová, I., Elson, T. P., & Cheesman, D. J. (1995). Fall of spherical particles through non-Newtonian suspensions. *Chemical Engineering Science*, *50*(20), 3323–3327. https://doi.org/10.1016/0009-2509(95)00168-5

Malhotra, S., & Sharma, M. M. (2012). Settling of spherical particles in unbounded and confined surfactant-based shear thinning viscoelastic fluids: An experimental study. *Chemical Engineering Science*, *84*(January), 646–655. https://doi.org/10.1016/j.ces.2012.09.010

Maxey, J., Hughes, B., & Fluids, D. (2007). AADE-07-NTCE-37 Thixotropy and Yield Stress

Behavior in Drilling Fluids.

McCabe, W., & Harriot, P. (1987). Unit Operations Of Chemical Engineering, 5th Ed, McCabe And .pdf. https://doi.org/10.1016/j.eplepsyres.2011.07.014

Metzner, A. B., & Reed, J. C. (1955). Flow of Non-Newtonian Fluids-Correlation of the Laminar , Transition , and Turbulent-flow Regions, (4). https://doi.org/10.1002/aic.690010409

Mezger T. G., "Rheology Handbook," 2nd Edition, Vincentz Network, Hannover, 2006.

Miura, H., Takahashi, T., Ichikawa, J., & Kawase, Y. (2001). Bed expansion in liquid-solid two-phase fluidized beds with Newtonian and non-Newtonian fluids over the wide range of Reynolds numbers. *Powder Technology*, *117*(3), 239–246. https://doi.org/10.1016/S0032-5910(00)00375-2

Mohammed, M. A. R. (2013). Studying the Factors Affecting the Settling Velocity of Solid Particles in Non-Newtonian Fluids Terminal Settling Velocity :, *16*(1), 41–50.

Møller, P. C.F., Fall, A., & Bonn, D. (2009). Origin of apparent viscosity in yield stress fluids below yielding. *Epl*, *87*(3). https://doi.org/10.1209/0295-5075/87/38004

Moller, P., Fall, A., Chikkadi, V., Derks, D., & Bonn, D. (2009). An attempt to categorize yield stress fluid behaviour. *Philosophical Transactions of the Royal Society A: Mathematical, Physical and Engineering Sciences*, *367*(1909), 5139–5155. https://doi.org/10.1098/rsta.2009.0194

Møller, Peder C.F., Mewis, J., & Bonn, D. (2006). Yield stress and thixotropy: On the difficulty

of measuring yield stresses in practice. *Soft Matter*, *2*(4), 274–283. https://doi.org/10.1039/b517840a

Morrison, F. A. (2013). Data Correlation for Drag Coefficient for Spheres. *Cambridge University Press, New York*, *10*(November), 1–2.

Nobbs, D., Tang, P., & Raper, J. . (2002). The Design, Construction and Commissioning of a Low-Cost Optical Particle Size Analyser Specifically for Measuring of Settling Velocities and Size of Flocs. *Measurement Science and Technology*, *29*, 1–3.

Ovarlez, G., Cohen-Addad, S., Krishan, K., Goyon, J., & Coussot, P. (2013). On the existence of a simple yield stress fluid behavior. *Journal of Non-Newtonian Fluid Mechanics*, *193*, 68–79. https://doi.org/10.1016/j.jnnfm.2012.06.009

Petrie, C. J. S. (2006). Extensional viscosity: A critical discussion. *Journal of Non-Newtonian Fluid Mechanics*, *137*(1–3), 15–23. https://doi.org/10.1016/j.jnnfm.2006.01.011

Pinelli, D., & Magelli, F. (2001). Solids settling velocity and distribution in slurry reactors with dilute pseudoplastic suspensions. *Industrial and Engineering Chemistry Research*, *40*(20), 4456–4462. https://doi.org/10.1021/ie0010518

Prashant, & Derksen, J. (2011). Direct simulations of spherical particle motion in Bingham liquids. *Computers and Chemical Engineering*, *35*(7), 1200–1214. https://doi.org/10.1016/j.compchemeng.2010.09.002

Putz, A. M. V., Burghelea, T. I., Frigaard, I. A., & Martinez, D. M. (2008). Settling of an isolated spherical particle in a yield stress shear thinning fluid. *Physics of Fluids*, *20*(3).

https://doi.org/10.1063/1.2883937

Raffel, M., Willert, C., Wereley, S., & Kompenhans, J. (2007). *Particle image velocimetry. [electronic resource] : a practical guide.* Retrieved from https://search.ebscohost.com/login.aspx?direct=true&db=cat00164a&AN=cran.553115&site=eds-live

Rao, M. A. (2014). *Rheology of Fluid, Semisolid, and Solid Foods*. *Rheology of Fluid, Semisolid, and Solid Foods*. Springer US. https://doi.org/10.1007/978-1-4614-9230-6

Remondino, F., & Fraser, C. (2006). Digital Camera Calibration Methods : In *ISPRS Commission V Symposium "Image Engineering and Vision Metrology"* (pp. 266–272).

Reynolds, P. A., & Jones, T. E. R. (1989). An experimental study of the settling velocities of single particles in non-Newtonian fluids. *International Journal of Mineral Processing*, *25*(1–2), 47–77. https://doi.org/10.1016/0301-7516(89)90056-2

Richardson, J. F., Harker, J. H., & Backhurst, J. R. (2002). Chemical engineering Voulume 2. *Chemical Engineering Science*, *2*. https://doi.org/10.1016/0009-2509(60)80030-9

Rushd, S., Hassan, I., Sultan, R. A., Kelessidis, V. C., Rahman, A., Hasan, H. S., & Hasan, A. (2018). Terminal settling velocity of a single sphere in drilling fluid. *Particulate Science and Technology*, *0*(0), 1–10. https://doi.org/10.1080/02726351.2018.1472162

Saha, G., Purohit, N. K., & Mitra, A. K. (1992). Spherical particle terminal settling velocity and drag in Bingham liquids. *International Journal of Mineral Processing*, *36*(3–4), 273–281. https://doi.org/10.1016/0301-7516(92)90049-3

Shah, S. N., El-Fadili, Y. E., & Chhabra, R. P. (2007). New model for single spherical particle settling velocity in power law (viscoinelastic) fluids, *33*, 51–66. https://doi.org/10.1016/j.ijmultiphaseflow.2006.06.006

Shahi, S. (2014). *An Experimental Investigation of Settling Velocity of Spherical and Industrial Sand Particles in Newtonian and Non Newtonian Fluids using Particle Image Shadowgraph*. University of Alberta.

Shahi, S., & Kuru, E. (2015). An experimental investigation of settling velocity of natural sands in water using Particle Image Shadowgraph. *Powder Technology*, *281*, 184–192. https://doi.org/10.1016/j.powtec.2015.04.065

Shahi, S., & Kuru, E. (2016). International Journal of Mineral Processing Experimental investigation of the settling velocity of spherical particles in Power-law fl uids using particle image shadowgraph technique. *International Journal of Mineral Processing*, *153*, 60–65. https://doi.org/10.1016/j.minpro.2016.06.002

Shokrollahzadeh, A. (2015). Terminal Settling Velocity of a Sphere in a non-Newtonian Fluid. https://doi.org/10.7939/R3Q23R76B

Song, X., Xu, Z., Li, G., Pang, Z., & Zhu, Z. (2017). A new model for predicting drag coefficient and settling velocity of spherical and non-spherical particle in Newtonian fluid. *Powder Technology*, *321*, 242–250. https://doi.org/10.1016/j.powtec.2017.08.017

Sorbie, K. . (1992). *Polymer-Improved Oil Recovery*. *International Journal of Qualitative Studies in Education* (Vol. 5). Blackie and Son Ltd. https://doi.org/10.1080/0951839920050110

Stokes, G. G. (1905). On the Theories of the Internal Friction of Fluids in Motion, and of the Equilibrium and Motion of Elastic Solids. *Mathematical and Physical Papers Vol.1*, 75–129. https://doi.org/10.1017/CBO9780511702242.005

Tabuteau, H., Coussot, P., & de Bruyn, J. R. (2007). Drag force on a sphere in steady motion through a yield-stress fluid. *Journal of Rheology*, *51*(1), 125–137. https://doi.org/10.1122/1.2401614

Terfous, A., Hazzab, A., & Ghenaim, A. (2013). Predicting the drag coefficient and settling velocity of spherical particles. *Powder Technology*, *239*, 12–20. https://doi.org/10.1016/j.powtec.2013.01.052

Turton, R., & Levenspiel, O. (1986). A short note on the drag correlation for spheres. *Powder Technology*, *47*(1), 83–86. https://doi.org/10.1016/0032-5910(86)80012-2

Valentik, L., & Whitmore, R. L. (1965). The terminal velocity of spheres in Bingham plastics. *British Journal of Applied Physics*, *16*(8), 1197–1203. https://doi.org/10.1088/0508-3443/16/8/320

van den Brule, B. H. A. A., & Gheissary, G. (1993). Effects of fluid elasticity on the static and dynamic settling of a spherical particle. *Journal of Non-Newtonian Fluid Mechanics*, *49*(1), 123–132. https://doi.org/10.1016/0377-0257(93)85026-7

Walters, K., & Tanner, R. (1992). The Motion of a Sphere through an Elastic Fluid. *Transport Processes in Bubbles, Drops and Particles*.

Werner, B., Myrseth, V., & Saasen, A. (2017). Werner, B., Myrseth, V., & Saasen, A. (2017).

Viscoelastic properties of drilling fluids and their influence on cuttings transport. Journal of Petroleum Science and Engineering. http://doi.org/10.1016/j.petrol.2017.06.063scoelastic properties of drilling . *Journal of Petroleum Science and Engineering*. https://doi.org/10.1016/j.petrol.2017.06.063

Wilson, K. C., Horsley, R. R., Kealy, T., Reizes, J. A., & Horsley, M. (2003). Direct prediction of fall velocities in non-Newtonian materials. *International Journal of Mineral Processing*, *71*(1–4), 17–30. https://doi.org/10.1016/S0301-7516(03)00027-9

Wilson, K. C., & Thomas, A. D. (1985). A new analysis of the turbulent flow of non-newtonian fluids. *The Canadian Journal of Chemical Engineering*, *63*(4), 539–546. https://doi.org/10.1002/cjce.5450630403

Yoshioka, N., & Adachi, K. (1971). On variational principles for a non-Newtonian fluid. *Journal of Chemical Engineering of Japan*, *4*, 41–47. https://doi.org/10.1007/bf01073578

Zell, A., Gier, S., Rafaï, S., & Wagner, C. (2009). Is there a Relationship between the Elongational Viscosity and the First Normal Stress Difference in Polymer Solutions?, 1–22. Retrieved from http://arxiv.org/abs/0909.2506